Imperial College London

PhD Thesis

Double Network Hydrogels for Cartilage Repair and Their Nanocomposite Structure

---

Ali Mohammed

October 2017

Department of Materials

Imperial College London

Declarations

Declaration of originality

I hereby declare that the material presented in this thesis is the result of my own research that was carried out at Imperial College London, except where otherwise appropriately referenced.

Copyright

The copyright of this thesis rests with the author and is made available under a Creative Commons Attribution Non-Commercial No Derivatives licence. Researchers are free to copy, distribute or transmit the thesis on the condition that they attribute it, that they do not use it for commercial purposes and that they do not alter, transform or build upon it. For any reuse or redistribution, researchers must make clear to others the licence terms of this work.

Ali Mohammed

October 2017

Acknowledgments

First and foremost, I'd like to thank Professor Julian Jones for the great opportunity of being part of his lab, for his insight, his confidence in me and the freedom to conduct my research and apply my ideas freely. It has been an unforgettable journey as part of the LG01 family.

I would also like to thank all the past and current members of our lab. For the struggles and laughs we've shared through countless hours of lab work, for sharing our ideas openly and supporting each other when our experiments weren't working and all seemed doomed, we reassured each other until it all clicked. I thank you all. From you, I learned never to leave my lab book unattended.

I would like to thank my scholarship body, Qatar Foundation, for funding my scholarship. Thank you to Dr Siwei Li for conducting the cytotoxicity studies on my polymers and invaluable advice throughout my research. I would also like to thank Dr Alessandra Pinna and my co-supervisor Dr Theoni Georgiou for both their scientific advice and guidance.

Finally, I would like to thank both my parents, for putting all their effort into making sure I always obtained the best education, and for making it obvious at home that I was their favourite from all my siblings, despite their denials. Now that this thesis is published, it's official!

Abstract

Strong focus has been directed at cartilage tissue engineered biomaterials in the last decade. Cartilage defects affect a large global population with current treatments lacking the ability to provide a route to healthy hyaline cartilage, or a road to full recovery and normal mobility. Synthetic materials such as scaffolds and hydrogels are making breakthroughs as advanced biomaterials and have gathered momentum in providing a solution. In particular, double network hydrogels (DNHG) have become a standard for developing materials that replicate the properties of cartilage. DNHG consist of two contrasting polymers that are synthesised sequentially by free radical polymerization (FRP).

This thesis focuses on DNHG and their ability to be cross linked using silica nanoparticles (SNP) and nanoceria (NC) for the purpose of cartilage repair. These two nanostructures were chosen to provide the DNHG with tailorable mechanical properties. Polyacrylic acid (PAAc) and a poly2-acrylamido-2-methylpropane sulfonic acid (PAMPS) were chosen as the basis for the first networks, while polyacrylamide (PAAm) was chosen as the second network for both. The chemical, morphological and mechanical properties of these materials were investigated using several characterization techniques. Further, investigating the kinetics of FRP in an open-vessel environment revealed oxygen species impact conversion and reaction rates. The impact of GOx on cytotoxicity levels was also conducted on the separate polymers. The addition of glucose oxidase (GOx) as a degassing agent enhanced reaction kinetics, leading to faster and more efficient polymerizations that achieved 100 % polymer conversion. This allowed for optimization of the synthesis route, as well as reducing toxic monomers left in the material. The combination of NC and GOx proved to enhance the polymerization by utilising reaction by-products to create a cyclic reaction route. Finally, polymers were grafted on the surface of the nanostructures of both networks to form new DNHGs.

Table of Contents

Declarations 1
Acknowledgments 3
Abstract 5
List of Figures 10
List of Tables 16
List of abbreviations 19
1 Introduction 24
1.1 Thesis roadmap 26
2 Literature review 28
2.1 Cartilage anatomy, repair and regeneration 28
2.2 Developments in current clinical treatments and their limitations 31
2.3 Hydrogels for cartilage tissue engineering 35
2.4 Existing double network hydrogels 38
2.5 Silica nanoparticles 46
2.6 Hydrogel Polymerization techniques 49
2.7 Open vessel photopolymerization and oxygen inhibition 54
2.8 Degassing by glucose oxidase (GOX) 56
2.9 Graft polymerization from the surface of nanoparticles 58
2.10 Aims and objectives 62
3 Characterisation techniques 66
3.1 Dynamic Light Scattering (DLS) 66
3.2 Zeta potential 67
3.3 Scanning Electron Microscopy (SEM) 67
3.4 Transmission Electron Microscopy (TEM) 68
3.5 Proton Nuclear Magnetic Resonance (^{1}H NMR) Spectroscopy 69
3.6 Attenuated Total Reflection Fourier Transform Infrared Spectroscopy (FTIR) 69
3.7 Thermo Gravimetric Analysis (TGA) and Differential Scanning Calorimetry (DSC) 70
3.8 Ultraviolet and visible absorption spectroscopy light (UV-Vis) 71
3.9 Gel Permeation Chromatography (GPC) 72

3.10 Swelling studies 72
3.11 Mechanical Testing 73
4 Hybrid double network hydrogels with polyacrylic acid as a first network 76
4.1 Introduction 76
4.2 Methods and materials 77
4.3 Results and discussion 83
4.4 Conclusion 107
5 Hybrid nanocomposite double network hydrogels with silica nanoparticle cross linkers 112
5.1 Introduction 112
5.2 Methods and materials 113
5.3 Results and discussion 115
5.4 Conclusion 138
6 Optimizing open vessel photopolymerization using glucose oxidase 142
6.1 Introduction 142
6.2 Methods and materials 144
6.3 Results and discussion 147
6.4 Optimized double network hydrogels 159
6.5 Conclusion 168
7 Polymer grafts silica nanoparticle networks for double network hydrogels 172
7.1 Introduction 172
7.2 Methods and materials 173
7.3 Results and discussion 176
7.4 Conclusion 194
8 Polymer grafts on nanoceria via redox self-catalysis, for double network hydrogels .. 198
8.1 Introduction 198
8.2 Methods and materials 198
8.3 Results and discussion 203
8.4 Conclusion 226
9 Final remarks 230
9.1 Conclusions 230
9.2 Future work 235

References 237

List of Figures

Figure 1 - Schematic representation of the zonal layers of articular cartilage. Figure adapted from *Castro et al.*[12] 30
Figure 2 - Compressive (a) and tensile (b) stress-strain curves of bacterial cellulose (BC), gelatin and a BC / gelatin double network hydrogel (DNHG). Adapted from *Wu et al.* [66].....40
Figure 3 - Schematic representation of the compressive fracture mechanism of a double network hydrogel (DNHG) with silica nanoparticle (SNP) grafts before yielding (left), PAMPS/SNP broken into clusters (middle), and complete fracture (right). Figure adapted from *Fu et al.* [7] 44
Figure 4 - (a) the hydrolysis of tetraethyl orthosilicate (TEOS) under basic conditions, and (b) the condensation of silicic acid to form silica nanoparticles (SNPs).....47
Figure 5 - Photoinitiator Irgacure 2959 and its free radical form, under UV light[116]. 53
Figure 6 – The role of GOx as a catalyser for the β-D-glucose oxidation reaction and consequent oxygen inhibition. 57
Figure 7 - Formation of silica nanoparticles using TEOS. 78
Figure 8 - Surface functionalization of silica nanoparticles by APTES. 78
Figure 9 - Carbodiimide reaction of PAAc with EDC/NHS[173, 174]. 79
Figure 10 - Cross linking route between intermediate PAAc/NHS-ester and amine functionalized silica nanoparticles (ASNP).....80
Figure 11 - Schematic representation of a first network PAAc system cross linked with silica nanoparticles. 81
Figure 12 - Schematic representation showing the synthesis route for forming PAAc/PAAm double network hydrogels. 83
Figure 13 - (a) DLS graph showing size profile for 50 nm, 100 nm and 150 nm silica nanoparticles, (b) zeta potential graph showing bare and amine functionalized silica nanoparticle peaks. 84
Figure 14 - TEM images of silica nanoparticles with mean modal diameters of approximately (a) 50 nm, (b) 100 nm and (c) 150 nm silica nanoparticles. 84
Figure 15 - Freshly made PAAc/PAAm hydrogels before swelling (top) and after swelling for 150 h (bottom). Hydrogels shown from left to right: control, 2.5 wt %, 10 wt %, 20 wt %, 40 wt % loading with 150 nm amine silica nanoparticles (ASNPs). 86
Figure 16 - Swelling profile for PAAc/PAAm hydrogels with 150 nm amine silica nanoparticles (ASNPs) at different loading concentrations compared to control. 87
Figure 17 - Swelling profile for PAAc/PAAm hydrogels with 100 nm amine silica nanoparticles (ASNPs) at different loading concentrations compared to control. 88
Figure 18 - Swelling profile for PAAc/PAAm hydrogels with 50 nm amine silica nanoparticles (ASNPs) at different loading concentrations compared to control. 89
Figure 19 - FTIR spectra of Fresh PAAc/PAAm hydrogels with 150 nm silica nanoparticles (ASNP) at different loading concentrations compared to control. 91

Figure 20 - Fresh and Swollen samples of PAAc/PAAm hydrogels with 150 nm amine silica nanoparticles (ASNP) at 2.5 wt % loading. 92
Figure 21 - TGA showing nanoparticle retention for PAAc/PAAm hydrogels for 150 nm amine silica nanoparticles (ASNP) at different loading concentrations compared to control. 94
Figure 22 - TGA showing nanoparticle retention for PAAc/PAAm hydrogels for 100 nm silica nanoparticles (ASNP) at different loading concentrations compared to control. 95
Figure 23 - TGA showing nanoparticle retention for PAAc/PAAm hydrogels for 50 nm amine silica nanoparticles (ASNP) at different loading concentrations compared to control. 97
Figure 24 - A comparison of nanoparticle retention for PAAc/PAAm hydrogels with silica nanoparticles (ASNP) sizes of 150 nm, 100 nm and 50 nm at different loading concentrations. 99
Figure 25 - PAAc/PAAm hydrogel with 150 nm amine silica nanoparticles (ASNPs) at 20 wt % loading, under compression until fracture. 100
Figure 26 - Compression curves for PAAc/PAAm hydrogels with 150 nm amine silica nanoparticles (ASNPs) at different loading concentrations compared to control. 100
Figure 27 - Compression curves for PAAc/PAAm hydrogels with 100 nm amine silica nanoparticles (ASNPs) at different loading concentrations compared to control. 102
Figure 28 - Compression curves for PAAc/PAAm hydrogels with 50 nm amine silica nanoparticles (ASNPs) at different loading concentrations compared to control. 103
Figure 29 - Summary of compressive strengths of the DNHGs with varying sizes at varying ASNP concentrations, compared to a control 104
Figure 30 - Freeze dried PAAc/PAAm hydrogel with 150 nm amine silica nanoparticles (ASNPs) at 10 wt % loading. 105
Figure 31 - SEM image of a control PAAc/PAAm hydrogel. 106
Figure 32 - SEM images of control PAAc/PAAm hydrogels with 150 nm amine silica nanoparticles (ASNPs) at 10 wt % loading. ASNP are highlighted with red arrows, and polymer structures with white arrows. 107
Figure 33 - Surface functionalization of silica nanoparticles with VTEOS. 113
Figure 34 - Synthesis route for PAMPS/PAAm double network hydrogels containing vinyl silica nanoparticles (VSNPs). 115
Figure 35 - PAMPS/ PAAm hydrogel containing 150 nm vinyl silica nanoparticle (VSNPs) at 2.5 wt % loading swelling from 0 h to 6 d (top) and from right to left: control hydrogel, hydrogels containing 150 nm VSNP at 2.5 wt %, 5 wt %, 10 wt % and 20 wt % loading (bottom). 116
Figure 36 - Swelling profile for PAMPS/PAAm hydrogels with 150 nm vinyl silica nanoparticles (VSNPs) at different loading concentrations compared to control. 118
Figure 37- Swelling profile for PAMPS/PAAm hydrogels with 100 nm vinyl silica nanoparticles (VSNP) at different loading concentrations compared to control. 119
Figure 38 - Swelling profile for PAMPS/PAAm hydrogels with 50 nm vinyl silica nanoparticles (VSNP) at different loading concentrations compared to control. 120

Figure 39 - FTIR spectra for Fresh PAMPS/PAAm hydrogels with 150 nm vinyl silica Hydrogels containing 150 nm VSNP were freeze dried and investigated under SEM. ...122
Figure 40 - FTIR spectra for Swollen PAMPS/PAAm hydrogels with 150 nm vinyl silica nanoparticles (VSNP) at different loading concentrations compared to control.....123
Figure 41 - FTIR spectra comparing Fresh and Swollen PAMPS/PAAm hydrogels of 150 nm vinyl silica nanoparticles (VSNP) at 2.5 wt % loading. 124
Figure 42 - TGA and nanoparticle retention for PAMPS/PAAm hydrogels with 150 nm vinyl silica nanoparticles (VSNP) at different loading concentrations compared to control.....126
Figure 43 - TGA and nanoparticle retention for PAMPS/PAAm hydrogels with 100 nm vinyl silica nanoparticles (VSNP) at different loading concentrations compared to control.....128
Figure 44 - TGA and nanoparticle retention for PAMPS/PAAm hydrogels with 50 nm vinyl silica nanoparticles (VSNP) at different loading concentrations compared to control.....129
Figure 45 - A comparison of nanoparticle retention for PAMPS/PAAm hydrogels with 150 nm, 100 nm and 50 nm vinyl silica nanoparticles (VSNPs) at different loading concentrations. 131
Figure 46 - PAMPS/PAAm hydrogel with hydrogel containing 150 nm at 20 wt % vinyl silica nanoparticles (VSNP) loading, at different strains. 132
Figure 47 - Compression curves for PAMPS/PAAm hydrogels with 150 nm vinyl silica nanoparticles (VSNP) at different loading concentrations compared to control.....133
Figure 48 - Compression curves for PAMPS/PAAm hydrogels with 100 nm vinyl silica nanoparticles (VSNP) at different loading concentrations compared to control.....134
Figure 49 - Compression curves for PAMPS/PAAm hydrogels with 50 nm vinyl silica nanoparticles (VSNP) at different loading concentrations compared to control.....135
Figure 50 - PAMPS/PAAm hydrogel with 150 nm vinyl silica nanoparticles (VSNPs) at 20 wt % loading, before and after freeze drying. 136
Figure 51 - SEM images of control PAMPS/PAAm hydrogels. 137
Figure 52 – (a – f) SEM images of PAMPS/PAAm hydrogels with 150 nm, 20 wt % VSNP at different magnification. 138
Figure 53 - Schematic representation of the synthesis route for PAMPS/PAAm hydrogels in the presence of GOx. 146
Figure 54 - pKa of AMPS and PAMPS showing the equivalence point and 1/2 equivalence point. 148
Figure 55 - ^{1}H NMR of AAm monomers prior to polymerization in the presence of GOx (top) and at 100 % conversion to PAAm (bottom). Hydrogen protons near each atom are labelled with letters, representing ppm peaks on the graph. 149
Figure 56 - ^{1}H NMR of AMPS monomers prior to polymerization in the presence of GOx (top) and at 100 % conversion to PAMPS (bottom). Hydrogen protons near each atom are labelled with letters, representing ppm peaks on the graph. 150
Figure 57 - Conversion profiles at varying PI concentrations for AAm (left) and AMPS (right), in the presence of GOx compared to their respective controls. 151

Figure 58 - Kinetic profiles for AAm (left) and AMPS (right) at 0.5 wt % PI in the presence of GOx compared to their respective controls. 152
Figure 59 - (a) PAMPS (left) and PAAm (right) controls after photopolymerization with GOx, (b) PAMPS (left) and PAAm (right) controls after photopolymerization without GOx. 155
Figure 60 - Live/dead cell viability assay for PAAm in the presence of GOx at varying PI concentrations. 156
Figure 61 - Cell viability graph for PAAm in the presence of GOx at varying PI concentrations. * $p<0.05$ compared to 0 h and 24 h (room temperature). + $p<0.05$ compared to control 0.5 wt % PI, GOx 0.05 wt % PI and GOx 0.1 wt % PI). 157
Figure 62 - Live/dead cell viability assay for PAMPS in the presence of GOx at varying PI concentrations. 158
Figure 63 - Cell viability graph for PAMPS in the presence of GOx at varying PI concentrations. * $p<0.05$ compared to 0 h and 24 h (room temperature). 159
Figure 64 – PAMPS/PAAm hydrogel with 150 nm 20 wt % silica nanoparticles (VSNPs), before and after swelling. 161
Figure 65 – Swelling profile for PAMPS/PAAm hydrogels with 150 nm and 50 nm silica nanoparticles (VSNPs) with 20 wt % loading in the presence of GOx, compared to a control with GOx. 162
Figure 66 – TGA and nanoparticle retention for PAMPS/PAAm hydrogels with 150 nm silica nanoparticles (VSNPs) at 20 wt % loading in the presence of GOx, and control with GOx. .164
Figure 67 – TGA and nanoparticle retention for PAMPS/PAAm with 50 nm VSNP at 20 wt % loading in the presence of GOx, and control with GOx. 165
Figure 68 – Compression curves for hydrogels containing 150 nm and 50 nm vinyl silica nanoparticles (VSNPs) at 20 wt % loading, compared to control.....167
Figure 69 - SEM images of PAMPS/PAAm hydrogels with 150 nm vinyl silica nanoparticles (VSNPs). VSNPs are highlighted with white arrows. 168
Figure 70 – Grafting AMPS and AAm on the surface of amine functionalized SNP via CAN and SDS. 174
Figure 71 – Schematic representation showing the synthesis route for double network hydrogels (DNHG) containing silica nanoparticle (SNP). 176
Figure 72 – UV-Vis of bare and amine silica nanoparticles (SNP).....177
Figure 73 – UV-Vis of AAm monomer. 177
Figure 74 – UV-Vis of AMPS monomer. 178
Figure 75 – UV-Vis of AMPS in combination with SNP, SNP/CAN, and SNP/CAN/SDS compared to amine SNP. 179
Figure 76 – UV-Vis of AAm in combination with SNP, SNP/CAN, and SNP/CAN/SDS compared to amine SNP.....180
Figure 77 – FTIR spectra post graft polymerization of AAm onto amine silica nanoparticles (ASNP) compared to ASNPs and PAAm. 182
Figure 78 – FTIR spectra post graft polymerization of AMPS onto amine silica nanoparticles (ASNP) compared to ASNPs and PAMPS.....184

Figure 79 – TGA and DTG profiles for AAm graft polymerizations compared to bare and amine silica nanoparticles (ASNP). 185
Figure 80 – TGA and DTG profiles for AMPS graft polymerizations compared to bare and amine silica nanoparticles (ASNP). 187
Figure 81 – TEM images of an AMPS/ amine silica nanoparticles (ASNP)/CAN sample, showing polymeric mass surrounding ASNPs, highlighted with white arrows. 188
Figure 82 – TEM images of an AAm/ amine silica nanoparticles (ASNP)/CAN/SDS sample..189
Figure 83 – Conversion profile of AAm (left) and AMPS (right) with argon and GOx. 190
Figure 84 - Swelling profile for the amine silica nanoparticle (ASNP) hydrogel with PAMPS and PAAm polymer grafts. 192
Figure 85 - Images of a double network amine silica nanoparticles (ASNP) hydrogel with PAMPS and PAAm polymer grafts under compression at different strains. 193
Figure 86 - Compression curves for the amine silica nanoparticle (ASNP) hydrogel with PAMPS and PAAm polymer grafts. 194
Figure 87 – Schematic representation showing the synthesis and functionalization of nanoceria with APTES. 200
Figure 88 – Schematic showing the self-catalysis of polymer grafts on the surface of amine functionalized nanoceria. 201
Figure 89 – Schematic showing the synthesis route of nanoceria based double network hydrogels in the presence of GOx.....202
Figure 90 – TEM images of (a – b) bare nanoceria, (c –d) amine functionalized nanoceria. 204
Figure 91 – FTIR spectra of bare (NC) and amine nanoceria (ANC).....205
Figure 92 – UV-Vis spectra of bare (NC) and amine nanoceria (ANC).....206
Figure 93 – UV-Vis of AAm reactions with amine nanoceria (ANC), ANC/CAN and ANC/CAN/SDS compared to ANC.....207
Figure 94 – UV-Vis of AMPS reactions with amine nanoceria (ANC), ANC/CAN and ANC/CAN/SDS compared to ANC.....208
Figure 95 – FTIR spectra of AAm reactions with amine nanoceria (ANC), ANC/CAN and ANC/CAN/SDS compared to ANC and PAMPS. 210
Figure 96 – FTIR spectra of AMPS reactions with amine nanoceria (ANC), ANC/CAN and ANC/CAN/SDS compared to ANC and PAMPS. 211
Figure 97 – TGA and DTG profile of AAm with amine nanoceria (ANC), ANC/CAN and ANC/CAN/SDS compared to bare and amine ANC. 213
Figure 98 – TGA and DTG profile of AMPS with amine nanoceria (ANC), ANC/CAN and ANC/CAN/SDS compared to bare and amine ANC. 214
Figure 99 – TEM images of an AMPS/ANC sample at different magnifications showing ANC (white arrows) and newly formed porous AMPS based particles (red arrows). 215
Figure 100 – TEM images of an AAm/ANC sample at different magnifications showing ANC (white arrows) and newly formed AAm based particles (red arrows) and AAm polymeric masses. ANC were found to attach around the circumference of the newly formed AAm particles.....216

Figure 101 – Conversion profiles of reactions for AAm (left) and AMPS (right) with amine nanoceria (ANC), under argon and GOx. 218
Figure 102 – Conversion profiles for AAm and AMPS and with varying amine nanoceria (ANC) concentrations, in the presence of GOx. 219
Figure 103 – TGA and DTG profiles for AAm in the presence of GOx at varying amine nanoceria (ANC) concentrations. 220
Figure 104 – TGA and DTG profiles for AMPS in the presence of GOx at varying amine nanoceria (ANC) concentrations. 221
Figure 105 – images of (a) AMPS/ANC first network hydrogel after synthesis, (b) double network hydrogel after sequential synthesis containing PAMPS and PAAm. 222
Figure 106 – Swelling profile for a double network amine nanoceria (ANC) hydrogel with PAMPS and PAAm polymer grafts. 223
Figure 107 – Images of a double network amine nanoceria (ANC) hydrogel with PAMPS and PAAm polymer grafts under compression at different strains. 224
Figure 108 – Compression curves for the double network amine nanoceria (ANC) hydrogel with PAMPS and PAAm polymer grafts. 225
Figure 109 - SEM images of amine nanoceria (ANC) hydrogels with PAMPS and PAAm polymer grafts at varying magnifications. ANC are highlighted with white arrows. 226

List of Tables

Table 1 - Joint replacement surgeries under the NHS during 2016 and 2017[1] 24
Table 2 - Mechanical properties of articular cartilage[52-55] 37
Table 3 - Varying ASNP concentrations with equivalent carbodiimide reagent concentrations. 82
Table 4 - Swelling and water content for PAAc/PAAm hydrogels with 150 nm amine silica nanoparticles (ASNPs) at different loading concentrations compared to control. 88
Table 5 - Swelling and water content for PAAc/PAAm hydrogels with 100 nm amine silica nanoparticles (ASNPs) at different loading concentrations compared to control. 89
Table 6 - Swelling and water profile for PAAc/PAAm hydrogels with 50 nm amine silica nanoparticles (ASNPs) at different loading concentrations compared to control. 89
Table 7 - Summary of FTIR bands for PAAc/PAAm hydrogels. 90
Table 8 - nanoparticle retention for PAAc/PAAm hydrogels for 150 nm amine silica nanoparticles (ASNPs) at different loading concentrations compared to control. 94
Table 9 - nanoparticle retention for PAAc/PAAm hydrogels for 100 nm amine silica nanoparticles (ASNPs) at different loading concentrations compared to control. 96
Table 10 - nanoparticle retention for PAAc/PAAm hydrogels for 50 nm amine silica nanoparticles (ASNP) at different loading concentrations compared to control. 97
Table 11 - Compression and strain for PAAc/PAAm hydrogels with 150 nm amine silica nanoparticles (ASNPs) at different loading concentrations compared to control. 101
Table 12 - Compression and strain for PAAc/PAAm hydrogels with 100 nm amine silica nanoparticles (ASNPs) at different loading concentrations compared to control. 102
Table 13 - Compression and strain for PAAc/PAAm hydrogels with 50 nm amine silica nanoparticles (ASNPs) at different loading concentrations compared to control. 103
Table 14 - VSNP concentrations used in the first network. 114
Table 15 - Swelling and water content for PAMPS/PAAm hydrogels with 150 nm vinyl silica nanoparticles (VSNPs) at different loading concentrations compared to control. 118
Table 16 - Swelling and water content for PAMPS/PAAm hydrogels with 100 nm vinyl silica nanoparticles (VSNP) at different loading concentrations compared to control.....119
Table 17 - Swelling and water content for PAMPS/PAAm hydrogels with 50 nm vinyl silica nanoparticles (VSNP) at different loading concentrations compared to control.....121
Table 18 - Summary of FTIR bands for PAMPS/PAAm hydrogels. 121
Table 19 - nanoparticle retention for PAMPS/PAAm hydrogels with 150 nm vinyl silica nanoparticles (VSNP) at different loading concentrations compared to control.....126
Table 20 - nanoparticle retention for PAMPS/PAAm hydrogels with 100 nm vinyl silica nanoparticles (VSNP) at different loading concentrations compared to control.....128
Table 21 - nanoparticle retention for PAMPS/PAAm hydrogels with 50 nm vinyl silica nanoparticles (VSNP) at different loading concentrations compared to control.....130

Table 22 - Compression and strain for PAMPS/PAAm hydrogels with 150 nm vinyl silica nanoparticles (VSNP) at different loading concentrations compared to control.....133
Table 23 - Compression and strain for PAMPS/PAAm hydrogels with 100 nm vinyl silica nanoparticles (VSNP) at different loading concentrations compared to control.....134
Table 24 - Compression and strain for PAMPS/PAAm hydrogels with 50 nm vinyl silica nanoparticles (VSNP) at different loading concentrations compared to control.....135
Table 25 - Conversion for PAMPS and PAAm at varying PI concentrations in the presence of GOx, and without GOx (control). 151
Table 26 - GPC data for PAMPS at 0.05, 1 and 2 wt % PI in the presence of GOx compared to controls. 154
Table 27 - Swelling and water content for PAMPS/PAAm hydrogels with 150 nm and 50 nm silica nanoparticles (VSNPs) with 20 wt % loading in the presence of GOx, compared to a control with GOx. 162
Table 28 - nanoparticle retention for PAMPS/PAAm hydrogels containing 150 nm silica nanoparticles (VSNPs) at 20 wt % loading in the presence of GOx, and control with GOx. .164
Table 29 - Nanoparticle retention for PAMPS/PAAm containing 50 nm vinyl silica nanoparticles (VSNPs) at 20 wt % loading in the presence of GOx, and control with GOx. .166
Table 30 - Compression and strain for hydrogels containing 150 nm and 50 nm vinyl silica nanoparticles (VSNPs) at 20 wt % loading, compared to control.....167
Table 31 – Summary of FTIR bands for AAm grafted polymers on amine silica nanoparticles (SNPs) 181
Table 32 - Summary of FTIR bands for AAm grafted polymers on amine silica nanoparticles (SNPs) 183
Table 33 - Swelling and water content for the amine silica nanoparticle (ASNP) hydrogel with PAMPS and PAAm polymer grafts. 192
Table 34 - Fracture stress and strain for amine silica nanoparticle (ASNP) gels with PAMPS and PAAm polymer grafts. 194
Table 35 - Summary of FTIR bands for AAm grafted polymers on the surface of amine nanoceria (ANC) [71, 161, 192, 203]. 209
Table 36 - Summary of FTIR bands for AMPS grafted polymers on the surface of amine nanoceria (ANC) [80, 161, 192, 203]. 211
Table 37 - Swelling and water content for the double network amine nanoceria (ANC) hydrogel with PAMPS and PAAm polymer grafts. 223
Table 38 - Compression and strain values for the double network amine nanoceria (ANC) hydrogel with PAMPS and PAAm polymer grafts. 225
Table 39 - A summary of the properties of articular cartilage and the properties of the double network hydrogels developed in this thesis.....232

List of abbreviations

1^{st} NW: First network

^{1}H-NMR: Proton Nuclear Magnetic Resonance

2^{nd} NW: Second network

AAm: Acrylamide

AMPS: 2-Acrylamido-2-methylpropane sulfonic acid

ANC: Amine nanoceria

APTES: Amino propyl triethoxysilane

ASNP: Amine silica nanoparticles

ATR: Attenuated total reflection

BIS: N, N'-methylenebisacrylamide

CAN: Cerium (IV) ammonium nitrate

CTG: CellTrackerTM green

Đ: Dispersity

D_2O: Deuterium oxide

DLS: Direct light scattering

DMEM: Dulbecco's modified eagle medium

DMSO: Dimethyl sulfoxide

DNHG: Double network hydrogel

EDC: N-(3-dimethylaminopropyl)-N'-ethylcarbodiimide hydrochloride

EtOH: Ethanol

FCS: Foetal calf serum

FRP: Free-radical polymerization

FTIR: Fourier Transform Infrared Spectroscopy

G: Glucose

GOx: Glucose oxidase

GPC: hydrogel permeation chromatography

DTG: Derivative thermo gravimetric analysis

H_2O_2: Hydrogen peroxide

HCl: Hydrochloric acid

MES: 2-(N-morpholino) ethanesulfonic acid

MW: Molecular weight

M_w: Weight average molecular weight

MTT: 3-(4, 5-Dimethylthiazol-2-yl)-2, 5-diphenyltetrazolium bromide

M_n: Number average molecular weight

M_w/M_n: Polydispersity or molecular weight distribution

NaOH: Sodium hydroxide

NH_4OH: Ammonium hydroxide

NHS: N-hydroxysuccinimide

PAAc: Polyacrylic acid

PAAm: Polyacrylamide

PAMPS: Poly 2-acrylamido-2-methylpropane sulfonic acid

PBS: Phosphate-buffered saline

PDI: Polydispersity index

PFA: Paraformaldehyde

PI: Photoinitiator

PPM: Parts per million

SDS: Sodium dodecyl sulfate

SEM: Scanning electron microscopy

SNP: Silica nanoparticles

TEOS: Tetraethyl orthosilicate

TEM: Transmission electron microscopy

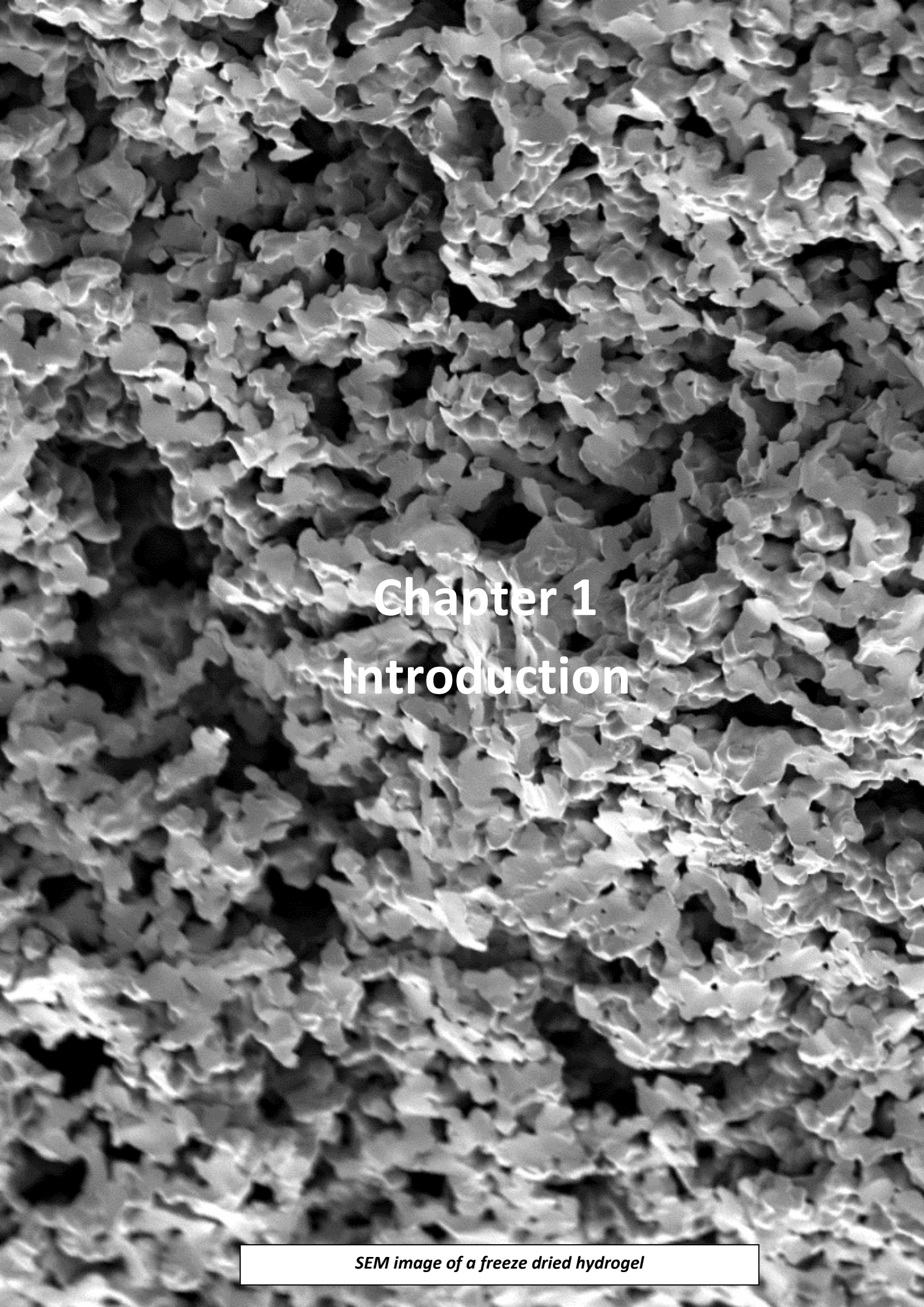
TGA: Thermo gravimetric analysis

VSNP: Vinyl silica nanoparticles

VTEOS: Vinyl tetra ethyl orthosilicate

Wt %: Weight %

Wt/v %: Weight/ volume %



Chapter 1
Introduction

SEM image of a freeze dried hydrogel

1 Introduction

Defects in articular cartilage can lead to severe pain, limited mobility and progressive degradation in the joint. The most common causes for defects in cartilage are physical trauma, wear and tear and degenerative joint diseases. Cartilage lacks the ability to self-repair due to its avascular nature and low local cell density; therefore small defects deteriorate until there is bone-on-bone contact. These are called osteochondral defects and can cause intense pain, ultimately requiring surgery. Hips and knees are the most commonly replaced joints in the body. According to the National Joint Registry in the UK, 69,121 knee replacement surgeries took place in 2016, and 38,285 knee replacements occurred in 2017 to date (Table 1)[1], all under the NHS. Surgery often leads to short term relief of symptoms. However, full functionality and mobility is not normally reached and follow up surgeries are commonly required.

Table 1 - Joint replacement surgeries under the NHS during 2016 and 2017[1]

NHS	2016	Year to date: 2017
Total completed ops	143,877	78,925
Hip procedures	67,568	36,589
Knee procedures	69,121	38,285
Ankle procedures	707	410
Elbow procedures	714	429
Shoulder procedures	5,767	3,212

Current medical treatments have had limited success due to their invasive character, and inability to form hyaline type cartilage. Rather, fibrocartilage tends to form resulting in further degradation and progression in osteoarthritis (OA). Tissue engineering aims at developing synthetic biomaterials that have the ability to regenerate, or replace, organs in the body. The avascular nature and poor repair mechanism of articular cartilage makes it a feasible candidate for 3D scaffolds. Cells can be incorporated into these 3D scaffolds, or matrices, whilst *in vitro* or implanted directly to recruit cells locally *in vivo*. The development of a host matrix for

implantation must meet certain requirements first. It must be biocompatible; this means that the material must not be harmful or toxic to the living tissue surrounding the implant, and must not cause immunological rejection. The material must also be bioactive, mimic the mechanical properties of the material, and for articular cartilage implants, must have low friction resistance[2]. Bioactive materials have the ability to stimulate a beneficial response from the body, such as bonding to host tissue. This could lead to cell attachment, and therefore initiate matrix formation that could result in hyaline cartilage formation. Many 3D scaffolds are designed to degrade simultaneously as the extracellular matrix (ECM) forms and develops tissue that resembles its native structure. This design allows a transition from synthetic material to natural tissue without the loss of mechanical integrity. Non-biodegradable scaffolds have also been developed where the scaffold remains in the body whilst forming tissue around it without immune-rejection[3].

Hydrogels have developed over the last two decades to become highly tailorable biomaterials that are able to mimic varying tissue in the body. Hydrogels are covalently bonded polymeric networks that possess similar mechanical, lubrication and swelling properties as native articular cartilage. Their intrinsic nature allows them to be synthesised from natural polymers (e.g. chitosan, alginate, hyaluronic acid) or synthetic polymers (e.g. polyacrylic acid, polyglycolic acid, polyethylene oxide), or a combination of the two. Cross linking density between polymer chains plays a significant role in determining the final properties of the material[4], as well as monomer composition and polymerization conditions. Hydrogels are classified based on whether the network is covalently or ionically cross linked, or physically entangled. Even though hydrogels are biocompatible and support cell growth, they still suffer from insufficient mechanical properties and a difficulty in aiding the regeneration of natural cartilage. This is due to chondrocytes synthesizing proteoglycans within 3 – 5 weeks whereas collagen production is significantly slower[5], and both are required to play key roles in the compression and tensile properties, respectively. Recent attempts to improve the mechanical properties of hydrogels for load bearing applications have included the incorporation of nanofibres (e.g. poly-ε-caprolactone[6] based nanofibres by

electrospinning), silica nanoparticles[7] as macro cross linkers, and the use of chemical cross linking agents.

The focus of this PhD will be to form hybrid hydrogels consisting of silica nanoparticles (SNPs) and nanoceria (NC) as cross linking agents, for cartilage tissue engineered applications.

1.1 Thesis roadmap

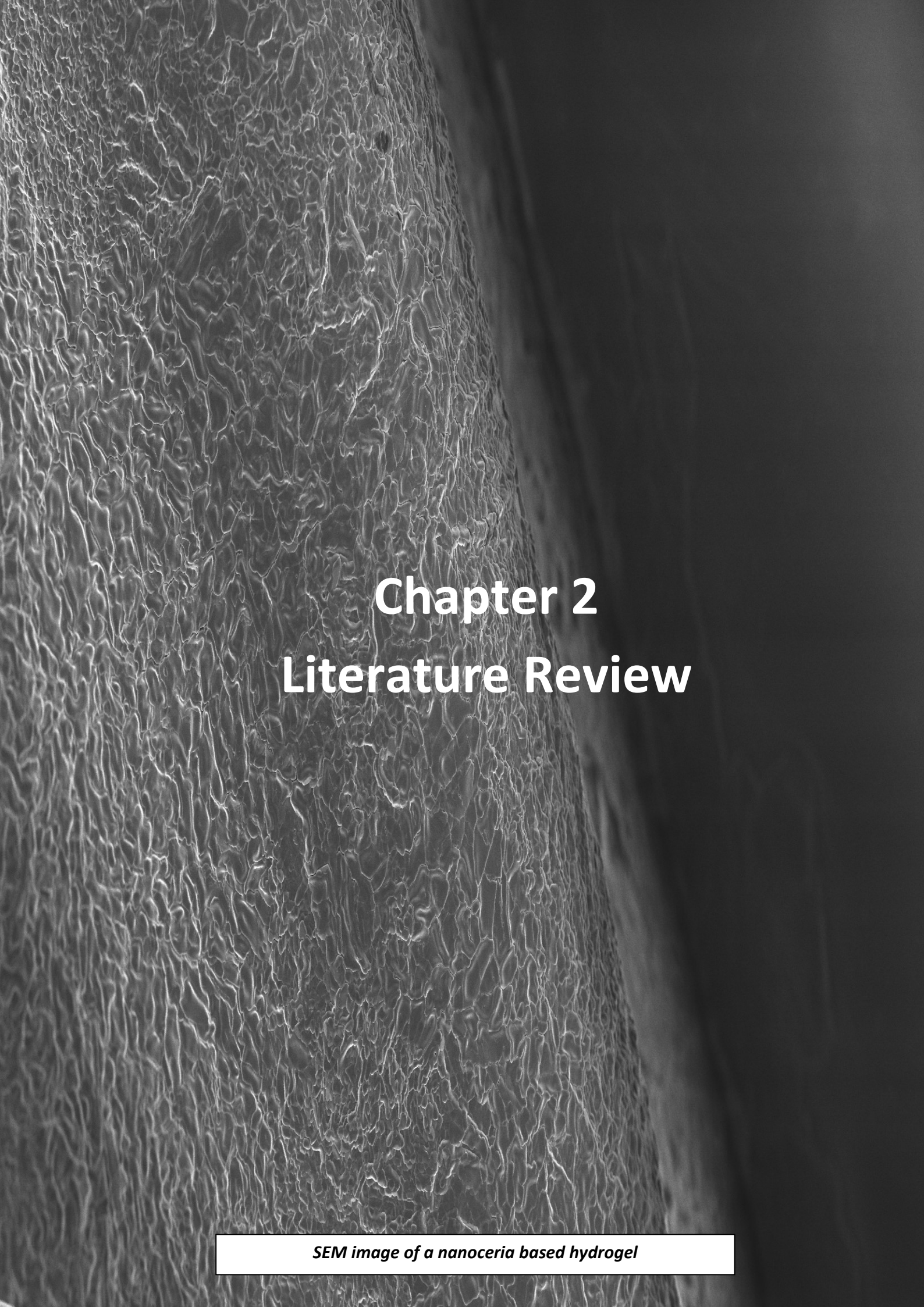
A literature review of current scientific progress will be conducted in Chapter 2, focussing on cartilage repair, double network hydrogels and the impact of oxygen on polymerization kinetics. The concluding section of Chapter 2 will include the aims and objectives of this thesis. The theory and operating conditions of the characterization techniques used throughout this thesis will be described in Chapter 3.

Chapter 4 and 5 will explore two separate sets of double network hydrogels DNHG with different polymers in the first network. Different cross linking techniques will be used for the two DNHG to examine the effects that size and concentration of SNPs have on mechanical properties. Chapter 6 will explore the optimization of the synthesis route, based on results from Chapter 5, by introducing a degassing agent called glucose oxidase (GOx).

Chapter 7 and 8 will investigate a new method of DNHG synthesis that aims to improve the properties of the materials by grafting polymers on the surface of SNP and NC. A comparison with argon degassing and GOx degassing will be conducted for these materials to examine the impact on the synthesis kinetics.

Chapter 9 will discuss the final conclusions and future work based on the results of this research.

Chapter 2
Literature Review



SEM image of a nanoceria based hydrogel

2 Literature review

2.1 Cartilage anatomy, repair and regeneration

Cartilage is a flexible, tough and elastic connective tissue that is found at different parts throughout the body, such as the nose, ear, knees, hips, and intervertebral disks. Cartilage has the intrinsic ability to withstand cyclic compressive and tensile forces that are part of daily routines. Hyaline cartilage, or articular cartilage, is thin (0.5 – 5.0 mm) multi-layered and fibre-reinforced, containing water and chondrocytes in an extracellular matrix (ECM)[2]. It is found at the end of articulating bones in diarthrodial joints. Its inherent anisotropic and viscoelastic properties, as well as low friction and wear-resistance, allow for shock absorbance and smooth articulating movement in the joints[2]. Water makes up for approximately 72 wt % of cartilage. The remaining 28 wt % of articular cartilage is composed of ECM and cells. Of that 28 wt %, 75 % are collagens, 17 % glycosaminoglycans (GAG)[8]. Chondrocyte cells are encapsulated in a dense matrix containing a high concentration of proteoglycans and Type VI collagen for cells to anchor onto the ECM[9]. Proteoglycans are polar proteins with a high density of fixed negative charges resulting in a significant Donnan osmotic pressure effect[2]. Proteoglycans are glycosylated, consisting of core proteins with one or more covalently attached GAG chain, and are considered as linear polymers with repeating amino sugar units with negative charges. The negative charges attract positively charged ions such as Na^+ from the surrounding interstitial fluid, this in turn causes the proteoglycans to repel each other and attract water molecules causing swelling by water uptake. Aggrecan is a proteoglycan with a bottlebrush structure and is a critical component for cartilage due to its ability to resist compressive loads. The hydrated state of aggrecans is within a collagen Type II network, creating reinforcement to the structure through cross linking. Therefore, when under physical pressure, a reversible deformation occurs due to water molecules being forced out[8].

The composition of mature articular cartilage varies with depth into four structurally different zones; superficial, intermediate, deep and calcified zones (Figure 1). The complex zonal structure of cartilage provides it with its unique mechanical properties to tolerate loads and cushion impacts. The thin (200 μm) superficial zone contains a high density of flat chondrocyte cells and parallel aligned collagen fibres that provide the high lateral tensile strength against shear and compressive stresses[10]. In the intermediate to the deeper zones, a gradually increasing concentration of aggrecans and fibres are found, with random physical orientation. As the deep zone becomes the subchondral zone, a transition from hyaline cartilage to calcified cartilage develops. Here, collagen fibres are perpendicularly orientated with a low density of large and vertically well-organized chondrocytes. Hyaline cartilage can therefore be damaged up to different depths; matrix disruption, partial thickness defects, and full thickness defects. Matrix disruptions occur from physical trauma, causing the ECM to become damaged. Chondrocytes are able to increase their synthetic activity to repair the tissue, if the damage is not excessive. Partial thickness defects are more extreme but do not reach the subchondral bone, with immediate cellular response proliferation occurring, though defect repair is low[11]. Full thickness defects extend to the subchondral bone through the entire thickness of the cartilage[11].

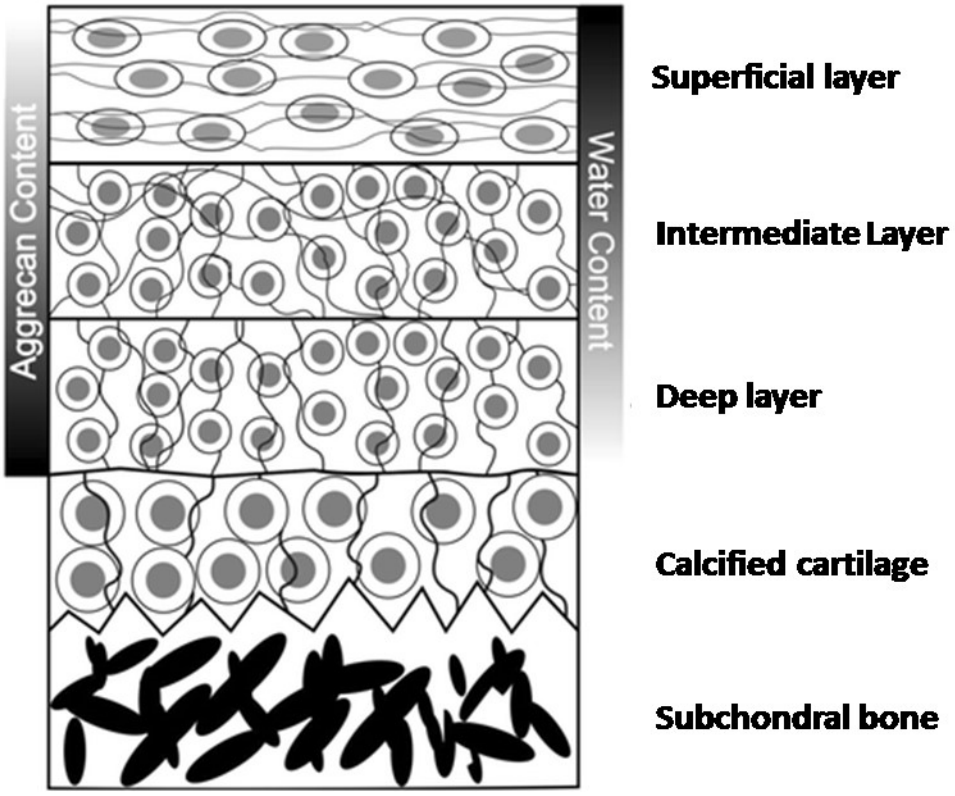


Figure 1 - Schematic representation of the zonal layers of articular cartilage. Figure adapted from *Castro et al.*[12]

Cartilage has a limited ability to regenerate itself due to its avascular nature and its low local chondrocyte population. Chondrocytes have low apoptotic (programmed cell death) activity and are postmitotic (do not exhibit cell division after foetal development is completed), therefore chondrocytes have a low turnover and limited ability for self-repair[13]. Chondrocytes, when mature, have slow metabolisms and fail to differentiate and proliferate at fast enough rates to result in tissue regeneration[14]. The degradation of the ECM, either by physical trauma, age or autoimmune diseases, can lead to the dedifferentiation of the chondrocyte phenotype which can in turn negatively impact the mechanical, viscoelastic and compressive resistance properties[15]. The avascularised nature of cartilage means that chondrocytes function with a hypoxic (low oxygen content) metabolism where nutrients and oxygen are supplied to cells mainly by diffusion through the subchondral bone and the synovial fluid surrounding the cartilage. Cartilage regeneration may occur to a limited extent if the defect reaches the

subchondral bone, thus stimulating the release of bone marrow stem cells and signalling molecules from the bone marrow. This would allow the pluripotent bone marrow stem cells to mobilize and migrate into the defect, creating a fibrin clot that would differentiate into chondrocytes and osteoblasts[16]. Overtime, this could aid in tissue repair. This strategy is used in the surgical "microfracture" technique. The resulting repaired cartilage differs from the native hyaline cartilage; instead, mechanically inferior fibrocartilage forms which has a denser matrix containing fewer chondrocytes and thicker collagen fibres, due to the lack of molecular signalling and organization. This inferior form of cartilage tends to be less stiff and more permeable than native cartilage, and does not provide complete relief of symptoms from the defect. This contributes to the newly formed tissues' degradation overtime (6 months – 5 years) [17, 18]. The formation of fibrocartilage occurs in such defects due to the presence of dedifferentiated chondrocytes with elongated morphologies, rather than spherical differentiated chondrocytes that are capable of forming hyaline cartilage[18, 19]. Therefore, the limited ability for articular cartilage to repair itself has encouraged the development of surgical treatments and tissue engineered solutions.

2.2 Developments in current clinical treatments and their limitations

Clinicians often opt for resections to reduce symptoms of articular cartilage defects, and to restore partial functionality of the joint. For severe cartilage defects, resection will commonly be followed with implanting a prosthetic joint. Knee replacement procedures involve a significant loss of healthy cartilage and bone tissue. Other options for less severe cartilage defects include; microfracture surgery, autologous chondrocyte implantation, mosaicplasty or osteochondral grafts, and tissue engineered scaffolds[20].

Surgeons select complete joint replacement for extreme cases where the patient suffers intolerable pain, severe loss of mobility, usually due to bone on bone contact. Current techniques use computer-aided minimally invasive procedures (incisions of 7 – 10 cm as opposed to 20 cm with traditional methods) [21, 22]. This increases the alignment accuracy of the prosthesis. Common implants include metal cobalt chrome and/ or

ultra-high molecular weight polyethylene as the articulating surface. Cementing the knee in place causes eventual issues such as loosening of the tibial component due to degradation of the cement-metal implant interface because of cement shrinkage. Total joint replacements replace the tissue rather than regenerating it, providing pain relief and return to function, but not to 100 % functionality of the original joint mechanics, with implants wearing out over time leading to revision surgeries.

Microfracture surgery is the least invasive cartilage repair procedure that can be performed completely arthroscopically. It has low associated morbidity and a comparatively short postoperative rehabilitation time[23]. The basics of this procedure is to cause a micropenetration puncture wound in the subchondral plate of the affected area and expose it to the inner part of the bone. This causes an influx of pluripotent marrow-derived stem cells into the defect site. The cells then differentiate and promote fibrocartilage growth containing type II collagen[24]. This procedure has proven most effective if done within the first 12 months for a lesion size < 2 cm^2. Initial improvements in knee functionality were between 58 % - 95 % for athletes that have undergone this procedure. However, a decline in functionality of 47 % - 80 % was also reported between 12 - 36 months, although this was still better than the pre-procedure[25-27]. Drawbacks of this technique include the development of fibrocartilage which is biomechanically inferior to the original native hyaline cartilage. Also, a brief period of non-weight bearing movement is required from the patient. The impact this procedure has on the long term effects on the development of arthritis remains unclear.

Mosaicplasty is a surgical technique that is used to treat damaged lesions between 1 – 4 cm^2 in the hyaline cartilage. This is done by harvesting cylindrical osteochondral grafts from relatively low-weight bearing regions from the patients' femur that are used to fill the defect in the knee by press-fitting the pieces in place. Mosaicplasty takes millimetre sized pieces from the patient to fill the whole damaged site. Studies offer evidence that this technique provides up to 95 % positive results of improved knee function in athletes leading up to 36 months, with a decrease in athletic activity and a need for some revision after a 7 year follow up with low long-term morbidity at the donor site[28-30]. The drawbacks along are mid to long term decrease in functionality of the knee post-

op, a lack of graft integration with the surrounding tissue, the inability of donor grafts to recreate native joint mechanics, and the restriction of treating larger lesions with this method.

Autologous chondrocyte implantation (ACI) was devised in 1994 as the first FDA-approved cell-therapy product to be released for clinical use[31]. This technique has evolved over time with current developments in tissue engineering technology and application, allowing for better and more accurate control over this procedure. ACI is usually preformed on patients between the ages of 15-55 years for chondral lesions up to 10 cm^2. Autologous chondrocytes are initially harvested arthroscopically from a low-weight bearing area of the patients joint and multiplied *in vitro* over the course of a few weeks. They are then re-implanted under a periosteum flap during a second procedure into the affected area of the patient. An advantage of this procedure is the partial development of hyaline-like cartilage that leads to a better longevity of the healing tissue. Follow up studies show that there is an increased longer-term durability up to 20 years[32]. The limitations are; it is a two-step surgical procedure with prolonged post-operative rehabilitation, poor cell retention at defect site, more overall fibrocartilage formation than hyaline formation, and complications such as graft delamination due to periosteal hypertrophy[33].

A developing method of implanting chondrocytes into defect sites to induce matrix and hyaline cartilage formation is by the use of scaffolds. This is considered the third generation development of ACI. The concept is to have a biodegradable scaffold with similar mechanical properties to native cartilage that temporarily supports the chondrocytes until a matrix is synthesised by the implanted cells. A wide range of scaffold materials have been developed using different synthesis techniques, such as 3D printing, freeze thawing, freeze drying, self-assembly hydrogels etc. These scaffolds can be based on carbohydrates (alginate, hyaluronan, polylactic/ polyglycolic acids), protein polymers (fibrin, gelatin, and collagen), artificial polymers (polysiloxane, polytetrafluoroethylene, polyurethane) or composite polymer matrices[34]. Scaffolds seeded with chondrocytes have a lower likelihood of chondrocyte leakage, better homogeneous chondrocyte distribution and less chance of graft hypertrophy (enlargement of graft due to an increase in the number of the cells). A study shows that

this method, using hyaluronic acid based scaffolds, provided improved functionality in the knee with minimal graft hypertrophy and hyaline-like cartilage formation by the 12 month mark and durable improvement at 5 years, with the best results for patients under the age of 30[35, 36].

The methods described offer a wide range of choices for patients with different levels of cartilage damage and different size defects (1 - 10 cm^2), using minimally invasive methods to total knee replacements. So far, the clinical research provides evidence of short to mid-term improvement in functionality but there is still room for development. The aim to develop hyaline cartilage falls short, instead mechanically inferior fibrocartilage tends to develop that degrades over time resulting in follow up surgeries. ACI techniques are becoming less complicated and less invasive though clinical research does not support a functional benefit over older techniques such as microfracture, with a lack of evidence that the presence of hyaline cartilage filling the defects delays or stops arthritis progression[37]. Literature suggests that there are improvements such as reduced complications and revision rates with the developing techniques mentioned in this chapter, but without an answer to whether they have long-term impacts on the rate of arthritis, and with little translation into human use by clinical trials. The direction is moving towards a more multifunctional tissue engineering approach to regenerate cartilage, combining cells, scaffolds and drugs for an optimum biologically active graft that is financially feasible and readily available. This shift aims to reduce surgical aggressiveness. The challenge lies in finding the right material and the right cells to differentiate to the appropriate chondrocyte type that will produce a matrix similar to native hyaline cartilage with the potential to halt the progression of arthritis, as well as the conditions required to induce the integration of the engineered scaffold into the host.

2.3 Hydrogels for cartilage tissue engineering

Tissue engineering has become a dynamic science over the past two decades, with several branches of biomaterials and synthesis techniques being developed for tissue regeneration. Cartilage engineered tissue aims to replicate the low friction, shock absorption and load distribution properties of native cartilage. Hydrogels are 3D polymer networks that have the ability to consist of 90 – 99 wt % water, and have become a suitable research candidate for cartilage[38].

Hydrogel properties and functionalities can vary widely due to the wide range of polymers, network structures and chemistries they can be formed by. Hydrogel mechanical, swelling and degradation properties are often tailored to fit different applications, for example skin grafts, cardiac patches, cartilage tissue replacement etc. Despite their poor mechanical properties, difficulty in sterilisation and cell/drug loading into hydrogels systems, they usually; are biocompatible; can hold high water content; have a wide range of chemistries; can be injectable for minimally invasive procedures; and can be pH and temperature responsive[39-42].

Hydrogels can consist of: networks with one polymer (homopolymers); more than one polymer (copolymers); interpenetrating networks (polymerization of one polymer through an already existing polymer network); and graft polymers using natural polymers and their derivatives, synthetic polymers or a combination of the two. Different hydrogel networks have varying physical properties. Introducing fibres or particles into the system can also alter the overall properties of the hydrogel[43-45]. Physical hydrogels occur when ionic interactions, hydrogen bonds or molecular entanglements hold the polymer chains together, for example alginate and calcium ions (Ca^{2+}), or hydrophobic/hydrophilic block polymers. Physical gels degrade by detangling the chains, or by degradation of the polymer backbone[46, 47].

Hydrogels can also be made by chemical gelation. This involves covalent bonding of polymer chains through active functional groups, by the use of radiation for example, or

the use of chemical cross linkers. For example, polyacrylamide can be cross linked using a photo initiator and UV light[48, 49]. Other polymer chains may consist of reactive functional groups at the end, as a side group, or along the monomer backbone. Changing the polymerization conditions, such as temperature, light intensity and initiator concentration can affect the gel properties.

Cross links in hydrogel networks provide the hydrogel network with its mechanical properties and prevent the dissolution of the hydrophilic polymer chains when placed in an aqueous environment, maintaining the materials properties. Hydrogel porosity is also an important property for nutrient and oxygen diffusion, waste/ degradation material removal, vascularization, cell ingrowth and dispersion, and drug release profiles; 100 – 300 µm is considered the optimum size[50]. It is important for the pores in this case to be interconnected through the material rather than superficial pores. Mercury intrusion porosimetry (MIP) is often used to determine porous properties of materials. Low pressure MIP can determine pore diameters between 14µm – 200 µm, whereas high pressure MIP can be used to investigate pores of 3 nm – 14 µm.

Other criteria to design ideal hydrogels for cartilage tissue engineering applications are as follows[51]:

- Mechanical properties; match local tissue, sustain appropriate loads (Table 2);
- Controllable degradation rates with non-toxic degradation products;
- Biocompatibility;
- Colourless and odourless;
- Replicable, lowest content of residual monomer, stable in storage;
- Potential for chemical modification, e.g. with cells or drugs;
- Appropriate cell adhesion, proliferation and differentiation for local tissue;
- Ability to promote hyaline-like cartilage (rather than fibrocartilage);
- Shape, size and volume; ability to adjust based on defect size;
- Ease of handling and injectable if applicable;
- Sterilizability.

Table 2 - Mechanical properties of articular cartilage[52-55]

Properties of articular cartilage	
Compressive strength	22 - 37 MPa
Compressive strain	30 - 80 %
Ultimate tensile strength	0.8 - 25 MPa
Ultimate tensile strain	10 - 40 %

Smart hydrogels are formed *in situ* by covalently cross linking polymers with complementary functional groups under physiological conditions with minimal toxicity, and allow for tailorable properties such as mechanical strength, degradation rates, release kinetics and swellability.

In situ chemically cross linked hydrogels have been developed for drug delivery, tissue engineering applications and as adhesive materials, and their formation is catalysed by enzymes[56]. Enzymatically cross linked hydrogels are limited by the stability of the enzyme used. Hydrogels formed through reactive functional groups provide tuneable properties e.g. mechanical stability, degradation rates and gelation kinetics. Michael addition has been used for *in situ* chemical cross linking for its relatively fast kinetic reactions under physiological conditions without the use of a catalyst, making the hydrogel less toxic with fewer impurities[57]. Chemo-selective cross linking reactions can be done without toxic additives and usually require no purification, the most popular reaction is click chemistry[58].

Radical polymerization based on thermal or photo initiated reactions have also been explored for hydrogel formation. Photopolymerization is becoming more popular due to its fast gelation time, less-toxic initiators and spatiotemporal control[59]. Photopolymerization is initiated by forming free radicals from the photoinitiators (e.g. ketone based initiators or potassium persulfate) that lead to network formation between the monomers. This method was first described by Hubbell *et al.* for the release of BSA over a 2 month period[60]. An example for cartilage regeneration is a multicomponent photo cross linked hydrogel made of hyaluronic acid/ gelatin/ chondroitin that produced similar ECM to cartilage with good mechanical properties[61].

Double network hydrogels have been a main area of focus for hydrogel synthesis due to their interpenetrating networks of contrasting polymer that allow for great control over the overall properties of the material. This class of hydrogels allows for improvements on previously researched polymers that were not mechanical suitable for load bearing applications such as poly N-isopropylacrylamide (PNIPAAm), which has been cross linked with polyamidoamines (PAMAM) by Michael addition to increase its mechanical properties and swelling ability[62]. Double network hydrogels have the most suitable characteristics for cartilage regeneration and will be discussed in detail in the next section.

2.4 Existing double network hydrogels

Double network hydrogels (DNHG) are innovative material structures developed by Jian Ping Gong[63] that have the ability to hold high water content, and possess high mechanical strength and toughness. They are characterised by a unique network structure of two polymers with contradicting physical natures such as network density, rigidity, and monomer molecular weight and cross linking density[60]. The minor polymer is a tightly cross linked polyelectrolyte (polymer with several ionisable groups along the molecule) offering a rigidity to the structure (this is considered the first network), whilst the major network is a loosely cross linked neutral polymer that is more ductile in nature (considered the second network). Together they form a DNHG system with increased mechanical strength[18]. DNHG show common features with natural and ductile nanocomposite materials such as bone, dentins and cartilage, therefore offer an exciting starting platform for advanced research. Cartilage saturated with 75 wt % water has a compressive fracture stress of 36 MPa[64] allowing cartilage to sustain the dynamic compressive stresses of daily movement, DNHG gels have been able to replicate these values using methods such as void-DNHG, microgel-reinforced nanocomposite hydrogels, liquid crystalline DNHG, ultrathin DNHG, inverse DNHG and interpenetrating polymer network (IPN) DNHG, along with many other novel DNHG concepts. Several different examples will be discussed in this section.

The general method of preparing DNHG consists of a two-step sequential free radical polymerization where the brittle tightly cross linked polyelectrolyte network is formed. This brittle gel is then soaked into an aqueous solution of the neutral monomer that will polymerize and form a loosely cross linked flexible network within the first gel. The optimum structure for a DNHG consists of the following[63]:

1- The first network should be brittle and rigid (e.g. polyelectrolytes), while the second network should be soft and ductile (e.g. neutral polymer)
2- The molar concentration of second network is should be 20 – 30 times higher than first network
3- A high molecular weight for second polymer network to form the loosely cross linked structure within the first network

This binary structure provides a synergistic effect of the two networks creating a unique toughening mechanism as is seen in fibre-reinforced and conventional IPN hydrogels, rather than a linear effect that may be expected of the two networks[63]. Gong and Katsuyama[44] produced a hydrogel of poly2-acrylamido-2-methylpropanesulfonic acid (PAMPS)/ polyacrylamide (PAAm) with unusually high mechanical properties. PAMPS, a polyelectrolyte, was used as the first network where it was cross linked using n n'-methylenebisacrylamide (MBAA), then soaked in an aqueous solution of PAAm, a neutral polymer, also cross linked with MBAA to form the second network. With 90 wt % water the DNHG had a compressive fracture stress of up to 20 MPa with a 92 % strain, whereas the single network gel components had sub-MPa fracture stresses at 80 % strain for PAAm and 40 % for PAMPS[44].

A biocompatible anisotropic DNHG with high mechanical strength was synthesised using bacterial cellulose (a natural occurring polymer with an ultra-fine fibre network with a stratified structure providing the anisotropic property) as the first polymer network which is then immersed in a gelatin solution containing EDC as a cross linker to form the second network[65]. This DNHG was formed with 90 wt % water, and a compressive stress of 3.7 MPa with repeated compressions, 31 times higher than gelatin[65]. The

compressive elastic modulus of the DNHG was 1.7 MPa in the perpendicular direction to the stratified structure, 240 times higher than BC and 11 times higher than gelatin gels[65]. Figure 2 shows a BC/gelatin DNHG in comparison with its single polymer components under compressive and tensile stresses. BC/PAAm DNHG were also produced as a successful attempt to improve further the mechanical properties, with a tensile stress of 40 MPa as opposed to the 2.9 MPa of BC/gelatin[66].

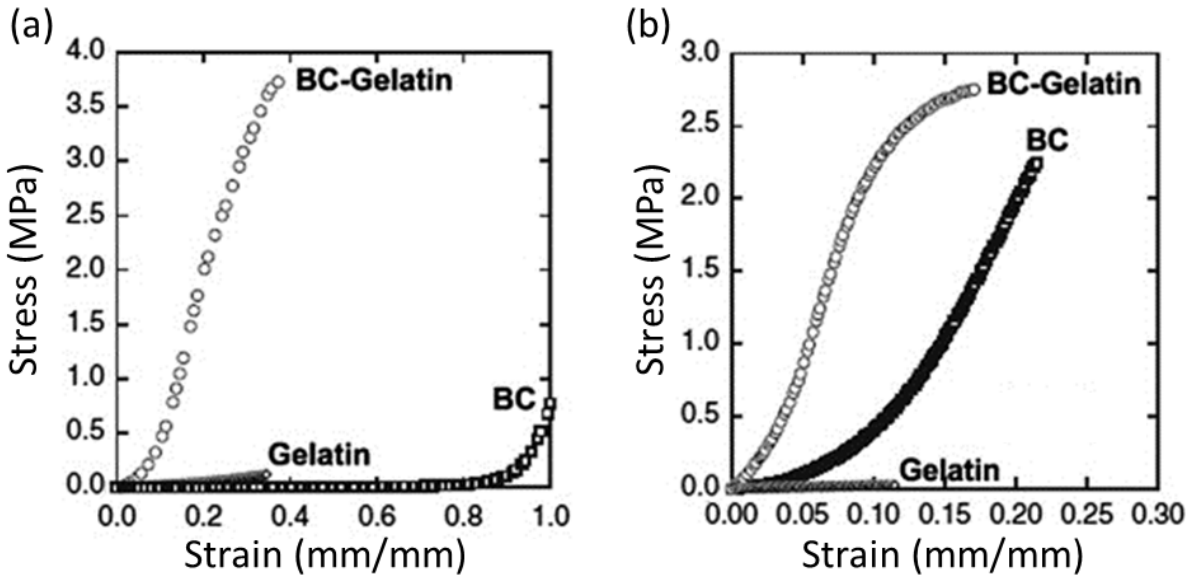


Figure 2 - Compressive (a) and tensile (b) stress-strain curves of bacterial cellulose (BC), gelatin and a BC / gelatin double network hydrogel (DNHG). Adapted from *Wu et al.* [66].

Frank *et al.*[67] developed an inverse double network hydrogel with an interpenetrating polymer network (IPN) system that used the reverse concept of DNHG synthesised by Gong *et al.* Meaning, the first network was a neutral polymer network of poly (ethylene glycol)-diacrylate (PEG-DA) with a set molecular weight, and the second network was loosely cross linked ionisable polymer polyacrylic acid (PAAc), also synthesised by a two-step sequential polymerization[63, 65]. PEG-DA/PAAc hydrogel was formed via photopolymerization, using a photoinitiator and cross linker to form the interpenetrated polymer network. Hydrogen bonds between the ether groups on PEG

and the carboxyl groups of PAAc form complexes. PEG-DA and PAAc are both quite brittle networks. PEG-DA possesses low compressive fracture strength of 0.5 MPa at a strain of 40 %[63, 65]. The DNHG showed a dramatic increase to 8 MPa at 90 % strain[63, 65]. At low pH and using pure water, this hydrogel showed pronounced strain hardening due to the hydrogen bonding effect, whereas in physiological pH buffer solution they exhibit properties with a high Young's modulus because of the effect that the constrained tightly cross linked PEG network has on the ionized PAAc network[63, 65]. A study by *Goddard et al.* was carried out to understand the dynamic effects of the two networks when under tensile load; there was a close-to-linear stress of the DNHG compared to the SN of both polymers when at a strain of < 100 %, but the stress of the DNHG PEG-DA/PAAc increased rapidly at a strain > 100 % suggesting that the cross linking becomes effective at a strain over 100 %[68].

Chen *et al.* synthesised a DNHG of hyaluronan (HA) and poly (N, N'-dimethylacrylamide) (PDMAAm) by a two-step photo cross linking method[69]. HA is a natural polysaccharide that is abundant in biological tissues, it is a biocompatible but brittle polymeric hydrogels. PDMAAm is a known for its exceptional biocompatibility and hydrophilic nature, and is widely used in the biomedical field[70]. HA was modified with glycidyl methacrylate and photo cross linked to form the first network (PHA) at 365 nm UV light. PHA was then immersed in different concentrations of DAAm solutions at ambient temperature with varying amounts of cross linker MBAA with a fixed photoinitiator concentration of 0.1 mol% to form the second network PDMAAm by photopolymerization for two hours under 365 nm UV light, hence an interpenetrating double network was formed. As with other DNHG, it experienced a synergistic effect while saturated with 90 % water, showing good a compressive modulus and high fracture stress of 0.5 MPa and 5.2 MPa, respectively. PHA on its own exhibited 50 µm pore sizes, whereas PHA/DAAm had a pore size range of 10 – 20 µm depending on cross linker concentration and the PDMAAM ratio used, which is a suitable size for chondrocytes to enter the hydrogel[69]. These pores also increase in size once hydrated. PHA/DAAm showed slow biodegradation (PDMAAm is non-biodegradable), maintaining its mechanical properties for 2 months after being co-cultured with fibroblasts without cytotoxic effects on the cells with ECM (mainly collagen type I) being secreted; Chen *et*

al. concluded that this material has potential for further investigation for spinal disc substitutes since it is non-biodegradable as well as for knee cartilage repair.

Mooney *et al.* developed a highly stretchable DNHG of alginate and polyacrylamide which consists of ionic cross links and covalent cross links, as well as physical entanglements of the polymer networks[71]. The ionic links that were formed between the alginate and calcium ions provided an unzipping-like mechanism of the cross links The ionic cross links are damaged when stretched but re-heal once unloaded. The covalent cross links between the acrylamide and MBAA (cross linker) provided a crack bridging mechanism when the gel is loaded.

A step further into complex hydrogel networks include nanocomposite hydrogels, which have been developed to tailor materials that lack the appropriate mechanical properties, for example PEG, which alone is limited to soft tissue application, space filling scaffolds or drug delivery application[72]. Nanoparticles in polymer networks can enhance the mechanical strength, biocompatibility and bioactivity (if the nanoparticles are bioactive) of the material. They can be physically or chemical cross linked, or dispersed within the gels network. Laponite is a silicate based nanomaterial, with a disc-like morphology, with composition $(Na_{+0.7}[(Mg_5.5LiO_3)\ Si_8O_{20}\ (OH)_4]0.7)$[72] that has been used to enhance the properties of hydrogels such as polyacrylic acid[73] and PEG[74], showing good osteoblast (bone producing cells) proliferation and differentiation. Schmidt *et al.* showed that Laponite and PEG provide physical (between PEG and Laponite) and covalent cross linking interactions (between the PEG polymer chains) allowing for extension to 1,500 % under tension of the PEGs original size with Laponite. A reduction in hydration is seen from 1,100 % (0 % Laponite) to 900 % (5 % Laponite) suggesting successful covalent and physical bonding, with increased cell adhesion and proliferation. However, nanodisc sizes may be too small in that they may be internalised into cells; therefore an alternative nanoparticle group was required.

As such, silica nanoparticles (SNP) can be formed from 5 nm to over 100 µm with functionalised groups on their surface allowing them to cross link to polymer network. For example Zhao *et al.* synthesised polyacrylic acid with vinyl silica nanoparticles at different concentrations, using the SNPs as macro cross linkers and MBAA as a control

for comparison of the effects[75]. The hydrogel exhibited homogenous dispersion of the SNP and an increase in compressive stress with increasing SNP concentration compared to PAAc hydrogel with MBAA.

Taking this concept one step further, it is possible to develop DNHG with a nanocomposite structure. Fu *et al.* developed a "super-tough" DNHG with covalently bonded vinyl functionalised SNPs[7]. PAMPS/PAAm were synthesised in the usual two-step polymerization reaction, initially forming the PAMPS network using MBAA with the addition of the vinyl SNPs forming a PAMPS/SNP composite gel. The vinyl SNPs acted as macro cross linkers in the DNHG providing a denser network. This was then immersed in a monomer solution of AAm/MBAA to form the double network. Controls used were PAMPS/PAAm without SNPs, and PAMPS/PAAm with SNP filled (i.e. not covalently bonded) into the DNHG. SNPs used in were 150 nm and 300 nm in diameter for comparison on the effect of size. SNP grafted gels showed lower equilibrium swelling ratios (ESR) compared to SNP filled gels, and lower ESR for smaller SNP sizes. This proves that there was a tighter network when grafted SNP were used, suggesting they acted as macro cross linkers. SNP grafted gels reached a strain of 0.98 without fracture, and up to 73.5 MPa fracture stress, a 16.5 MPa compressive strength and a 0.33 MPa elastic modulus for 300 nm SNP (1 wt %) grafted gels[7]. Mechanical properties improved with increasing SNP size and SNP grafts rather than filling; the best mechanical property values were witnessed at 1 wt % and decreased slightly with increasing wt %. Pore sizes also decreased with increasing SNP % suggesting an increase in cross linking density. The loading/ unloading behaviour was examined of these gels, providing evidence that the PAMPS (first) network fractures into clusters; these clusters have physical entanglements and chemical cross links through the SNPs with the PAAm/SNP network and hence provide the extraordinary compressive toughness exhibited by these materials (Figure 3).

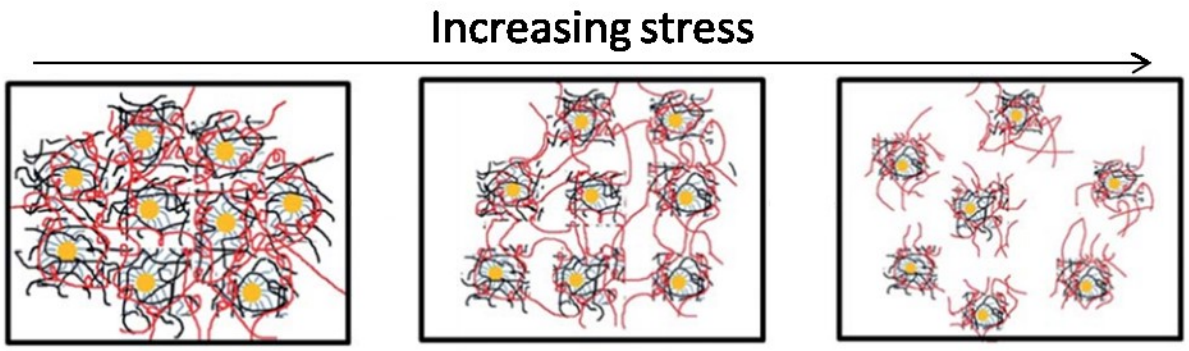


Figure 3 - Schematic representation of the compressive fracture mechanism of a double network hydrogel (DNHG) with silica nanoparticle (SNP) grafts before yielding (left), PAMPS/SNP broken into clusters (middle), and complete fracture (right). Figure adapted from *Fu et al.* [7]

Therefore, surface modified SNPs have the potential to introduce an improved fracture mechanism with higher resistance to strain. Previous research has explored a narrow range of SNP size and wt % loading in DNHG. This has left unanswered questions such as what range of size and concentration achieves the best results. Smaller nanoparticles provide larger surface areas, but may be easier to lose during synthesis due to percolation and could potentially have adverse effects on cells. Larger nanoparticles however may work less effectively as cross linkers due to their relatively smaller surface area, but are safer to use in combination with cells. The incorporation of nanoparticles as a nanocomposite structure opens the door to the addition of drugs or ions for local delivery in order to combat against progressive diseases such as arthritis[76]. Therefore, the advancement of DNHG with nanocomposite structures requires a detailed approach in order to fully utilise the potential of the material. Previous DNHGs have been synthesised in either closed systems with inert gas atmospheres, or in open vessel oxygen-rich atmospheres[63]. These costly systems often lead to longer polymerization times due to reduced kinetics in the presence of low to high concentrations of oxygen. Therefore, they often require higher concentrations of chemical initiators and monomers to compensate. Open vessel systems are useful in production lines due to cheaper costs and bespoke free-form synthesis. The impact of these facts may lead to

inherently weaker materials as well as toxic unreacted monomers remaining in the final products. Therefore it is necessary to adopt a more cost effective and efficient synthesis route for the synthesis of biomaterials in open vessel systems. This thesis aims to understand the impact of nanocomposite structures on DNHGs, and to optimize the polymerization route in order to achieve enhanced material properties.

2.4.1 Double Network Hydrogels in Cartilage Repair

Yasuda *et al.* took four of Gong's DNHG a step further to be tested for biological application, mainly cartilage regeneration: PAMPS/PAAm, PAMPS/PDAAm, cellulose/ PDAAm and cellulose/ gelatin. The most promising from the four was PAMPS/PDAAm for its suitable wear properties, relative to ultra-high molecular weight polyethylene used regularly in the medical applications, whereas the other three DNHG showed weak resistance against wear[77]. These hydrogels (size 10 x 10 x 5 mm^3) were implanted into the subcutaneous tissue of rabbits for 6 weeks and harvested for comparison of their mechanical properties, and the tissue surrounding the gels were histologically examined[78]. The PAMPS/ PDAAm ultimate stress increased after being implanted from 3.10 MPa to 5.40 MPa, with a reduction in tangent modulus from 3.10 MPa to 0.20 MPa, and reduction in water content from 94.0 % to 91.2 % after implantation[77]. As mentioned before, the aggregate modulus of natural cartilage is between 0.50 – 0.90 MPa (average 0.71 MPa)[79], therefore the PAMPS/ PDMAAm had a higher value for ultimate compressive strength and a similar tangent modulus to that of natural cartilage. Slight inflammation at 1 week was seen in the PAMPS/ PDMAAm implant that disappeared at week 4, similar to the negative control. Pin-on-flat wear testing shows excellent results for PAMPS/ PDAAm[78], as well as low biodegradation when implanted in the rabbit[77]. A defect in the femoral trochlea of the right knee was made and the hydrogel was implanted purposely without filling the entire defect, and the left knee was used as a control; the mean friction of the normal cartilage and the implant were compared showing that the PAMPS/ PDMAAm has a very low friction coefficient (0.029, as opposed to that of normal cartilage 0.188) on normal cartilage without damaging

effects on the implanted counter face *in vivo*. Hyaline cartilage was formed at 4 weeks of implantation into the chondral lesion of the rabbit; measurements were taken at 4 and 12 weeks using confocal laser scanning microscopy for histological and immune-histochemical evaluation[80]. This *in vivo* test also showed no significant difference between the mean surface roughness of the PAMPS/ PDMAAm gel vs normal cartilage. Therefore, such DNHG show progressive development in achieving hyaline-like cartilage repair without cell encapsulation. A current limitation in DNHG is their weak fatigue resistance that stems from the natural toughening mechanism of the materials irreversible failure of covalent bonds within the first network[81, 82], leaving room for further development and the potential to change these irreversible covalent bonds to reversible bonds i.e. a strong self-healing DNHG. Furthermore studies *in vivo* with cells encapsulated in these materials will be required to show the effectiveness of cartilage (and other tissue) repair before it can be applied in the medical field. The effective use of both PAMPS and PAAm can be used to further expand the tailorability of the DNHG. One strategy is to improve the material by introducing nanoparticles as a nanocomposite structure.

2.5 Silica nanoparticles

Spherical monodispersed silica nanoparticles (SNPs) in the range 50 nm – 2 µm were first synthesised by Stöber *et al* in 1968[83]. Nucleation and growth of SNPs starts with the hydrolysis of silica alkoxides groups, usually from the common precursor tetraethyl orthosilicate (TEOS), in water forming intermediate Si compounds followed by the condensation reaction. The general process for the formation of the SNPs is, silica alkoxide precursors are hydrolysed under basic conditions to form a large number of primary particles that rapidly aggregate to form stable particles, and as the reaction continues the stable particles grow in a mono-disperse order, and stay dispersed due to surface charges repelling them at high pH (Figure 4). Five primary parameters that affect the size distribution of the SNPs are[84]:

1) TEOS concentration
2) Ammonia concentration
3) Water concentration
4) Polarity of the solvent
5) Reaction temperature

Ammonium hydroxide is used as a basic catalyst that favours condensation reactions during the sol-gel process. Negative -OH groups prevent the forming particles from aggregating, allowing silica tetrahedrons to bridge each other through Si-O-Si bonds[84]. Ammonium hydroxide has the most prominent effect on particle size and distribution in for TEOS in a concentration range 0.05 to 0.28[85].

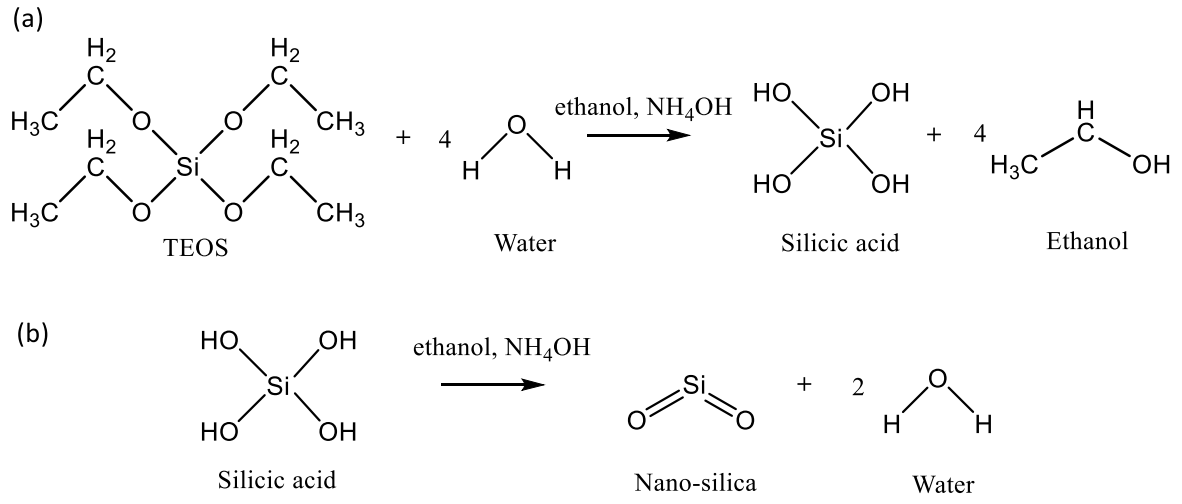


Figure 4 - (a) the hydrolysis of tetraethyl orthosilicate (TEOS) under basic conditions, and (b) the condensation of silicic acid to form silica nanoparticles (SNPs)

Silica nanoparticles can be used for different applications in biomedical engineering such as drug delivery and cancer treatment[86] where the optimal nanoparticle size for endocytosis by cells has been found to be 25 – 30 nm in radius and is regulated by membrane tension[87], but can be small enough to cross the blood brain barrier therefore particles 50 – 100 nm in

radius are preferable for drug delivery[88]. Recently, nanoparticles have been used as fillers in polymers and hydrogels to improve the mechanical, chemical and thermal properties of the materials[89-91]. An ultimate aim is to introduce functional groups, such as amine and vinyl groups, onto the surface of the silica nanoparticle to use them not only as fillers, but also as macro cross linkers between the polymer chains. Post synthesis surface modification of SNPs was previously achieved using 3-aminopropyl triethoxysilane (APTES)[92] and vinyl triethoxysilane (VTEOS)[93] resulting in amine groups and vinyl groups on the surface of SNPs, respectively. Vinyl SNPs are able to react and form cross links with polymers by UV induced or free radical initiator induced reactions that open the $–CH=CH_2$ bond[7]. Amine SNPs can form amide bonds with carboxylic acid groups on polymer chains[92], such as polyacrylic acid (PAAc), or protein based polymers[94]. This can be achieved through a carbodiimide compound called 1-(3-dimethylaminopropyl)-3-ethylcarbodiimide hydrochloride (EDC)[95]. EDC chemistry is readily available and has low toxicity, which makes it a common cross linking method for biomaterials in biomedical applications[95, 96]. EDC is water soluble therefore suitable for aqueous cross linking, whereas its counterpart dicyclohexyl carbodiimide (DCC) is water insoluble making it suitable for non-aqueous organic solvents. EDC based cross linking achieves efficient bonds in acidic conditions (pH 4.5); hence water soluble sulfo-N-hydroxysuccinimide (sulfo-NHS) is used to help form intermediate compounds when at neutral pH to ensure EDC coupling occurs[97]. Therefore, carbodiimide chemistry has great potential to covalently bond amine SNPs and carboxylic acid groups on polymer chains to form nanocomposite materials such as the first network as part of a double network hydrogel.

The addition of SNPs to the first network of DNHG can be used to achieve tight cross linking as a way to introduce tailorability into the materials properties, such as increased mechanical strength and toughness, better resistance to strain deformation and controllable swelling rates[7]. A requirement for the first network is to be tightly cross linked[89], therefore this allows for a wide variation in cross linking concentration to be explored in an attempt to tailor the mechanical properties of the DNHG. In contrast, the second network requires a loosely cross linked structure, making it difficult to vary the concentration of cross linking using nanocomposite structures. The ultimate aim of

incorporating functional SNPs into hydrogels is to improve the mechanical properties and offer potential anchorage for cells by changing the topography of the material.

2.6 Hydrogel Polymerization techniques

The intrinsic nature of polymer chemistry allows for a range of polymerization techniques to be used to form hydrogels, such as [98]:

i. **Chemically cross linked hydrogels through radical polymerization:** Hydrogels with low molecular weight monomers can be formed using radical polymerization in the presence of cross linking agents. Altering the concentration of cross linking agent determines the physical properties of the gel. Stimuli sensitive gels can also be formed when suitable monomers are added, for example pH sensitive gels can be formed by adding methacrylic acid, or thermosensitive gels from N-isopropylacrylamide[98].

ii. **By complementary functional group reactions:** Covalent bonds can be formed between polymer chains through complementary functional groups, e.g. OH, COOH, and NH2 by addition or condensation reactions[98].

By addition: Cross linking agents such as N, N'-methylenebisacrylamide (BIS) can react with the functional groups (e.g. carboxylic groups) on water-soluble polymers to turn them into hydrogels by addition reactions; usually carried out in organic solvents since BIS can also react with water. The concentration of cross linking agent determines the network properties. Cross linking agents are usually quite toxic therefore purification steps are required after cross linking, and the links between the polymers are quite stable therefore degradation

occurs when the polymer backbone is enzymatically degraded[99].

By condensation: Hydrogels can be prepared with polymers containing carboxylic acids by linking with hydroxyl or amine groups through condensation reactions to form polyesters and polyamides respectively. A common agent to allow cross linking to occur with these water soluble groups is N, N-(3-dimethylaminopropyl)-N-ethyl carbodiimide (EDC), usually in combination with N-hydroxysuccinimide (NHS) to stop side reactions for more accurate control over cross linking. For example, alginate-PEG-diamine was synthesised by controlling the chain length of the cross linking molecule and/or the cross linking density of the hydrogel by using EDC and NHS[98, 99].

iii. **Physically cross linked hydrogels by ionic interactions:** Ionic cross links can take place at room temperature and physiological pH to form hydrogels, without the use of cross linking agents or additives that will be extracted or that can potentially be toxic, therefore cell encapsulation is possible. Polycations can be cross linked with anions, polyanions with metallic ions and polysaccharides with mineral ions. (Sodium) Alginate is a popular example, where the mannuronic and glucuronic acids form salt bridges by cross linking with calcium ions (divalent cations)[100], and is used for gentle cell encapsulation. Alginate can also be cross linked with cationic polymers such as chitosan and polylysine[98].

iv. **By crystallization:** Homopolymers such as polyvinyl alcohol (PVA) are water soluble and form mechanical weak hydrogels when they gel. Freeze thawing polymers such as PVA forms crystallites that become cross linking sites in the hydrogel network, the properties of the hydrogel will depend on the polymer molecular weight and concentration (in water), number of freeze cycles and temperature used for freezing[101]. Copolymer solutions can also be used in the freeze thawing method to tailor the properties of the hydrogel[98].

i. **By hydrogen bonds:** Hydrogen bonds can form between lone pairs of electrons between hydrogen and carbon, nitrogen, oxygen and fluoride, therefore polymers with available bonding sites can form gels. Polymethacrylic acid (PMA) and polyethylene glycol (PEG) can form gels by hydrogen bond cross links through the oxygen on the PEG with the protonated carboxylic part of PMA; they are usually prepared at low pH and dissolved in ethanol so as the ethanol leaves the system they transform into gels[98].

ii. **By photoinitiated polymerization:** Photopolymerizable hydrogels are used in several biomedical applications such as drug delivery, tissue engineering, cell encapsulation, tissue barriers, fillers, biomimetic coatings and materials, dental restorative materials etc.[59]. Photopolymerization, by free radical polymerization (FRP), has become a common synthesis technique for hydrogels due to its favourable kinetics at room temperature at neutral pH and high energy efficiency at an economical cost[102]. A basic photopolymerization system consists of a UV light source, monomer solution and photoinitiator, with the addition of suitable cross linkers, biological molecules or cells. Monomers for photopolymerization require a backbone that has at least one functional group located at one or both ends that is photopolymerizable. Commonly researched monomers for photopolymerization are dimethacrylic/ diacrylic PEGs derivatives, polyvinyl alcohol (PVA), polyethylene oxide (PEO), PEG-PCL, polyurethanes, collagen, anhydrides etc.[59]. This offers an extensive combination of monomers for hydrogel formation allowing for tuneable properties. Photopolymerization is radical induced polymerization method with 4 steps; initiation, propagation, termination and inhibition[103]. Equations (a – d) below represent the general steps in photo-FRP[104-106].

Initiation (Equation a):

$$I \xrightarrow{hV} 2R^{\bullet}$$

$$R^{\bullet} + M \xrightarrow{k_i} P_l^{\bullet}$$

Propagation (Equation b):

$$P_n^{\bullet} + M \xrightarrow{k_p} P_{n+l}^{\bullet}$$

Termination (Equation c):

$$P_n^{\bullet} + P_m^{\bullet} \xrightarrow{k_t} P_{n+m} \quad (P_n + P_m)$$

$$P_n^{\bullet} + R^{\bullet} \xrightarrow{k_{tp}} P_n R$$

Inhibition (Equation d):

$$P_n^{\bullet} + O_2 \xrightarrow{k_o} P_n OO$$

In the equations above, *hv* represents UV light, I represents the photoinitiator, M is the monomer, P_n, P_m, and P_l are dead polymer chains, and P_nR is the dead polymer produced by primary radical termination. K_i is the kinetic constant for the chain initiation step. $R^{\bullet}$ and $P_n^{\bullet}$ represent primary radicals and growing macro-radical chains with n repeating units, respectively. Photo-initiation consists of two steps: first, photo-cleavage of the photoinitiator molecules to produce primary radicals, and secondly the initiation of growing polymer chains. The effect of the inhibition step by O_2 depends on its concentration in the system and can vary at different locations e.g. top and bottom of walls of the reaction system[106]. It is assumed that O_2 inhibition can dominate the radical termination step at initial reaction times[106]. Depending on the rate of reaction of

the photoinitiator radicals and the kinetics of the monomer, O_2 inhibition can cause issues during photo-FRP.

Photoinitiators should have high light adsorbing capacity for the maximum polymerization effect, high photosensitivity to match the UV light that in the system, have quick initiation rates and efficiency, soluble in the appropriate aqueous solutions, biocompatible and non-toxic to the cells, body and easy to remove any residue once material is formed[59]. Research has shown that 2-Hydroxy-4'-(2-hydroxyethoxy)-2-methylpropiophenone (Irgacure 2959) (Figure 5) is a common ketone based photoinitiator that has been regularly used and investigated for hydrogel synthesis, and is considered the most cytocompatible photoinitiator for several cell types such as fibroblasts, bovine chondrocytes, human foetal osteoblasts, and human mesenchymal stem cells (hMSCs) suggesting safe concentrations between 0.03 – 0.1 w/v % can be used[107, 108]. Examples of hydrogels synthesised with good cell viability using Irgacure 2959 are; PEGDA-PNIPA[109], PEGDA-Silica nanoparticles[110], PEG-fibrinogen[111], gelatin methacrylate-silk fibroin (Gel-MA-SF)[112], chitosan-PEGDA[113] and agarose–PEGDA-RGD peptides[114]; these hydrogels were formed under 365 nm UV light. Other effects to take into account are time of UV light exposure, light intensity and photoinitiator concentration[115].

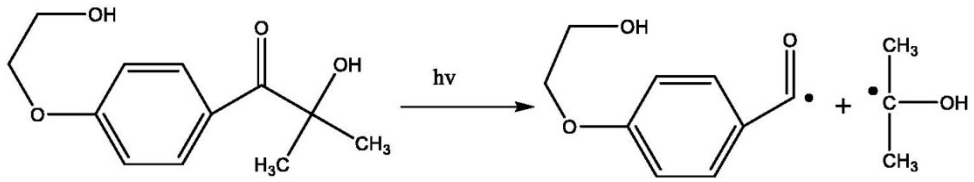


Figure 5 - Photoinitiator Irgacure 2959 and its free radical form, under UV light[116].

2.7 Open vessel photopolymerization and oxygen inhibition

Photopolymerization kinetics slows down significantly in the presence of O_2. This is due to the more favourable reaction between free radicals from the photoinitiator reacting with O_2 molecules, rather than the monomers in the system. This forms peroxy radicals that cause lowered conversion by halting the photopolymerization. Methods have been deployed to reduce the effectiveness of O_2 as a radical quencher, such as nitrogen or argon purging, which have practical issues, particularly with UV systems. It is also possible to overwhelm O_2 by increasing PI concentration so that the free radical species outnumber the O_2 molecules, and by increasing the intensity of the UV light[117]. Increasing the PI concentration can cause cytotoxicity if the material is used in biomedical applications[118, 119]. These methods, despite their somewhat successful rates of O_2 evasion, require further cost and design to facilitate their use. Examples of other common methods to remove O_2 that have been explored in the past include[119, 120]:

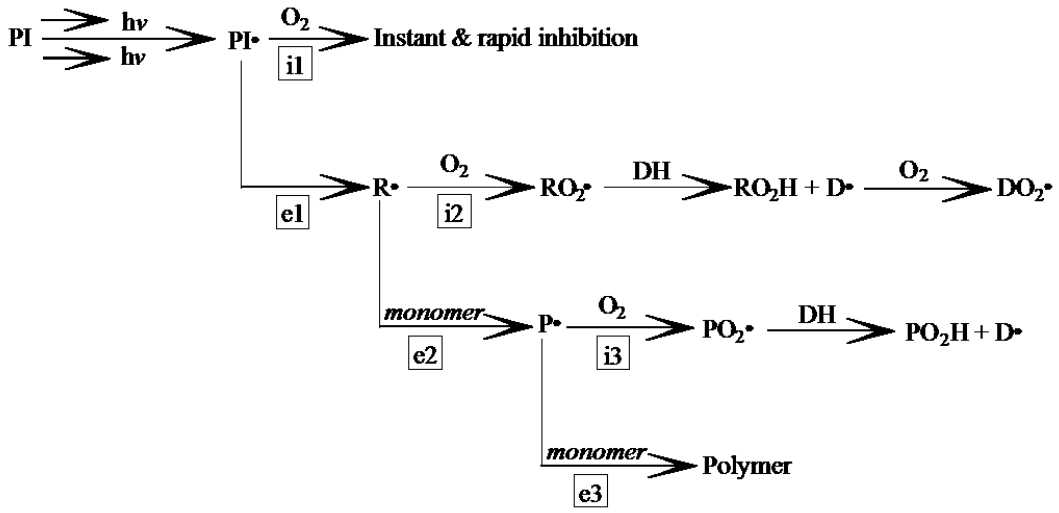
1) Physical barriers such as paraffin waxes and UV-transparent foils to avoid O_2 ingress[121];
2) O_2 scavenger molecules such as thiols, phosphines, acrylic amines, and sensitizer photoinitiators in their triplet state (e.g. benzophenones). These scavengers have the ability trap O_2 in its singlet state that makes it energetically unfavourable for O_2 to react with free radicals. However, this does not completely inhibit the effect of O_2 but slows it down[122];
3) Active long chain photoinitiators that have fluoride substitutions as end-groups or sulphated photoinitiators[119, 123, 124];
4) Molecular inerting. This is a mechanism that activates certain radical initiators, such as azo compounds, which decompose into initiating molecules and nitrogen molecules[125];
5) Hydrogen donors. These are molecules that have a hydrogen atom and a radical as a reaction by-product. The hydrogen atoms that are released will turn off

peroxyl radicals, whilst the newly formed radical takes part in the polymerization[126];

6) Peroxide decomposition. This is a process that can yield RO· or HO· initiating radicals by cleavage of O-O bonds. Photolytic irradiation that combines peroxides with triplet sensitizer photoinitiators and carbonyl complexes of a variety of metals (e.g. Fe, Cu, Cr, and Mo) can be used for peroxide decomposition[127-129].

O_2 inhibition pathways depend on the kinetics of photoinitiator and the monomers in use. Scheme 1 outlines the possible pathways which O_2 can inhibit FRP, labelled i1, i2 and i3, plus their corresponding O_2 evasion pathways e1, e2 and e3 [118, 130-132]. Pathway i1 highly depends on the efficiency and speed at which photoinitiators (PI) react. If the PI speed is fast enough, O_2 scavenging cannot compete[133]. This pathway is also affected by factors such as O_2 concentration in the media, the type (organic, inorganic) and viscosity of the media and the rate constant of bimolecular quenching of the triplet state[133]. As a consequence of i1, initiating radicals created by photolysis are scavenged leading to the inhibition of radical polymerization. i1 can be evaded as expressed in e1 – e3 by increasing PI concentration or increasing UV light intensity. However, O_2 would still be detrimental to the polymer kinetics and final conversion due to pathways i2 and i3. The combination of these inhibition pathways increases the induction time, resulting in a slower kinetic profile and yielding a low conversion ratio[133]. Propagating microradicals are converted to highly stable peroxy radicals that don't participate in, and can potentially hinder, photopolymerization[134].

Ultimately, the net efficiency of FRP is significantly altered leading to non-homogenous, sticky and wet polymer solutions, slower kinetics and low conversions. Therefore, creating an O_2 free environment is essential in restoring the efficiency of polymerization[117, 135].



Scheme 1 - The oxygen inhibition (i1–i3) and evasion (e1–e3) pathway in photopolymerization [118, 130-132].

Therefore, it is important to ensure an O_2 free atmosphere during photopolymerization, taking into account the complexity of the setup, cost and energy required. A more efficient approach using a naturally occurring enzyme called glucose oxidase was therefore explored.

2.8 Degassing by glucose oxidase (GOX)

A naturally occurring oxido-reductase enzyme, glucose oxidase (GOx), previously aided in complete removal of O_2 in an open vessel system for a reversible addition-fragmentation chain-transfer (RAFT) polymerization of hydroxethyl acrylate and dimethylacrylamide[136]. This reaction was proved to be effective in phosphate buffered saline (PBS), water (pH range of 6-7) and several organic solvents such as tert-butanol, acetonitrile and dioxane[136]. The use of glucose oxidase (GOx) as a degassing agent has proven to be innovative and effective[136]. In the presence of O_2, GOx will catalyse the oxidation of β-D-glucose to D-glucono-δ-lactone and hydrogen peroxide (H_2O_2). As the reaction continues, H_2O_2 molecules begin to naturally dissociate into O_2 and H_2O in an aqueous environment, none of which are cytotoxic (Figure 6)[137].

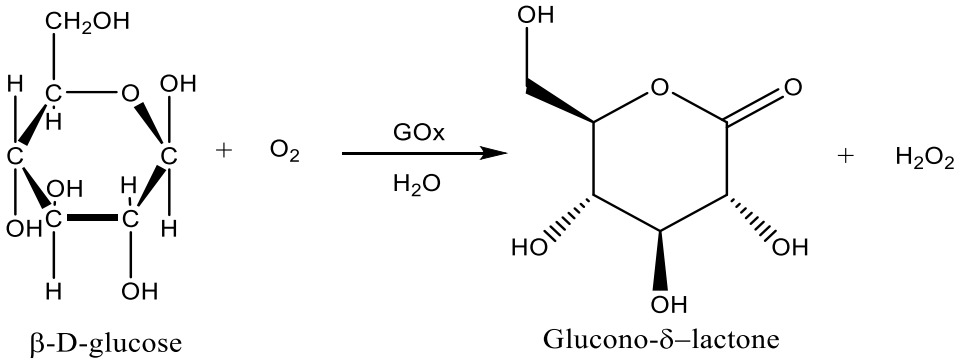


Figure 6 – The role of GOx as a catalyser for the β-D-glucose oxidation reaction and consequent oxygen inhibition.

Chapman *et al.* investigated the effect of GOx on the conversion of a tetra-block polymer, hydroxethyl acrylate (HEA), using low concentrations (0.5 - 2.5 mM) of 2,2'-azobis [2-(2-imidazolin-2yl) propane] dihydrochloride (VA044) initiator for thermal polymerization (20 h at 45 °C) in an organic solvent[136]. Conversions > 95 % were achieved by introducing 1 - 4 µM GOx in solution. The experiment was repeated with varying monomers such as methacrylic acid (MA), N, N-dimethylacrylamide (DMAm), and 2-hydroxypropylmethacrylamide (HPMA). Conversion profiles for these polymers resulted in 96 % to 99 % conversion with 4 µM GOx and 2.5 mM initiator. The study concluded that concentrations as low as 1 - 4 µM of GOx were successful at compensating for low initiator concentrations due to successful degasseing[136]. In a similar study by Chapman *et al.* GOx and glucose concentrations as low as 200 nM and 100 mM, respectively, were required to completely remove O_2 from an entire open vessel system for reactions to occur[136, 138].

Previously, for open vessel FRP of PAAm, only 24 % conversion was achieved using type-1 initiator 2, 2-dimethoxy-2-pheyl acetophenone (DMPA) at 1 wt % in the presence of GOx, only a 2 % increase in conversion compared to the control without GOx[118]. This leaves a high concentration of toxic monomers in solution, therefore requiring further treatment to remove unreacted reagents. Another limitation of the study was that cell studies with the initiator DMPA showed significant loss of cell viability at 0.05 w/v % (0.5 wt %) and higher[139]. In contrast, Irgacure-2959, a highly efficient type 1 α-cleavage photoinitiator[140, 141] only

exhibits cell toxicity at 0.1 wt/v % (1 wt %)[115, 142 139]. Other studies used GOx as a mediator for redox initiation polymerizations based on the by-product hydrogen peroxide forming hydroxyl radicals[143, 144] but not as a means for complete degassing of O_2 in open vessel FRP.

Ultimately, GOx is a viable option for degassing monomeric solutions prior to photopolymerization. Removing O_2 from monomeric solutions can largely benefit the resulting polymeric products by improved kinetics, higher conversion and less residual toxic monomers remaining in the system. The low concentrations of GOx explored in previous suggest better degassing than inert gas purging, opening the door for a more energy efficient and economically viable option.

2.9 Graft polymerization from the surface of nanoparticles

An alternative to cross linking polymers via nanoparticles is grafting polymers on the surface of nanoparticles. Previous studies have successfully achieved polymer grafts on the surface of SNPs, for example: polystyrene with controlled/ living radical polymerizations[145], polystyrene by atom transfer radical polymerization (ATRP)[146], thermoresponsive poly-n-isopropylacrylamide (PNIPAM) brushes by ATRP[147], polymethyl methacrylate (PMMA) by UV-induced graft polymerization[148], polyacrylamido-2-methyl-1-propane sulfonic acid (PAMPS) and polystyrene sulfonic acid sodium salt (PSSA) by surface initiated redox polymerization[149]. As DNHG require a polyelectrolyte first network, PAMPS and PSSA under redox polymerizations were explored. SNPs were functionalised with APTES to form amine groups covalently linked to the surface of the SNPs. The resulting amine SNPs were dispersed in 0.1 M nitric acid solution and AMPS monomers, before adding the redox initiator cerium ammonium nitrate (CAN) and stabilizer sodium dodecyl sulfate (SDS). The system was purged with nitrogen and heated to 40 °C to commence the graft polymerization of monomers on the surface of the amine SNPs. The graft polymerization was initiated by a redox pair of ceric ion (oxidant) and the alkyl amine (reductant), causing an intermediate free radical at the α-carbon atom of the alkyl amine group. This was a result from the redox reaction between Ce (IV) from CAN and alkyl amine group attached to the surface of

the SNP. At this point, the graft polymerization of AMPS or SSA was initiated and polymer growth occurred from the surface of the SNP. The presence of polymers on the surface of SNPs was confirmed by FTIR and thermo gravimetric analysis (TGA). From TGA, grafting percentage and polymer conversion were 46 % and 4.6 % for PAMPS, and 22 % and 2.2 % for PSSA, respectively. The resulting grafting percentage and polymer conversion were considered relatively low; however, successful grafting occurred resulting in a polymer nanocomposite that has the potential to be used as a first network in DNHGs. The use of CAN as an initiator has the potential to propagate the reaction further if it is optimized under the right conditions. Since cerium ions have auto-catalytic antioxidant properties and two valence states that provide efficient redox behaviour, cerium can be targeted for optimization to increase reaction kinetics and conversion. This can be achieved by forming nanoparticles made of cerium oxide, and the addition of a catalyst that regenerates the redox valence states of the ions.

2.9.1 Nanoceria

Cerium oxide (CeO_2) nanoparticles, also known as nanoceria (NC), are inorganic structures that have a catalytic antioxidant nature. In the past, NC has been used in applications such as UV light absorbers, catalytic converters in exhaust systems for automobiles, solar cells etc., and more recently in research antioxidants for therapeutic treatments to combat neurodegenerative disorders and cancer[150]. NC has two valence states; Ce(III) and Ce(IV), that provide efficient redox behaviour. This allows cerium atoms to cyclically change their oxidation states between reduced Ce^{3+} and oxidised Ce^{4+} states. In the form of nanoparticles, NC has an abundance of reduced Ce^{+3} atoms on the surface with a core consisting of mainly oxidised Ce^{4+} atoms. This intrinsic oxygen vacancy system enables NC to have an auto-catalytic mechanism[151]. The oxygen vacancy is related to the crystallite structure, which allows ceria to switch between oxidation states. In the form of nanoparticles, the abundance of oxygen vacancies increases. The catalytic nature of NC is highly dependent on its surface structure, which in turn is influenced by the local surrounding environment. NC is commonly dispersed in

water, creating an environment that promotes the formation of vacancies that allows the change in oxidation states[152]. This allows for NC to be used in biomaterial synthesis routes that involve water soluble monomers. The most efficient method for NC synthesis to date is the treatment with microwaves[153]. The microwave synthesis method is characterized by rapid and homogenous heat treatment as opposed to conventional methods[153]. Conventional methods include high-temperature synthesis using spray pyrolysis[154], hydrothermal[155], solvothermal[156], sol-gel[157], Pechini (a modified sol-gel technique using citric acid)[158], and micro emulsion[159]. Of the many benefits of the microwave method, some examples are: rapid volumetric heating, higher reaction rates during synthesis, higher production yield, lower energy cost and shorter synthesis time[153, 160]. This method is considered more economic for preparing nanocrystalline particles, providing better crystallinity to the nanostructures in a shorter period of time. The main reagents NC synthesis are cerium (III) nitrate hexahydrate ($Ce(NO_3)_3 \cdot 6H_2O$), urea, and sodium hydroxide (NaOH)[161].

When NC is active in aqueous solution its surface becomes reduced from Ce^{4+} to Ce^{3+} by reacting with reactive oxygen species, releasing O_2 as a by-product[162]. However, in the presence of H_2O_2, Ce^{3+} can be re-oxidized to Ce^{4+} [162], as expressed in the equations below.

$$O_2^{\bullet -} + Ce^{4+} \rightarrow O_2 + Ce^{3+} \qquad \text{(Equation 2.1)}$$

$$O_2^{\bullet -} + Ce^{3+} + 2H^{+} \rightarrow H_2O_2 + Ce^{4+} \qquad \text{(Equation 2.2)}$$

This is a reversible oxidation and reduction reaction, although the mechanism is unclarified to date, it occurs for a long duration in aqueous solution until H_2O_2 has completely degraded[162, 163]. H_2O_2 can be used to play a role in NCs oxidase activity; therefore it is possible to combine GOx/G and NC to benefit from this system. The combination of NC and GOx/G has been proven to work effectively from previous

studies aimed for glucose sensing[164, 165]. GOx/G produces H_2O_2 as a by-product once the reaction takes place in the presence of O_2. Therefore, as discussed earlier as part of graft polymerizations, it is possible to benefit from the presence of GOx/G as a degassing agent and as a facilitator for H_2O_2 production which revitalises the cerium based initiators, or NC surface. This can be expressed with the equations below[166]:

$$\mathrm{GOx} \xrightarrow{\mathrm{G+O_2}} \mathrm{H_2O_2} \qquad \text{(Equation 2.3)}$$

$$\mathrm{Ce^{4+} + H_2O_2 \rightarrow\ Ce^{3+} + H^+ + HO_2} \qquad \text{(Equation 2.4)}$$

$$\mathrm{Ce^{4+} + HO_2 \rightarrow\ Ce^{3+} + H^+ + O_2} \qquad \text{(Equation 2.5)}$$

$$\mathrm{Ce^{3+} + H^+ + HO_2 \rightarrow\ Ce^{4+} + H_2O_2} \qquad \text{(Equation 2.6)}$$

In this case, Equation 2.5 replenishes O_2 that can be used again with GOx. GOx would be used in excess therefore able to release more H_2O_2 for Ce^{4+} to convert into O_2 and reactive oxygen species for Ce^{3+} to react with.

To date, this proposed mechanism has not been carried out in an attempt to utilise the combination of NC and GOx/G for graft polymerizations, and particularly for hydrogel formation.

2.10 Aims and objectives

Significant progress has been achieved in advancing hydrogels for specific tissue engineering applications, through the use of natural and synthetic polymers, in combination with nanocomposite structures. The discovery of double network hydrogels (DNHGs) has revealed polymers can interact in a synergetic manner, rather than linear, to provide the biomaterial with advanced properties.

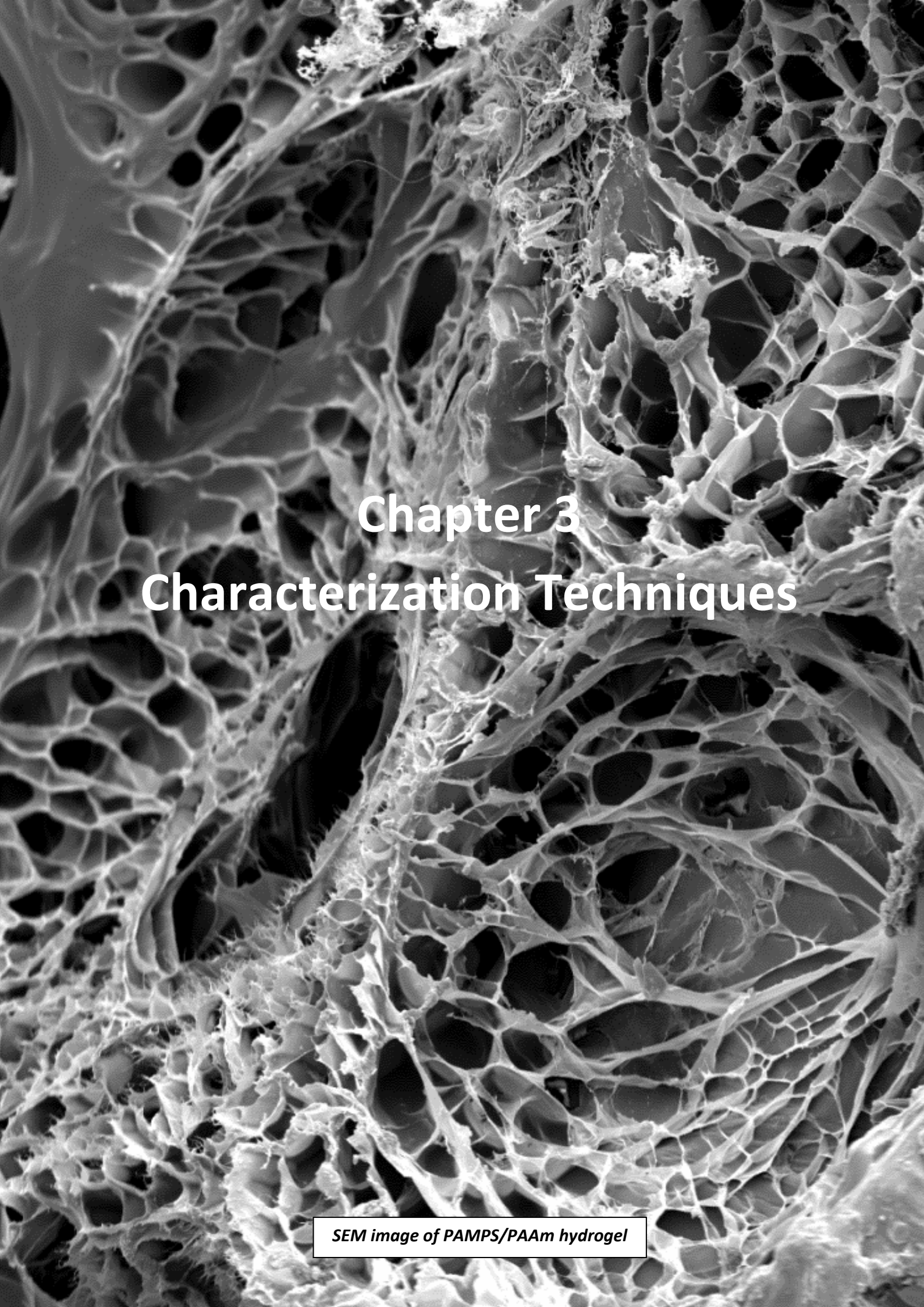
In this work, two polymers will be explored as first network polymers; polyacrylic acid (PAAc) and poly2-acrylamido-2-methylpropanesulfonic acid (PAMPS), with polyacrylamide (PAAm) as their second network. These first network polyelectrolytes have been chosen due to their inherent hydrophilic nature and significant swelling ability. PAAm has been chosen as the second network due to its extensive success for its ability to synergistically increase the mechanical properties when in combination with polyelectrolytes. Furthermore, silica nanoparticles (SNPs) and nanoceria (NC) will be used as the basis for the nanocomposite structures in this research, as nano cross linkers, and grafting surfaces for polymers.

The overall objective of this research is to explore the effect of size and loading concentration of nanoparticles as a cross linking mechanism in DNHGs. In particular, an aim of this research is to highlight the ability nanoparticles have at tailoring the properties of DNHGs. A comparison will be made between DNHGs consisting of polymers cross linked using nanoparticles, to DNHGs made of polymers that were grafted on the surface of nanoparticles. The objectives of this work are:

1- Develop a novel DNHG with a first network consisting of PAAc cross linked with amine SNPs, of varying size and loading concentration, using carbodiimide (EDC) chemistry and examine its physical properties. A DNHG consisting of a first network of PAAc that is cross linked solely with amine SNPs via EDC has not been explored, to date.

2- Investigate the impact of varying size and concentration of vinyl SNPs on the physical properties of a DNHG consisting of PAMPS in the first network, through *in-situ* cross linking and photopolymerization. To date, the detailed combined effect of size and concentration on a PAMPS/PAAm DNHG has not been explored.
3- Optimize the open vessel polymerization system by the addition of the degassing agent GOx and examine the kinetics, conversion and cytotoxic effects of the resulting polymers. GOx, to date, has not been used as a degassing agent, or reaction kinetics enhancer, in FRP systems for the synthesis of biomaterials.
4- Compare and contrast the effect of GOx as an O2 inhibitor, to controls with the absence of GOx, on the physical properties of DNHGs synthesized through open vessel synthesis.
5- Investigate and optimize polymer grafting on the surface of SNPs and NC and the impact GOx may have on the resulting nanocomposite structures compared to argon degassing. Followed by a subsequent synthesis of two novel DNHGs formed via graft polymerization in the presence of GOx in both networks. To date, graft polymerization on the surface of NC has not been explored, and NC has not been utilised as a nanocomposite in DNHGs. The two novel DNHGs will be the first of their kind, to have both networks formed through graft polymerization.

This work is intended to open the door to optimized DNHG synthesis techniques with optimized routes and novel combinations of biomaterials in the hopes of treating articular cartilage defects. The biomaterials explored in this research are intended for cartilage tissue repair and replacement.



Chapter 3
Characterization Techniques

SEM image of PAMPS/PAAm hydrogel

3 Characterisation techniques

3.1 Dynamic Light Scattering (DLS)

DLS is an analytical technique that is used to calculate the hydrodynamic radius of nanoparticles in suspension undergoing Brownian motion. Brownian motion is the random movement of nanoparticles as a result of continuous interaction with molecules from the solvent they are dispersed in. The nanoparticles are irradiated with monochromatic light, with wavelength λ, within the visible spectrum. The nanoparticles cause the light to scatter which is then analysed by a detector. The detector is kept at an angle, θ, with respect to the transmitted beam. Constructive and destructive interferences are generated due to the constantly changing local concentration of the nanoparticles caused by Brownian motion. Larger nanoparticles tend to scatter light at smaller angles than smaller nanoparticles. The diffusion coefficient (D), also considered nanoparticle speed, can be found through these interferences and through with an autocorrelation. The hydrodynamic radius (R_h) can be found using D in the Stokes-Einstein Equation (3.1) where T is temperature and v_s is solvent viscosity, and kB is the Boltzmann constant.

$$D = \frac{kBT}{6\pi vs(T)Rh} \qquad \text{Equation (3.1)}$$

T is kept constant during the analysis as changes in temperature have an effect on Brownian motion.

In this research, sample volumes of 100 µl were diluted in 1 – 1.5 ml of deionized water and sonicated using the CamSonix 1800T until the nanoparticles were suspended. A high dilution is required for a good reading. Glass quartz cuvettes were used for analysis in the Nano ZS ZEN3600 Zetasizer, and each sample was run 3 times with 12 scans.

3.2 Zeta potential

The surface charge of nanoparticles suspended in solution can be determined using zeta potential, giving an indication of their stability and aggregation, and modification. Nanoparticles have a charge on their surface that attracts ions of the opposing charge. This forms a Stern layer around the surface of the nanoparticles that then forms a second outer diffuse layer of ions, allowing the ions to move freely around the surface of the nanoparticle. This electrical double layer has an electro-kinetic potential that can be measured, referred to as the zeta potential. The zeta potential is calculated based on theoretical models and estimated using experimentally based on the nanoparticles electrophoretic mobility. This measurement depends on the zeta potential of the sample, and is also affected by the dispersant used. An electric field is applied through the dispersion causing relative movement between the nanoparticles and the fluid they are suspended in. This electrophoretic mobility of the nanoparticles is measured by Laser Doppler Velocimetry. The zeta potential is then calculated using the Henry equation, provided the viscosity of the medium, electric field strength and dielectric constant are all known.

For this research, the Nano ZS ZEN3600 Zetasizer was used to calculate the zeta potential. Samples were suspended and sonicated in ethanol prior to testing at room temperature. Each sample was run 3 times with 12 scans.

3.3 Scanning Electron Microscopy (SEM)

A material can be examined at a nanoscale using SEM imaging. A focused beam of electrons, generated from an electron gun, bombards the surface of the material. This causes inelastic scattering of secondary electrons and backscattered electrons by the sample atoms excited by the electron beam. Secondary electron scattering is the most common detection mode using in SEM imaging. The secondary electron detectors are close to the surface of the sample therefore produce high-resolution images that can reveal details of < 1 nm in size.

Samples for SEM have to be conductive to avoid electron beam charging of surface of the sample. Gold and chromium are commonly used, with silver around the edges of the sample to reduce sample charging.

Samples in this research were placed on SEM sample holders and held by carbon tape. Samples were then sputter coated for 2 minutes at 20 mA to form a 10 nm layer of chromium. The LEO Gemini 1525 FEG-SEM was used to image the surface morphology of freeze dried hydrogels using 3 – 5 kV and a working distance of 5 – 10 mm.

3.4 Transmission Electron Microscopy (TEM)

TEM is a technique used for high resolution imaging of nanoscale structures of thin samples. A focused electron beam is accelerated using an electron source through a vacuum into a specimen of < 100 nm in thickness. A tungsten filament emits the electrons which are initially focused by a pair of condenser lenses. The first condenser lens controls the beam current density. The second condenser lens varies the convergence of the beam and is manipulated during imaging. The electrons then interact with atoms in the sample by columbic forces, causing electron scattering. The objective lens receives and focuses these electrons from the specimen into a diffraction pattern, allowing for adjustments to be made to focus the image on the viewing screen. The objective aperture can be used to enhance mass-thickness image contrast by suppressing high angle diffracted electrons. This increases image contrast for mass-thickness dominated regions. Brighter regions contain more electron-scattering, whereas darker regions have fewer electrons transmitted through them.

In this research, the JEOL FX2000 was used, consisting of a tungsten filament as the electron source. An operating voltage of 200 kV was used and a 10 µm objective aperture. Samples were diluted in ethanol, sonicated and then carefully dropped onto 300 mesh copper TEM grids coated with holey carbon film.

3.5 Proton Nuclear Magnetic Resonance (^{1}H NMR) Spectroscopy

^{1}H NMR is a technique used to determine the chemical structure of molecules that are dissolved in a deuterated solvent. The structure of the molecules is determined by measuring the resulting spin experienced by the nuclei when they are exposed to a magnetic field. The energy level of the magnetic field affects the spin and electrical charge of the nuclei. This causes energy transfers between low energy levels (high population of nuclei) and higher energy levels (low population of nuclei). Low energy levels align the nuclei parallel to the external magnetic field, whereas higher energy levels align nuclei antiparallel to the external magnetic field. The energy transfers between the low and high levels in the nuclei are caused by pulses of radiofrequency radiation. These energies are represented as a chemical shift spectrum. The chemical shift of each nucleus is affected by electron density shielding, which can be surrounding atoms, bonds and other electronegative species. Electron shielding decreases the chemical shift whereas electron donating groups increase it. The intensity of the chemical shift peaks provides information of the abundance of the particular group in the sample. Chemical shifts are measured in parts per million (PPM) and are plotted against relative intensity.

In this research samples were dissolved in deuterated water (D_2O) and analysed using Bruker AV-400 spectrometer operating at 400 MHz. The resulting spectra were analysed using MestReNova software with a 'Whittaker smoother' baseline correction. All samples contained dissolved trioxane used to aid in assessing monomer to polymer conversion. Trioxane peaks were integrated to represent a value of 1. Monomer peaks were integrated relative to trioxane.

3.6 Attenuated Total Reflection Fourier Transform Infrared Spectroscopy (FTIR)

FTIR is a method used to analyse the chemistry of a material, by identifying specific chemical bonds in the sample. Covalent bonds that have dipole moments absorb

incident infrared radiation (IR) and are excited. These excitations cause covalent bond vibrations, stretching and bending. Molecules in the sample absorb the energy at specific IR wavenumber causing the covalent bonds to transition to the next vibrational state. These specific vibrations are correlated between the covalent bonds in the sample and the IR wavenumber absorbed. A detector evaluates the attenuation of the reflected IR beam from the sample, creating an IR spectrum against absorbance. The peaks on the spectrum are specific to covalent bonds present in the sample.

In this research, a Nicolet iS10 Thermo Scientific FTIR was used. Samples were scanned 32 times per run with a resolution of 6 in a wavenumber region of 4000 – 400 cm^{-1}. Prior to analysis, samples were dried at 60 °C and ground to a fine powder.

3.7 Thermo Gravimetric Analysis (TGA) and Differential Scanning Calorimetry (DSC)

TGA is method of analysing the mass loss profile of a material as a function of increasing temperature. This technique can reveal the organic/ inorganic ratio of a material, indicating the materials composition. The derivative of the mass loss curve (DTG) can be used to analyse the precise points where a material begins to experience mass loss, and when the mass loss stops. TGA works concurrently DSC. DSC is a technique that calculates the difference between the heat energy required to increase the temperature of a sample against that required to heat a reference, measured in mW mg^{-1}. DSC therefore measures the heat released or heat absorbed during transition phases.

The NETZSCH STA-449C Jupiter was used in this research to conduct TGA-DSC. Samples are ground to a powder after being heat and vacuum dried, and heated from room temperature to 800 °C. A heating rate of 10 °C min^{-1} was applied to all samples. TGA was used to determine the nanoparticle retention in (NPR) hydrogel samples. NPR was calculated using Equation (3.2).

Equation (3.2)

$$\text{NPR}\ (\%) = \frac{\text{residual mass}\ (\%)}{\text{theoretical mass}\ (\%)} \times 100\% = \frac{\text{residual mass}\ (\%)}{M_p \Big/ (M_p + M_1 + M_2)} \times 100\%$$

Where M_p is the nanoparticle mass used in the material, M_1 and M_2 are the monomer masses used for the first network and second network, respectively, in the material.

3.8 Ultraviolet and visible absorption spectroscopy light (UV-Vis)

UV-Vis measures the attenuation of a beam of light after it has been passed through a sample suspended in solution, or after reflection from a solid samples surface. UV-Vis radiation interacts with matter in samples causing electronic transitions. This promotes electrons from their ground state to higher energy states. Molecules can undergo electronic transitions involving σ, π and η electrons. A spectrometer records the degree of absorption by the sample at different wavelengths, which is then plotted on an absorbance vs wavelength plot. Measurements can be taken at a single wavelength, or between the range 190 – 750 nm, where 190 – 380 nm is the ultraviolet region, and 380 – 750 nm is the visible light region. Different molecules absorb radiation at different wavelengths. Therefore, it is possible to assess the structural groups of a sample based on the absorption bands from the spectrum.

For this research, samples were diluted to 3 – 5 mg in 1 ml deionized water solutions and sonicated until fully dispersed. Samples were then loaded into the PerkinElmer Lambda 25 UV/VIS spectrometer and run against a blank sample of deionised water.

3.9 Gel Permeation Chromatography (GPC)

GPC can be used to determine the polymer molecular weight (MW) and polymer molecular weight distribution (Đ) of a sample. GPC is a type of size exclusion chromatography that is used to separate polymers by size. Samples are prepared in known concentrations of solutions in eluents. The polymers pass through a column packed with organized porous beads where shorter chains, or chains with smaller hydrodynamic radii, will penetrate more into the pores than larger chains. Therefore, larger chain polymers are eluted faster from the column. Once the polymers are separated by size, the eluting solution is detected based by a three detector system that measures low angle light scattering, viscosity by a viscometer, and refractive index by a differential refractometer. This combination of a triple detection system provides more accurate MW measurements[167]. The retention time of the polymer sample leaving the column will be calculated relative to polymer standards chosen in the software.

In this research, MW and Đ were calculated using the Malvern TDA 305, with DMF (0.075 % LiBr) as the eluent at a rate of 0.7 ml min^{-1} at 35 °C and a polymethylmethacrylate standard for calibration. Polymer samples were dried and dissolved in DMF with 10 µM LiBr then filtered through 0.45 µm filters into GPC vials. A polymer concentration of 4 mg mL^{-1} was used.

3.10 Swelling studies

Swelling studies can give an indication of the extent of cross linking within a hydrophilic material such as a hydrogel. The higher the cross linking density within a material, the less it is able to physically swell and therefore the material holds less water content than a lightly cross linked material. Water is able to exert isotropic deformations on the polymer networks as the materials volume increases when water is taken up. This occurs more freely when wider spaces are available for water to be taken up, indicating lower cross linking densities and ultimately leads to weakened material properties[168].

Swelling studies were conducted on samples that were dried at 60 °C for 5 days and then swollen in deionised water until a plateau was reached. Mass measurements were taken at 0, 1, 2, 4, 8, 24, 48, 120, 168 hours. Swelling was measured using equation (3.3).

$$\text{Swelling}\ (\%) = \frac{M_{s(t)} - M_d}{M_d} \times 100\% \quad \text{Equation (3.3)}$$

Where $M_{s(t)}$ is the swollen mass of the sample at time (t), and M_d is the initial dry mass of the sample. Water content of the hydrogels was also calculated using equation (3.4).

$$\text{Water content}\ (\%) = \frac{M_{s(t)} - M_d}{M_{s(t)}} \quad \text{Equation (3.4)}$$

3.11 Mechanical Testing

Mechanical testing in compression was conducted on all swollen samples until mechanical failure of the material was achieved. Failure of the material was considered to be the first sign of breakage of the hydrogel. During sample preparation and synthesis care was taken to ensure samples had flat bottom and top surfaces. This was to allow even distribution of stress across the material during compression.

The samples were compressed using a Zwick Roell z2.5 machine fitted with a load cell of 10 kN, and a strain rate of 1.5 mm min^{-1}. Due to the nature of the hydrogel, the material was physically distorted under compression in the perpendicular direction to compression. The distortion causes an increase in the cross-sectional area where force is applied; this is known as 'barrelling'. The mass that is distorted will therefore yield a larger sample-compression plate interface that generates frictional forces that resist lateral spread[169]. This ultimately results in increased compressive forces that are required to counter the

additional frictional forces, resulting in inaccurate compression profiles for the samples tested. Therefore, to correct for the distortion, conventional stress and strain were converted to real stress and strain, using Equations (3.5 – 3.8) below.

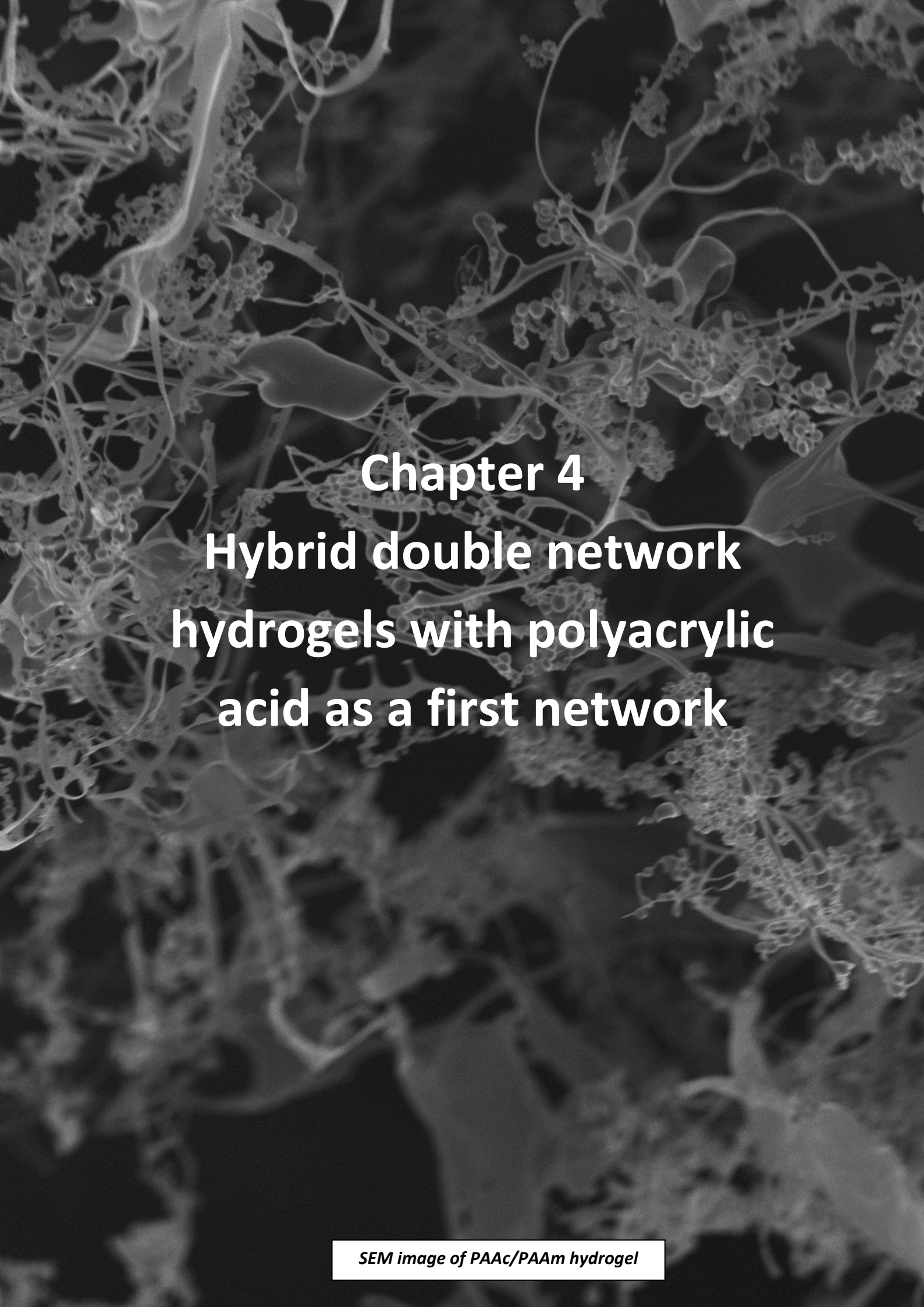
$$\text{Conventional stress (MPa)}\ \sigma_C = \frac{F}{A_0} \qquad \text{Equation (3.5)}$$

$$\text{Conventional strain (mm/mm)}\ \varepsilon_C = \frac{\Delta L}{L_0} \qquad \text{Equation (3.6)}$$

$$\text{Real stress (MPa)}\ \sigma_r = \sigma_c(1 + \varepsilon_C) \qquad \text{Equation (3.7)}$$

$$\text{Real strain (mm)}\ \varepsilon_r = \ln(1 + \varepsilon_C) \qquad \text{Equation (3.8)}$$

Chapter 4
Hybrid double network hydrogels with polyacrylic acid as a first network



SEM image of PAAc/PAAm hydrogel

4 Hybrid double network hydrogels with polyacrylic acid as a first network

4.1 Introduction

Double network hydrogels (DNHG) have generated considerable attention due to their advanced design of two contrasting polymeric networks[44]. Sequential synthesis of these two networks creates a synergetic effect within the materials, enhancing mechanical properties and physical integrity, whilst holding water content of up to 90 wt %[89]. One of the main requirements for DNHG is to consist of a first network polyelectrolyte with a rigid brittle structure, and a second network neutral polymer with a soft ductile network[44].

Polyacrylic acid (PAAc) is a weak polyacid with carboxylic groups that can act as proton acceptors at low pH or proton donors at neutral-high pH[170, 171]. This chapter explores high molecular weight PAAc (50,000 MW) that has bio-adhesive properties and the ability to create physical chain entanglements[172]. This leads to the hypothesis that PAAc has the potential to form a strong double network. The second network will be made of polyacrylamide (PAAm), a neutral hydrophilic polymer.

In this chapter, PAAc will be used as the polyelectrolyte first network polymer and cross linked using silica nanoparticles as micro cross linkers. A double network will be formed through a sequential photopolymerization step to form the neutral second network PAAm. This chapter will investigate the effect on mechanical strength and water uptake by varying both size and loading density of the nanoparticles in the first network. Through a combination of characterization techniques it will be possible to understand the extent of success of micro cross linking and the integration of the two networks to form a DNHG. The combination of this chemistry to form this hybrid nanocomposite DNHG has, to date, not been explored. During the initial trials of this chapter, 5,000 MW PAAc was tested but failed to form a consistent hydrogel for the first network. Therefore, 50,000 MW was used and formed a more consistent hydrogel.

4.2 Methods and materials

4.2.1 Materials

Polyacrylic Acid (PAAc; 50,000 MW) was purchased from Polysciences Inc. USA. N-(3-dimethylaminopropyl)-N'-ethylcarbodiimide hydrochloride (EDC) was purchased from Alfa Aesar UK. N-hydroxysuccinimide (NHS), ethanol (EtOH; 200 proof anhydrous; ≥ 99.5 %); acrylamide (AAm; ≥ 99 %), photoinitiator 2-hydroxy-4'-(2-hydroxyethoxy)-2-methylpropiophenone (synonym Irgacure 2959; 98 %), ammonium hydroxide (28-30 % NH_3 basis), tetraethyl orthosilcate (TEOS; 98 %), (3-aminopropyl) triethoxysilane (APTES; ≥ 98 %) and N, N'-methylenebisacrylamide (BIS; 99 %) were purchased from Sigma-Aldrich (UK). No additional processing and/or purifications were performed.

4.2.2 Method

4.2.2.1 Amine functionalised silica nanoparticles synthesis

Silica nanoparticles (SNP) were synthesized based on a previously optimized Stöber process to give monodispersed SNP[83]. SNP were synthesized by using fixed molar concentrations of TEOS (0.28 M) and water (6 M), and adjusting ammonium hydroxide to increase or decrease the diameter of SNP. 150 nm SNP were synthesized by measuring out 82.28 ml EtOH and 10.27 ml deionised H_2O into a beaker. 0.3 M NH_4OH, or 1.19 ml, were added to the solution followed quickly by 6.25 ml TEOS. The solution was left to stir at 500 rpm for 24 h. The final milky white solution was then centrifuged using the Eppendorf 5430 and washed with EtOH three times at 7,830 rpm to remove unreacted TEOS. The final precipitate was left to dry at 60 °C overnight. 50 nm SNP were synthesized using NH_4OH 0.2 M, and 100 nm was synthesized using NH_4OH 0.28 M. Figure 7 shows the reaction that forms the SNP.

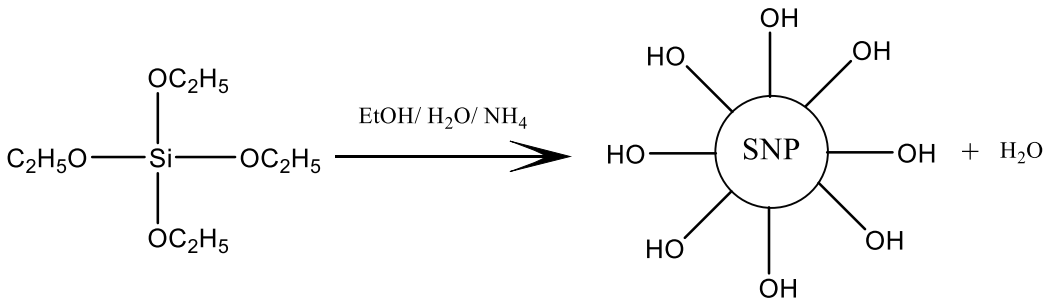


Figure 7 - Formation of silica nanoparticles using TEOS.

500 mg SNP were dispersed in 10 ml EtOH and sonicated using the CamSonix 1800T until fully dispersed then topped up with 90 ml EtOH on a stirring plate. 500 µl NH_4OH and 3 ml APTES were added to the solution and left to stir for 24 h. The solution was then centrifuged using the Eppendorf 5430 and washed three times with EtOH to remove unreacted APTES. The final precipitate was dried at 60 °C and stored under dry conditions. Figure 8 demonstrates the surface functionalization of SNP by APTES.

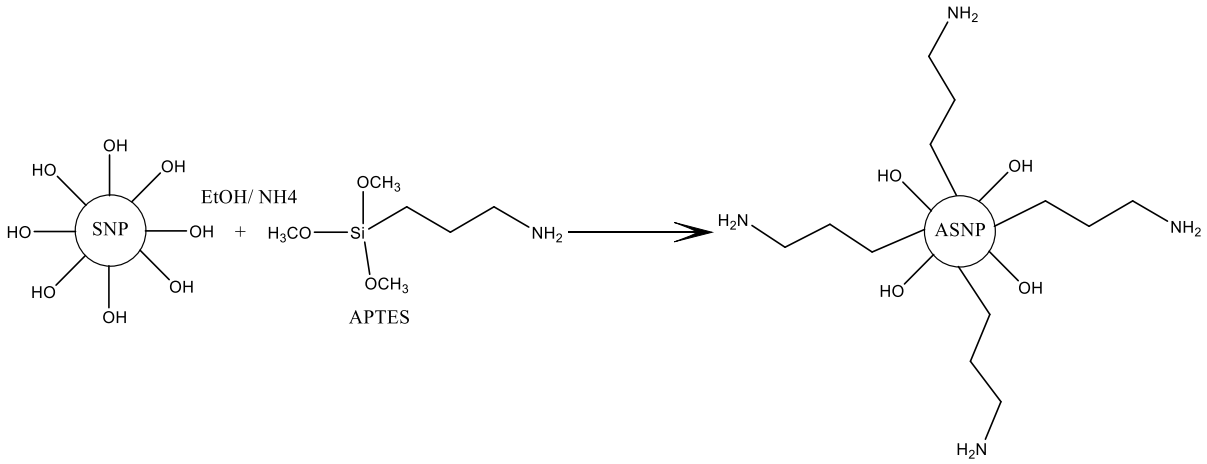


Figure 8 - Surface functionalization of silica nanoparticles by APTES.

4.2.2.2 Double network hydrogel synthesis

Carboxylic groups from PAAc were cross linked through amine functionalized silica nanoparticles (ASNP) by a carbodiimide reaction. PAAc was dissolved in MES buffer with 1-ethyl-3-(3-dimethylaminopropyl) carbodiimide (EDC) to form an unstable reactive ester (*O*-acylisourea), before *N*-hydroxysuccinimide (NHS) was added to form an intermediate semi-stable amine reactive NHS-ester, Figure 9[173, 174]. NHS was used to provide a more stable intermediate for reactions with primary amines, ASNP in this case, to form covalent amide bonds. *O*-acylisourea, in theory, has the ability to react directly with primary amines without the need for an intermediate; however the reaction rate is significantly low[173, 175].

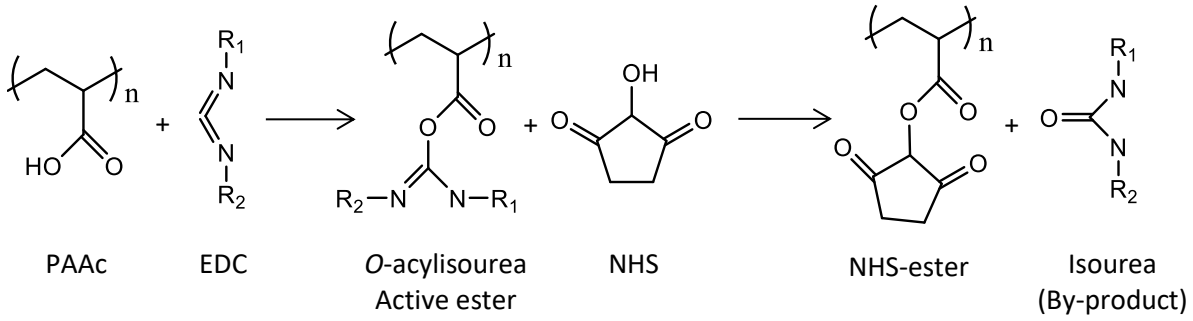


Figure 9 - Carbodiimide reaction of PAAc with EDC/NHS[173, 174].

Isourea by-products are easily washed out of the materials and do not interact with any other chemicals in the synthesis route. ASNP was added once the reaction to form the NHS-ester was complete, (Figure 10). PAAc then begins to form covalent amide cross links with the primary amine groups on the ASNP and releases the NHS back into the system. Longer chain PAAc is suited for such reactions due to the large surface area of ASNP providing potential sites for covalent bonding and the long chains, creating strong physical polymeric clusters.

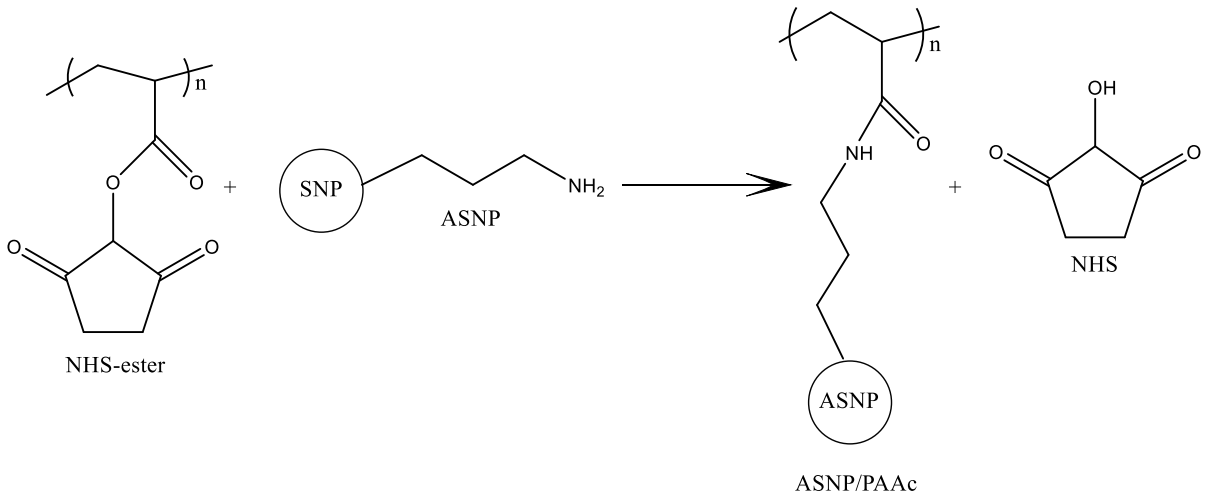


Figure 10 - Cross linking route between intermediate PAAc/NHS-ester and amine functionalized silica nanoparticles (ASNP).

The concentrations of EDC/ NHS were chosen carefully to ensure the intermediate NHS-ester formation takes place at the highest possible yield. This will ensure the reaction rate remains fast and efficient, and prevents the formation of unwanted by-products. Successful cross linking through carbodiimide reactions will allow a hydrogel to form by creating the first network, represented in Figure 11.The DNHG was then synthesized by the sequential photopolymerization of PAAm.

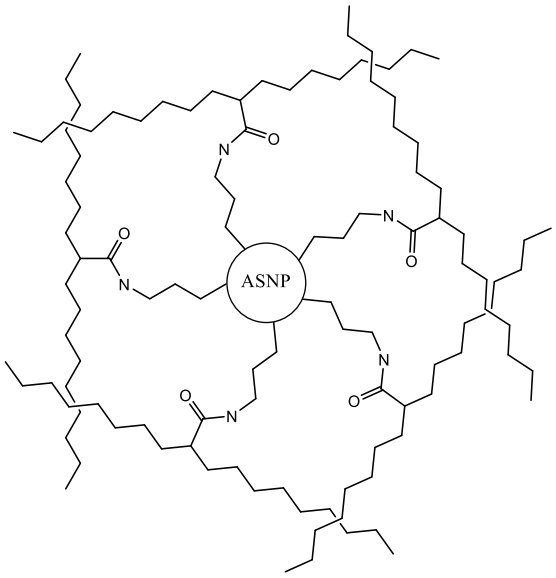


Figure 11 - Schematic representation of a first network PAAc system cross linked with silica nanoparticles.

2 ml of readymade PAAc (25 % solution in H_2O 50,000 MW), equivalent to 2 g, was dissolved in 4 ml MES buffer solution at pH 5.5. 2.5 wt % ASNP (50 nm) relative to PAAc was dispersed in 1 ml MES buffer and placed in a sonication bath for 30 minutes until fully sonicated. EDC was added in powder form to the PAAc solution at a mass ratio of 1:2.7 to ASNP, and NHS was added at a mass ratio of 1:0.3 to EDC based on previous works and systemic experimental trials[95, 176, 177], (Table 3). The sonicated ASNP were added when the solution was fully dissolved and clear, and left to stir until the solution became viscous. The solution was then poured into a polystyrene 48 cell culture well plate, which acted as a mould, allowing formation of the first network. Once the hydrogels were formed, they were removed from the well plate and prepared to be soaked in an AAm monomer solution.

Table 3 - Varying ASNP concentrations with equivalent carbodiimide reagent concentrations.

ASNP (wt%)	ASNP (mg)	EDC (g)	NHS (g)
0	0	0	0
2.5	12.5	0.03	0.01
10	50	0.13	0.04
20	100	0.27	0.08
40	200	0.53	0.16

2.5 g of AAm, 1 wt % (25 mg) Irgacure 2959 and 1 wt % (25 mg) BIS were dissolved in 5 ml deionised H_2O. The hydrogels were placed in the AAm monomer solution and left until they were swollen. Once the hydrogels were swollen they were placed in the UV-Cross linker for photopolymerization of the second network, to form the double network hydrogel. The UV-Cross linker was set to 5,400 seconds at maximum UV intensity (average 2900 $\mu W/cm^2$) of 365 nm light. 5,400 seconds was found to be sufficient time for gelation. The double network hydrogel is then removed and dried at 60 °C before being immersed in water for 14 days.

The process was repeated for 2.5, 10, 20 and 40 wt % for 50, 100 and 150 nm ASNP. A control double network hydrogel was formed following the same procedure without ASNP, EDC and NHS. The synthesis route is depicted in Figure 12 below.

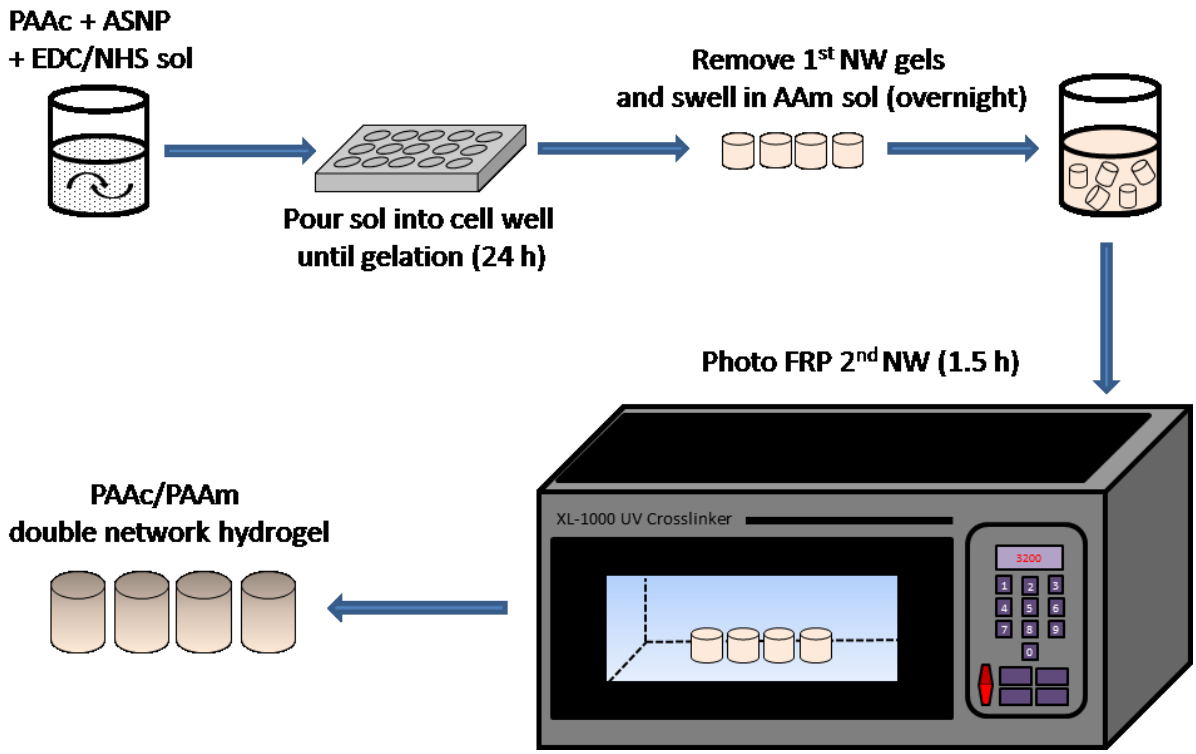


Figure 12 - Schematic representation showing the synthesis route for forming PAAc/PAAm double network hydrogels.

4.3 Results and discussion

4.3.1 Amine functionalised silica nanoparticles

ASNP were successfully synthesized by post synthesis functionalization using APTES. ASNP were dispersed in water and sonicated for size analysis by DLS. Figure 13 (a) shows mean modal diameters of 57 ± 3 nm (PDI 0.035), 108 ± 6 nm (PDI 0.095) and 153 ± 4 nm (PDI 0.029) were achieved with low polydispersity and high monodispersity. Figure 13 (b) shows bare nanoparticles had a zeta potential of -37 mV due to the abundance of OH groups on the surface, due to the deprotonated silanol groups. Amine functionalized nanoparticles had a surface zeta potential of + 27 mV due to the amine groups on the surface.

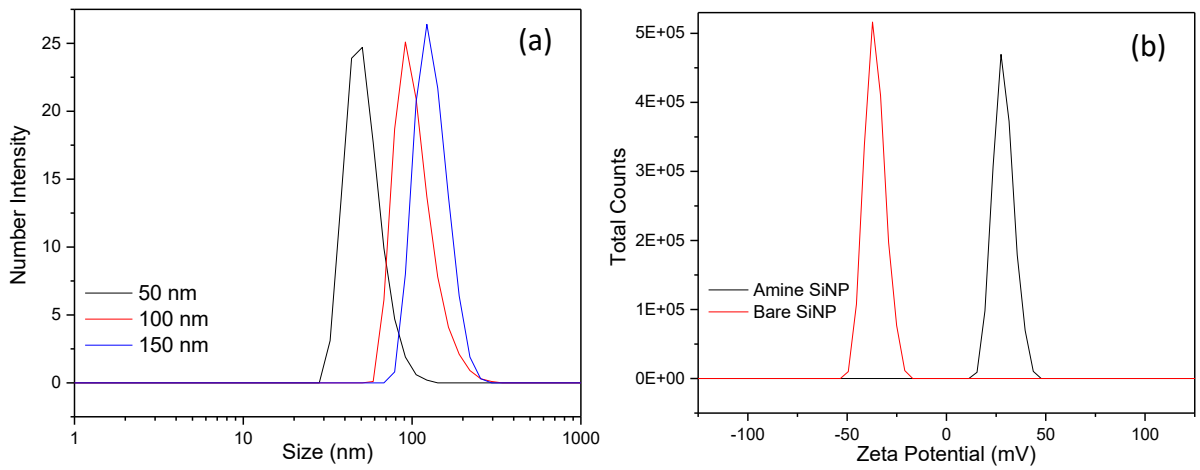


Figure 13 - (a) DLS graph showing size profile for 50 nm, 100 nm and 150 nm silica nanoparticles, (b) zeta potential graph showing bare and amine functionalized silica nanoparticle peaks.

Size and shape were confirmed using TEM imaging, Figure 14 (a – c), by taking an average diameter of 100 nanoparticles. Nanoparticles were dispersed in ethanol to measure their surface zeta potential and confirm surface functionalization.

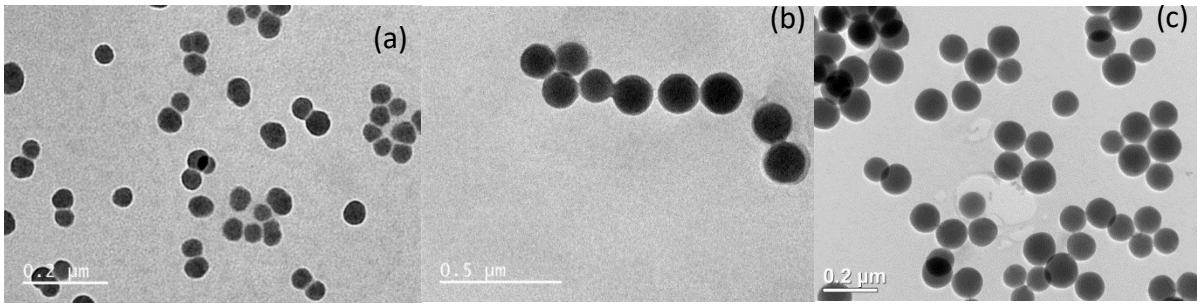


Figure 14 - TEM images of silica nanoparticles with mean modal diameters of approximately (a) 50 nm, (b) 100 nm and (c) 150 nm silica nanoparticles.

4.3.2 Hydrogels

PAAc/PAAm hydrogels were successfully synthesized with ASNPs as a cross linking nanocomposite structure. Five hydrogels of each size and composition were dried at 60 °C post synthesis for 5 days to reach a fully dry state. Of those five, one dried hydrogel was ground into a powder and used for FTIR to understand the hydrogels content post synthesis, referred to as 'Fresh' samples. Another sample for each was placed in water to be swollen in preparation for freezing and freeze drying to be imaged under SEM. The remaining three samples were used for the swelling study. The hydrogels were placed in deionised water and weighed at 0 h, 1 h, 2 h, 4 h, 8 h, 24 h, 48 h, 72 h, 120 h, 168 h, 240 h and 336 h. Compression studies were conducted on the fully swollen hydrogels once the swelling study was completed. Swollen hydrogels are referred to as 'swollen' samples and were also used for TGA and FTIR analysis.

In this section, double network hydrogels will be referenced to in terms of nanoparticle loading in their first network. For example, 40 wt % of 150 nm hydrogels refer to 40 wt % of silica nanoparticles with 150 nm diameter in the PAAc network of the entire double network hydrogel.

4.3.3 Swelling studies

All hydrogels reached a plateau at approximately 150 h after being swollen in water. By increasing nanoparticle cross linking density in the first network, the hydrogels were expected to exhibit a decrease in swelling properties.[178] Contrary to the expected results, swelling percentages and water content uptake in all the hydrogels experienced an increase relative to their control (no ASNPs). Figure 15 shows the control and hydrogels containing 150 nm SNPs before and after being swollen. 20 and 40 wt % hydrogels had a higher packing density in the upper half of the hydrogels in (Figure 15) which would have been the lower region when in the moulds. This could be due to inhomogeneous distribution and sinking nanoparticles during gelation.

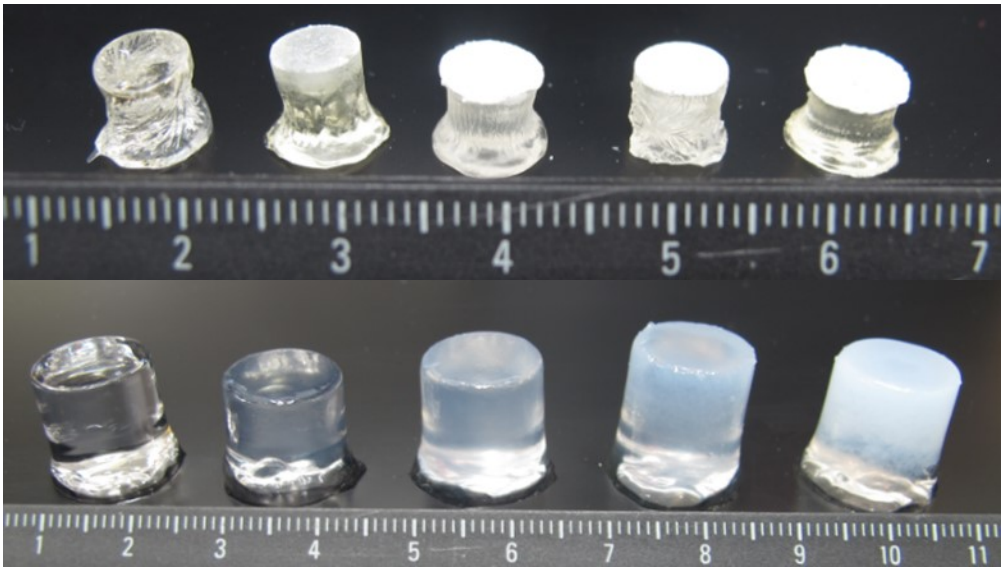


Figure 15 - Freshly made PAAc/PAAm hydrogels before swelling (top) and after swelling for 150 h (bottom). Hydrogels shown from left to right: control, 2.5 wt %, 10 wt %, 20 wt %, 40 wt % loading with 150 nm amine silica nanoparticles (ASNPs).

The hydrogels began to swell immediately when they were placed in water. This was mainly due to the hydrophilic nature of the two polymeric networks. The polymeric matrix complex becomes bound with water, known as 'primary bound water'[179]. Once this complex of the polymeric network began to swell, it exposed the hydrophobic groups. This ultimately resulted in hydrophobic bound water known as 'secondary bound water'[179]. 'Total bound water', or the collective bound water of the primary and secondary states, are considered the initial swelling states. Due to the osmotic driving forces in the hydrogel, the polymeric networks continue to absorb water until an equilibrium state is reached. This equilibrium would be due to osmotic forces being cancelled out by retraction forces of the swollen polymer networks. This addition water is considered 'bulk water'[179].

Control hydrogels had a water content of 88.67 ± 0.03 % with swelling of 783 ± 2.56 %. Figure 16, Figure 17 and Figure 18 show the swelling data for hydrogels with 150 nm, 100 nm and 50 nm ASNPs, respectively, compared to a control sample without ANSPs. The

highest value exhibited for water content was 91.96 % ± 0.03 for hydrogels with 150 nm ASNPs at 2.5 wt % loading. The lowest water content value exhibited was 88.34 % ± 0.04 for with 50 nm ASNPs at 20 wt % loading. This narrow range of change in water content suggests that there the addition of ASNPs has little impact on the water content, and swelling behaviour, of the double network hydrogels. Swelling studies were conducted on multiple samples from the same synthesis batch. This resulted in small standard error in the mean of each time point for water content, as seen in Figure 16, Figure 17 and Figure 18.

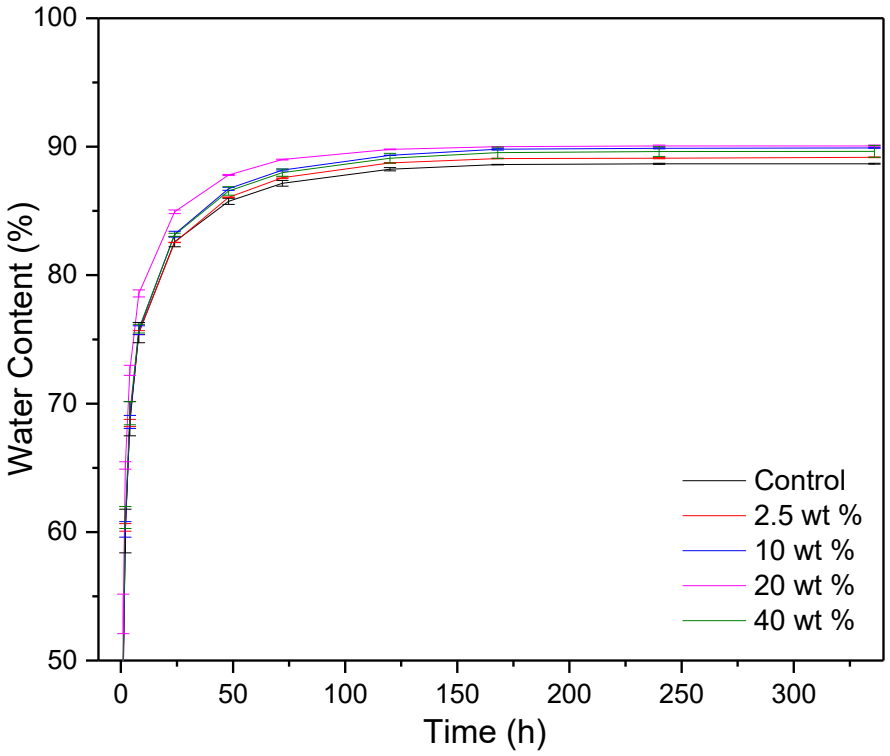


Figure 16 - Swelling profile for PAAc/PAAm hydrogels with 150 nm amine silica nanoparticles (ASNPs) at different loading concentrations compared to control.

Table 4 - Swelling and water content for PAAc/PAAm hydrogels with 150 nm amine silica nanoparticles (ASNPs) at different loading concentrations compared to control.

		Loading of 150 nm ASNPs			
	Control	2.5 wt%	10 wt%	20 wt%	40 wt%
Water Content (%)	88.67 % ± 0.03	91.96 % ± 0.02	91.17 % ± 0.14	90.48 % ± 0.14	92.04 % ± 0.04
Swelling (%)	783 % ± 26	824 % ± 24	891 % ± 28	907 % ± 67	866 % ± 42

Hydrogels containing 100 nm ASNPs followed the same trend as those containing 150 nm ASNPs (Figure 17) with the exception of 20 wt % which had the only swelling % lower than the control, at 758 ± 28 %.

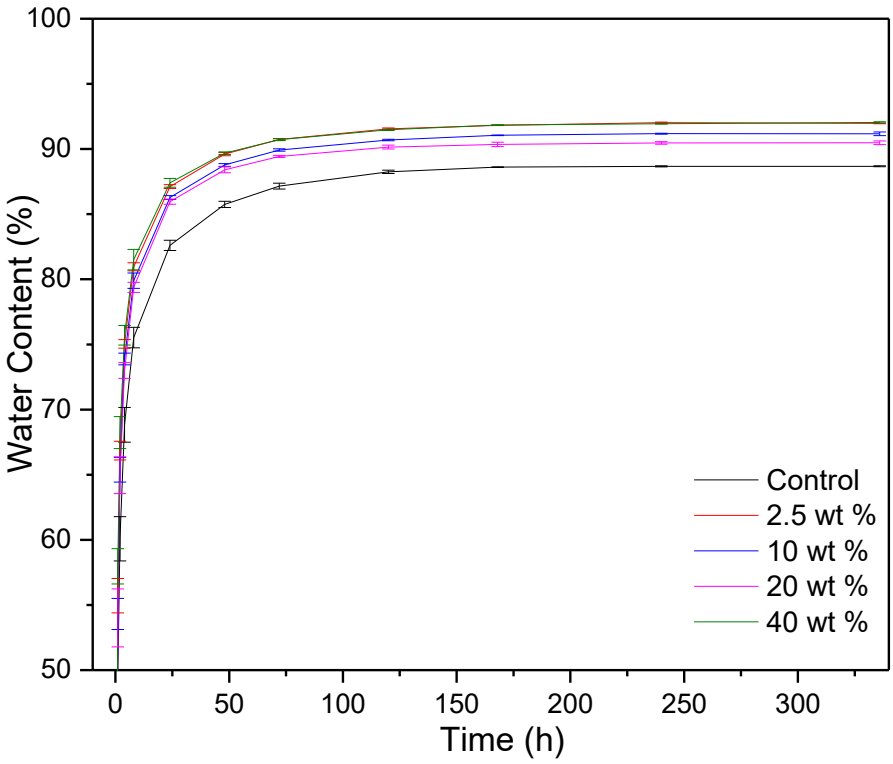


Figure 17 - Swelling profile for PAAc/PAAm hydrogels with 100 nm amine silica nanoparticles (ASNPs) at different loading concentrations compared to control.

Table 5 - Swelling and water content for PAAc/PAAm hydrogels with 100 nm amine silica nanoparticles (ASNPs) at different loading concentrations compared to control.

		Loading of 100 nm ASNPs			
	Control	2.5 wt%	10 wt%	20 wt%	40 wt%
Water Content (%)	88.67 % ± 0.03	89.17 % ± 0.03	89.91 % ± 0.03	90.06 % ± 0.07	89.64 % ± 0.46
Swelling (%)	783 % ± 26	873 % ± 40	813 % ± 47	758 % ± 28	1019 % ± 13

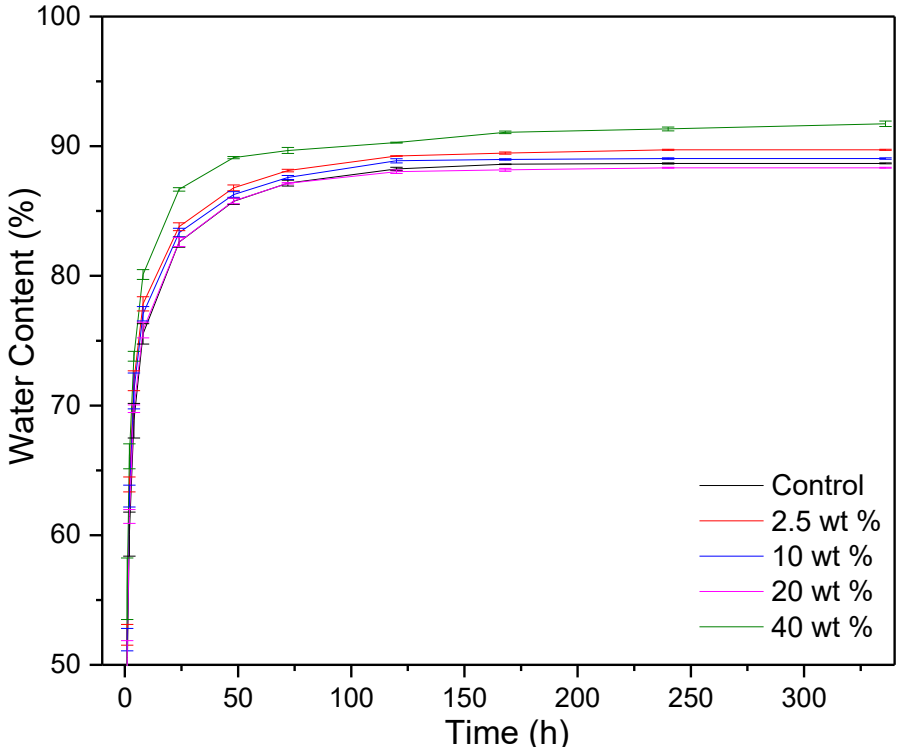


Figure 18 - Swelling profile for PAAc/PAAm hydrogels with 50 nm amine silica nanoparticles (ASNPs) at different loading concentrations compared to control.

Table 6 - Swelling and water profile for PAAc/PAAm hydrogels with 50 nm amine silica nanoparticles (ASNPs) at different loading concentrations compared to control.

		Loading of 50 nm ASNPs			
	Control	2.5 wt%	10 wt%	20 wt%	40 wt%
Water Content (%)	88.67 ± 0.03	89.73 ± 0.04	89.05 ± 0.06	88.34 ± 0.04	91.72 ± 0.21
Swelling (%)	783 % ± 26	1144 % ± 36	1032 % ± 19	950 % ± 16	1157 % ± 69

Compression studies were conducted on the swollen samples from this study to highlight whether nanoparticles were acting as fillers, cross linking agents, or as a combination. This would also help examine the combined effect of nanoparticle loading and size in the first network. After compression studies, dried samples were used for thermo gravimetric analysis (TGA) and FTIR. This was to further investigate the distribution and retention of nanoparticles in the hydrogels, and examine changes in chemical structure, respectively.

4.3.4 FTIR

FTIR was carried out on Fresh and Swollen samples that were dried and grounded for all hydrogels, to examine any changes post swelling. Table 7 below gives a summary of the bonds present in the FTIR spectra labelled (A-L) with their corresponding wavenumbers.

Table 7 - Summary of FTIR bands for PAAc/PAAm hydrogels.

	Bond	Type	Wavenumber (cm^{-1})
A	N-H	Stretching	3324
B	O-H	Water remaining in sample	3082
C	C-H	Alkyl stretching	2950
D	C=O	Stretching, coupled with N-H bending	1650
E	N-H	Primary amine	1620
F	C-N	Stretching primary amide	1420
G	C-H	Deformation	1350
H	N-H	Bending	1238
H	C-O	Carboxylic acid stretch	1240
I	Si-O-Si	Silica nanoparticles	1160
J	NH_2	In-plane rocking	1120
K	C-OH	Side group vibrations	1043
L	O-H	Carboxylic acid stretch	943

Figure 19 shows the stacked FTIR spectra for Fresh samples of hydrogels containing 150 nm ASNP. Carboxylic groups (-COOH) bands are 1240 cm^{-1}, 1043 cm^{-1}, and 943 cm^{-1} [180-182]. These bands show the presence and integration of PAAc into the double network hydrogel.

Bands of 1650 cm^{-1}, 1420 cm^{-1}, 3324 cm^{-1}, and 3082 cm^{-1} are generated by C=O stretching coupled with N-H bending, C-N stretching coupled with N-H bending, and medium to weak recordings of N-H stretching, respectively[183, 184]. N-H bending is also found at 1238 cm^{-1} [184]. These bands are produced due to the presence of PAAm in the hydrogel.

Polymer backbones are found in the band of 2950 cm^{-1} which represents vibrations of C-H alkyl stretching[185, 186].

C=C vibrations at 1635 cm^{-1} – 1676 cm^{-1} and 822 cm^{-1} give evidence of unreacted AAm monomers[7, 187, 188]. The intensity of these vibrations should decrease with higher polymer conversion, although it is difficult to conclude due to overlapping bands with C=O stretching coupled with N-H bending. Si-O-Si are found at 1160 cm^{-1} [189] indicating presence of ASNPs.

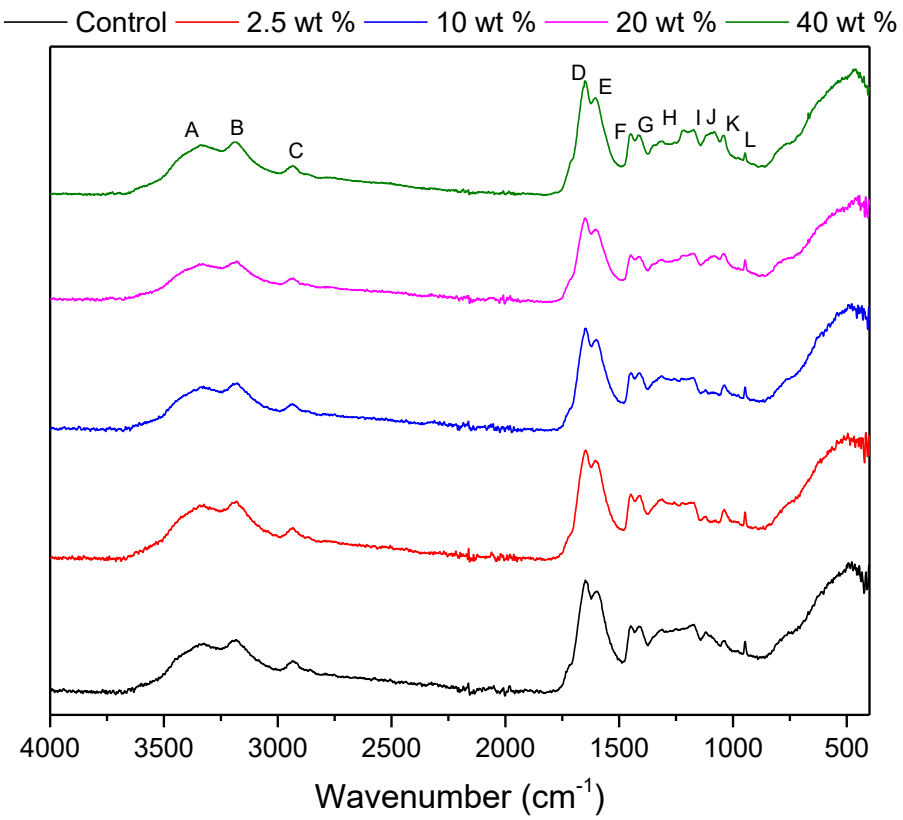


Figure 19 - FTIR spectra of Fresh PAAc/PAAm hydrogels with 150 nm silica nanoparticles (ASNP) at different loading concentrations compared to control.

Figure 20 shows the difference between Fresh and Swollen 2.5 wt % of hydrogels containing 150 nm ASNP. A clear decrease for O-H carboxylic acid stretch at 943 cm^{-1} can be seen. This indicates that loose PAAc chains were removed. A decrease in intensity of band 1160 cm^{-1} indicates nanoparticles have leaked out. PAAm chains may have also been washed out of the hydrogel, due to the decreased intensity of C-H in 2950 cm^{-1}. The decrease in absorbance at 1050 cm^{-1} due to leaked PAAc chains allows the NH2 band at 1120 cm^{-1} to become more prominent in the Swollen spectra.

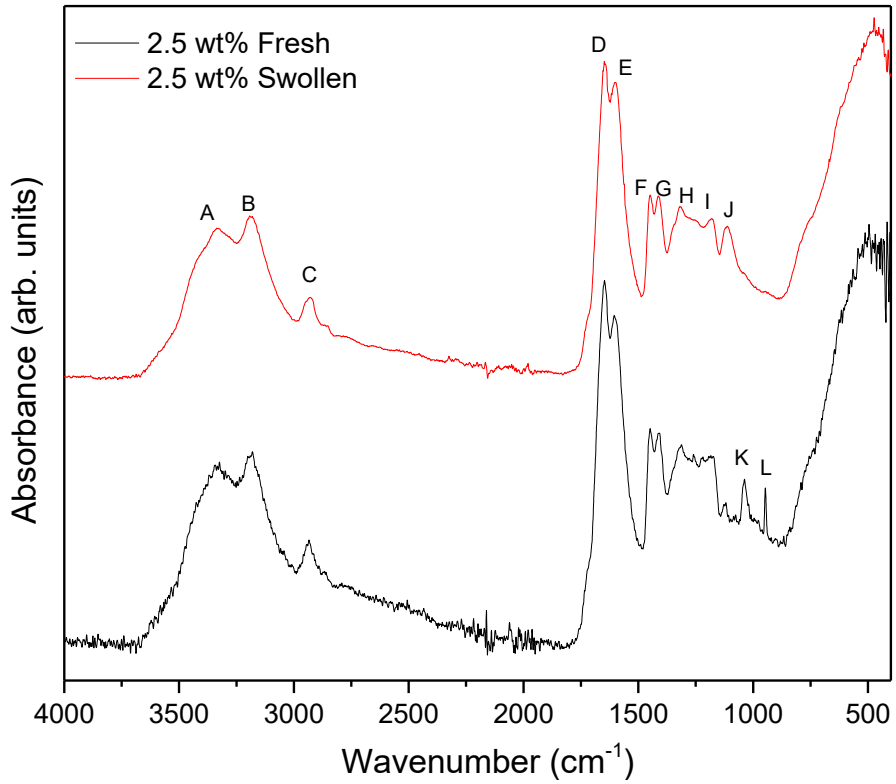


Figure 20 - Fresh and Swollen samples of PAAc/PAAm hydrogels with 150 nm amine silica nanoparticles (ASNP) at 2.5 wt % loading.

Therefore, FTIR concludes that unreacted AAm monomers and loose uncross linked PAAc are present in the system and are washed out after swelling in water, along with nanoparticles. Loss of nanoparticles during swelling suggests cross linking may not have been entirely successful for the first network, or that nanoparticles may be floating loosely and are therefore washed out during swelling. It is not possible to quantify the amount of

nanoparticles that remain in the hydrogels through FTIR. Therefore, nanoparticle retention was then calculated using thermo gravimetric analysis (TGA) on Swollen hydrogels.

4.3.5 TGA and nanoparticle Retention

TGA was used to calculate nanoparticle retention, using Equation 2 from Chapter 3, in Swollen samples of hydrogels post swelling. TGA was also used to gain an understanding on nanoparticle distribution within the hydrogels. Swollen samples were dried for 5 days at 60 °C and ground to a powder. Polymeric material in the samples is expected to be burnt off by 600 °C and any remaining residues were considered to be silica nanoparticles.

Figure 21 shows the TGA profile of hydrogels containing 150 nm ASNP with their corresponding DTG profiles. As expected, control samples reached 100 % mass loss at 630 °C and no residue was found once the platinum crucible was removed. Nanoparticle retention was over 95 % and above for all hydrogels containing 150 nm ASNP, except for 40 wt % which only had 81 % retention. The lowered retention for hydrogels containing 40 wt % ASNP (the highest ASNP concentration used) could be caused due to ASNP leaking out during swelling. This is perhaps due to excess ASNPs that were not bonded to the polymer; or nanoparticle loss during synthesis of the first network; or inhomogeneous distribution of ASNPs due to a sinking effect of nanoparticles during gelation of the first network. If ASNPs are not cross linked in the first network, they can potentially seep through the hydrogel pores while being soaked in the monomer solution of the second network. 150 nm nanoparticles have the smaller specific surface areas compared to smaller nanoparticles; therefore have less functional groups available for cross linking per unite mass of ASNPs. The DTG curve for 10 wt % shows a shift to the right compared to the control, meaning higher temperatures are required to break the bonds and burn off the material. This suggests 10 wt % nanoparticle loading had better cross linking than the other samples.

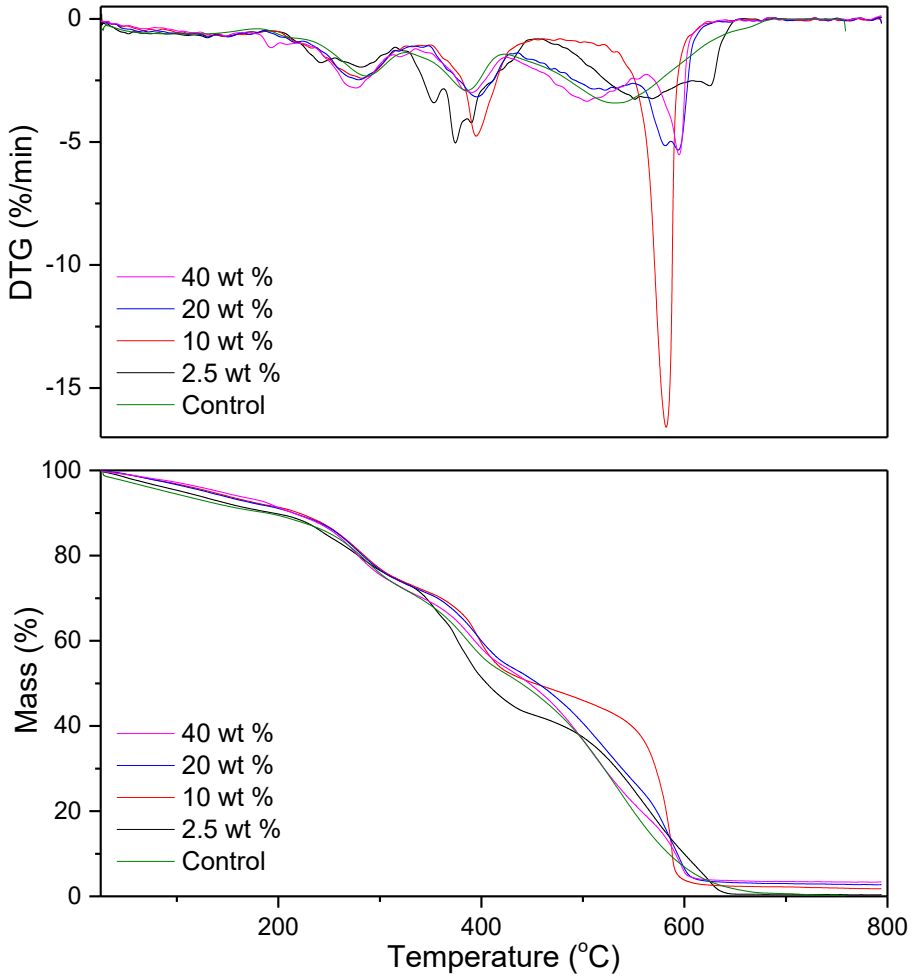


Figure 21 - TGA showing nanoparticle retention for PAAc/PAAm hydrogels for 150 nm amine silica nanoparticles (ASNP) at different loading concentrations compared to control.

Table 8 - nanoparticle retention for PAAc/PAAm hydrogels for 150 nm amine silica nanoparticles (ASNPs) at different loading concentrations compared to control.

	Loading of 150 nm ASNPs			
	2.5 wt%	10 wt%	20 wt%	40 wt%
Theoretical %	0.42	1.67	3.33	6.67
Residual %	0.40	1.60	3.33	5.40
Particle Retention %	95	96	100	81

Figure 22 shows the TGA and DTG profiles for hydrogels containing 100 nm ASNP. Hydrogels containing 100 nm ASNP follow a similar trend to 150 nm with the exception

of 10 wt % which only had 56 % nanoparticle retention. The increased loss can be due to the same reasons explained above. In general, hydrogels with 100 nm ASNP loading had less nanoparticle retention compared to 150 nm and 50 nm, with the exception of 20 wt % for 50 nm hydrogels, as can be seen in Figure 24.

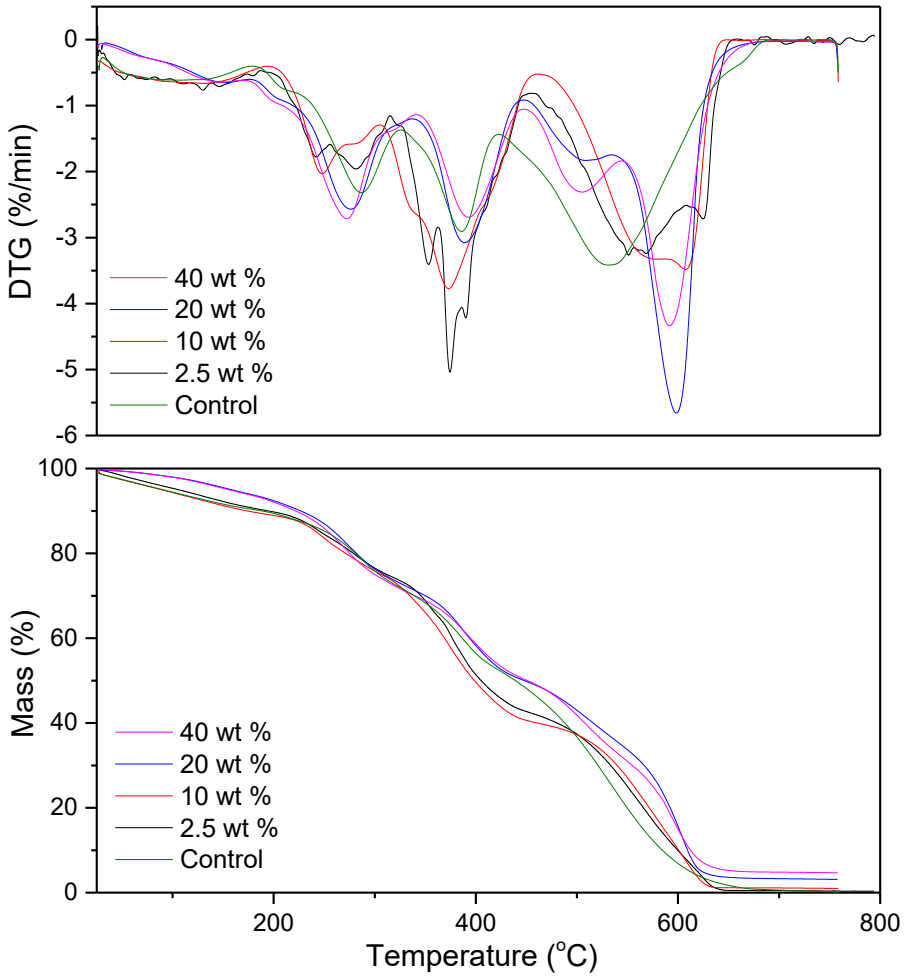


Figure 22 - TGA showing nanoparticle retention for PAAc/PAAm hydrogels for 100 nm silica nanoparticles (ASNP) at different loading concentrations compared to control.

Table 9 - nanoparticle retention for PAAc/PAAm hydrogels for 100 nm amine silica nanoparticles (ASNPs) at different loading concentrations compared to control.

	Loading of 100 nm ASNPs			
	2.5 wt%	10 wt%	20 wt%	40 wt%
Theoretical %	0.42	1.67	3.33	6.67
Residual %	0.34	0.94	3.09	4.66
Particle Retention %	82	56	93	70

Figure 23 shows the TGA and DTG profiles for hydrogels containing 50 nm SMP, which follows a similar trend to 100 nm and hydrogels containing 150 nm ASNP. For all 40 wt % hydrogels, a trend is seen where nanoparticle retention is lower. Although it was expected that larger specific areas for 50 nm and 100 nm ASNPs would result in better nanoparticle retention, an effect of easier percolation could have caused higher nanoparticle losses.

At 40 wt % loading the first network could be over loaded and over saturated with nanoparticles that are consequently washed out or lost during synthesis. Oversaturation of the first network at the highest ASNP concentration could have caused aggregates of ASNPs that resulted in the sinking effect that cause inhomogeneous distribution. This was evident during synthesis as a longer sonication time was required for samples with 40 wt % loading. These clusters of ASNPs aggregates are potentially detrimental to the mechanical properties of the hydrogels as they create voids in the sample that are uncross linked.

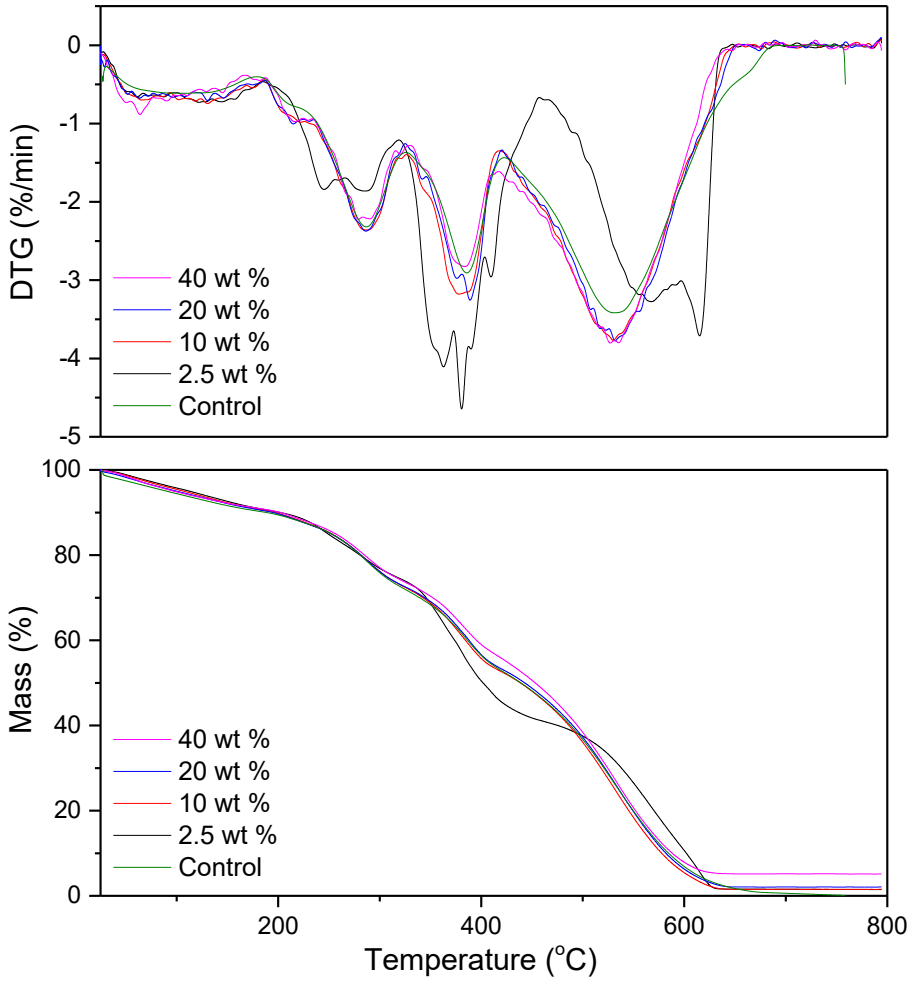


Figure 23 - TGA showing nanoparticle retention for PAAc/PAAm hydrogels for 50 nm amine silica nanoparticles (ASNP) at different loading concentrations compared to control.

Table 10 - nanoparticle retention for PAAc/PAAm hydrogels for 50 nm amine silica nanoparticles (ASNP) at different loading concentrations compared to control.

	Loading of 50 nm ASNPs			
	2.5 wt%	10 wt%	20 wt%	40 wt%
Theoretical %	0.42	1.67	3.33	6.67
Residual %	0.39	1.48	2.00	5.10
Particle Retention %	94	89	60	76

DTG curves for the control and hydrogels loaded with ASNPs show a difference due to different energies required to break bonds and physical interactions. A notable

difference can be seen in 2.5 wt % for 50 nm hydrogels where the DTG curve has larger double-peaks at 350 °C and a 550 °C. This suggests that strong interactions and bonds are present between the nanoparticles and PAAc in the first network, and possible interactions between the second and first network. A strong interaction between the two networks creates a synergetic effect in strength and bond energy[71] therefore requires higher temperatures to burn the material.

Ultimately, TGA and DTG show that there nanoparticles are likely bonded with PAAc in the first network, and that there are physical interactions with in the two networks.

Figure 24 provides a summary of nanoparticle retention based on ASNP wt % for 50 nm, 100 nm and 150 nm hydrogels. Smaller nanoparticles have a larger specific surface area and more likely to be affected by water during swelling. During the two weeks in water, hydrogels containing 50 nm and 100 nm nanoparticles that were weakly cross linked or loose in the hydrogel have a higher chance of being washed out. This explains the hydrogels increased water uptake and swelling percentages along with decreased nanoparticle retention.

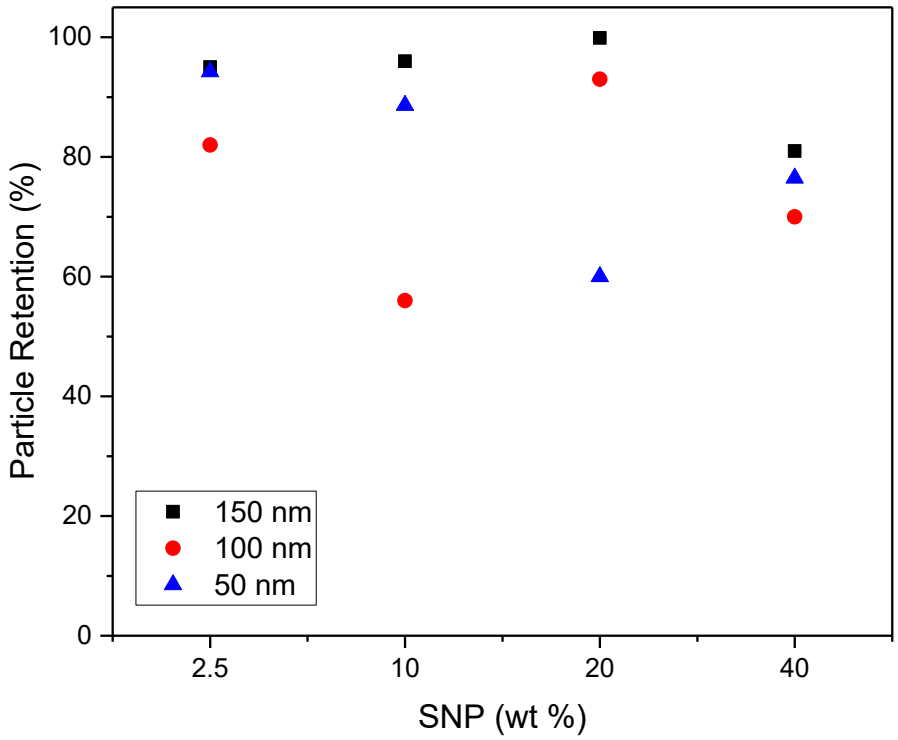


Figure 24 - A comparison of nanoparticle retention for PAAc/PAAm hydrogels with silica nanoparticles (ASNP) sizes of 150 nm, 100 nm and 50 nm at different loading concentrations.

4.3.6 Mechanical testing

Mechanical testing was conducted using uniaxial compression for swollen hydrogels. The initial hypothesis was that smaller ASNPs have a larger surface area therefore have the potential to cross link and interact more with PAAc in the first network, increasing stiffness compared to larger ASNPs. Results from TGA and swelling studies show that cross linking occurs at smaller nanoparticle sizes but also leads to higher loss in the nanocomposite structure, giving space for more water uptake. This in turn may have an impact on the mechanical strength, due to void spaces where nanoparticles may have washed out. This could ultimately lead to the increased water content that deemed the hydrogel more fragile. Contrary to this hypothesis, larger ASNPs were more stable in the hydrogels, according to TGA, and therefore have the potential to maintain the mechanical integrity of the hydrogels. Figure 25 shows a hydrogel under compression.

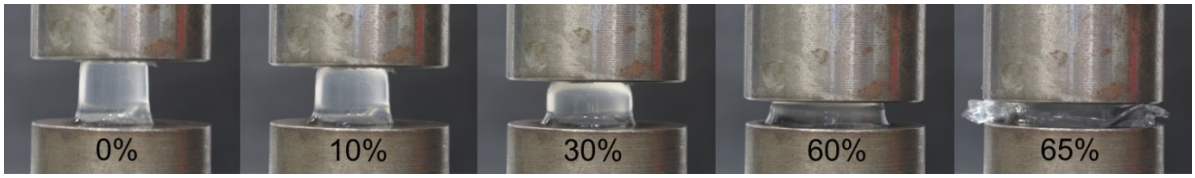


Figure 25 - PAAc/PAAm hydrogel with 150 nm amine silica nanoparticles (ASNPs) at 20 wt % loading, under compression until fracture.

The compressive stress at failure for controls was 0.10 ± 0.03 MPa at 45 ± 2 % strain. Figure 26 shows that the control was stiffer than the hydrogels containing 150 nm ASNP, and that 40 wt % ASNPs produced hydrogels with marginally reduced stiffness. The nanoparticles provide increased elasticity and allowed the material to be compressed up to 70 %. The highest compressive stress at failure was at 0.88 ± 0.04 MPa and 72 ± 4 % with 10 wt % ASNP in the first network. It is clear that the nanocomposite structure in the hydrogels has an impact on the mechanical properties of the hydrogel. This is likely due to the bonds between PAAc and amine ASNP that hold the polymer chains together while under stress, which is not present in control hydrogels. This is also reflected in TGA where more energy is required to burn off the polymer and break the bonds.

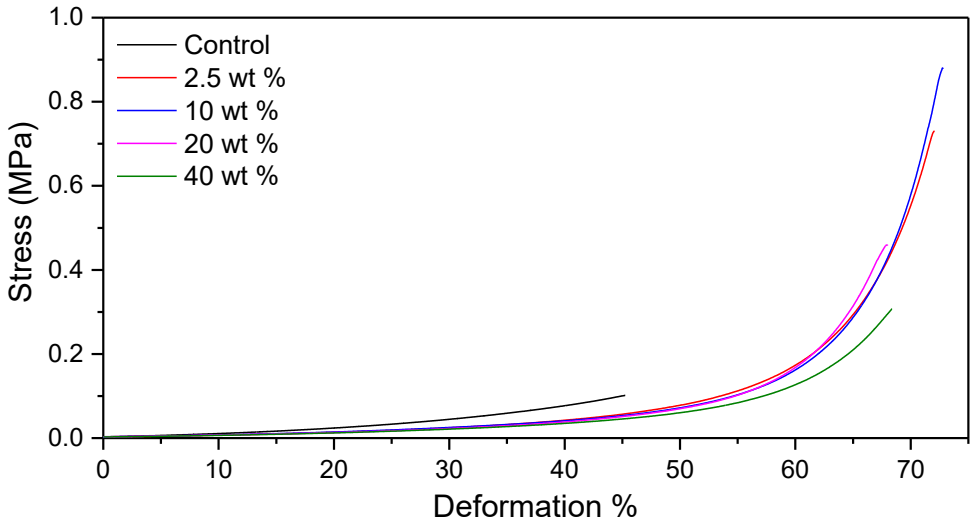


Figure 26 - Compression curves for PAAc/PAAm hydrogels with 150 nm amine silica nanoparticles (ASNPs) at different loading concentrations compared to control.

Table 11 - Compression and strain for PAAc/PAAm hydrogels with 150 nm amine silica nanoparticles (ASNPs) at different loading concentrations compared to control.

		Loading of 150 nm ASNPs			
	Control	2.5 wt%	10 wt%	20 wt%	40 wt%
Fracture Compressive Stress (MPa)	0.10 ± 0.03	0.73 ± 0.08	0.88 ± 0.04	0.46 ± 0.05	0.31 ± 0.11
Fracture Strain %	45 ± 2	72 ± 5	72 ± 4	67 ± 2	68 ± 5

Figure 27 shows the compression curves for hydrogels containing 100 nm ASNP. Similarly to the hydrogels containing 150 nm ASNP, it can be seen that the control was stiffer than the nanocomposite hydrogels. Again, the nanoparticles seem to increase the hydrogels ability to withstand higher strains but do not alter the fracture strength to the same extent as hydrogels containing 150 nm ASNP. 2.5 wt % hydrogels have similar compressive failure values, 0.14 ± 0.02 MPa, to the control, contrary to the 2.5 wt % for 150 nm that witnessed 0.73 ± 0.08 MPa compressive failure strength. This can suggest that the combination of size and concentration for 2.5 wt % and 100 nm does not have sufficient impact on the hydrogels. It has been suggested in previous works that for 150 nm nanoparticles, no significant difference was noted in cross linked and filler based DNHG[7]. The study also suggested 3 wt % was the ideal cross linking density. For 2.5 wt % 150 nm hydrogels, a 7.3 times increase in fracture failure is observed compared to the control, though an even bigger improvement was made for 10 wt % ASNP loading, at 8.8 times. The efficiency of cross linking and forming strong covalent bonds likely increases the properties of the hydrogels. Accordingly, if parts of the hydrogel aren't fully or properly cross linked those parts would act as nanoparticle fillers. This can lead to a decrease in the physical integrity.

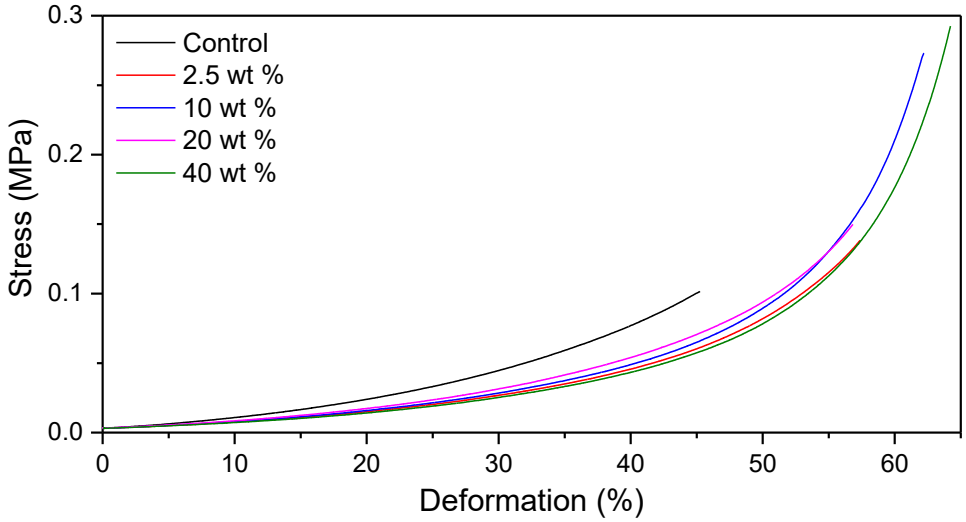


Figure 27 - Compression curves for PAAc/PAAm hydrogels with 100 nm amine silica nanoparticles (ASNPs) at different loading concentrations compared to control.

Table 12 - Compression and strain for PAAc/PAAm hydrogels with 100 nm amine silica nanoparticles (ASNPs) at different loading concentrations compared to control.

		Loading of 100 nm ASNPs			
	Control	2.5 wt%	10 wt%	20 wt%	40 wt%
Fracture Compressive Stress (MPa)	0.10 ± 0.03	0.14 ± 0.02	0.27 ± 0.08	0.15 ± 0.07	0.29 ± 0.19
Fracture Strain %	45 ± 2	57 ± 10	62 ± 4	58 ± 2	64 ± 1

Figure 28 shows compression curves for hydrogels containing 50 nm ASNP. Hydrogels with 2.5 wt % for 50 nm had little impact on the compressive failure strength, similarly to 2.5 wt % of 100 nm hydrogels. Again, this means a combination of low ASNP loading at 2.5 wt % and a smaller ASNP size of 50 nm does not have sufficient impact on hydrogel properties. Increasing the 50 nm ASNP loading to 10 wt % had a significant impact on failure at compression, at 1.28 ± 0.26 MPa with 74 ± 13 % strain. 20 wt % and 40 wt % hydrogels for 50 nm had similar values again to the control. A trend can be seen across all hydrogels where 10 wt % loading in the first network provides the best results for increasing strain and failure. This is most likely due to 2.5 wt % being too low of an amount to have an impact, with 50 nm and 100 nm in particular, and 20 wt % and 40 wt % potentially creating voids in the structure leading to less favourable properties.

ASNP may act as fillers rather than cross linking agents and therefore create some structural integrity at high concentrations, highlighting that the desirable effects may be reached with lower concentrations in the range of 10 wt %.

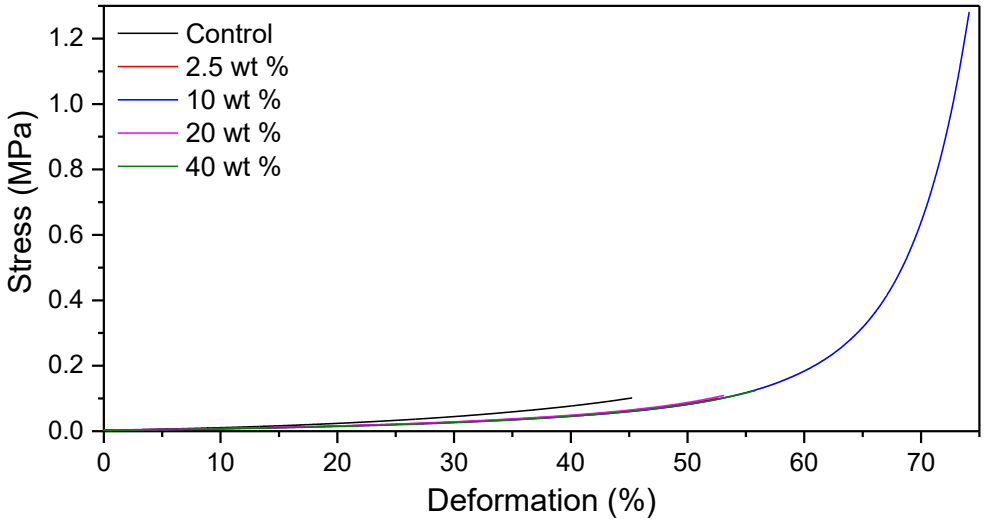


Figure 28 - Compression curves for PAAc/PAAm hydrogels with 50 nm amine silica nanoparticles (ASNPs) at different loading concentrations compared to control.

Table 13 - Compression and strain for PAAc/PAAm hydrogels with 50 nm amine silica nanoparticles (ASNPs) at different loading concentrations compared to control.

		Loading of 50 nm ASNPs			
	Control	2.5 wt%	10 wt%	20 wt%	40 wt%
Fracture Compressive Stress (MPa)	0.10 ± 0.03	0.10 ± 0.06	1.28 ± 0.26	0.11 ± 0.08	0.12 ± 0.06
Fracture Strain %	45 ± 2	52 ± 4	74 ± 13	53 ± 4	56 ± 3

From the compression studies conducted, it is clear that the combination effect of nanoparticle loading and size can impact the mechanical properties of the hydrogels. The right combination is required to create an efficiently cross linked first network with the least amount of aggregates, which helps avoid nanoparticle losses during swelling. This stops voids from forming within the hydrogels, and limiting the amount of water uptake, allowing the sample to maintain structural integrity and mechanical properties

that are desired for the application. The synthesis route also plays a very important role. Strong sonication to ensure a monodisperse system will create a larger surface area for PAAc to react with. Ensuring no aggregates from the start also eliminates the possibility of nanoparticles acting as fillers rather than cross linking grafts.

Previous work, from Zaragoza *et al.* with nanocomposite DNHG suggests that a concentration over 3 wt % for any nanoparticle size does not add improvements to the materials elasticity, and that elasticity is reduced with increasing size[178]. Contrary to previous findings, the findings in this chapter reveal much higher concentrations can be used to tailor the mechanical properties of a DNHG. Ultimately, the cross linking chemistry is vital to the success of such alterations in physical properties. This is summarised and highlighted in Figure 29. ASNP loading concentrations over 2.5 wt %, particularly for 150 nm, show enhanced mechanical strengths. It can also be concluded from the summary in Figure 29 that 10 wt % ASNP loading provides the best results in terms of mechanical properties for all 3 sizes.

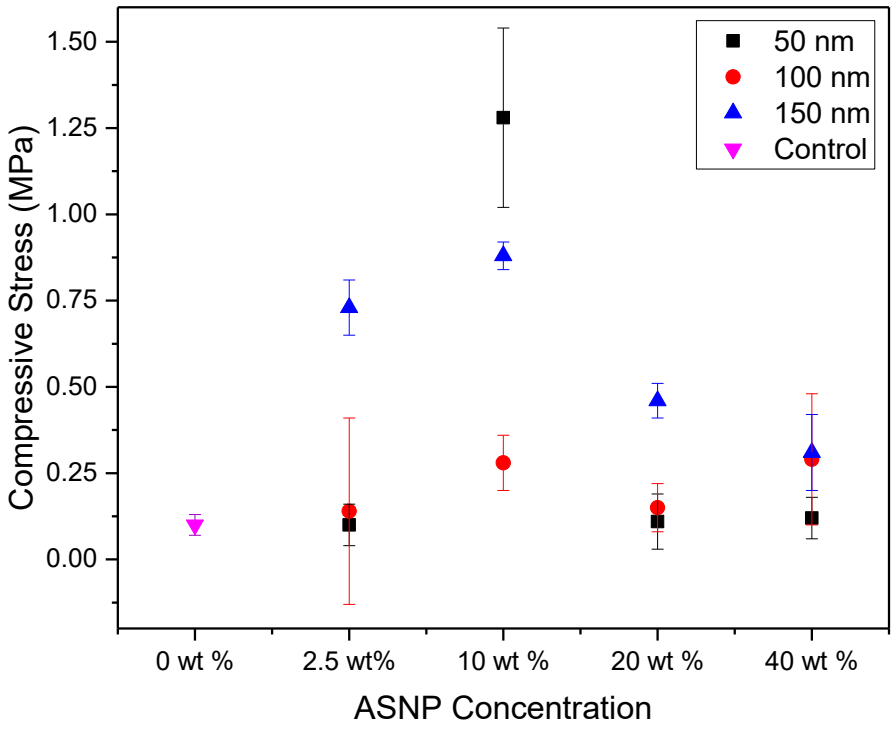


Figure 29 - Summary of compressive strengths of the DNHGs with varying sizes at varying ASNP concentrations, compared to a control

4.3.7 SEM

Hydrogel samples were placed in a -80 °C freezer overnight, to avoid structural collapse, before being freeze dried for 2 days, Figure 30. An average decrease in size of 15 ± 4 % in diameter and 12 ± 4 % in height was measured after the samples were removed from the freeze dryer. Freeze dried hydrogels were imaged using the LEO 1525 Gemini microscope in secondary electron mode at 3 – 5 kV with a working distance of 8 – 13 mm. SEM samples were cut 3 mm in length, 2 mm in width and 2 mm in height, from the centre point of the hydrogel. Images were taken for 10 wt % (150 nm) hydrogels and for the controls. Samples were sputter coated with chromium for 2 minutes at 20 mA to form a 10 nm layer.



Figure 30 - Freeze dried PAAc/PAAm hydrogel with 150 nm amine silica nanoparticles (ASNPs) at 10 wt % loading.

Figure 31 shows the internal structure of freeze dried control hydrogels. The images reveal porous structures characteristic with freeze drying. Pore sizes range between 5 – 20 µm and with sections containing pores of 30 – 100 µm. It is difficult to ascertain whether they are the native structure of the hydrogel or pores created during cryogenic sample preparation. As these structures are imaged from the mid-section of the hydrogel it can be assumed that the structure is porous and interconnected.

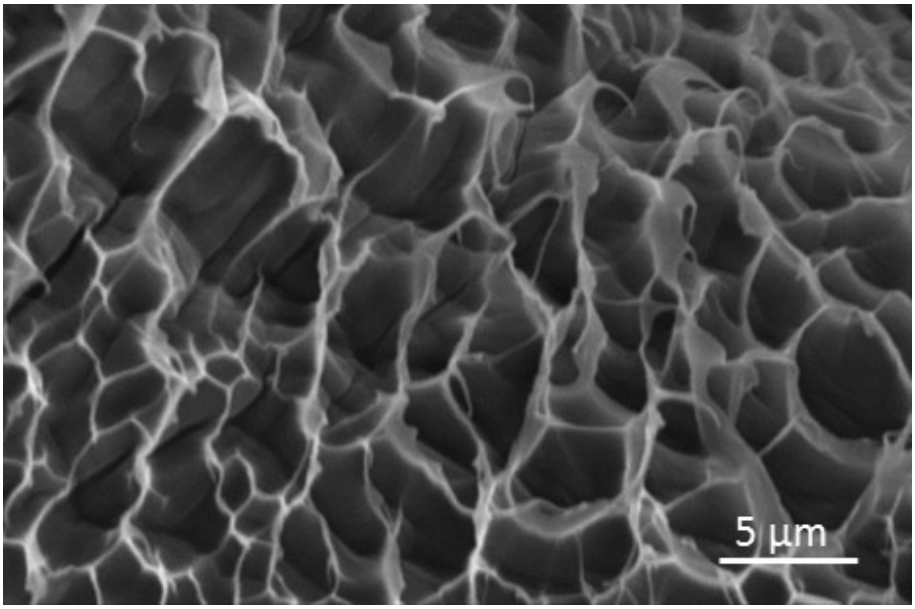


Figure 31 - SEM image of a control PAAc/PAAm hydrogel.

Figure 32 (a) and (b) suggests the presence of polymeric interactions on a micro and nano scale with the nanoparticles. In image (a) the pore-like structure is made of entangled polymeric material that wraps around many ASNPs. This suggests that the carbodiimide chemistry successfully created cross links between the amine functionalized ASNPs and the carboxylic groups of PAAc. These structures likely occurred during gelation of the first network. Thicker sections in the images could be related to the second network, PAAm. The internal structure of the hydrogels based on the images show a stark difference. Pores are more spaced out and larger. It is also easier to focus on structures in the background, revealing a possible more porous and interconnected system. The internal arrangement of the hydrogel containing 150 nm ASNP explains the increased water uptake, where structures are tightly cross linked but further apart, therefore allowing more water to be held in. Silica nanoparticles provide polymeric links across pores as seen in Figure 32 (b); this could be useful for cell attachment and proliferation.

The lack of uniformity in pore sizes for these hydrogels cannot be concluded from SEM imaging, but would require more a detailed analysis such as mercury porosimetry.

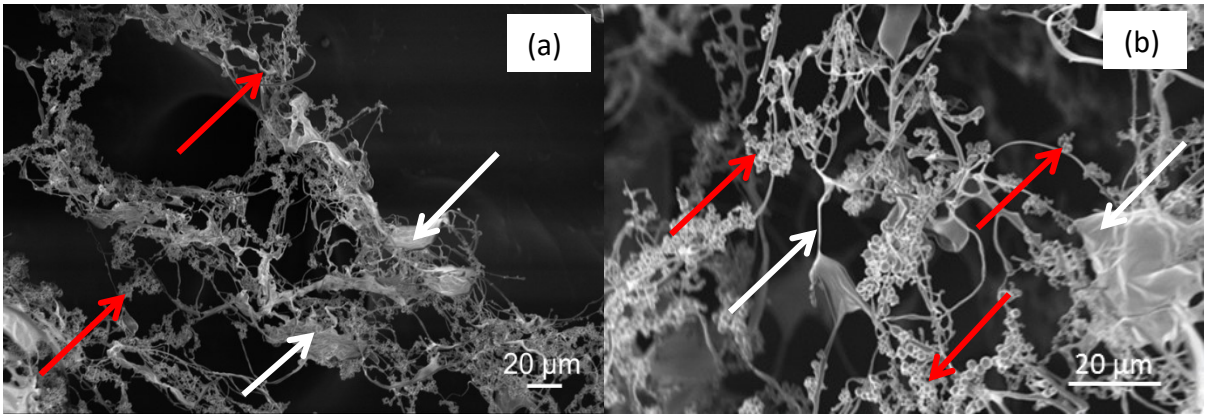


Figure 32 - SEM images of control PAAc/PAAm hydrogels with 150 nm amine silica nanoparticles (ASNPs) at 10 wt % loading. ASNP are highlighted with red arrows, and polymer structures with white arrows.

4.4 Conclusion

In this chapter the aim was to successfully use carbodiimide chemistry to covalently cross link amine functionalised silica nanoparticles by forming amide bonds through the carboxylic groups of PAAc. Carbodiimide chemistry was chosen as its by-products can be easily washed out during swelling and are nontoxic. This was considered a way of forming the first network hydrogel without the need for conventional cross linking agents, such as BIS, to introduce a more dynamic form of cross linking. This can be considered dynamic due to the potential of loading ASNPs with ions or drugs as a delivery system, and by allowing more tailorability of the material properties through size and concentration of ASNPs. Initially, reactions were conducted in deionised water with a 6.5 pH. All components dissolved except for EDC. Deionised water was replaced with MES buffer at 5.5 pH and EDC became soluble after mixing for up to 3 h. Hence, the correct pH was an important factor to allow for the carbodiimide reaction to occur. Deciding on whether the nanoparticles were dispersed was subjective. Due to the high loading concentrations in small volumes of solution, there was a high chance of re-aggregation and nanoparticles settling at the bottom once the solution was kept for gelation. Consequently, this may have had an impact on the results of the PAAc/PAAm

double network hydrogels by creating uneven distribution and partial agglomeration within the hydrogel.

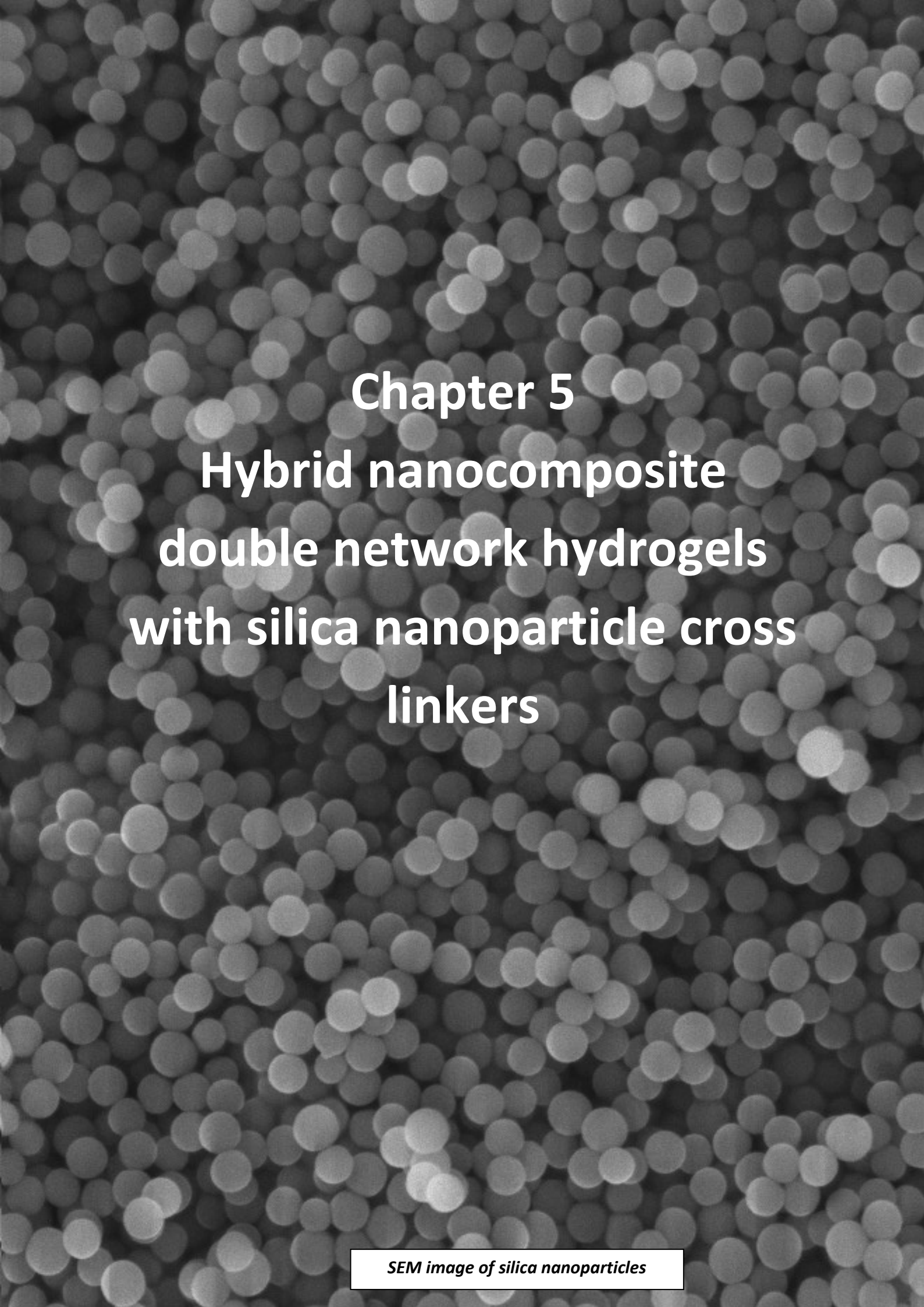
Ultimately, a hybrid hydrogel system with PAAc cross linked with amine ASNP as the first network by carbodiimide chemistry, and PAAm as the second network was successfully synthesized. This chapter provides evidence that nanostructures such as silica nanoparticles can be used to cross link the first network of double network hydrogels. The results highlight the difficultly and intrinsic nature of finding the right combination of size and ASNP loading. 10 wt % ASNP loading for was found to be the best loading density for all three sizes tested. FTIR results provided an insight into the unreacted AAm monomers that were present in the Fresh samples, which were washed out during swelling as indicated in FTIR spectra of Swollen samples, along with ASNPs and loose PAAc chains. Unreacted AAm monomers give an indication that the photopolymerization does not reach full monomer to polymer conversion. This results in toxic monomers remaining in the system and also means that the full potential of the polymer was not achieved. Chapter 6 explores a more efficient way to conduct photopolymerization for hydrogel synthesis to utilise the full potential and ensure no toxic monomers remain in the hydrogel post synthesis. SEM imaging provided an interesting insight into the way nanoparticles integrate into the polymeric networks, forming pore like structures and bridging polymeric chains together. It is important to mention that the loading densities are diluted when the entire hydrogel is formed. For instance, a hydrogel with 40 wt % ASNP loading in the first network is equivalent to 6.7 wt % of the final DNHG, and 2.5 wt % ASNP loading in the first network is equivalent to 0.08 wt % of the final DNHG. Despite the apparent low concentrations of ASNPs in the DNHG, an effect was seen across all concentrations when looking at water content uptake and TGA. This leads to the conclusion that even with successful cross linking and gelation, the effects may be diluted when the double network forms. This raises the need for further investigations into the concentrations of the first network relative to the second network. Regardless of the effect of dilution, compressive strength increased by 880 % and 1,280 % for hydrogels containing 150 nm ASNPs at 10 w % loading and hydrogels containing 50 nm ASNPs at 10 wt % loading, respectively,

compared to control hydrogels. All hydrogels experienced increased resistance to strain, with a maximum of 74 %, compared to 45 % for the control.

Next Chapter

The next chapter explores the use of vinyl functionalised silica nanoparticles in the first network in a two-step sequential photopolymerization. The double network hydrogels formed in Chapter 5 will be of consist of polymers of opposing characteristic properties, to help attain a strong synergetic effect relative to simple interpenetrating polymeric network hydrogels.

Chapter 5
Hybrid nanocomposite double network hydrogels with silica nanoparticle cross linkers



SEM image of silica nanoparticles

5 Hybrid nanocomposite double network hydrogels with silica nanoparticle cross linkers

5.1 Introduction

The previous chapter proved that nanocomposite structures have the potential to be used as sole cross linkers in the first network of double network hydrogels. Therefore, this chapter will further explore the use of silica nanoparticles as cross linking agents in first networks. A systematic approach will be conducted by exploring nanoparticle size and loading density on nanoparticle retention and mechanical strengths of the hydrogels. Similarly to Chapter 4, the sizes will vary between 50 nm, 100 nm and 150 nm. Nanoparticle concentrations will vary between 2.5 wt %, 10 wt %, 20 wt % and 40 wt %.

As required for double network hydrogels, two contrasting polymers have been chosen for investigation in this chapter[89], poly 2-acrylamido-2-methyl-1-propanesulfonic acid (PAMPS and polyacrylamide (PAAm). Surface functionalization of silica nanoparticles with vinyl groups will provide the cross linking platform required to for the first network hydrogel. The vinyl groups, once exposed to UV light and in the presence of a photoinitiator, are able to form cross links with the –OH functional groups of AMPS. A sequential photopolymerization process, developed by Jian Ping Gong[44], will be used to synthesize the double network hydrogels.

The intent of this chapter is to find the best combination of size and SNP loading concentration. Also, to understand if first networks can become oversaturated with SNPs and the impact that may have on the hydrogels mechanical strength. Finally, the hydrogel that performs the best will be studied under SEM to understand the internal structure and behaviour of SNP distribution within the material.

5.2 Methods and materials

5.2.1 Materials

Ammonium hydroxide (NH_4OH; 28-30 % NH_3 basis), tetraethyl orthosilicate (TEOS, 98 %), ethanol (EtOH; 200 proof, anhydrous; ≥ 99.5 %), acrylamide (AAm; ≥ 99 %) 2-acrylamido-2-methyl-1-propanesulfonic acid (AMPS; 99 %), N, N'-methylenebisacrylamide (BIS; 99 %), photoinitiator 2-hydroxy-4'-(2-hydroxyethoxy)-2-methylpropiophenone (synonym Irgacure 2959; 98 %), triethoxyvinylsilane (VTEOS; 97 %) were purchased from Sigma-Aldrich (UK). No additional processing and/or purifications were performed.

5.2.2 Silica nanoparticle synthesis

Silica nanoparticles were synthesized as described in section 4.2.2.1, with vinyl triethoxyvinylsilane (VTEOS) used as the functionalizing agent, in lieu of APTES (

Figure **33**). 50 nm, 100 nm and 150 nm vinyl functionalized silica nanoparticles (VSNP) were formed and stored under dry conditions. Zeta potential results for VSNP showed -35 mV on average, similar results in previous studies[190].

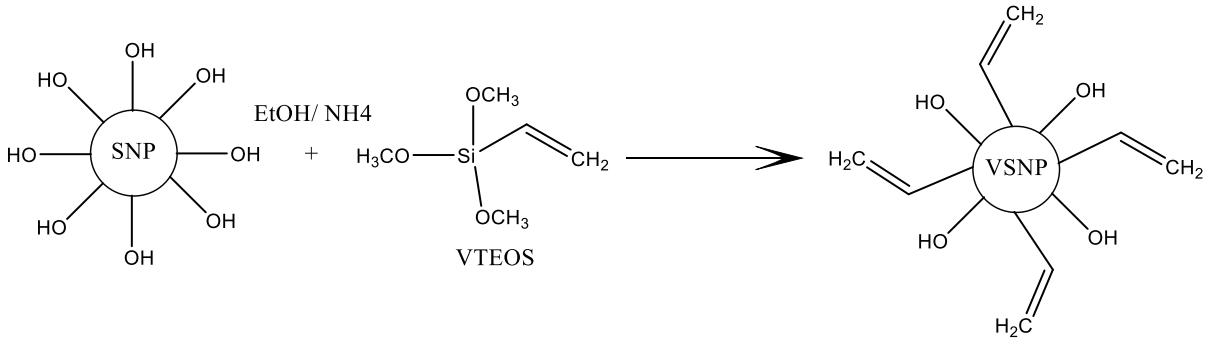


Figure 33 - Surface functionalization of silica nanoparticles with VTEOS.

5.2.3 Double network hydrogel synthesis

0.48 M of AMPS and 1 wt % Irgacure 2959 were dissolved in 4 ml deionised H_2O. 2.5 wt % of 50 nm VSNP (relative to AMPS) were sonicated in 1 ml deionised H_2O and added to the AMPS monomer solution whilst stirring. The solution was poured into a 48 cell culture well and placed in the UV-Crosslinker for 5,400 s with an average UV intensity of 2900 $\mu W/cm^2$ of 365 nm light. Once the first network hydrogels were formed, they were taken out of the cell and prepared to be soaked in an AAm monomer solution.

Table 14 - VSNP concentrations used in the first network.

VSNP (wt%)	VSNP (mg)
0	0
2.5	12.5
10	50
20	100
40	200

1.41 M of AAm, 0.1 wt % BIS and 1 wt % Irgacure 2959 were dissolved in 5 ml deionised H_2O. AMPS first network hydrogels were then swollen in the AAm monomer solution. Once fully swollen, the hydrogels were placed in the UV-Crosslinker for 5,400 s under the same conditions as the first network. Once the double network was formed the hydrogels were dried at 60 °C and then placed in water for 14 days until a plateau was reached in their swelling state.

This was repeated for 2.5, 10, 20 and 40 wt % VSNP loading for hydrogels containing 50, 100 and 150 nm VSNP. A control double network hydrogel without VSNP was formed under the same conditions, with 2.5 wt % BIS in the first network. The synthesis route is depicted in Figure 34 below.

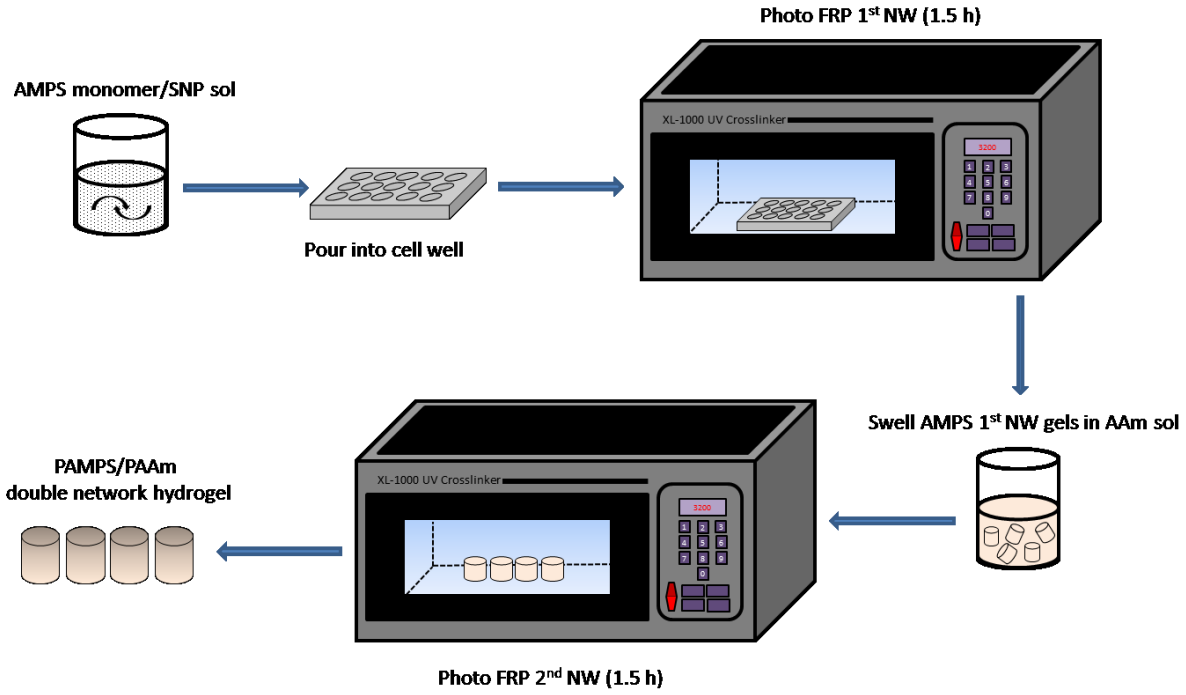


Figure 34 - Synthesis route for PAMPS/PAAm double network hydrogels containing vinyl silica nanoparticles (VSNPs).

5.3 Results and discussion

PAMPS/PAAm hydrogels were successfully synthesized with VSNP as a cross linking nanocomposite structures. Post synthesis, five hydrogels of each size and composition were dried at 60 °C post for 5 days. The 5 hydrogels were prepared for swelling studies, FTIR, TGA and SEM in the same manner as discussed in Chapter 4.

In this section, hydrogels will be referred to in terms of VSNP loading in their first network. For example, a PAMPS/PAAm double network hydrogel will be referred to as a 'hydrogel containing 150 nm VSNP with 40 wt % loading'.

5.3.1 Swelling and water content

Samples were swollen in water and their mass was measured until a swelling plateau was reached. An interesting observation of 'flowering' was made during the swelling process, shown in Figure 35. The hydrogels formed a flower like structure during the first day before becoming cylindrical again. This is mainly due to the difference in hydrophilicity of the two networks, causing water uptake at different rates until both networks become saturated.

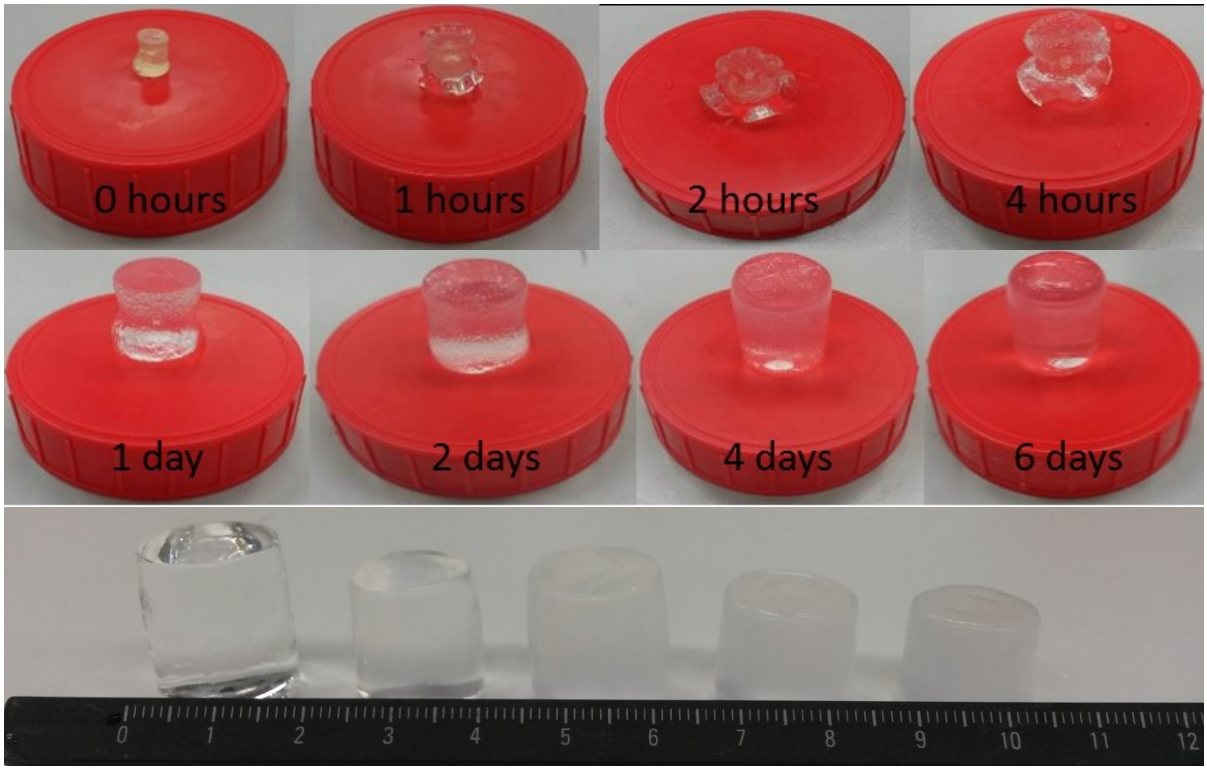


Figure 35 - PAMPS/ PAAm hydrogel containing 150 nm vinyl silica nanoparticle (VSNPs) at 2.5 wt % loading swelling from 0 h to 6 d (top) and from right to left: control hydrogel, hydrogels containing 150 nm VSNP at 2.5 wt %, 5 wt %, 10 wt % and 20 wt % loading (bottom).

The bottom part of Figure 35 compares the control DNHG with SNP grafted DNHGs, in ascending order of SNP loading. It can be seen that as SNP loading density increases,

the swollen size of the DNHGs decreases. Figure 36 shows the swelling profile of hydrogels containing 150 nm VSNP against control hydrogels. Control hydrogels reach a maximum water content of 96.7 ± 0.36 % and swelling of 2757 ± 157 %. Control samples plateaued close to 24 h, whilst VSNP loaded hydrogels plateaued closer to 72 h. Water content uptake decreased systematically with increased VSNP loading density. A significant difference in swelling, swelling rate and water content occurred when the first network was tightly cross linked with VSNP. At 40 wt % loading, water content was reduced by approximately 9 %, to 87.9 ± 0.38 %, compared to the control. 2.5 wt % VSNP loading in the first network had a similar effect on swelling as 40 wt % VSNP loading; this suggests the effectiveness of VSNP loading could be reached with as little as 2.5 wt %. The results are in line with previous work that demonstrated increased silica content above 1 wt % caused a reduction in the equilibrium swelling ratio due to the formation of a cross linked rigid network[7]. The DNHG containing VSNP synthesized in this chapter were better homogeneously dispersed (Figure 35) compared to the DNHG synthesized in Chapter 4. VSNP cross linking points in the hydrogel will reduce the free volume in the hydrogels structure, reducing the swelling ability of the hydrogel[191].

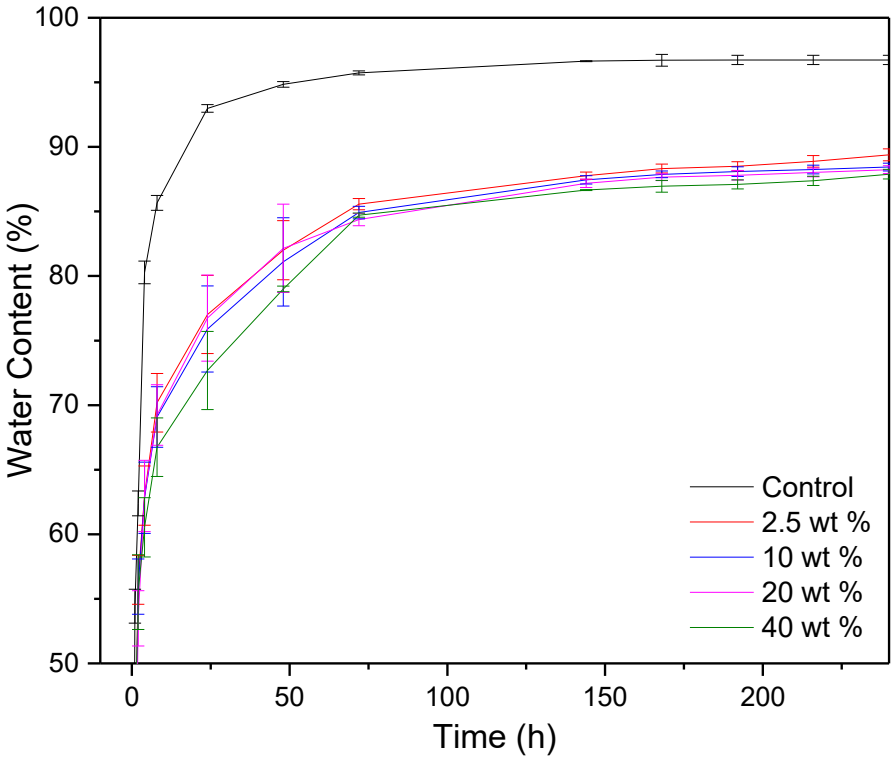


Figure 36 - Swelling profile for PAMPS/PAAm hydrogels with 150 nm vinyl silica nanoparticles (VSNPs) at different loading concentrations compared to control.

Table 15 - Swelling and water content for PAMPS/PAAm hydrogels with 150 nm vinyl silica nanoparticles (VSNPs) at different loading concentrations compared to control.

		Loading of 150 nm VSNPs			
	Control	2.5 wt%	10 wt%	20 wt%	40 wt%
Water Content (%)	96.73 % ± 0.36	89.39 % ± 0.46	88.44 % ± 0.30	88.24 % ± 0.30	87.89 % ± 0.38
Swelling (%)	2757 % ± 157	1287 % ± 34	1168 % ± 24	1320 % ± 31	1220 % ± 29

Hydrogels containing 100 nm VSNP did not have the same impact on swelling rate and water content as hydrogels containing 150 nm VSNP, as seen in Figure 37. A maximum decrease of 5 % in water content was witnessed with hydrogels containing 100 nm VSNP with 40 wt % loading, compared to the control. These results suggest that hydrogels containing 100 nm are successful at creating cross links in the first network, but the resulting first network may not be as rigid as hydrogels containing 150 nm VSNP. The swelling rate of the hydrogels containing 100 nm VSNP matches that of the

control, contrary to the 150 nm. This, again, points out that the first network may not be as tightly cross linked as that of hydrogels containing 150 nm VSNP. The difference in size may have an effect on the swelling rate, due to the free volume available.

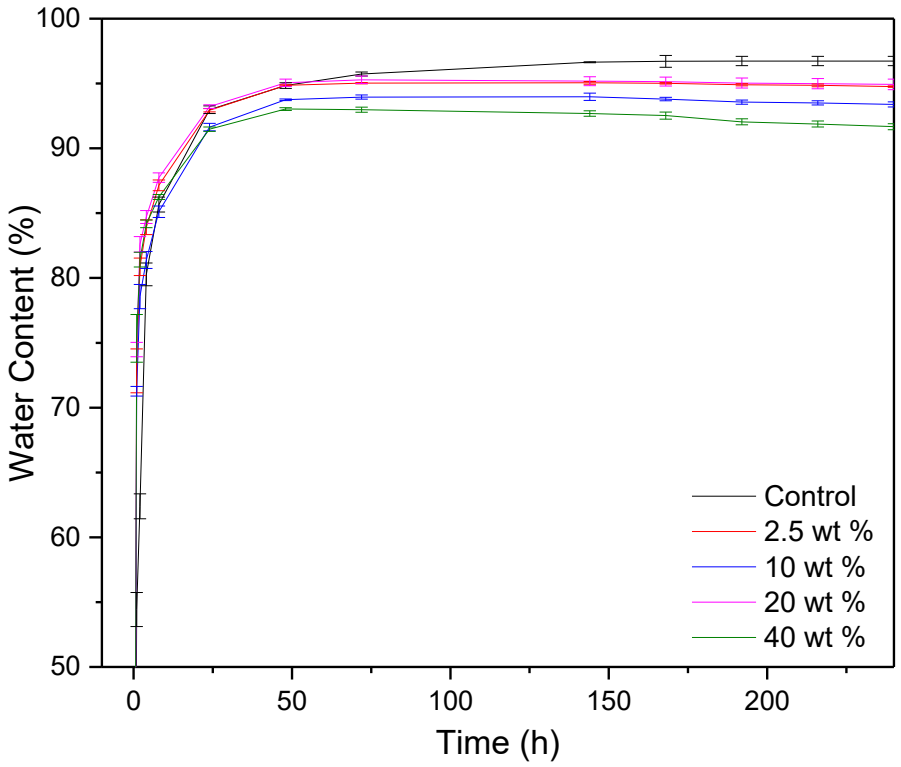


Figure 37- Swelling profile for PAMPS/PAAm hydrogels with 100 nm vinyl silica nanoparticles (VSNP) at different loading concentrations compared to control.

Table 16 - Swelling and water content for PAMPS/PAAm hydrogels with 100 nm vinyl silica nanoparticles (VSNP) at different loading concentrations compared to control

		Loading of 100 nm VSNPs			
	Control	2.5 wt%	10 wt%	20 wt%	40 wt%
Water Content (%)	96.73 % ± 0.36	94.76 % ± 0.05	93.38 % ± 0.19	94.93 % ± 0.41	91.67 % ± 0.24
Swelling (%)	2757 % ± 157	1811 % ± 39	1415 % ± 45	1890 % ± 65	1695 % ± 20

Hydrogels containing 50 nm VSNP had the smallest change in water content compared to the control, as shown in Figure 38. A maximum decrease in approximately 4.4 % was

observed between the hydrogels containing 50 nm VSNP at 40 wt % loading and the control. Hydrogels containing 50 nm VSNP exhibited the highest water content uptake for all hydrogels. One reason can be that smaller VSNPs have less of an effect on the free volume in the system; therefore water was still able to fill in the spaces causing more water uptake.

Loading with 40 wt % VSNP for all 3 sizes witnessed the biggest change in water content. Under this case, it is important to understand whether the VSNPs act as cross linkers, void fillers or a combination. The extent of which they are either cross linkers or void fillers will impact the mechanical properties and physical integrity of the hydrogel. Smaller VSNPs have larger specific surface areas for cross linking, but are more likely to leak out during swelling.

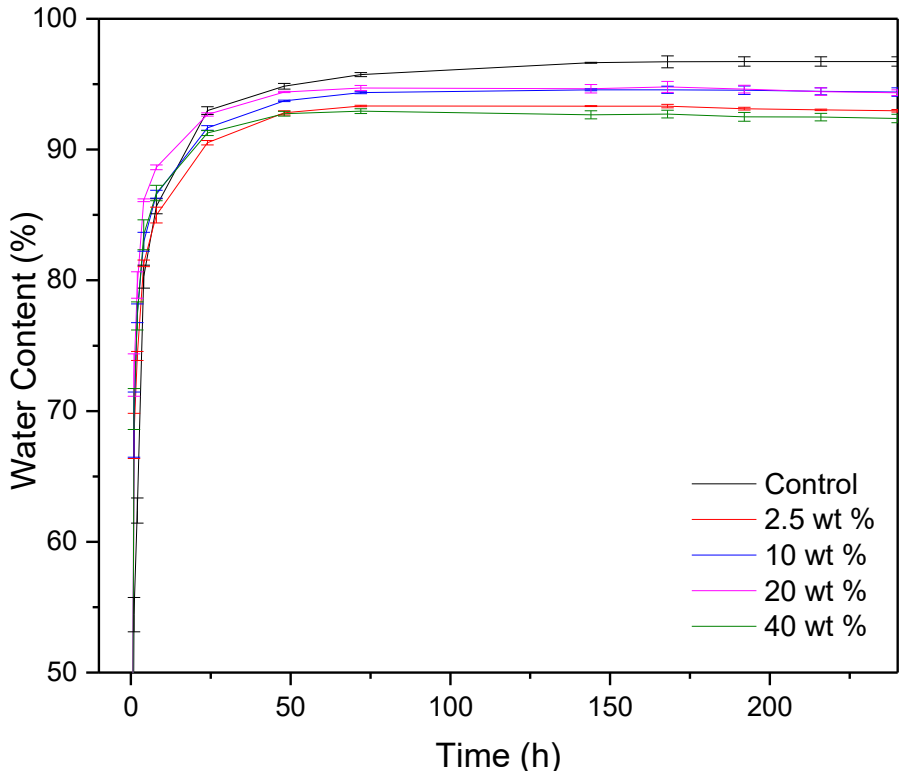


Figure 38 - Swelling profile for PAMPS/PAAm hydrogels with 50 nm vinyl silica nanoparticles (VSNP) at different loading concentrations compared to control.

Table 17 - Swelling and water content for PAMPS/PAAm hydrogels with 50 nm vinyl silica nanoparticles (VSNP) at different loading concentrations compared to control.

		Loading of 50 nm VSNPs			
	Control	2.5 wt%	10 wt%	20 wt%	40 wt%
Water Content (%)	96.73 % ± 0.36	92.96 ± 0.10	94.40 ± 0.32	94.35 ± 0.22	92.38 ± 0.33
Swelling (%)	2757 % ± 157	1321 % ± 20	1686 % ± 13	1673 % ± 40	1218 % ± 49

5.3.2 FTIR

Fresh and Swollen samples for hydrogels containing 150 nm VSNP were dried and ground to a fine powder for FTIR analysis. Table 18 provides a summary of the bonds present and their respective bands present in the hydrogels, labelled (A-L), for the FTIR spectra below.

Table 18 - Summary of FTIR bands for PAMPS/PAAm hydrogels.

	Bond	Type	Wavenumber (cm^{-1})
A	N-H	Stretching	3324
B	O-H	Water remaining in sample	3082
C	C-H	Alkyl stretching	2950
D	C=O	Stretching, coupled with N-H bending	1652-1659
E	N-H	Primary amine	1620
F	C-N	Stretching primary amide	1420
G	C-H	Deformation	1350
H	S=O	Symmetric stretching	1317
H	N-H	Bending	1238
I	SO_2	Symmetric stretching	1100-1250
I	Si-O-Si	Silica nanoparticles	1160
J	NH_2	In-plane rocking	1120
K	R–S(=O)–R'		1040
L	C-H	Out-of-plane rocking	942

Figure 39 shows the FTIR spectra for Fresh samples for 150 nm. Bands found at 3324 cm^{-1} represent N-H stretching from PAMS and PAAm networks[71, 192]. 1652 cm^{-1} – 1659 cm^{-1} show C=O stretching coupled with N-H bending, that are attributed to both PAMPS and PAAm[71, 192]. 1620 cm^{-1} N-H primary amine deformation, 1350 cm^{-1} C-H deformation indicates the amine groups from acrylamide. 1420 cm^{-1} C-N primary amide stretching, 1350 cm^{-1} C-H deformation, and 1120 cm^{-1} NH_2 in-plane rocking indicate are present due to both polymers[71, 192]. Strong N-H stretching at 3324 cm^{-1} for PAAm was masked by OH, possibly due to incomplete dehydration of the sample, and as part of the sulfonic acid groups. Peaks found at 2950 cm^{-1} represent alkyl vibrations of C-H bonds, from the presence of polymeric backbones[185, 186]. Sulfonic acid SO_2, $–SO_3H$ and S=O for PAMPS were found in the range 1100 cm^{-1} – 1250 cm^{-1}, 1040 cm^{-1} and 1317 cm^{-1}, respectively[192]. Loose unreacted monomer containing C-H bonds can be seen at 942 cm^{-1} and disappeared as VSNP loading increased, likely due to its lower abundance in the system.

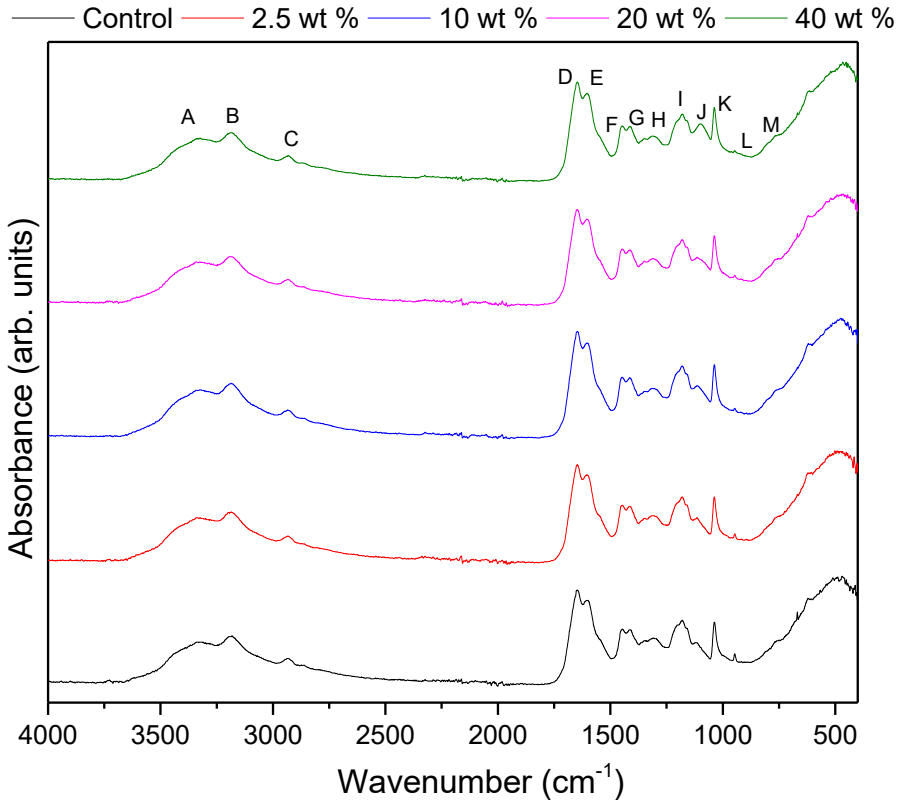


Figure 39 - FTIR spectra for Fresh PAMPS/PAAm hydrogels with 150 nm vinyl silica

Hydrogels containing 150 nm VSNP were freeze dried and investigated under SEM.

Figure 40 shows the FTIR spectra for Swollen samples. A noticeable reduction in intensity was noted at 1040 cm^{-1} with increasing nanoparticle loading. This can be linked to broader band width associated with silica nanoparticles covering the peak of sulfonic acid groups.

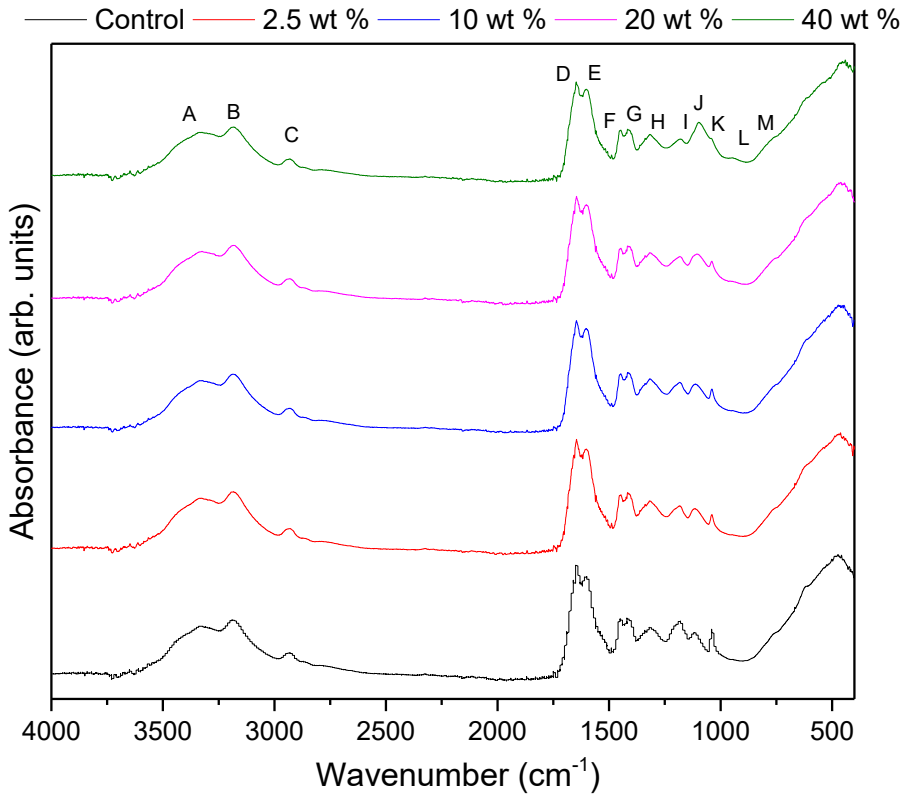


Figure 40 - FTIR spectra for Swollen PAMPS/PAAm hydrogels with 150 nm vinyl silica nanoparticles (VSNP) at different loading concentrations compared to control.

Figure 41 compares Fresh and Swollen samples of hydrogels containing 150 nm VSNP at 2.5 wt % loading. Unreacted monomers and loose polymers are washed out of the samples during swelling, as seen in the reduction of intensity in the band regions 1000 cm^{-1} – 1500 cm^{-1}. In particular, the reduction of symmetric stretching of SO_2 at approximately 1100 cm^{-1} – 1250 cm^{-1}, likely due to polymeric chains that are not cross linked. A reduction in the 1120 cm^{-1} NH_2 in-plane rocking allows the silica nanoparticle bands, Si-O-Si band at 1160 cm^{-1} [189], to become clearer. Unreacted monomers and loose

polymers indicate that the synthesis route does not reach 100 % conversion, and physical entanglements may be too weak to hold loose polymers within the hydrogels. The unreacted monomers are washed out from the Fresh hydrogel, as indicated by C-H out-of-plane rocking at 942 cm^{-1}, when compared to the Swollen hydrogel.

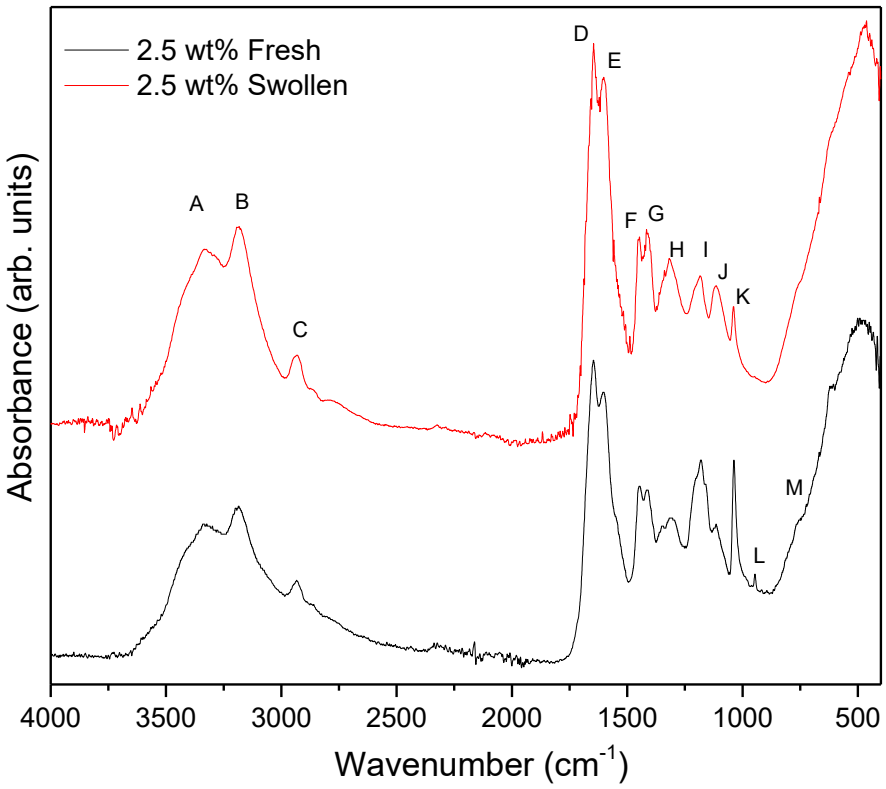


Figure 41 - FTIR spectra comparing Fresh and Swollen PAMPS/PAAm hydrogels of 150 nm vinyl silica nanoparticles (VSNP) at 2.5 wt % loading.

5.3.3 TGA

TGA was carried out for all Swollen samples to calculate nanoparticle retention using Equation 3.2, from Section 3.7. Swollen samples were dried for 5 days at 60 °C and ground to a powder. Polymeric material in the samples was expected to be burnt off by 600 °C and any remaining residues are considered to be VSNPs.

Previous TGA studies of AAm-co-AMPS copolymers revealed initial degradation of PAMPS at 182 °C and PAAm at 245 °C[193]. This suggests that PAMPS is less thermally stable than PAAm. There are three main degradation steps involved in the thermal decomposition of PAMPS/PAAm hydrogels; amide groups from PAAm, sulfonic groups from PAMPS, and the degradation of the polymeric backbones. The largest thermal degradation, reflected in the largest DTG peak, was noted in region between 250 – 300 °C and relates to the desulfonation of the material[194, 195].

Figure 42 shows the thermal degradation of hydrogels containing 150 nm VSNP and control. The control had 0 % residual mass at approximately 660 °C. The best retention was at 2.5 wt % loading and lowest at 40 wt % loading. This can be attributed to VSNP leakage during swelling, uneven distribution of VSNPs and potential losses during synthesis due to VSNPs sinking to the bottom. DTG profiles reveal the first peak, representing desulfonation, was reduced in the presence of VSNPs. The DTG region between 350 – 450 °C shows more prominent peaks relative to the control, suggesting more energy was required to break bonds likely created by VSNPs in the first network.

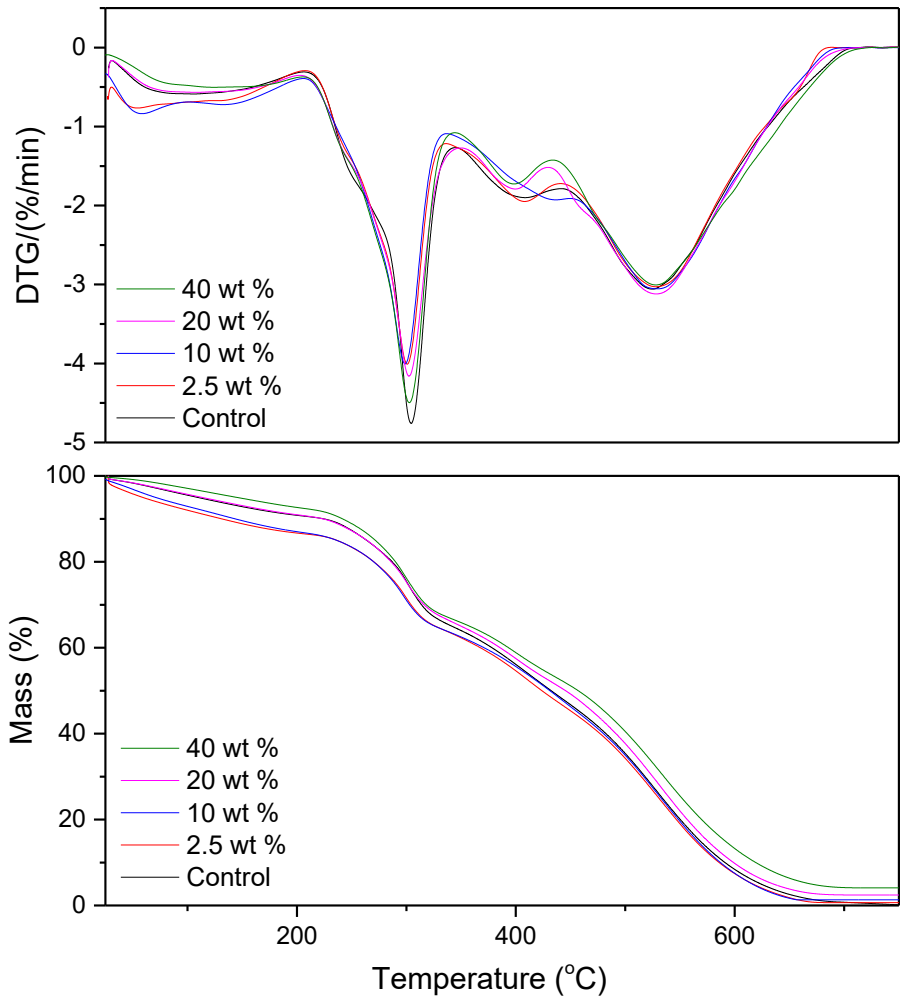


Figure 42 - TGA and nanoparticle retention for PAMPS/PAAm hydrogels with 150 nm vinyl silica nanoparticles (VSNP) at different loading concentrations compared to control.

Table 19 - nanoparticle retention for PAMPS/PAAm hydrogels with 150 nm vinyl silica nanoparticles (VSNP) at different loading concentrations compared to control.

	Loading of 150 nm VSNPs			
	2.5 wt%	10 wt%	20 wt%	40 wt%
Theoretical %	0.42	1.67	3.33	6.67
Residual %	0.40	1.57	2.43	4.08
Particle Retention %	96	94	73	61

Figure 43 shows the thermal degradation profiles for hydrogels containing 100 nm VSNP. A similar trend can be seen compared to hydrogens containing 150 nm VSNP. Nanoparticle retention was at 100 % for 2.5 wt % VSNP loading, but below 80 % retention for the rest of the samples. Smaller VSNPs are more likely to percolate through structural pores while swelling the first network hydrogel in the monomer solution of the second network, and for reasons explained above. The DTG profiles show the region between 350 – 450 °C shifts to the right, therefore required more energy to burn off the polymers likely due to stronger cross links than found in hydrogels containing 150 nm VSNP. Markedly, 2.5 wt % loading had the biggest shift to the right; this suggests strong cross links are present between the nanoparticles and the polymers, and potentially stronger physical entanglements between the two networks.

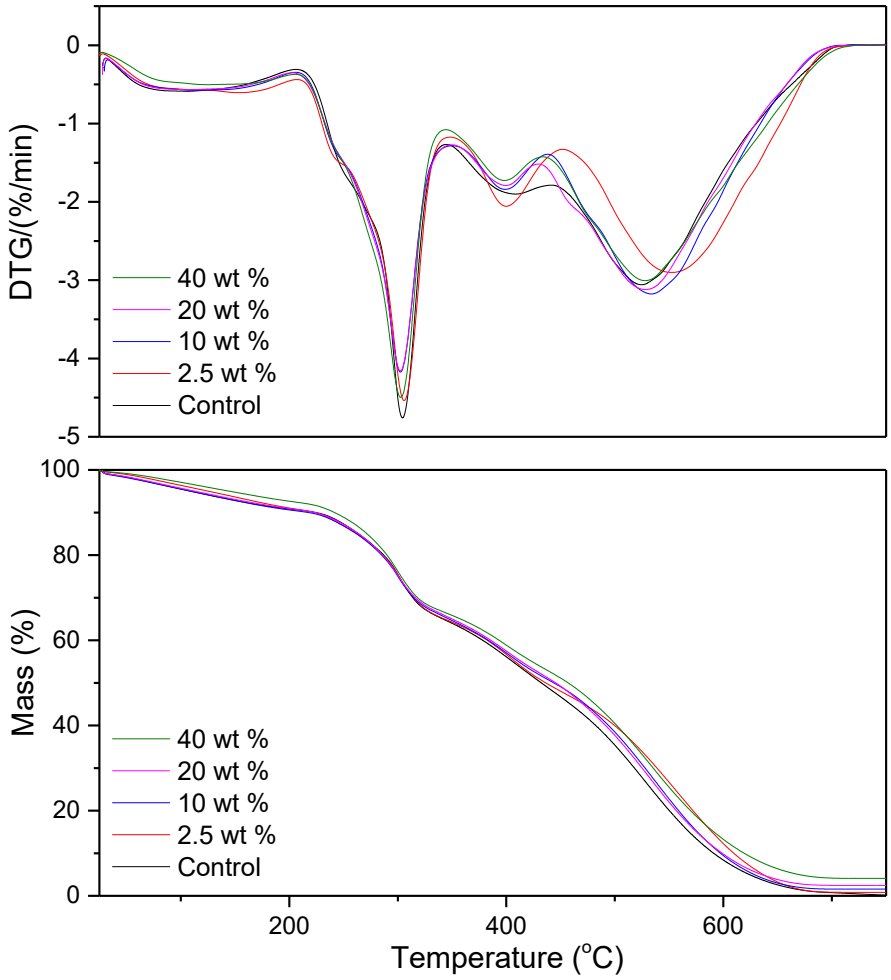


Figure 43 - TGA and nanoparticle retention for PAMPS/PAAm hydrogels with 100 nm vinyl silica nanoparticles (VSNP) at different loading concentrations compared to control.

Table 20 - nanoparticle retention for PAMPS/PAAm hydrogels with 100 nm vinyl silica nanoparticles (VSNP) at different loading concentrations compared to control.

	Loading of 100 nm VSNPs			
	2.5 wt%	10 wt%	20 wt%	40 wt%
Theoretical %	0.42	1.67	3.33	6.67
Residual %	0.45	1.30	2.32	4.25
Particle Retention %	108	78	70	64

Figure 44 shows the thermal degradation of hydrogels containing 50 nm VSNP, with the region 350 – 450 °C also shifting to the right. Again, notably 2.5 wt % loading had the

biggest shift which suggests that the lower concentration of VSNPs could have the greatest cross linking effect.

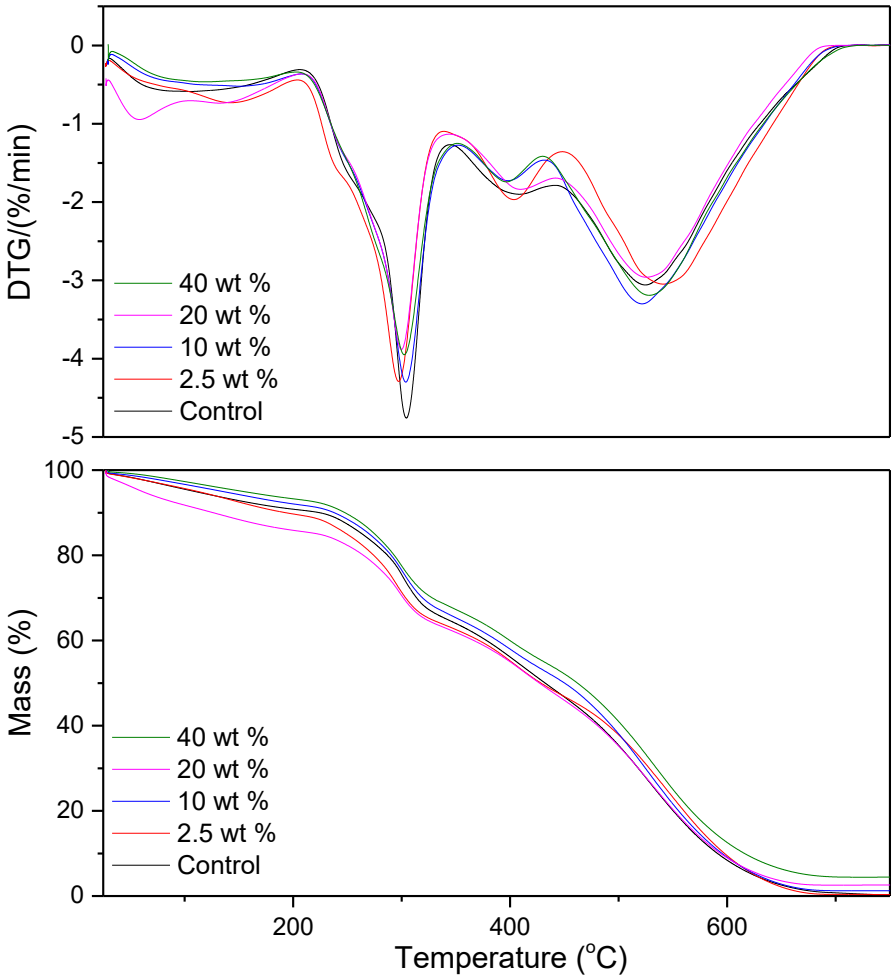


Figure 44 - TGA and nanoparticle retention for PAMPS/PAAm hydrogels with 50 nm vinyl silica nanoparticles (VSNP) at different loading concentrations compared to control.

Table 21 - nanoparticle retention for PAMPS/PAAm hydrogels with 50 nm vinyl silica nanoparticles (VSNP) at different loading concentrations compared to control.

	Loading of 50 nm VSNPs			
	2.5 wt%	10 wt%	20 wt%	40 wt%
Theoretical %	0.42	1.67	3.33	6.67
Residual %	0.33	1.24	2.55	4.41
Particle Retention %	79	74	77	66

Ultimately, results provided insight into the decreased retention at higher VSNP loading densities, Figure 45. At 2.5 wt % loading it was difficult to retain all 50 nm VSNPs in the first network likely due to their size. This indicates that the effect of smaller VSNP percolating out of the hydrogel was greater than the effect of higher cross linking due to larger specific surface areas. Up to 10 % more retention was seen for larger VSNPs. An average of 64 % retention was calculated for hydrogels with 40 wt % VSNP loading. This indicated that hydrogels could be oversaturated with VSNP, resulting in higher VSNP losses. Cross linking may not be as effective in retaining the nanocomposite structure in the hydrogels, meaning many of the remaining VSNPs may be acting as fillers that create structural voids in the hydrogel when washed out, or hindering the structural integrity as aggregates if they remain.

The impact of the VSNPs on mechanical structure and integrity will be explored next in mechanical compression studies.

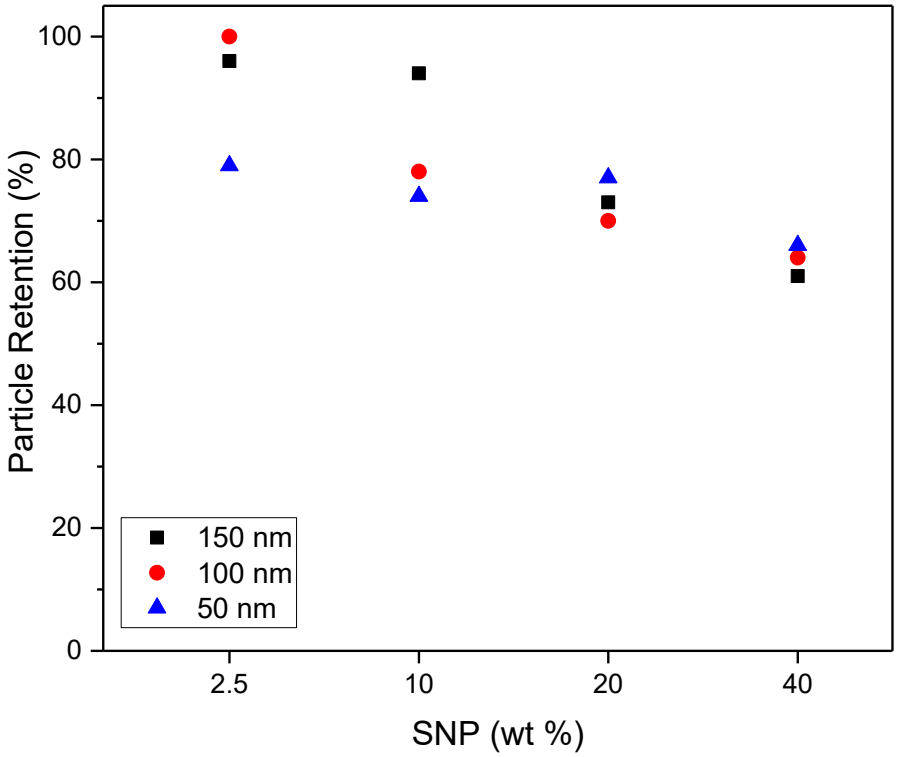


Figure 45 - A comparison of nanoparticle retention for PAMPS/PAAm hydrogels with 150 nm, 100 nm and 50 nm vinyl silica nanoparticles (VSNPs) at different loading concentrations.

5.3.4 Mechanical testing

Fully swollen hydrogels were tested under compression until failure. The hypothesis was that increased VSNP concentration would result in a higher concentration of cross links, therefore enhancing the mechanical properties of the hydrogels. It was also hypothesized that a limit would be reached in which VSNPs would begin to hinder the internal structure by acting as fillers, and creating voids. Following the results of nanoparticle retention from TGA, it is already clear that oversaturation of VSNPs was significant at loading above 10 wt %. This provides an initial indication that the highest loading, 40 wt %, may reveal internal hindrance due to the VSNPs. Figure 46 shows a PAMPS/PAAm hydrogel in compression under different strains.

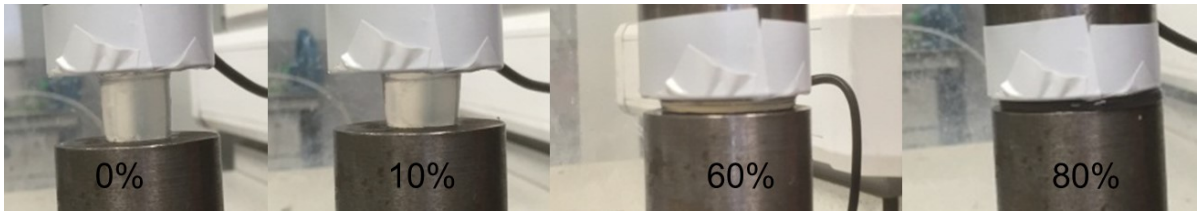


Figure 46 - PAMPS/PAAm hydrogel with hydrogel containing 150 nm at 20 wt % vinyl silica nanoparticles (VSNP) loading, at different strains.

Control hydrogels had fracture compressive strengths of 0.09 ± 0.02 MPa with 40 ± 3 % deformation. VSNP loading of 2.5 wt % in the first network produced a marked improvement in mechanical strength for hydrogels containing 150 nm VSNP with a compressive strength of 0.29 ± 0.04 MPa and 67 ± 5 % deformation, as seen in Figure 47. The lowest concentration therefore was effective at enhancing the compressive strength 3 times, and increasing the fracture resistance by 27 %. The largest improvement was noted at 20 wt % VSNP loading, with a compressive strength of 0.81 ± 0.08 MPa and 75 ± 6 % deformation. This was an improvement of 900 % in compressive strength, compared to the highest increase of 1280 % in the hydrogel synthesized in Chapter 4. The effect of increasing the VSNP loading further from 20 wt % to 40 wt % showed a decrease in mechanical properties. Only 0.3 ± 0.06 MPa was exhibited at 40 wt % VSNP loading, close to the value of exhibited by 2.5 wt % VSNP loading, leading to the conclusion that oversaturation of VSNP had occurred and hindered the integrity of the hydrogel. The shift further to the right of the curves for 40 wt % also suggests that the material is 'softer', therefore the first network is less rigid and less tightly cross linked, forming a weaker double network hydrogel. Combined with the TGA results discussed previously, it can be concluded that 20 wt % loading was the suitable loading density for the first network for hydrogels containing 150 nm VSNPs.

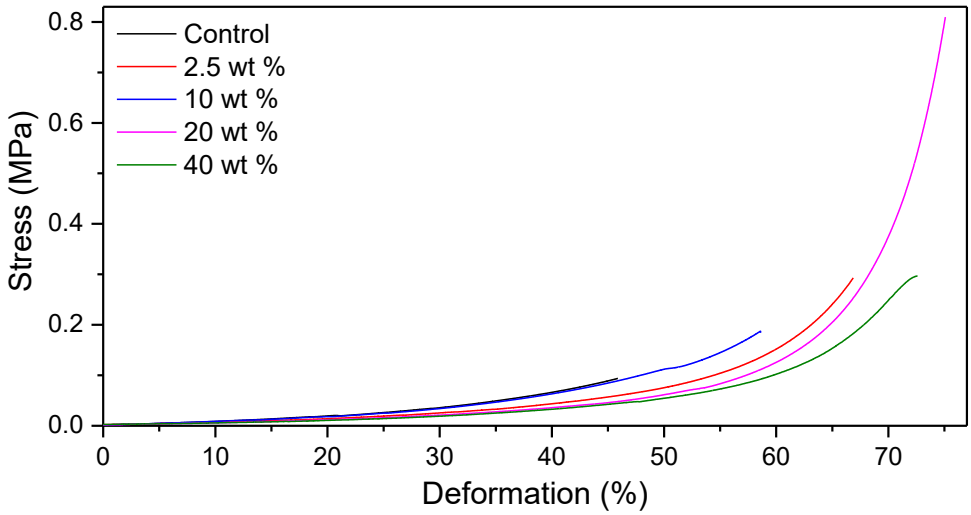


Figure 47 - Compression curves for PAMPS/PAAm hydrogels with 150 nm vinyl silica nanoparticles (VSNP) at different loading concentrations compared to control.

Table 22 - Compression and strain for PAMPS/PAAm hydrogels with 150 nm vinyl silica nanoparticles (VSNP) at different loading concentrations compared to control.

		Loading with 150 nm VSNPs			
	Control	2.5 wt%	10 wt%	20 wt%	40 wt%
Fracture Compressive Stress (MPa)	0.09 ± 0.02	0.29 ± 0.05	0.19 ± 0.04	0.81 ± 0.08	0.3 ± 0.06
Fracture Strain %	40 ± 3	67 ± 6	60 ± 5	75 ± 6	73 ± 7

Reducing the size of the nanoparticles ideally provides larger specific surface areas for polymer-nanocomposite interactions. Figure 48 shows that for hydrogels containing 100 nm, 20 wt % loading was the best result was achieved, though the improvements were not as strong as hydrogels containing 150 nm VSNP. The same trend can be seen with hydrogels containing 100 nm VSNP at 40 wt % loading where a decrease in mechanical properties was noted, likely due to overloading the first network.

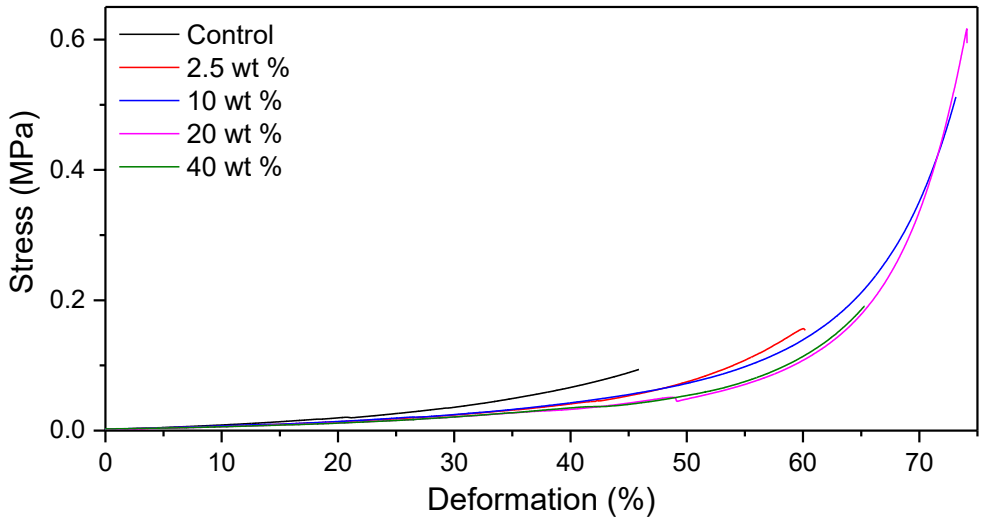


Figure 48 - Compression curves for PAMPS/PAAm hydrogels with 100 nm vinyl silica nanoparticles (VSNP) at different loading concentrations compared to control.

Table 23 - Compression and strain for PAMPS/PAAm hydrogels with 100 nm vinyl silica nanoparticles (VSNP) at different loading concentrations compared to control.

		Loading with 100 nm VSNPs			
	Control	2.5 wt%	10 wt%	20 wt%	40 wt%
Fracture Compressive Stress (MPa)	0.09 ± 0.02	0.24 ± 0.06	0.24 ± 0.03	0.42 ± 0.04	0.22 ± 0.04
Fracture Strain %	40 ± 3	61 ± 7	64 ± 4	72 ± 5	66 ± 7

Further reduction in the size of the VSNPs in the first network to 50 nm proved to be less effective. Again, in line with the trends explained above, hydrogels containing 50 nm VSNP with 20 wt % loading showed the best improvement. An increase was noted, compared to the control, a compressive strength of 0.42 ± 0.04 MPa and 72 ± 5 % strain for 20 wt % loading. Additionally, hydrogels containing 50 nm VSNP at 40 wt % loading showed a decrease in properties compare to 20 wt % loading. A shift to the right of the graph in Figure 49 for hydrogels with 40 wt % loading suggests that the material has become softer. The hydrogels therefore benefited at 40 wt % from the cross linked first network but was also oversaturated with VSNPs to its disadvantage.

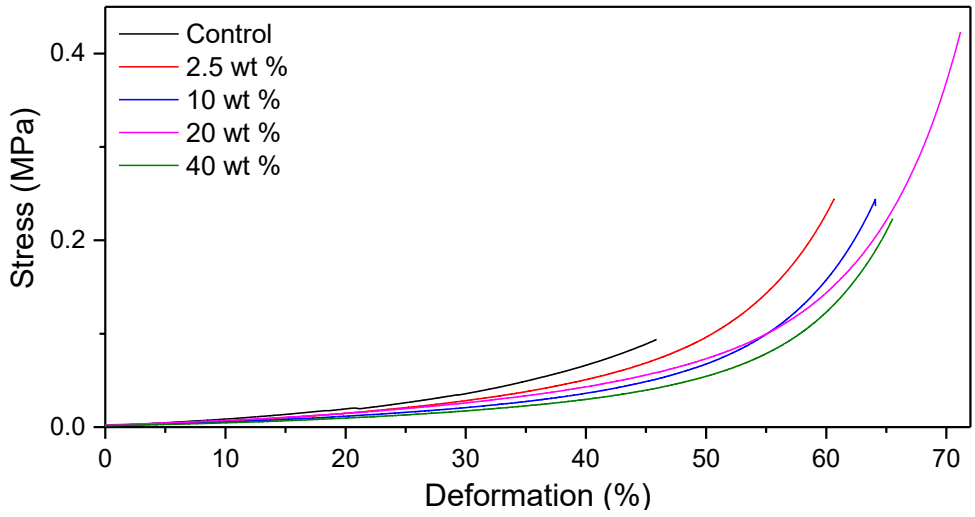


Figure 49 - Compression curves for PAMPS/PAAm hydrogels with 50 nm vinyl silica nanoparticles (VSNP) at different loading concentrations compared to control.

Table 24 - Compression and strain for PAMPS/PAAm hydrogels with 50 nm vinyl silica nanoparticles (VSNP) at different loading concentrations compared to control.

		Loading with 50 nm VSNPs			
	Control	2.5 wt%	10 wt%	20 wt%	40 wt%
Fracture Compressive Stress (MPa)	0.09 ± 0.02	0.15 ± 0.02	0.51 ± 0.05	0.59 ± 0.05	0.19 ± 0.03
Fracture Strain %	40 ± 3	60 ± 4	73 ± 4	74 ± 6	65 ± 5

Compression studies revealed that improvements to the hydrogels provide impact with the lowest concentration of VSNP loading. Overloading was also found to be in the region between 20 wt % and 40 wt % loading for all hydrogels, with the best results found at 20 wt % VSNP loading. 150 nm samples showed significant improvements in strain and fracture strength, and therefore will be looked at under SEM in the following section.

5.3.5 SEM

Hydrogel samples frozen at -80 °C freezer overnight and then freeze dried for 2 days, Figure 50, to avoid structural collapse. An average decrease in size of 24 ± 6 % in diameter and 14 ± 5 % in height was measured after the samples were freeze dried. Images were taken for hydrogels containing 150 nm VSNP at 20 wt % loading and for the control.

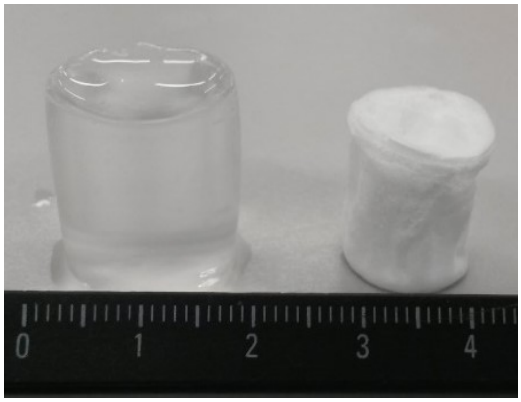


Figure 50 - PAMPS/PAAm hydrogel with 150 nm vinyl silica nanoparticles (VSNPs) at 20 wt % loading, before and after freeze drying.

Control hydrogels in Figure 51 (a) and (b) show web-like porous structures with thick polymeric walls. Control hydrogels from Chapter 4 did not exhibit similar thick polymeric walls; rather they had thin typical freeze dried structures. From observational analysis, pore structures are between 10 – 40 µm in the control samples and maintain a smooth circular pattern across the surface of the hydrogel, compared to 30 – 100 µm pores in control samples from Chapter 4 Section 4.3.7.

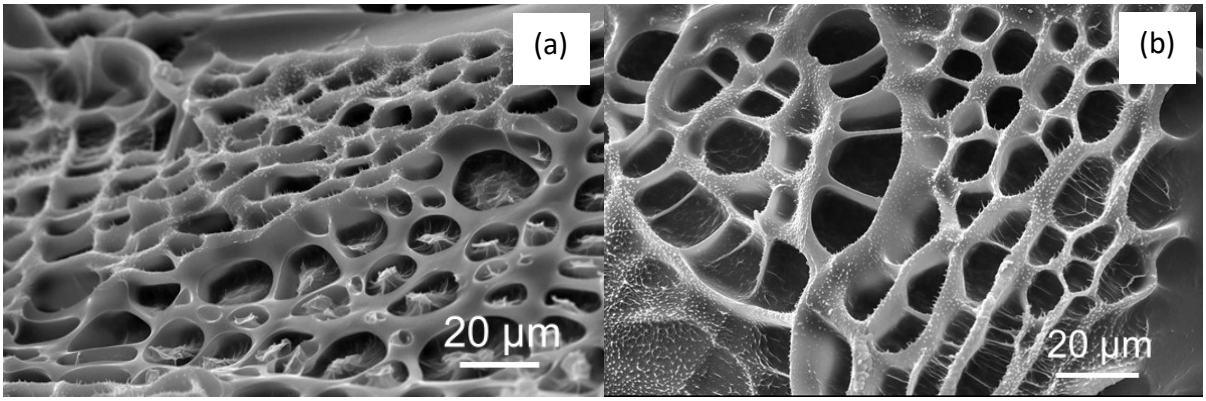


Figure 51 - SEM images of control PAMPS/PAAm hydrogels.

Figure 52 (a – f) shows the structure of hydrogels containing 150 nm VSNP at 20 wt % loading. Images show sharper edges and thinner polymeric walls which would explain enhanced strength, relative to the control. Pore sizes ranged between 10 – 50 µm with more elongated structures. Struts between pores and pore walls were examined to understand the integration and how the nanoparticles cross link with the first network.

VSNPs were found within struts as seen in Figure 52 Figure 51(c – f) and within walls as seen in Figure 52 (d). This gives a clear indication that for the parts of the examined hydrogel, nanoparticles are within the polymer matrix, potentially acting as cross linkers rather than aggregates that fill voids. The connections between the pores were examined and revealed polymer struts that are infused with nanoparticles. This leads to the conclusion that the first network hydrogels retain the nanoparticles as a covalently linked part of their structure. During compression and tension, the nanoparticles displayed in Figure 52 (e) and (f) are likely to hold the material together and act as physical reinforcements to withstand damage and resist breakage. Thus, clarifying the method in which strain is improved in VSNP loaded hydrogels compared to control hydrogels.

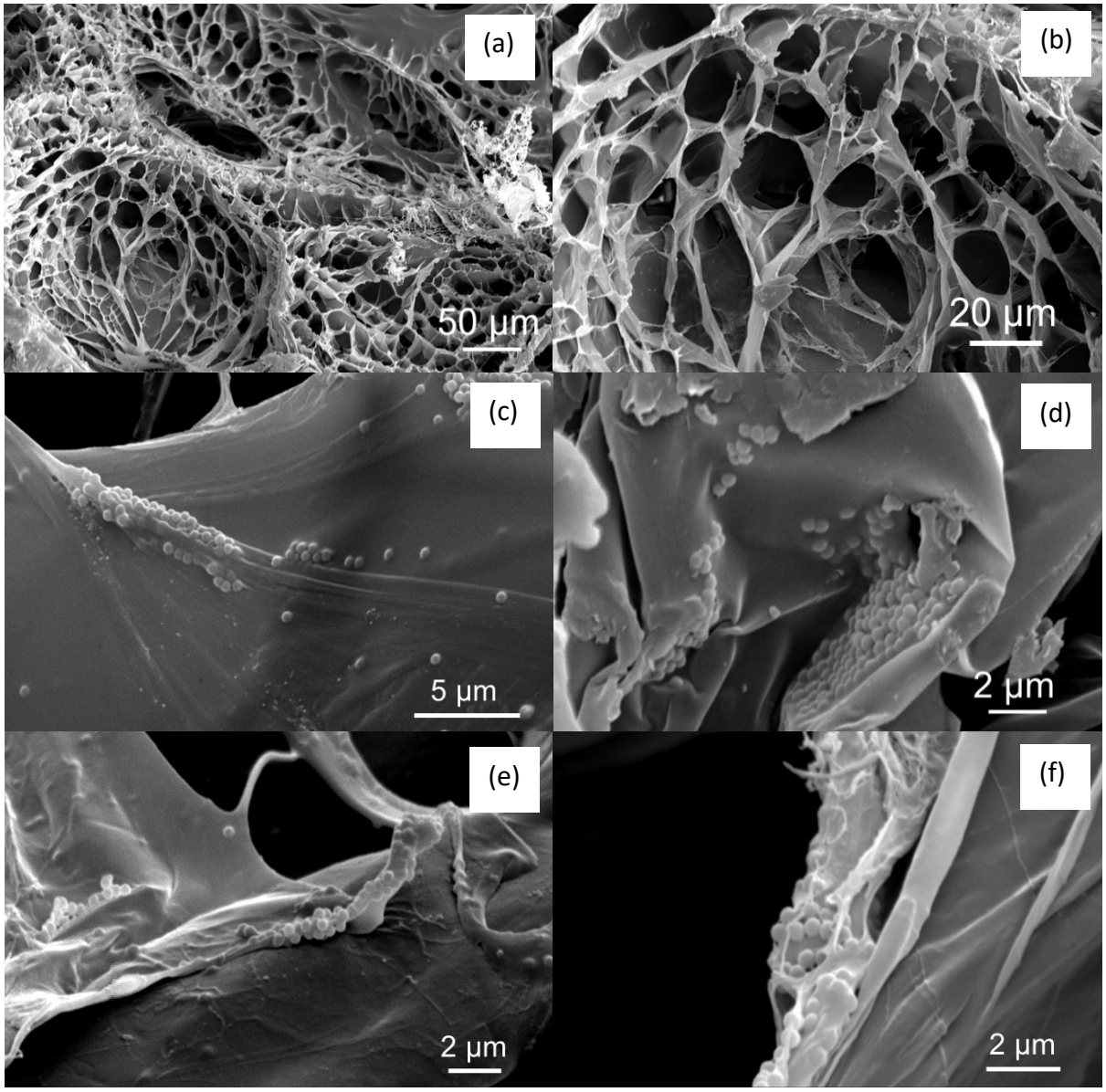


Figure 52 – (a – f) SEM images of PAMPS/PAAm hydrogels with 150 nm, 20 wt % VSNP at different magnification.

5.4 Conclusion

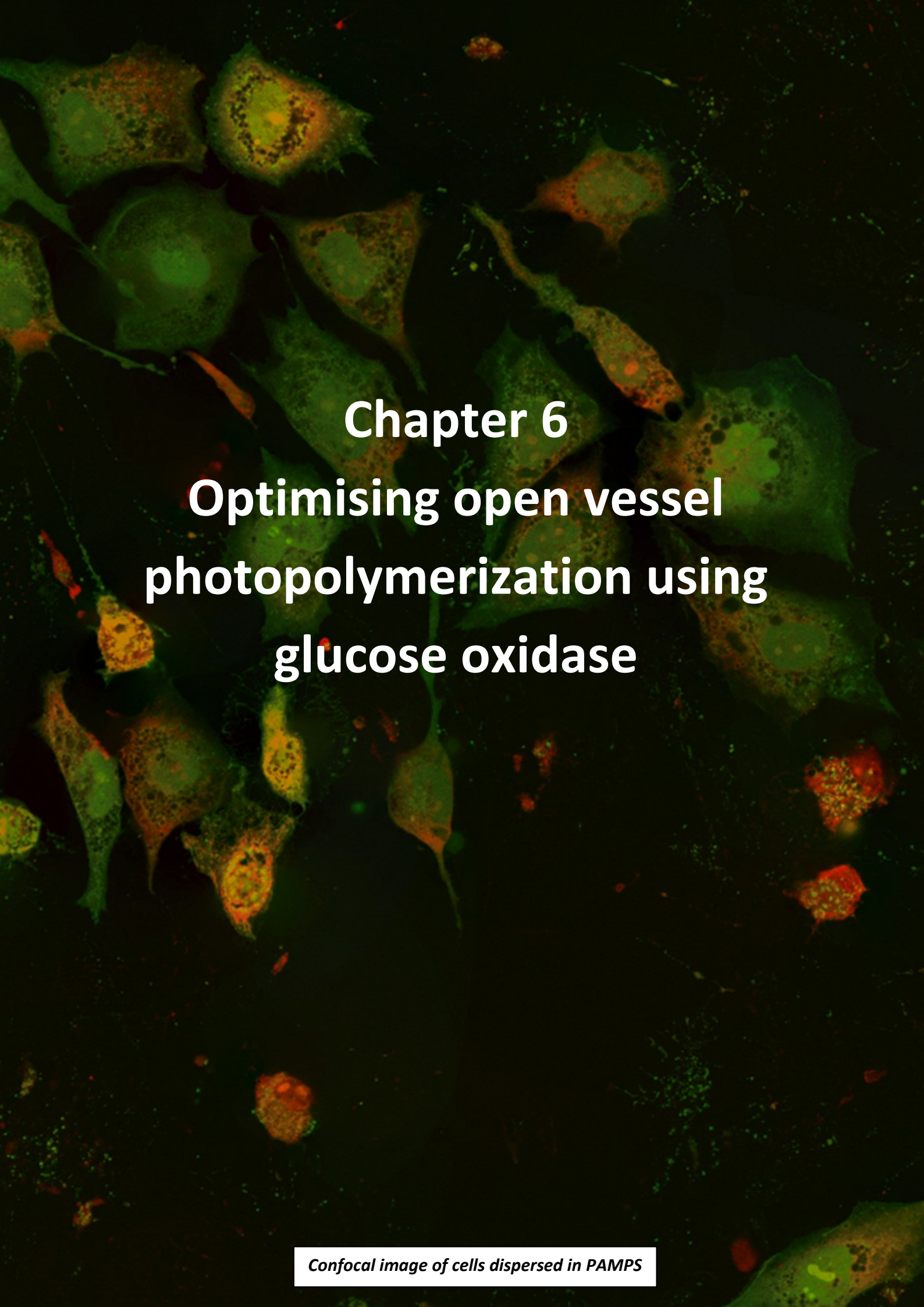
The double network hydrogels synthesized in this chapter revealed that hydrogels containing 150 nm VSNP witnessed the best improvement in mechanical properties, and benefited the most from the addition of nanoparticle cross linkers to their first network. In contrast, Chapter 4 revealed that improvements in the properties of the

DNHG were exhibited at 10 wt % ASNP loading for all three nanoparticle sizes. The combination of size and loading density of 150 nm at 20 wt % was deemed the most effective. Similarly, 20 wt % loading was the optimal choice for loading density in all hydrogels, proving that 40 wt % lead to oversaturation of the first network and nanocomposite hindering of the material. SEM images revealed the interaction between nanoparticles and polymeric struts, providing insight into the potential mechanism in which the nanoparticles help sustain increased compressive strains. Nanoparticle retention exhibited a downward trend where more of the nanocomposite structure was lost at higher loading densities. FTIR data revealed incomplete polymerization through the presence of monomers. The combination of incomplete polymerization and the loss of nanoparticles exposed the need for improvements in the synthesis route to utilise the full potential of these materials.

Next chapter

Incomplete polymerization could be due to insufficient photoinitiator concentrations in the monomer system or due to the inhibition of radicals formed through the presence of oxygen. Ultimately, partial polymerization may hinder the material from utilising the full potential of its individual components. Therefore, the next chapter explores the kinetics and conversion profiles of both polymers and provides additional steps to the synthesis route to ensure full polymerization. A comparison will be made with the new system and Chapter 5 to investigate improvements made to polymer conversion, nanoparticle retention, and mechanical properties.

Chapter 6
Optimising open vessel photopolymerization using glucose oxidase



Confocal image of cells dispersed in PAMPS

6 Optimizing open vessel photopolymerization using glucose oxidase

6.1 Introduction

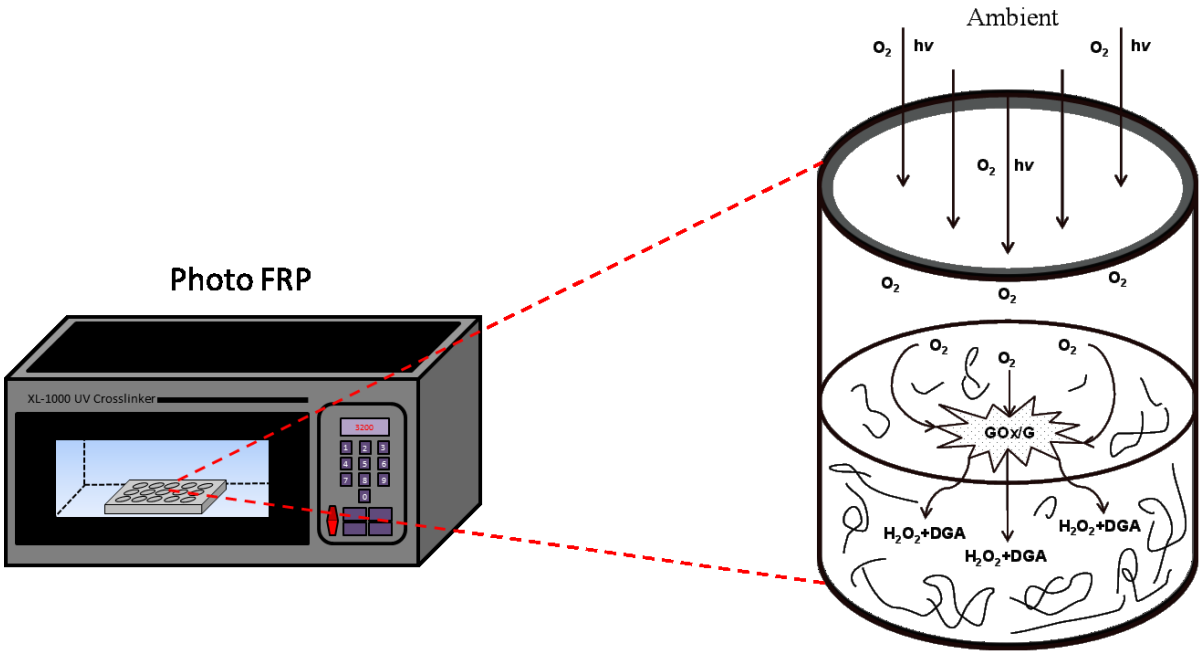
The previous chapters have explored synthesis routes in open air systems to create hydrogels of particular shapes. Polymeric biomaterials are often synthesized under inert conditions. Hydrogel synthesis commonly takes place under closed nitrogen or argon purged systems, but this limits the size and shape of the material due to practical aspects of purging. The properties of these materials are affected by the presence of oxygen during synthesis; this is due to oxygen inhibition of the free radicals that initiate the polymerization.

In this chapter, the aim is to produce PAAm and PAMPS through FRP in an open-air system that would allow facile production of double network hydrogels or other biomaterials. The polymerization should occur with superior kinetics and conversion ratios under lower photoinitiator concentrations than the methods described above, at lower cost. A naturally occurring oxido-reductase enzyme, glucose oxidase (GOx), previously aided in complete removal of O_2 in an open vessel system for a reversible addition-fragmentation chain-transfer (RAFT) polymerization of hydroxethyl acrylate and dimethylacrylamide[136]. GOx reacts with glucose in the presence of O_2 to generate soluble byproducts hydrogen peroxide and D-glucono-δ-lactone that are non-cytotoxic at low concentrations. This reaction was shown to be effective in phosphate buffer saline (PBS), water (pH range of 6-7) and several organic solvents such as *tert*-butanol, acetonitrile and dioxane[136]. GOx and glucose concentrations as low as 200 nM and 100 mM, respectively, were required to completely remove O_2 from an entire open vessel system for reactions to occur[136, 138]. Here, an objective was to apply this process to FRP of PAMPS and PAAm.

Other studies used GOx as a mediator for redox initiation polymerizations based on the by-product hydrogen peroxide forming hydroxyl radicals[143, 144] but not as a means for degassing O_2 in open vessel FRP. Previously, for open vessel FRP of PAAm, only 24 % conversion was achieved using type-1 initiator 2, 2-dimethoxy-2-pheyl acetophenone (DMPA) at 1 wt % in

the presence of GOx, only a 2 % increase in conversion compared to the control without GOx[118]. Another limitation of the study was that cell studies with the initiator DMPA showed significant loss of cell viability at 0.05 wt/v % (0.5 wt %) and higher[139]. In contrast, Irgacure-2959, a highly efficient type 1 α-cleavage photoinitiator[140, 141] only exhibits cell toxicity at 0.1 wt/v % (1 wt %)[115, 142, 139]. Another objective here was to investigate the combinatorial use of Irgacure-2959 and GOx.

Therefore the kinetics and conversion profiles of open vessel photo-FRP for PAAm and PAMPS at different Irgacure-2959 concentrations, in the presence and absence of GOx will be explored (Scheme 2).



Scheme 2 - Schematic of open vessel FRP, in the presence of glucose oxidase.

6.2 Methods and materials

6.2.1 Materials

Acrylamide (AAm; ≥ 99 %) and 2-acrylamido-2-methyl-1-propanesulfonic acid (AMPS; 99 %); N, N'-methylenebisacrylamide (BIS; 99 %); photoinitiator 2-hydroxy-4'-(2-hydroxyethoxy)-2-methylpropiophenone (synonym Irgacure 2959; 98 %), 1, 3, 5 –trioxane (≥ 99 %); triethoxyvinylsilane (VTEOS; ≥ 98 %) , deuterium oxide (D2O; 99.9 atom % D) were purchased from Sigma-Aldrich (UK). No additional processing and/or purifications were performed. D-glucose (G) and glucose oxidase (GOx; from aspergillus niger as a lyophilized powder) were purchased from Sigma-Aldrich (UK) and stored in phosphate buffer saline (PBS) aliquots at -20 °C when received. ATDC5 murine chondrogenic cell line (ATCC, UK) was purchased from Sigma-Aldrich (UK) and used as purchased for cell cytotoxicity studies.

6.2.2 Methods

6.2.2.1 Silica synthesis

As described in section 4.2.2.1 . Here, surface functionalization was conducted using VTEOS rather than APTES.

6.2.2.2 Polymer synthesis

All photopolymerizations took place under the same conditions in a XL-1000 UV Crosslinker with 365 nm light for durations of 5400 s. AAm and AMPS monomers were dissolved in deionised water under stirring at room temperature with final concentrations of 1.41 M and 0.48 M, respectively. Photopolymerizations were carried out in open-to-ambient glass

beakers for AAm and AMPS using 0.05, 0.1, 0.5, 1 and 2 wt % PI Irgacure 2959, in the presence and absence of GOx/G. 10 mg crystals of trioxane were added to the monomer solutions to be used as a 1H NMR reference for polymer conversion calculations. For the photopolymer kinetics study, 1H NMR samples were taken from the solutions at time zero as a reference for the unreacted monomer solution. The chosen time points for the study were 1, 2, 5, 10, 20, 30, 40, 50, 60, 70 and 90 minutes. A single drop (approximately 50 mg) was extracted from the photopolymer solution at each time point and quickly diluted with 500 µL D2O to stop the reaction. In the case of PAMPS, the monomer solution was highly acidic and required neutralisation before GOx was used to prevent the enzyme becoming denatured. AMPS 2.41 M was titrated from pH 0.34 to pH 7.1 using 5.03 mL of 1 M NaOH, which allowed a final AMPS monomer concentration of 0.48 M.

6.2.2.3 Double network hydrogels with GOx synthesis

Double network hydrogels (DNHG) were synthesized in a two-step sequential photopolymerization, illustrated in Figure 53 . AMPS monomers were dissolved under stirring in deionised water, and titrated to pH 5.4 using NaOH (0.25 M), to a final concentration of 0.48 M. GOx/G, 0.05 wt % PI and 1 wt % BIS were then added to the solution and stirred for 5 minutes. The solution was then poured into a 48-well multi-well without being covered and placed into the XL-1000 UV Crosslinker for photopolymerization of the first network under 365 nm light for 1.5 h. Once completed, the hydrogels were removed from the multi-well and heated to 60 ºC overnight to denature GOx. The hydrogels were then soaked in a 1.41 M concentration solution of AAm monomers with 0.5 wt % PI, 0.1 wt % BIS, and GOx/G. The swollen hydrogels were placed back into the UV Crosslinker on glass plates for 1.5 h to form the second network. The final DNHGs were swollen in water and weighed daily until a plateau was reached.

The synthesis was repeated for hydrogels containing 150 nm and 50 nm VSNP with 20 wt % loading. These concentrations are based on the best results obtained from Chapter 5. The synthesis route is represented in Figure 53 below.

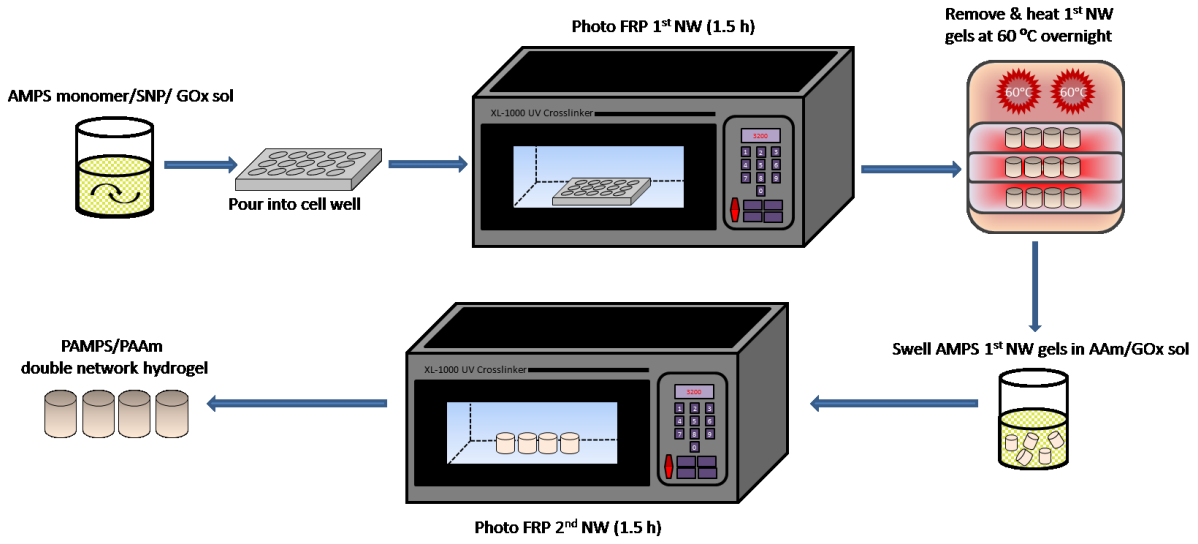


Figure 53 - Schematic representation of the synthesis route for PAMPS/PAAm hydrogels in the presence of GOx.

6.2.2.4 Cell studies

Cell seeding for viability analyses

ATDC5 cells were seeded at 3000 cells/ cm^2 in 96 - well multi-well tissue-culture plates and allowed to grow for 24 h in 100 µl basal DMEM (Dulbecco's modified eagle medium) containing 5 % (v/v) FCS (foetal calf serum), 1 % (v/v) penicillin-streptomycin and 1 × ITS (insulin-transferring-selenium) liquid supplement. Culture medium was then replaced with medium-monomer mixture containing basal supplements and cultured for further 24 h. The medium-polymer mixture consists of 20 % v/v polymer and DMEM.

Analysis of cell viability

Viability of cells following was determined by 3-(4, 5-dimethylthiazol-2-yl)-2, 5-diphenyltetrazolium bromide (MTT) metabolic activity assay. Culture medium was replaced with 1 mg/ml MTT solution. MTT solution was removed after 2 h and dimethyl sulfoxide (DMSO) was added to dissolve the formazan crystals converted by living cells. The

luminescence of the resulting solutions was measured at 570 nm. 570nm is the absorption spectrum of formazan. 630 nm is used as reference for noise, however for assays like MTT it's not always necessary as long as the optical density (the value measured) is around 0.2 – 0.7. SpectraMax M5 plate reader was used.

Live/dead staining

Visualisation of cell viability was achieved by live/dead staining using a combination of CellTrackerTM green (CTG) and ethidium homodimer-1 (EH-1). Cultured cells were washed in PBS and incubated in CTG (10 µg/ ml) and EH-1 (5 µg/ ml) dye working solution for 45 minutes. The dye solution was then replaced with fresh plain DMEM (i.e. no FBS) and incubated for further 30 minutes. Cells were washed and fixed with 4 wt/v % paraformaldehyde (PFA) for imaging under fluorescent microscopy. The Leica SP5 inverted confocal microscope was used.

Statistical analysis

Statistical analysis of cell viability was performed using Mann-Whitney U test, using Prism software. Results were deemed significant if the probability of occurrence by random chance was less than 5 % (i.e. $p < 0.05$).

6.3 Results and discussion

6.3.1 pKa titrations

In order to add GOx to the monomer solution, the pH was adjusted to 5.4. An AMPS monomer solution of 0.05 M was titrated with 0.25 M NaOH. A pKa value of 1.91 was calculated, indicating a strong acidic nature. A polymer solution of the same concentration was titrated to a pH of 5.4, with a pKa value of 1.04. Figure 54 shows the pKa curves for both

AMPS and PAMPS. Hence, the polymer solution was found to be more acidic than its monomer. An essential step to adding the enzyme is therefore the initial titration of the monomer solution to ensure the enzyme does not become denatured. At the pKa point and above the solution becomes deprotonated, dissociating into stable negative ions and conjugate base. If the pH falls below the pKa value then the solution will accept protons and form sulfonic acid groups. Both monomer and polymer solutions are strong acids that require low pH values to donate protons in aqueous solution to give rise to acidification.

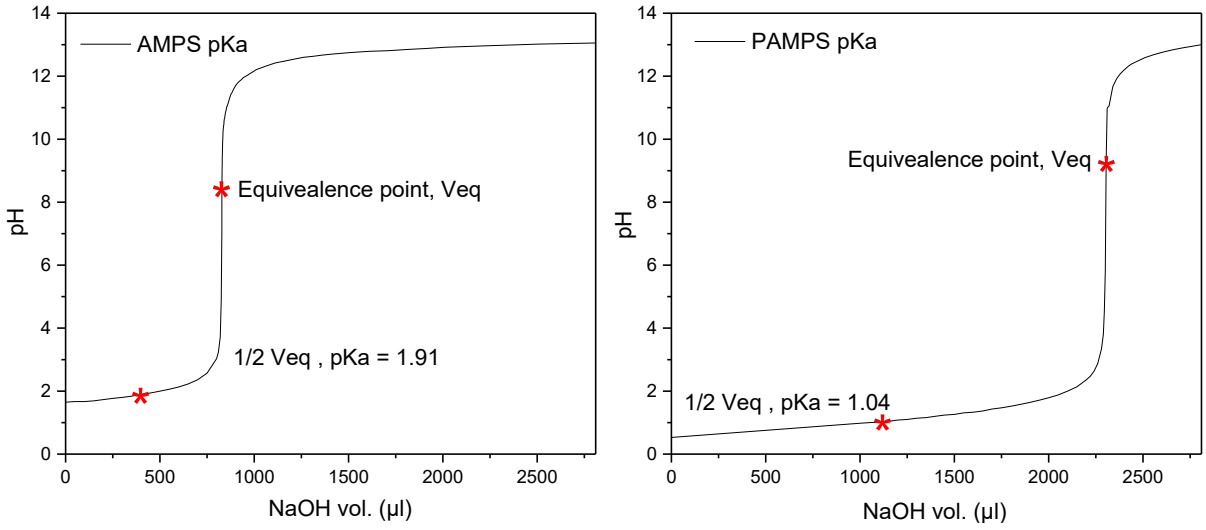


Figure 54 - pKa of AMPS and PAMPS showing the equivalence point and 1/2 equivalence point.

6.3.2 Kinetics and conversion

Polymer conversion and kinetics were then examined using ^{1}H NMR with the aim of achieving 100 % conversion for both polymers. This was successfully achieved with low PI and GOx concentrations. Figure 55 and Figure 56 show the ^{1}H NMR profile for PAAm and PAMPS, respectively, with no residual monomers remaining in their final solution.

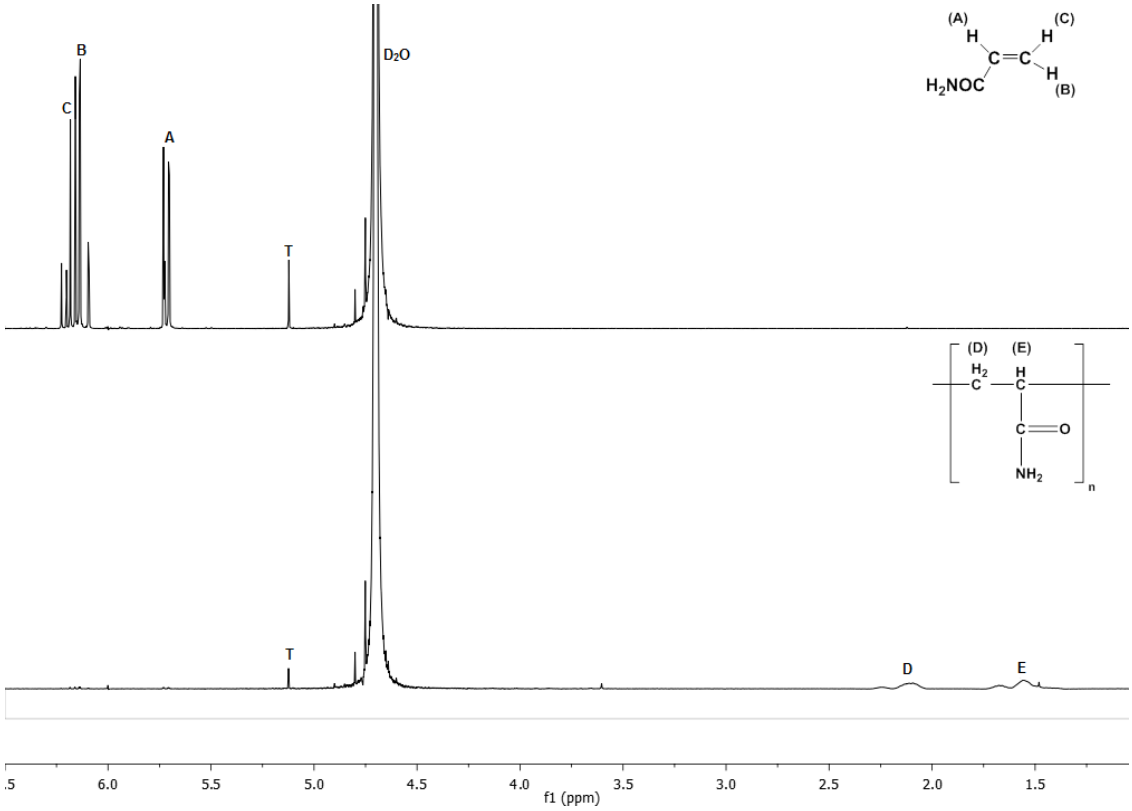


Figure 55 - ^{1}H NMR of AAm monomers prior to polymerization in the presence of GOx (top) and at 100 % conversion to PAAm (bottom). Hydrogen protons near each atom are labelled with letters, representing ppm peaks on the graph.

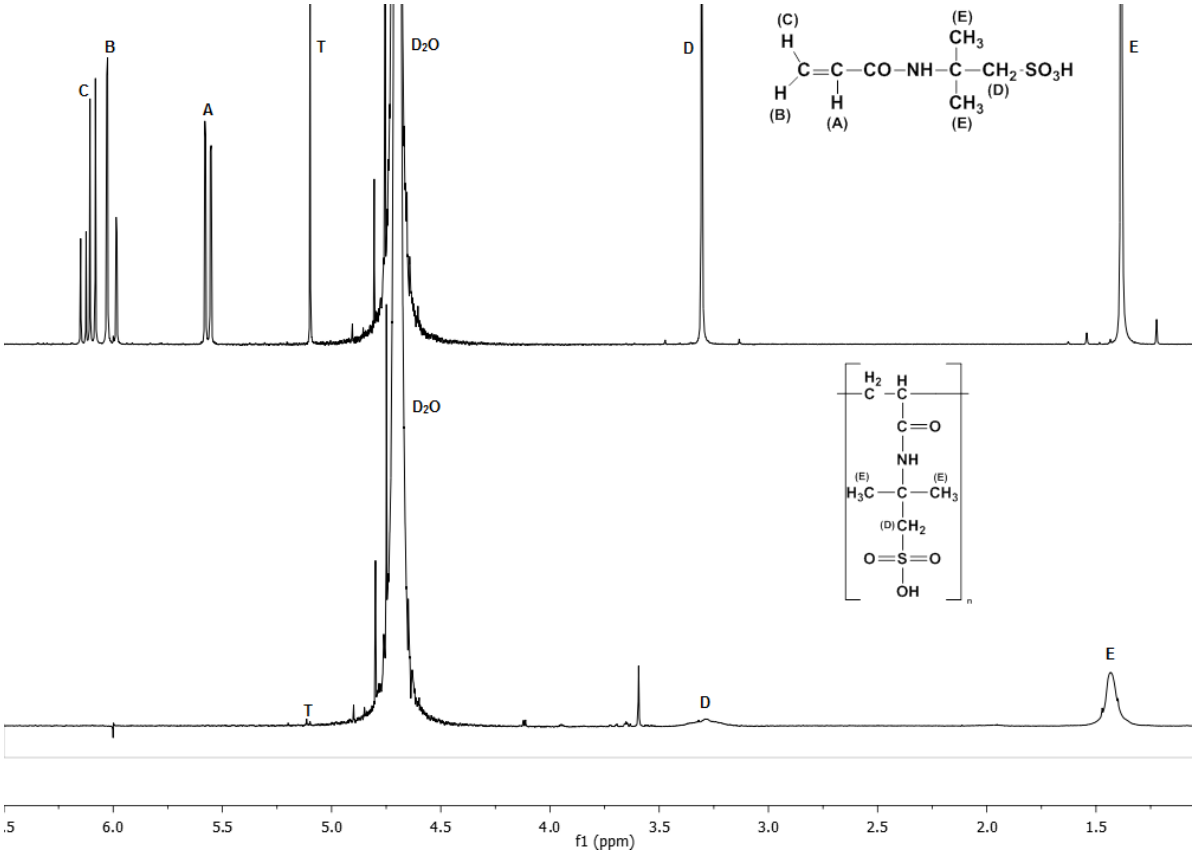


Figure 56 - ^{1}H NMR of AMPS monomers prior to polymerization in the presence of GOx (top) and at 100 % conversion to PAMPS (bottom). Hydrogen protons near each atom are labelled with letters, representing ppm peaks on the graph.

At 0.05 wt % PI, ^{1}H NMR of PAMPS showed 0 % conversion in the absence of GOx. This is due to instant and rapid inhibition of PI radicals caused by O_2 (Scheme 1). This step is considered unlikely in efficient PI systems where O_2 is not fast enough to compete.[133] This indicates that O_2 inhibition cannot be overcome, at the low PI concentrations needed to maintain cell viability, meaning free radicals are quenched at a faster rate by O_2 than they can react with monomers. In contrast, 100 % conversion was achieved at the same PI concentration of 0.05 wt % in the presence of GOx. These results prove polymerization kinetics of PAMPS were highly susceptible to ambient O_2. In this case, GOx evaded all O_2 inhibition steps as labelled e1, e2 and e3 in Scheme 1. Significantly, GOx at 200 nM was sufficient to eliminate the scavenging effects of O_2 despite its remarkably low concentration.[136]

Table 25 - Conversion for PAMPS and PAAm at varying PI concentrations in the presence of GOx, and without GOx (control).

PI wt%	PAMPS Conversion (%)		PAAm Conversion (%)	
	Control	GOx	Control	GOx
0.05	0	100	0	78
0.1	35	100	4	92
0.5	59	100	17	98
1	76	100	40	100
2	95	100	76	100

Higher concentrations of PI were used to investigate the kinetics and pathways of inhibition in more detail. Table 25 shows that at 0.1 wt % PI the PAMPS control (no GOx) exhibited 35 % conversion. Increasing the PI concentration for PAMPS 20 fold, from 0.1 wt % to 2 wt % increased the conversion from 35 % to 95 % (Figure 57). This increase agrees with the concept of overcoming the scavenging effects of O_2 in FRP by increasing PI concentration, but at several costs. PI concentrations above 0.1 wt % are not favoured in biomaterial applications due to their potential cytotoxic effects,[109] and using 20 times the concentration of PI still did not provide 100 % conversion. Furthermore, PI solubility is reduced significantly at 2 wt % and can reduce optical clarity, hindering the UV light interaction.

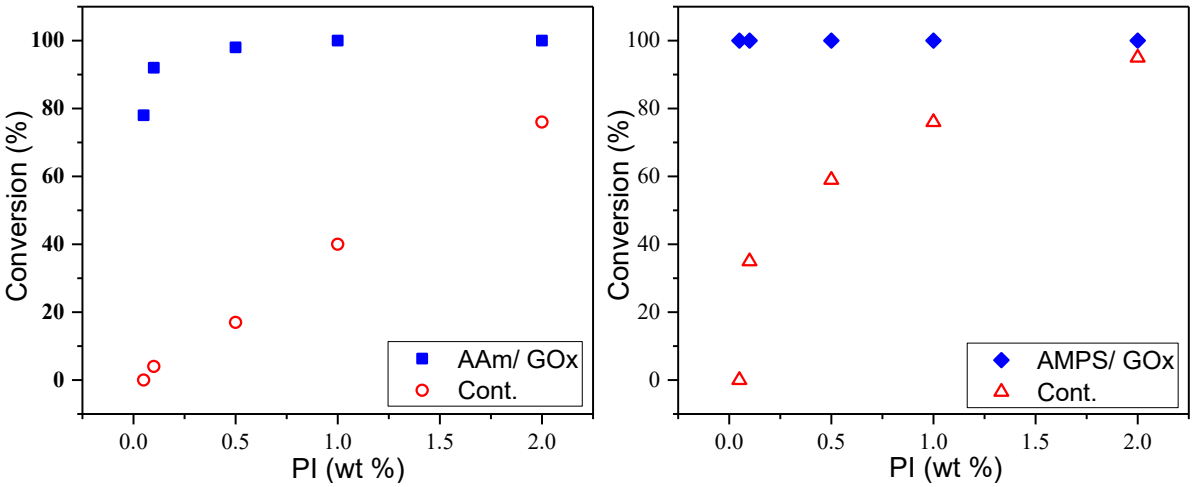


Figure 57 - Conversion profiles at varying PI concentrations for AAm (left) and AMPS (right), in the presence of GOx compared to their respective controls.

Figure 57 indicates that PAAm control conversions exhibited a near linear relationship with increasing PI concentration. Higher PI concentrations of 1 wt % were needed to reach 100 % conversion in the presence of GOx for PAAm, compared to the 0.1 wt % PI for PAMPS. Without GOx, the control PAAm only reached 40 % conversion (Figure 57) at 1 wt % PI and was below 80 % at 2 wt % PI. The viscosity and appearance of control PAAm the solution was wet, sticky and inconsistent. This is a consequence of the apparent long inhibition times caused by a lack of initiating radicals that are scavenged rapidly by O_2 [132, 196]. In contrast, PAAm formed with GOx exhibited hydrogel-like texture.

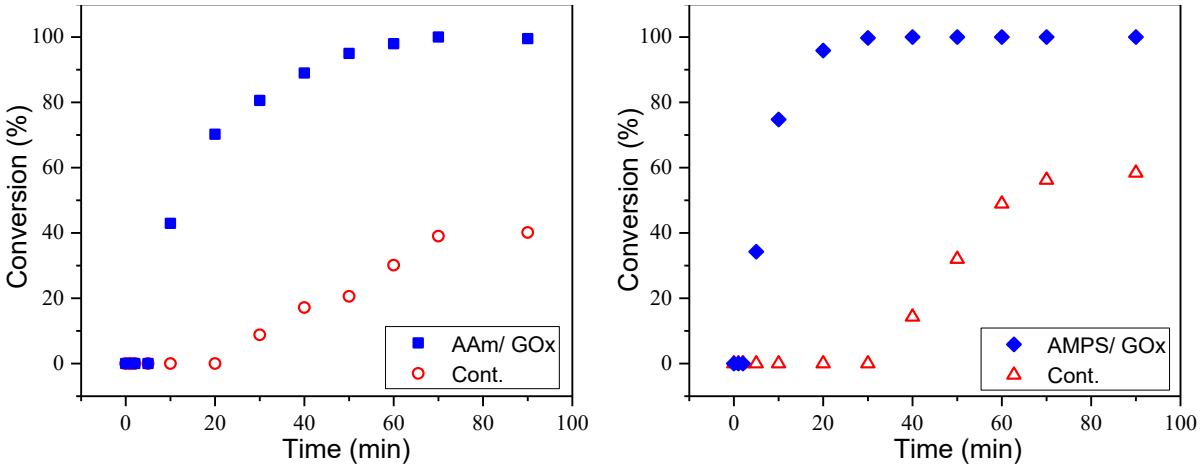


Figure 58 - Kinetic profiles for AAm (left) and AMPS (right) at 0.5 wt % PI in the presence of GOx compared to their respective controls.

The efficacy of GOx was better for PAMPS than PAAm, suggesting that PAAm is more sensitive to O_2 and exhibits slower reaction kinetics. Figure 58 shows the kinetic profile of PAMPS at 0.5 wt % PI drastically improved in the presence of GOx, achieving 100 % conversion in less than 30 minutes. In contrast, the control shows a lag of 30 minutes before the polymers began to form. PAAm kinetics follows a similar trend for the control, and improved kinetics with GOx reaching full conversion in less than 70 minutes. The improved reaction rate with GOx and low PI concentrations can have extremely useful implications for soft material synthesis such as hydrogels. The results give an indication that mechanical

properties could improve the mechanical properties and integrity of the material. This will be explored later in this chapter.

6.3.3 GPC

Gas permeation chromatography (GPC) was conducted on PAMPS polymer solutions to further understand the effect of GOx on the polymers being formed. PAAm could not be tested due to its cross linked nature once polymerized. Polymer solutions were dissolved in DMF with 10 µM LiBr to get a concentration of 4 mg mL^{-1}. 1 ml solutions were then filtered with 0.45 µm pores into GPC vials, to remove any cross linked or large polymer chains. The samples were loaded into the Malvern TDA 305 instrument with DMF (0.075 % LiBr) as the eluting solution at a rate of 0.7 mL min^{-1}. Calibration was done against a PMMA standard (65 kDa and Mw Mn^{-1} of 1.10 Malvern). M_w, M_n and M_w/M_n values were calculated using Omnisec 4.7.0 Software and a fixed dn/dc of 0.063. Table 26 shows the polydispersity (Đ) values for PAAm and PAMPS at three different PI concentrations with and without GOx. Uncontrolled FRP values for Đ are typically around 1.9. Higher Đ values indicate less control over the polymerization. Control PAMPS with 0.05 wt % showed 0 % conversion therefore could not be run through the GPC. PAMPS with GOx at PI 0.05 wt % resulted in a Đ value of 1.9, suggesting that it falls perfectly in line with uncontrolled FRP. At PI 1 wt % control PAMPS resulted in 454 kDa and Đ 2.1, compared to 421 kDa and Đ 1.9 when GOx was introduced. This was a significant finding, primarily due to increased level of control shown in Đ values and the reduced molecular weight of the polymer. Summarily, at PI 2 wt % control PAMPS had less control over the polymerization with results of 418 kDa and Đ 2.5. In contrast, when GOx was included for 2 wt % there was more control over the polymerization, resulting in 405 kDa and Đ 2.1. These results indicate that GOx enhanced the kinetics and added control to the polymerization.

Table 26 - GPC data for PAMPS at 0.05, 1 and 2 wt % PI in the presence of GOx compared to controls.

PI wt %	Control		GOx	
	M_n (kDa)	M_w/M_n (Đ)	M_n (kDa)	M_w/M_n (Đ)
0.05	-	-	476	1.9
1	454	2.1	421	1.9
2	418	2.5	405	2.1

Lower PI concentrations were expected to result in higher Mn due to less radicals being present to initiate new polymer chains. Therefore this allows already propagating chains to grow further, without competition from new ones. This finding was significant in terms of required polymeric interactions with in the hydrogels. Longer chains in non-degradable biomaterials, as in this case, are beneficial. This could lead to stronger entanglements along with a heightened probability of inter-network interactions. 0.05 wt % provided PAMPS with 100 % conversion in the presence of GOx, therefore would be used in future synthesis.

Figure 59 demonstrates the change in visible viscosity of the polymer solutions at 90 minutes. PAAm produced with GOx became hydrogel-like due to its high molecular weight and cross linking nature, whilst the control exhibited inconsistent and wet texture due to its incomplete polymerization. Polymers containing GOx changed colour from clear to yellow approximately 24 h post photopolymerization. This observation suggests that GOx continues degassing the system for up to, and possible over, 24 h before slowing down and halting. This gives an indication that 200 nM could be a sufficient value for polymerizations that last up to 24 h.

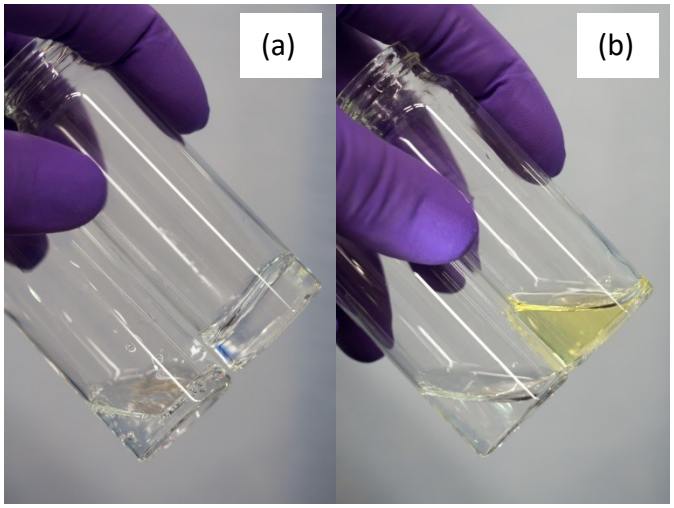


Figure 59 - (a) PAMPS (left) and PAAm (right) controls after photopolymerization with GOx, (b) PAMPS (left) and PAAm (right) controls after photopolymerization without GOx.

6.3.4 Cytotoxicity

Cytotoxicity studies using ATDC5 cells were carried out on PAAm and PAMPS at varying PI concentrations in the presence of GOx. PAAm and PAMPS controls were synthesized using 0.5 wt % PI. Results of the cytotoxicity studies were compared to DMEM and DMEM/PBS only controls. Chondrocytes were seeded at 0 h post synthesis, 24 h post synthesis and 24 h post synthesis with additional 60 C° heat treatment. The live/dead assay in Figure 60 showed low cell survival for PAAm control at 0 h post synthesis and after 24 h at room temperature, and after 24 h at 60 ^{o}C, due to unreacted monomers in the solution that are highly toxic. Cell survival was expected to increase in the presence of GOx because of the 100 % conversion of the toxic monomers; however cell survival only increased for PAAm in the presence of GOx when the hydrogel was heated to 60 ^{o}C 24 h post synthesis (Figure 61). The cell death occurring when the hydrogels were not heated was attributed to cell asphyxiation due to the effective nature of GOx. Cell survival increased once the enzyme was denatured at 60 ^{o}C, and any cell death exhibited at that point was due to toxic unreacted monomers. An asterisk represents a significant difference between cell survival for samples with GOx and control.

When the PI concentration was increased, and polymer solutions were heated to 60 °C, cell survival increased further, reaching 84 % of the DMEM positive control at 0.5 wt % PI, Figure 61. The plus symbol represents a significant different between samples of ≥ 0.5 wt % PI with GOx, compared to PI of 0.05 wt % and 0.1 wt % with GOx, and control.

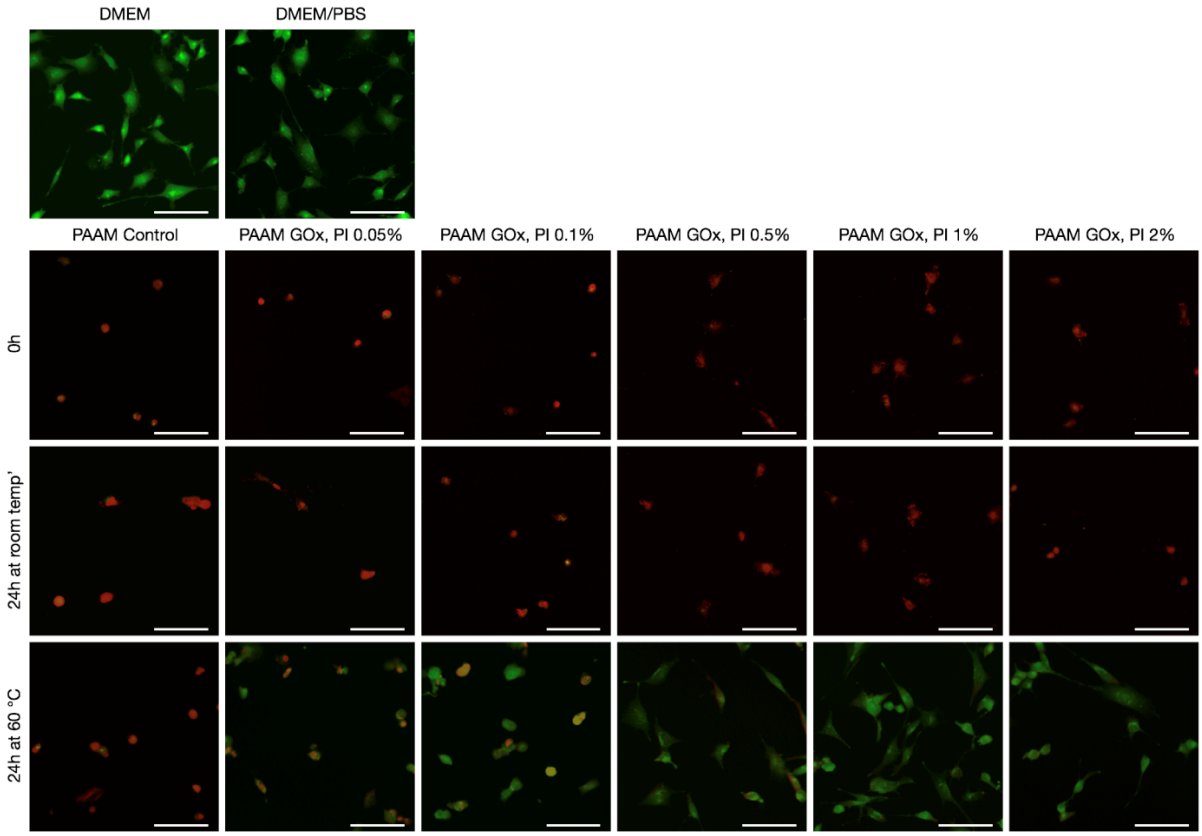


Figure 60 - Live/dead cell viability assay for PAAm in the presence of GOx at varying PI concentrations.

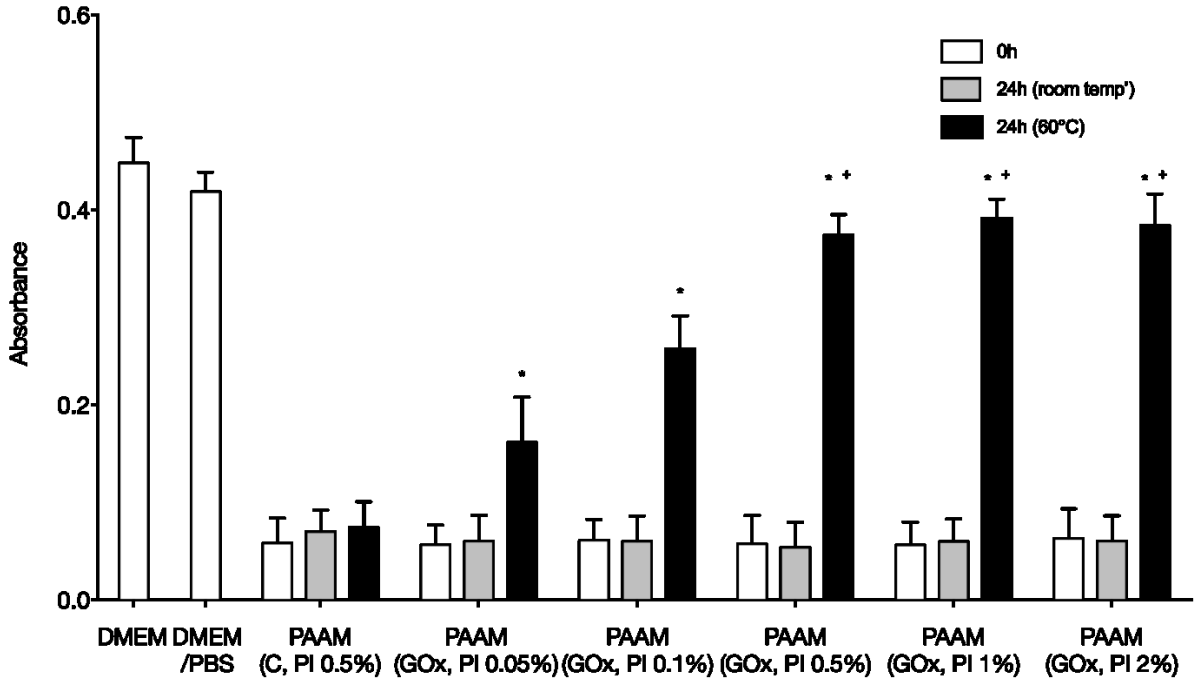


Figure 61 - Cell viability graph for PAAm in the presence of GOx at varying PI concentrations. * p<0.05 compared to 0 h and 24 h (room temperature). + p<0.05 compared to control 0.5 wt % PI, GOx 0.05 wt % PI and GOx 0.1 wt % PI).

Figure 62 and Figure 63 show PAMPS control was non-cytotoxic, suggesting that any remaining monomers are not toxic. PAMPS is usually toxic due to its highly acidic nature however it was neutralized prior to use. Cell death for PAMPS in the presence of GOx, Figure 62, was attributed to oxygen depletion in the presence of active GOx in the hydrogels that were not heated. High cell survival was observed for PAMPS once GOx was denatured at 60 °C. An asterisk is used to represent a significant difference between cell survivals of samples with GOx after heat treatment in comparison to 0 h and 24 h samples with GOx at room temperature (Figure 63).

Ultimately, denaturing GOx is essential for cell survival post hydrogel production as the enzyme is still active. This provides clearer proof that the enzyme is suitable for polymerizations that have longer kinetics that also require an oxygen free atmosphere. Lower concentrations of GOx can be used effectively for shorter polymerizations.

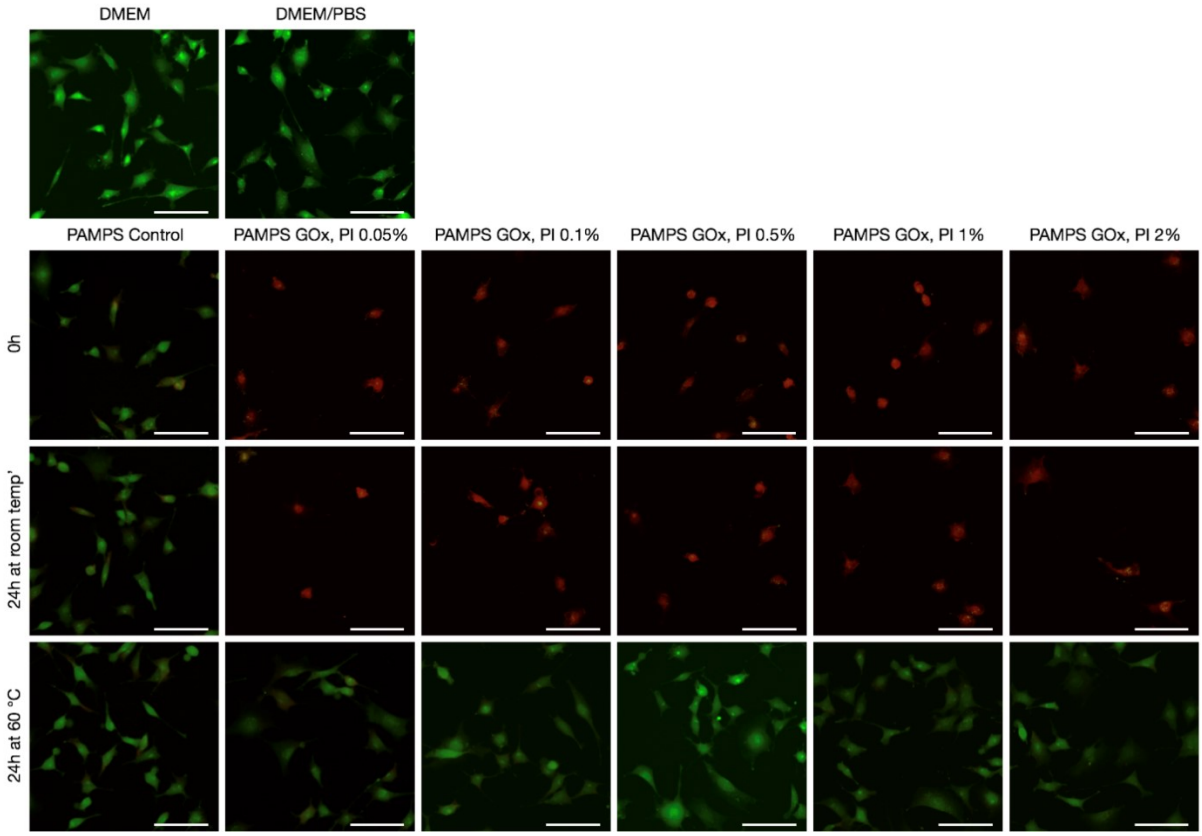


Figure 62 - Live/dead cell viability assay for PAMPS in the presence of GOx at varying PI concentrations.

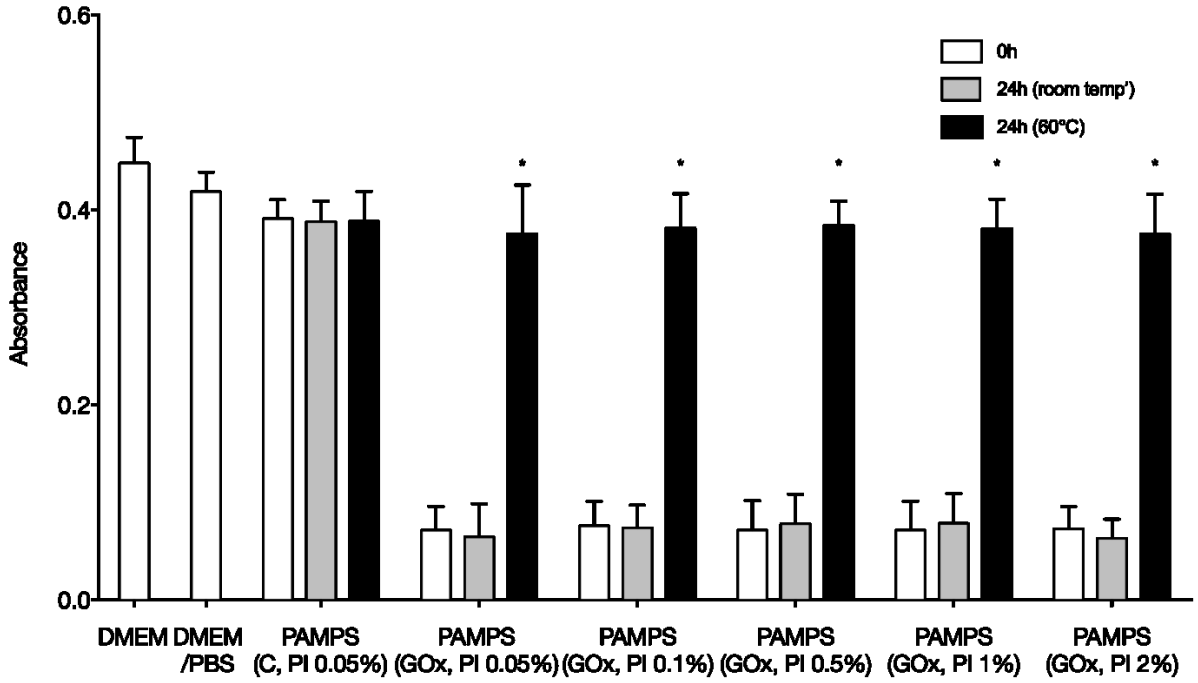


Figure 63 - Cell viability graph for PAMPS in the presence of GOx at varying PI concentrations. * p<0.05 compared to 0 h and 24 h (room temperature).

6.4 Optimized double network hydrogels

The double network hydrogels from Chapter 5 were optimized based on the results from this chapter. For the PAMPS network, PI 0.05 wt % was used based on ^{1}H NMR, cell studies and GPC data that reveal 100 % conversion with high molecular weight and no cytotoxic effects. For PAAm, 0.5 wt % was proved to be sufficient to achieve 100 % conversion from ^{1}H NMR with non-cytotoxic effects. From Chapter 5 the best result was found with the combination of 20 wt % nanoparticle loading. Therefore 20 wt % was used for 150 nm and 50 nm hydrogels in this chapter.

6.4.1 Swelling

Samples were dried for 5 days at 50 °C and weighed at 0 h prior to swelling in deionised water. All samples were swollen until a plateau was reached, as seen in Figure 65. Control with GOx samples witnessed a significant decrease in water uptake and swelling compared to control samples without GOx from the previous chapter. A reduction in swelling from 2757 ± 157 % for controls without GOx to 222 ± 2 % for controls with GOx was noted, marking a significant change in the materials ability to hold water. Controls with GOx also witnessed a large reduction in water content with 65.4 ± 3.1 % compared to controls without GOx that held 96.7 ± 0.36 %. These results are indicative of the changes in polymeric behaviour and interactions with in the hydrogels. The ability to reach full conversion for both polymers provides more polymer entanglements and more effectively cross linked networks. Similar reductions were made between the 20 wt % samples for 50 nm and 150 nm with GOx compared to their samples without GOx in the previous chapter. The swelling rate profile was also comparatively slower for controls with GOx, relative to controls without GOx.

Interestingly, the samples with 20 wt % nanoparticle exhibited more water uptake compared to their control, as seen in Figure 65. Although, the swelling % for both 50 nm and 150 nm are slightly lower than the control. The reduced swelling % suggests tighter cross linking within the hydrogel, whereas the increased water content may suggest void spaces have formed and have allowed increased water uptake. A reason behind this could be leakage of nanoparticles during the swelling process.

Ultimately, GOx has a strong influence the hydrogels swelling profiles due to its intrinsic ability to assist in the formation strong polymeric networks.

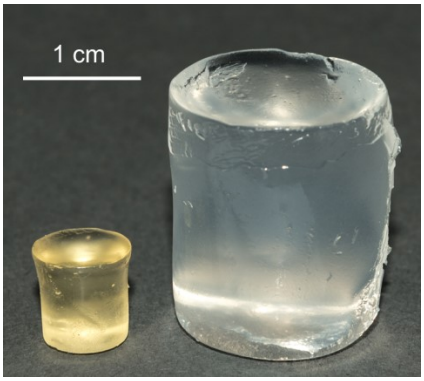


Figure 64 – PAMPS/PAAm hydrogel with 150 nm 20 wt % silica nanoparticles (VSNPs), before and after swelling.

Figure 64 shows the final product of the double network hydrogel formed in the presence of GOx, before and after swelling in water for 4 days. When fully swollen, the content of the hydrogel was 95 % water, and its volume increased by 825 %. The swelling ability of the hydrogel, as well as its mechanical properties, can be tailored based different concentrations of cross linker used in both the first and second network.

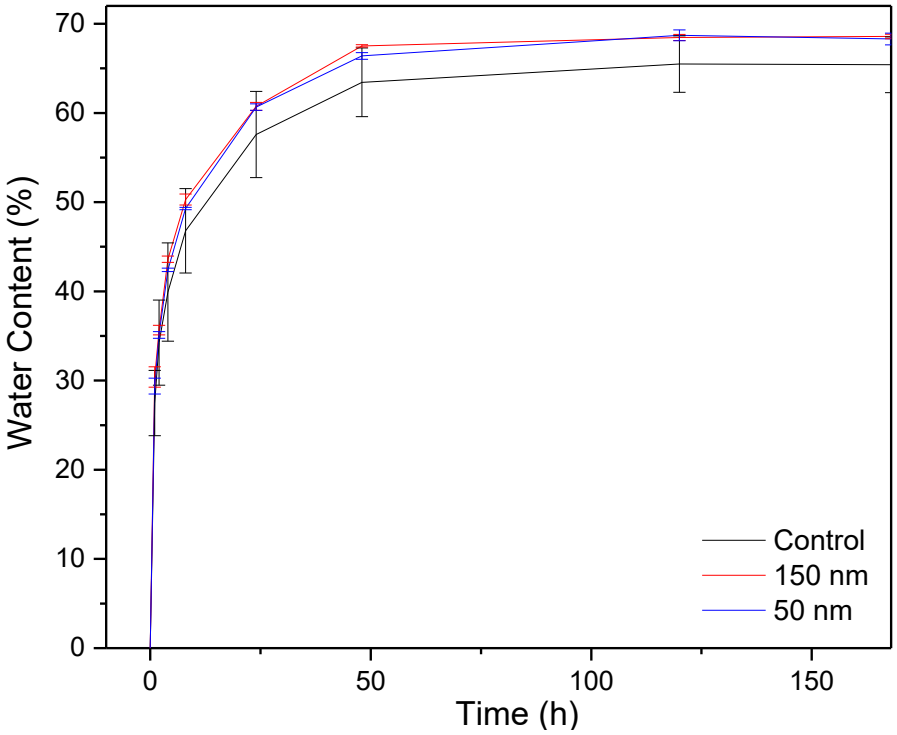


Figure 65 – Swelling profile for PAMPS/PAAm hydrogels with 150 nm and 50 nm silica nanoparticles (VSNPs) with 20 wt % loading in the presence of GOx, compared to a control with GOx.

Table 27 - Swelling and water content for PAMPS/PAAm hydrogels with 150 nm and 50 nm silica nanoparticles (VSNPs) with 20 wt % loading in the presence of GOx, compared to a control with GOx.

		Loading of 20 wt % VSNPs	
	Control w GOx	50 nm	150 nm
Water Content (%)	65.4 ± 3.1	68.3 ± 0.7	68.6 ± 0.3
Swelling (%)	222 ± 2	216 ± 7	218 ± 3

6.4.2 TGA

TGA was carried out for Fresh and Swollen samples of 20 wt % for 50 nm and 150 nm based hydrogels. Therefore it was possible to develop an understanding of whether nanoparticles are lost during synthesis or post swelling.

Samples were dried for 5 days at 60 °C and ground to a powder. 10 mg of sample was loaded into a platinum crucible and placed opposite an empty platinum crucible. The samples were heated to 800 °C using a heating rate of 10 °C min^{-1}, with a continuous flow of air. Polymeric material in the samples is expected to be burnt off by 600 °C and any remaining residues are considered to be silica nanoparticles.

Figure 66 shows the TGA and DTG profiles for Fresh and Swollen hydrogels containing 150 nm VSNP at 20 wt % loading. The control reached 0 % residual mass at 660 °C, with moderate DTG peaks suggesting weak covalent bonds and entanglements within the sample. Contrary to this, hydrogels containing 150 nm VSNPs showed stronger DTG peaks with sharper TGA drops, clearly defining the energy required to break strong covalent bonds and polymeric entanglements. The sharper and narrower peaks for DTG give an indication as to the tightly cross linked networks.

Fresh samples for hydrogels containing 150 nm VSNPs had 102 % retention of nanoparticles in their Fresh state. This concludes that no nanoparticles were lost during synthesis of both networks. Swollen samples showed nanoparticle retention of 40 %, a significant drop from the Swollen samples. This allows the conclusion to be drawn of losses during swelling, likely due to non-cross linked nanoparticles that manage to leak out through the porous structures. It is worth noting that a lower nanoparticle retention for hydrogels containing 150 nm VSNPs with 20 wt % loading was witnessed with GOx (41 %) compared to Chapter 5 results without GOx for the same combination (77 %). This was an unexpected result, mainly due to the assumption that tighter networks will have the ability to retain a higher percent of nanoparticles.

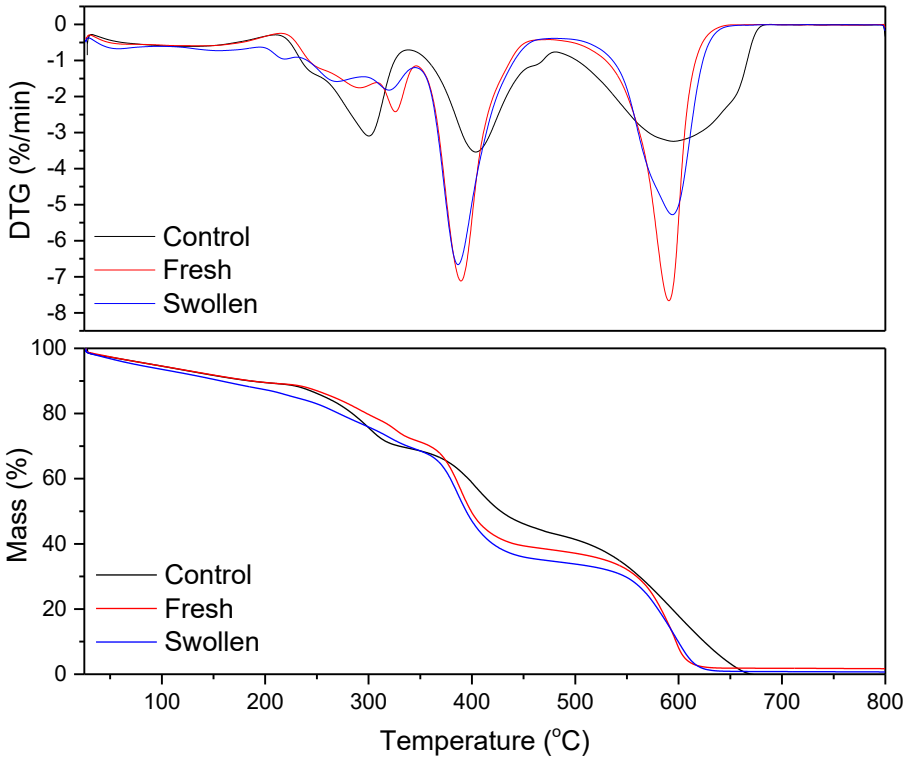


Figure 66 – TGA and nanoparticle retention for PAMPS/PAAm hydrogels with 150 nm silica nanoparticles (VSNPs) at 20 wt % loading in the presence of GOx, and control with GOx.

Table 28 - nanoparticle retention for PAMPS/PAAm hydrogels containing 150 nm silica nanoparticles (VSNPs) at 20 wt % loading in the presence of GOx, and control with GOx.

	Loading of 150 nm with 20 wt % VSNPs	
	Fresh	Pure
Theoretical %	3.33	3.33
Residual %	3.40	1.37
Particle Retention %	102	41

Figure 67 shows the TGA and DTG profiles for Fresh and Swollen samples of hydrogels containing 50 nm VSNP at 20 wt % loading. DTG profiles follow the same trend as hydrogels containing 150 nm VSNP described above. Interestingly, 50 nm Fresh samples had relatively low nanoparticle retention compared to 150 nm. This aids in the conclusion that nanoparticle losses during synthesis are more likely with smaller sized nanoparticles. This can occur during the synthesis of the first network, or the

subsequent step of swelling in the monomer solution of the second network. 38 % of nanoparticles were ultimately retained in the hydrogels containing 50 nm VSNP, close to that of 150 nm. For 50 nm samples without GOx of the same concentration, from Chapter 5, Swollen samples had 73 % nanoparticle retention. This result coincides with the finding mention above. Unexpectedly, nanoparticle retention was reduced with the introduction of GOx.

Ultimately, TGA and DTG results provided an insight into the point in which nanoparticles are lost and a clearer idea into the increased strength of their covalent bonds, or enhanced polymeric entanglements.

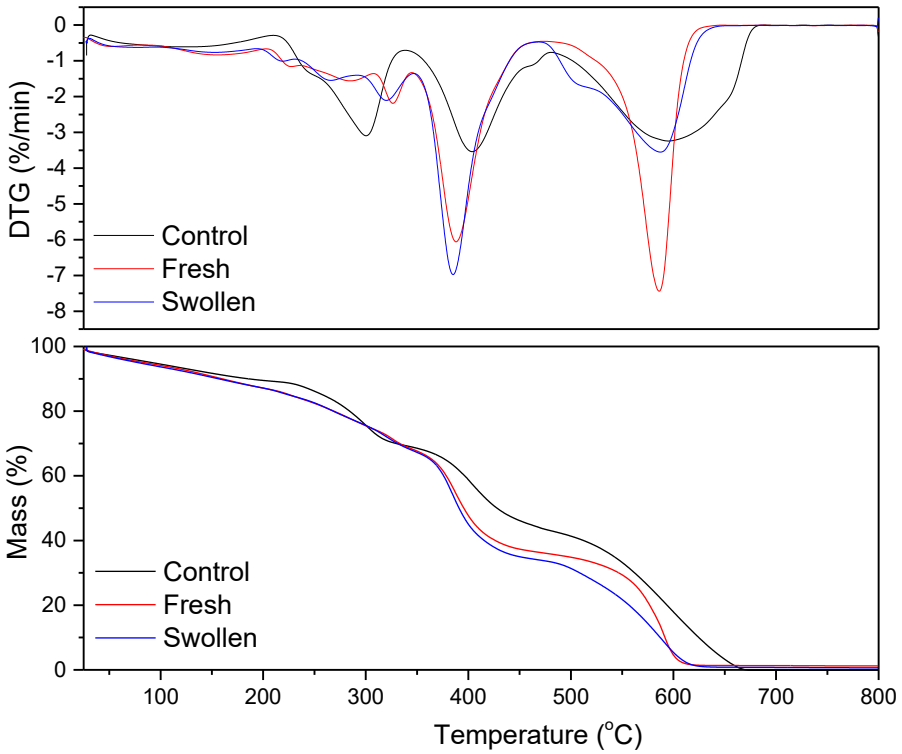


Figure 67 – TGA and nanoparticle retention for PAMPS/PAAm with 50 nm VSNP at 20 wt % loading in the presence of GOx, and control with GOx.

Table 29 - Nanoparticle retention for PAMPS/PAAm containing 50 nm vinyl silica nanoparticles (VSNPs) at 20 wt % loading in the presence of GOx, and control with GOx.

	Loading of 50 nm with 20 wt % VSNPs	
	Fresh	Pure
Theoretical %	3.33	3.33
Residual %	2.36	1.27
Particle Retention %	71	38

6.4.3 Mechanical tests

DNHGs containing 150 nm and 50 nm were tested under compression after a swelling plateau was achieved, and compared to control DNHGs. The introduction of GOx resulted in better conversion profiles, and more control over molecular weight as expressed previously. This evidently enhanced the mechanical properties of the DNHGs. Figure 68 shows that the compressive strength of DNHGs containing 150 nm and 50 nm at 20 wt % loading exhibited increased strength, relative to the control. The control here, which was synthesised in the presence of GOx, achieved a compressive strength of 0.99 ± 0.24 MPa, in contrast to the control in the previous chapter that only achieved 0.09 ± 0.02 MPa. The addition of GOx resulted in a marked improvement for DNHGs containing 150 nm VSNPs with 20 wt % loading, at 2.62 ± 0.48 MPa, compared to 0.81 ± 0.08 MPa without GOx. DNHGs containing 50 nm VSNPs at 20 wt % loading improved from 0.59 ± 0.05 MPa without GOx, to 3.55 ± 0.41 MPa with GOx. Interestingly, control DNHGs with GOx exhibited an increase in strain of approximately 10 %, whereas both DNHGs containing 150 nm and 50 nm VSNPs with GOx experienced a reduced strain of about 12 %, compared to their respective DNHGs without GOx in Chapter 5. The removal of O_2 from the reaction system allows for 100 % conversion of the monomers, resulting in a higher density of polymers in the material. This leads a higher density of cross linked polymers and interaction with VSNPs, as well as better polymer entanglement, resulting in the evident improved properties of the DNHGs. The addition of GOx improved the control for both compressive stress and strain, whereas DNHGs containing VSNPs only improved in compressive strength. The reduced strain values could be attributed to the apparent loss of VSNPs seen from the particle retention values.

This may have created voids in the material, resulting in reduced strain values. Ultimately; degassing oxygen plays a vital role in achieving mechanical properties for these DNHGs to match that of articular cartilage.

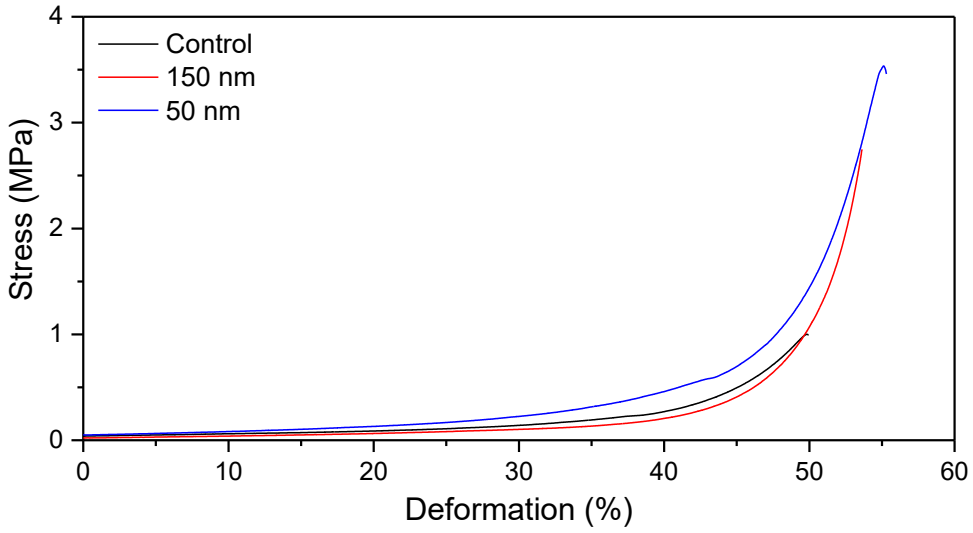


Figure 68 – Compression curves for hydrogels containing 150 nm and 50 nm vinyl silica nanoparticles (VSNPs) at 20 wt % loading, compared to control

Table 30 - Compression and strain for hydrogels containing 150 nm and 50 nm vinyl silica nanoparticles (VSNPs) at 20 wt % loading, compared to control

		Loading with 20 wt % VSNPs	
	Control	150 nm	50 nm
Fracture Compressive Stress (MPa)	0.99 ± 0.24	2.62 ± 0.48	3.55 ± 0.41
Fracture Strain %	50.15 ± 6.34	53.23 ± 4.14	55.36 ± 4.05

6.4.4 SEM

Hydrogels containing 150 nm VSNP were freeze dried and investigated under SEM. Figure 69 shows solid structures infused with silica nanoparticles. Figure 69 (a) shows a structure that makes up a pore in the hydrogel, indicating that silica nanoparticles are well integrated into arrangements that could increase the resistance to strain. Figure 69 (b) shows a cross section of the hydrogel, revealing silica nanoparticles are part of the integral walls of the hydrogel. This distribution suggests an even distribution with less agglomeration with in the material, although TGA results discussed previously indicated relatively high losses post swelling. Ultimately, it can be concluded that vital cross linking structures remain in the hydrogel, whereas non-cross linked structures are washed out.

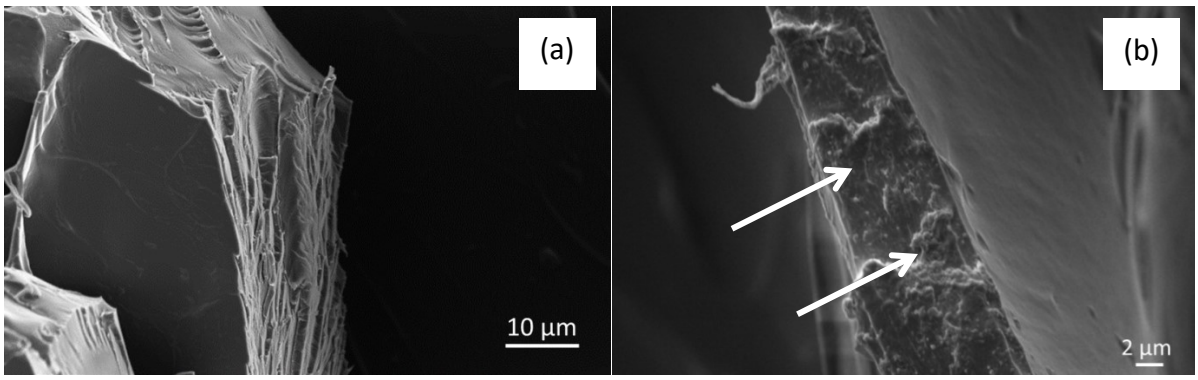


Figure 69 - SEM images of PAMPS/PAAm hydrogels with 150 nm vinyl silica nanoparticles (VSNPs). VSNPs are highlighted with white arrows.

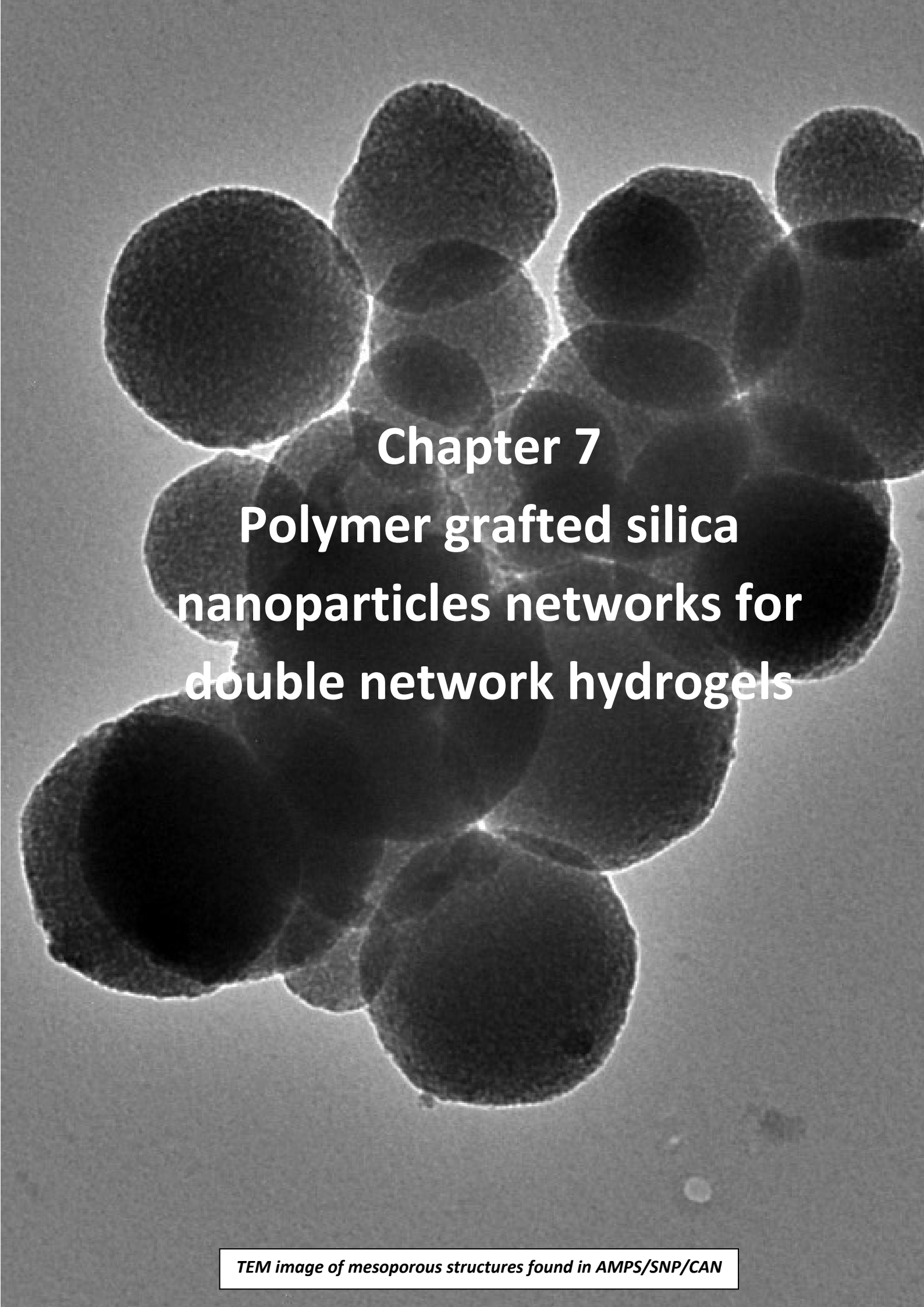
6.5 Conclusion

PAAm and PAMPS polymers were successfully synthesized through open vessel FRP at 100 % conversion with faster and improved kinetics in the presence of GOx compared to controls without GOx. The results prove that PAAm and PAMPS can be synthesized using low concentrations of photoinitiator that result in non-cytotoxic polymers, once

GOx is denatured using heat treatment. Strong indications from swelling profiles suggesting more rigid and tightly cross linked networks were made due to the significant change in water uptake. Chapter 5 showed an average of 95 % water content in the hydrogels whereas the addition of GOx has brought that down to 67 %, a value closer to native cartilage[197]. Reduced volumes of water mean less internal pressures on the material walls caused by swelling. This in turn gives the material the chance to sustain larger stresses and sustain stronger strains. Ultimately, this was proven with improved mechanical properties due GOx causing full conversion of monomers leading to more homogenous hydrogels, and tighter cross linking. Polymer interactions and entanglements were also likely increased due to higher conversion and better control over PDI. The material therefore acts in a more synergetic manner, as it was intended. Higher losses of nanoparticles were noted through TGA as a result of nanoparticle losses during synthesis and swelling, highlighting the need for improvement in nanoparticle retention.

Next chapter

In the previous chapters, polymers in the first network were cross linked by silica nanoparticles to create a tightly cross linked hydrogel. The next chapter looks at a different approach where polymerization occurs from the surface of nanoparticles to create stronger cross links and physical entanglements. This can ensure less nanoparticle loss during swelling and potentially a stronger first network. The enhanced properties through the addition of GOx will also be utilised in the following chapter, to ensure the highest conversion is achieved.



Chapter 7
Polymer grafted silica nanoparticles networks for double network hydrogels

TEM image of mesoporous structures found in AMPS/SNP/CAN

7 Polymer grafts silica nanoparticle networks for double network hydrogels

7.1 Introduction

The previous chapters have explored the effect of nanoparticle size and loading density in the first network of double network hydrogels. Enhanced kinetics and conversion profiles for PAMPS and PAAm were also achieved through the use of GOx, as an effective degassing agent. Low nanoparticle retention in the hydrogels was revealed through TGA, which meant many of the nanoparticles were aggregating without creating cross links and being washed out, or lost during synthesis.

Therefore, an alternative method was adopted in this chapter to redevelop the polymeric nanocomposite networks, with the aim of improving the mechanical properties and reducing nanoparticle losses. The surface of silica nanoparticles would be the building block for the polymers. In this case, PAMPS and PAAm would 'grow' from the surface of the silica nanoparticles to form hydrogels. The surface-initiated graft polymerizations will use Ce (IV) based redox initiators to form polymers on the surface of amine functionalised silica nanoparticles[149, 198]. The reactions would take place under inter conditions through argon degassing due to the sensitive nature of thermal redox initiated polymerizations. A comparison study will be conducted to compare the effect of GOx degassing in such a system, as the reaction temperature will be 40 °C which will still suited for the enzyme to be used.

7.2 Methods and materials

7.2.1 Materials

Acrylamide (AAm; ≥ 99 %) and 2-acrylamido-2-methyl-1-propanesulfonic acid (AMPS; 99 %); N, N'-methylenebisacrylamide (BIS; 99 %); photoinitiator 2-hydroxy-4'-(2-hydroxyethoxy)-2-methylpropiophenone (synonym Irgacure 2959; 98 %), 1, 3, 5 –trioxane (≥ 99 %); (3-aminopropyl) triethoxysilane (APTES; ≥ 98 %), deuterium oxide (D2O; 99.9 atom % D), cerium(IV) ammonium nitrate (CAN; ≥ 99.99 % trace metals basis), sodium dodecyl sulfate (SDS; ≥ 98.5 %) were purchased from Sigma-Aldrich (UK). No additional processing and/or purifications were performed. D-glucose (G) and glucose oxidase (GOx; from aspergillus niger as a lyophilized powder) were purchased from Sigma-Aldrich (UK) and stored in phosphate buffer saline (PBS) aliquots at -20 °C when received.

7.2.2 Methods

7.2.2.1 Aminated silica nanoparticles

Amine functionalised silica nanoparticle (ASNPs) were synthesized as described in section 4.2.2.1.

7.2.2.2 Polymer grafts on silica nanoparticles

150 mg amine ASNP were dispersed in 5 ml of water and sonicated for an hour until fully dispersed. 5 mg of trioxane and 4.5 g AMPS were dissolved in 35 ml deionized H_2O in a round bottom flask until the solution was clear. Dispersed ASNP were then added to the monomer solution and mixed for 5 minutes. A 20 µl sample was taken as 0 h

reference and topped up with 0.5 ml D_2O in a ^1H NMR tube to calculate polymer conversion. The solution was then degassed for 20 minutes with argon gas while mixing at 40 °C in a paraffin bath. The reaction was stopped at 24 h and a 20 µl sample was taken for ^1H NMR. The content of the round bottom flask was centrifuged using the Eppendorf 5430 at 7,380 rpm then washed twice and then dried at 40 °C. The process was repeated a second time with CAN 0.7 g being added to the monomer solution, and a third time with CAN 0.7 g with 1.5 g SDS being added to the monomer solution.

The same process was repeated for AAm under the same conditions. A chemical schematic is shown in Figure 70.

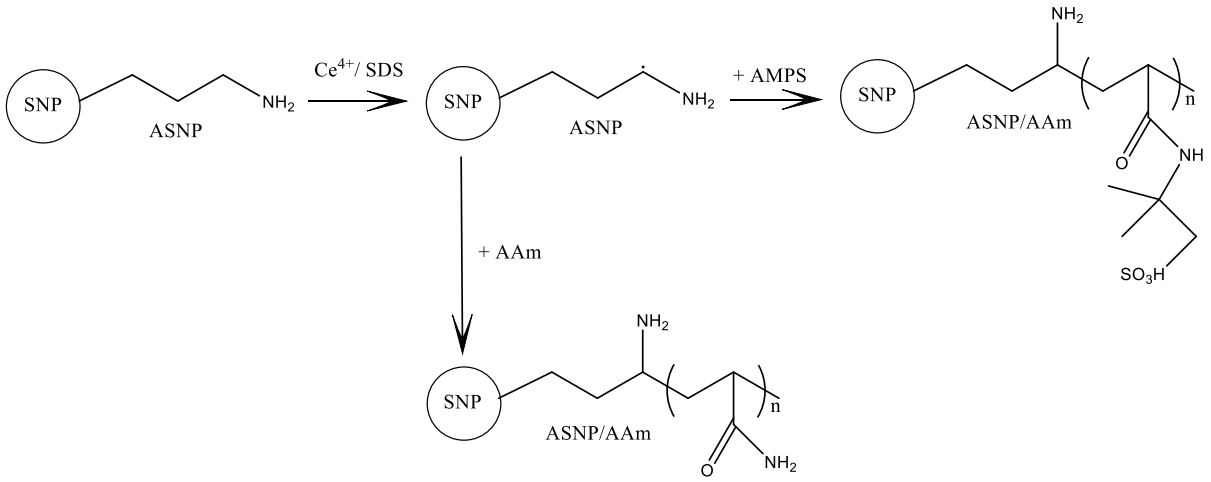


Figure 70 – Grafting AMPS and AAm on the surface of amine functionalized SNP via CAN and SDS.

7.2.2.3 Polymer grafts in the presence of GOx

5 mg of trioxane and 4.5 g AMPS were dissolved in deionized H_2O and titrated to 5.4 pH using NaOH (0.25 M), then topped up to 35 ml with deionized H_2O with a final concentration of 0.24 M AMPS. 150 mg ASNP was dispersed in 5 ml H_2O and sonicated for an hour then added to the monomer solution. GOx/G was added at a final

concentration of 200 nM. The solution was transferred to a round bottom flask and the process continued as described above. Repeats were also done to include CAN, and CAN/SDS.

The same process was repeated, without titration, for AAm.

7.2.2.4 Hydrogel synthesis

The first network was formed by dispersing 150 mg of ASNP in 5 ml H_2O and sonicating the mixture until it was fully dispersed. 4.5 g AMPS was titrated to 5.4 pH using NaOH (0.25 M), to a final concentration of 0.24 M AMPS. ANC was then added to the AMPS monomer solution. 1 wt % BIS and 200 nM GOx/G were added to the monomer/ASNP solution and mixed for 5 minutes. The solution was then put into aliquots of 2 ml in polystyrene moulds and placed in a sonication bath set to 40 °C to ensure homogenous ASNP distribution. Once the solutions in the moulds have gelled, the moulds were placed in an oven at 40 °C for 24 h followed by a further 6 h at 60 °C to denature GOx.

The hydrogels were removed from the moulds and soaked in a monomer solution of 2.54 M AAm containing 150 mg ASNP, 0.1 wt % BIS and GOx/G. Once the hydrogels were swollen, they were placed in moulds and put into a 40 °C oven to form the second network. The final hydrogels were then dried at 60 °C and, at their dry state, placed in water to swell for a week. Figure 71 shows a schematic representation of the hydrogel synthesis route described above.

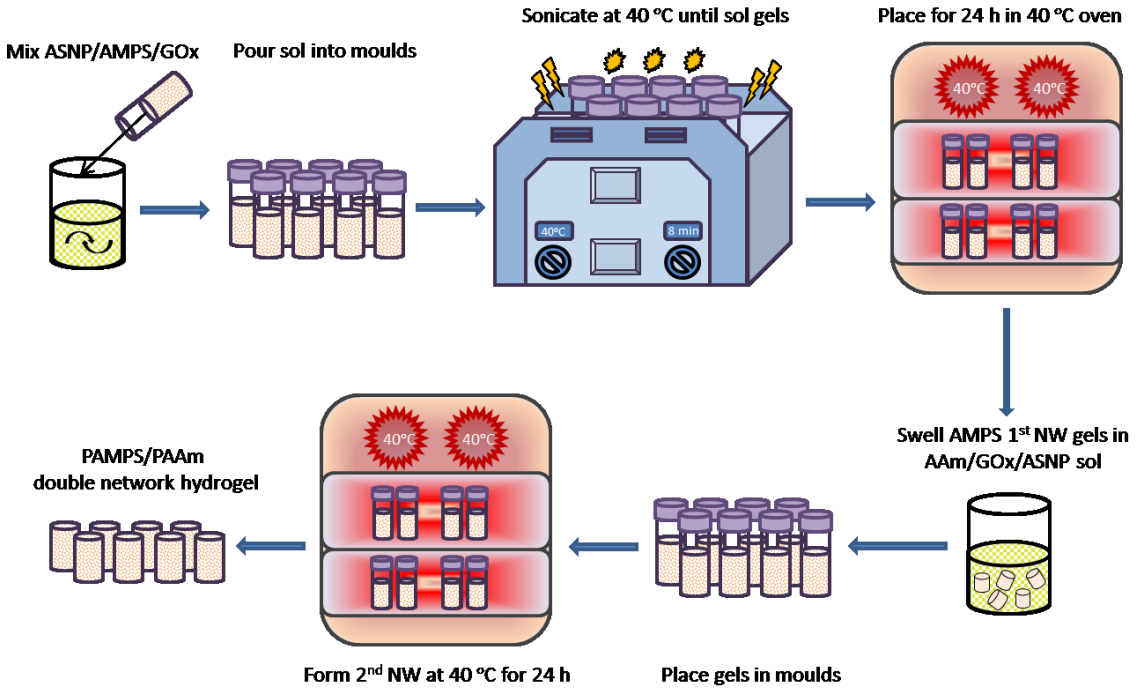


Figure 71 – Schematic representation showing the synthesis route for double network hydrogels (DNHG) containing silica nanoparticle (SNP).

7.3 Results and discussion

7.3.1 UV-Vis

UV-Vis was used to confirm surface modification of the silica nanoparticles through graft polymerization. Argon degassed samples were used to confirm the success of the reaction. All samples were prepared from a dry powder state and redisposed in deionised water at 4 mg ml^{-1}, followed by sonication. All absorbance curves were normalised by their highest number to 1.

Amine SNP had higher absorbance compared to bare SNP, as seen in Figure 72. A wide range of absorbance was seen at 190 nm to 500 nm without any distinguishable peaks.

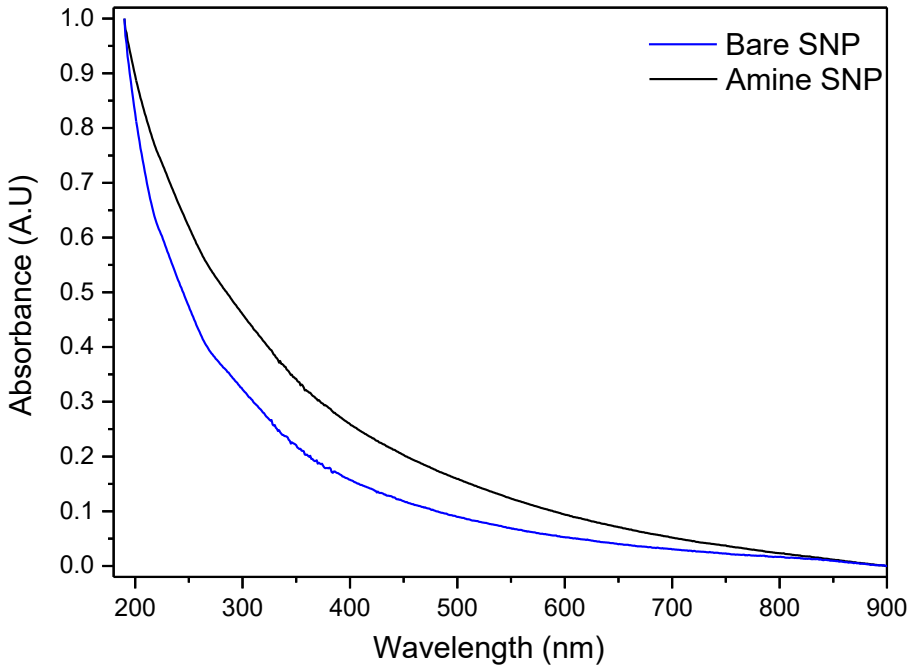


Figure 72 – UV-Vis of bare and amine silica nanoparticles (SNP).

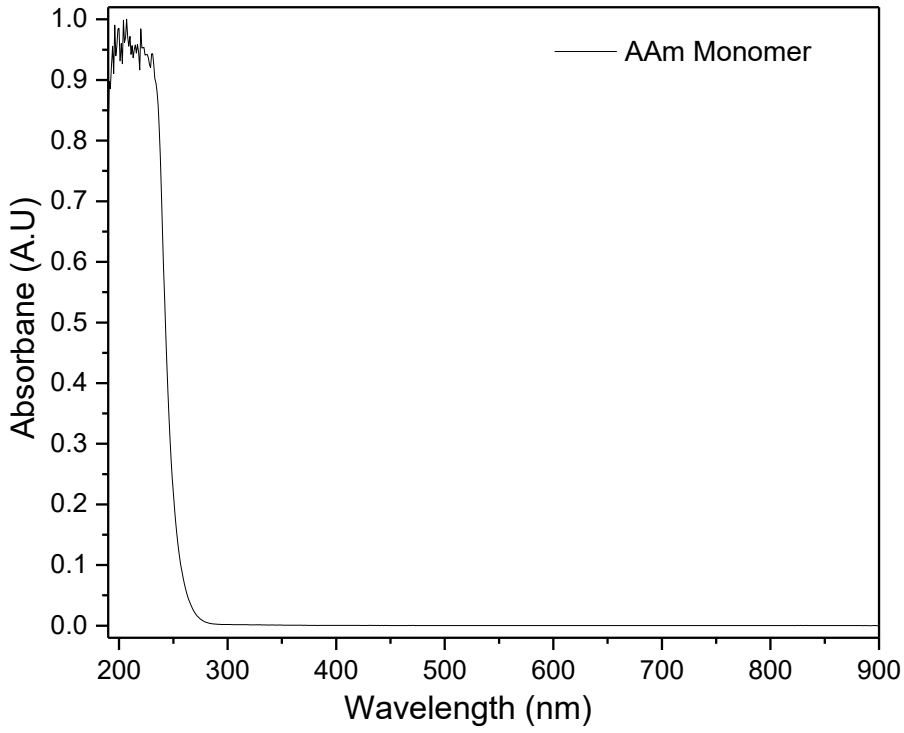


Figure 73 – UV-Vis of AAm monomer.

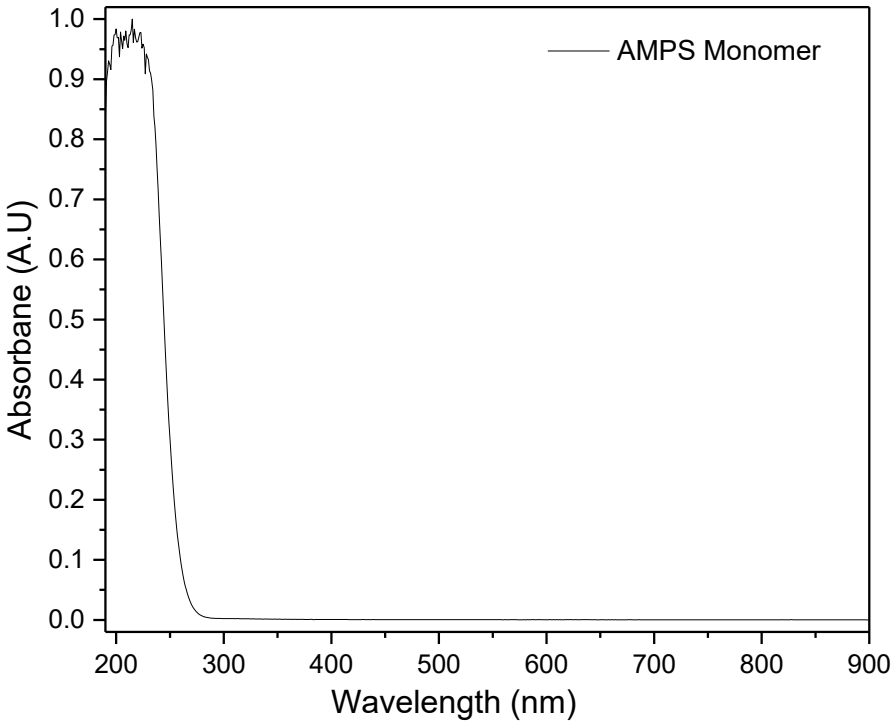


Figure 74 – UV-Vis of AMPS monomer.

AMPS/ SNP absorbance spectra, Figure 75, revealed that a reaction had taken place on the nanoparticles, although it was unexpected as the initiator was not present. The reduced absorbance for SNP in the AMPS/SNP suggests the nanoparticles were covered in polymer, though the peak at 190 nm was very subtle. AMPS/SNP/CAN spectra revealed graft polymerization was successful. The addition of SDS also revealed successful polymerization, with a peak at 220 nm – 260 nm suggesting SDS was still present in the sample.

These results indicate that grafting PAMPS on the surface of silica nanoparticles was successful.

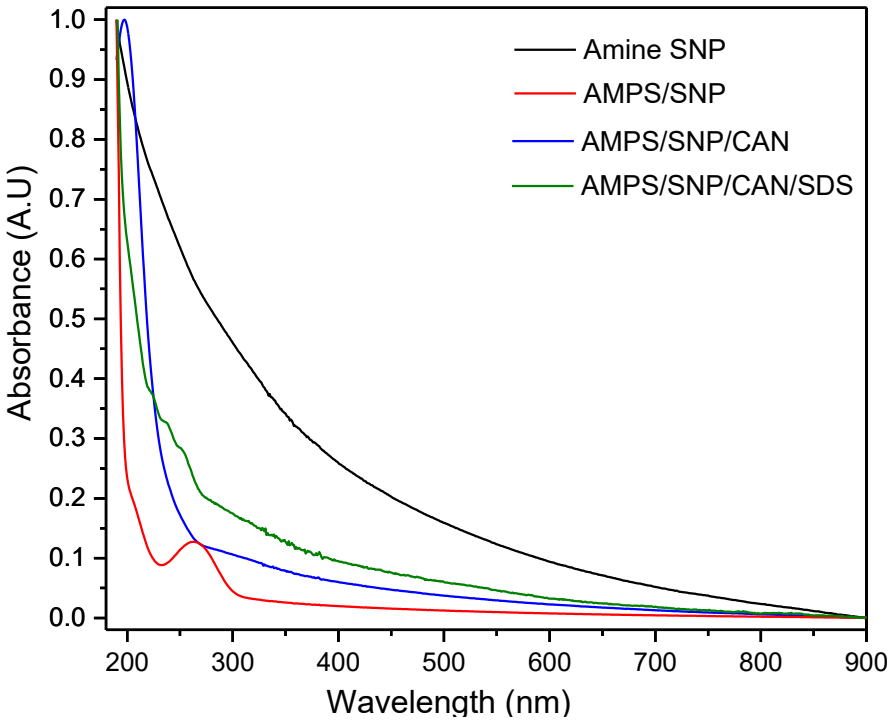


Figure 75 – UV-Vis of AMPS in combination with SNP, SNP/CAN, and SNP/CAN/SDS compared to amine SNP.

Figure 76 shows polymer grafts were successfully grafted on silica nanoparticles, with polymer peaks visible between 190 nm and 250 nm. Unexpectedly, AAm/SNP spectra showed successful polymer grafts although the reaction mechanism suggests no reaction should take place on the surface. SDS can also be seen between 220 nm – 260 nm, due to the difficulty in removing the stabiliser from end product. The strongest polymer peak with a reduced SNP peak was noted for AAm/SNP/CAN. This suggests a thick layer of polymer were grafted on the surface of the SNP.

These results provide an indication that the polymerization technique was successful. Surface chemistry and bonds were explored next to confirm the changes made to the nanoparticles, using FTIR.

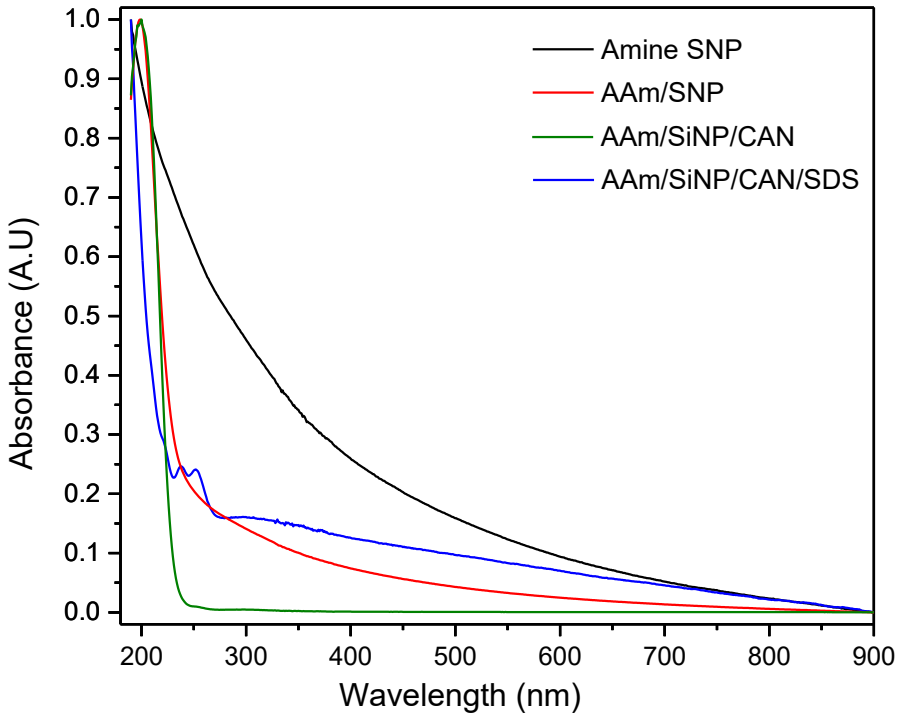


Figure 76 – UV-Vis of AAm in combination with SNP, SNP/CAN, and SNP/CAN/SDS compared to amine SNP.

7.3.2 FTIR

FTIR was used to reconfirm surface modification of the nanoparticles by graft polymerization of PAMPS and PAAm, under argon degassing. Samples were ground to a fine powder and dried at 60 °C prior to analysis.

Figure 77 shows the FTIR results for the combinations of PAAm with SNP, CAN and SDS compared to amine SNP and PAAm by itself. Table 31 provides a summary with the main bands associated with the AAm grafted polymers on the surface of amine SNPs. AAm/SNP showed no presence of polymer bands in the FTIR spectra, contrary to the UV-Vis result for the same sample. It is likely that UV-Vis was able to detect a thin layer on the surface of the SNP that was likely not covalent bonded. Ultimately, FTIR suggests that AAm/SNP did not result in any graft polymers on the surface. This follows the logic expected as there is no initiating chemical present to start the polymerization between AAm/SNP. The AAm/SNP/CAN spectrum shows clear polymer bands that reflect the

PAAm polymer spectra. Bands between 1620 cm^{-1} – 1659 cm^{-1} confirm the presence of N-H and C=O bonds from PAAm. 950 cm^{-1} and 1050 cm^{-1} correspond to Si-OH and Si-O-Si, respectively, which represent SNPs. Similar bands were seen with less intensity for AAm/SNP/CAN/SDS, with an additional bi-peak between 2850 cm^{-1} – 2956 cm^{-1} that represents the C-H stretching found from residual SDS[199]. SDS could not be removed from the system after several wash and centrifuge cycles. These results align with data from the UV-Vis spectra. Ultimately, FTIR suggests the best combination for grafting AAM on SNPs is with CAN alone due to evident polymer bands.

Table 31 – Summary of FTIR bands for AAm grafted polymers on amine silica nanoparticles (SNPs)

	Bond	Type	Wavenumber (cm^{-1})
A	C-H	Stretching	2956 2918 2850
B	C=O	Stretching, coupled with N-H bending	1652-1659
C	N-H	Primary amine	1620
D	CH_2	Bending	1467
E	C-H	Deformation	1350
F	N-H	Bending	1238
G	Si-O-Si	Asymmetric stretching	1050
H	Si-OH	Stretching	950
I	Si-O-Si	Bending	800
J	S-O-Si	Bending	440

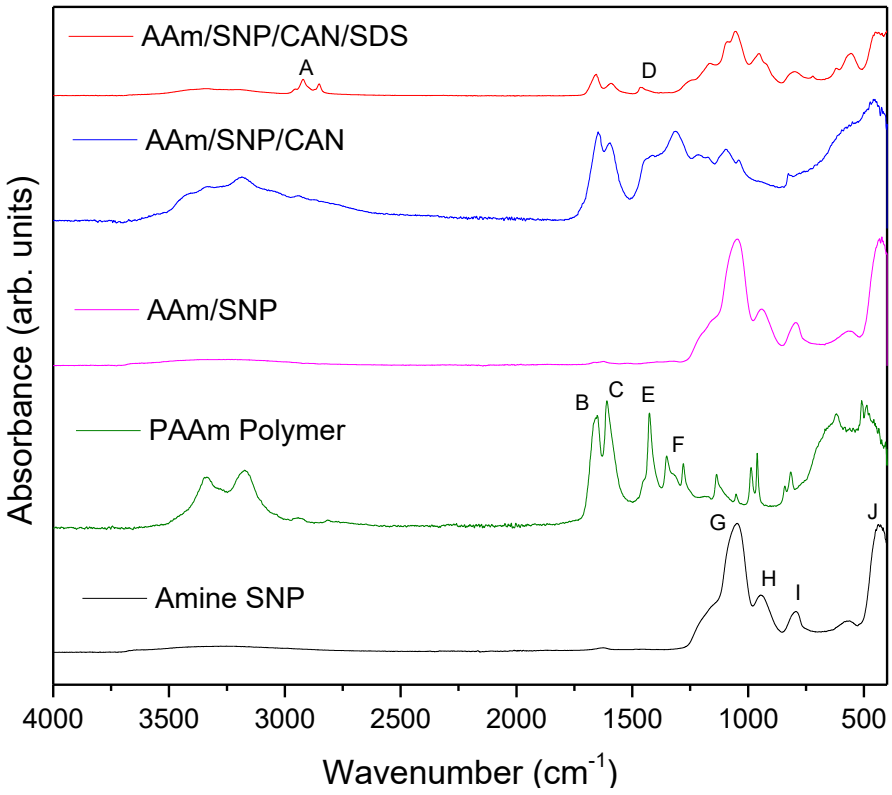


Figure 77 – FTIR spectra post graft polymerization of AAm onto amine silica nanoparticles (ASNP) compared to ASNPs and PAAm.

Figure 78 shows the spectra of AMPS in combination with SNP, CAN and SDS, compared to amine SNP and PAMPS polymer. Table 32 provides a summary of the main bands associated with AMPS grafted polymers on the surface of amine SNPs. AMPS/SNP from UV-Vis suggested polymer growth had occurred on the surface of the SNP. This was confirmed by FTIR where a reduction in the Si-O-Si and Si-OH peaks could be seen, and bands appearing at 1620 cm^{-1} and 1647 cm^{-1} representing N-H deformations for primary amide groups from AMPS. As discussed earlier, this was unexpected due to the lack of an initiating system between AMPS/SNP. AMPS/SNP/CAN shows a more predominant polymer profile imposed on an SNP profile, suggesting higher amounts of PAMPS are present on the nanoparticles. The presence of R–S(=O)–R' groups at 1040 cm^{-1} confirm the presence of AMPS, for all reaction spectrums. Finally, AMPS/SNP/CAN/SDS shows strong polymer bands suggesting growth was also present in the sample. Residual SDS was found between 2850 cm^{-1} – 2956 cm^{-1} showing C-H stretching[199]. This confirmed

the presence of SDS that could not be removed post synthesis after several wash/ centrifuge cycles. This confirms the results obtained from UV-Vis. Quantification of the polymer conversion and mass grafted will be discussed next.

Table 32 - Summary of FTIR bands for AAm grafted polymers on amine silica nanoparticles (SNPs)

	Bond	Type	Wavenumber (cm^{-1})
A	C-H	Stretching	2956 2918 2850
B	C=O	Stretching, coupled with N-H bending	1652-1659
C	N-H	Primary amine	1620
D	CH_2	Bending	1467
E	N-H	Bending	1238
F	R–S(=O)–R'		1040
G	Si-O-Si	Asymmetric stretching	1050
H	Si-OH	Stretching	950
I	Si-O-Si	Bending	800
J	S-O-Si	Bending	440

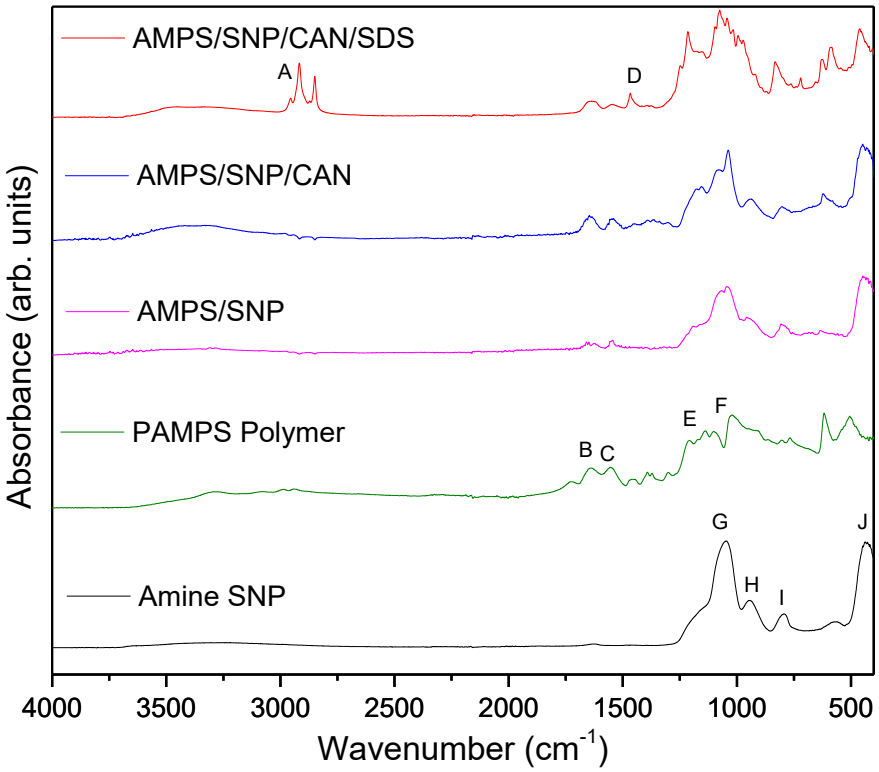


Figure 78 – FTIR spectra post graft polymerization of AMPS onto amine silica nanoparticles (ASNP) compared to ASNPs and PAMPS.

7.3.3 TGA

Samples were dried and ground to a powder for thermal analysis. Figure 79 shows the mass loss and DTG profiles for AAm based reactions. AAm/SNP exhibited approximately 1.5 % higher mass loss than SNP and ASNP, suggesting very low polymer grafting on the SNP surface. The slight increase in mass loss for AAm/SNP, and a monomer peak in DTG, could be due to a thin monomer monolayer, as UV-Vis spectra revealed a modification in surface chemistry. The highest mass loss was seen with AAm/SNP/CAN samples. This was expected as silica nanoparticles don't have the chemical ability to form radicals and initiate the polymerization. CAN was successful at initiating the polymerization on the surface of the ASN, as seen in the two sharp DTG peaks for AAm/SNP/CAN at 250 °C and 420 °C. The reaction including SDS showed a prolonged polymer loss with a distinctive DTG peak at 210 °C. This indicates that although polymer formation had occurred on

the surface, there was still residual SDS that could not be removed after washing and centrifuging the sample. Ultimately, the best combination was found to be using AAm/SNP/CAN.

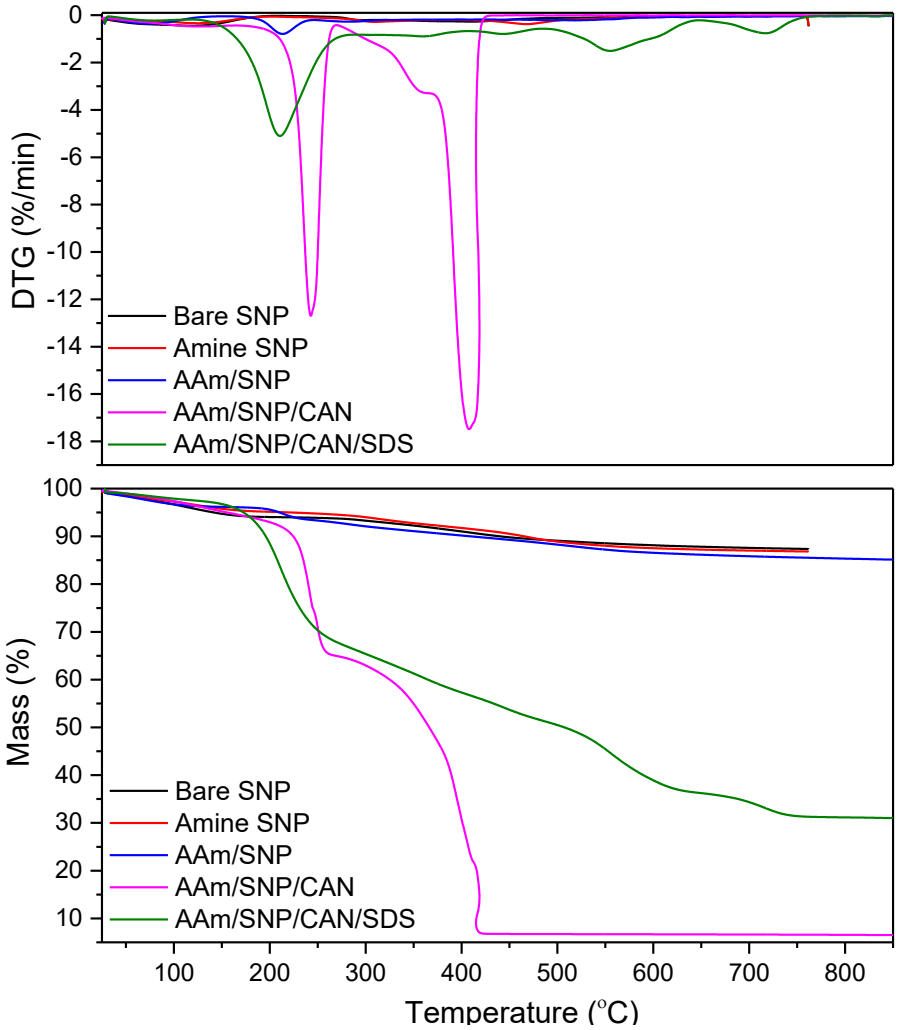


Figure 79 – TGA and DTG profiles for AAm graft polymerizations compared to bare and amine silica nanoparticles (ASNP).

DTG for AMPS/SNP revealed prominent polymer peaks and a mass loss of approximately 12.5 % highly suggestive of polymer grafts forming on the surface of the nanoparticles, Figure 80. As with the case of AAm, silica nanoparticles are unable to initiate PAMPS polymer formation although results from UV-Vis and FTIR indicated

PAMPS polymer growth had occurred. This confirms the presence of polymer growth in the AMPS/SNP samples. The sample containing SDS proves polymers were grafted on the surface through the presence of polymer DTG peaks although a strong peak for SDS was also present. This suggets SDS was not completely washed from the sample even after several washes. This confirms results from UV-Vis and FTIR on the residual SDS that is left in the system. The best result was found with AMPS/SNP/CAN, similarly to AAm, showing strong DTG polymer peaks and the largest mass loss based on polymer formation.

TGA data provides an indication on the mass polymer formation and residuals on the surface of the nanoparticles but is not indicative of polymer conversion in the system. Therefore ^{1}H NMR was conducted on all samples to calculate polymer conversion of the *in-situ* system.

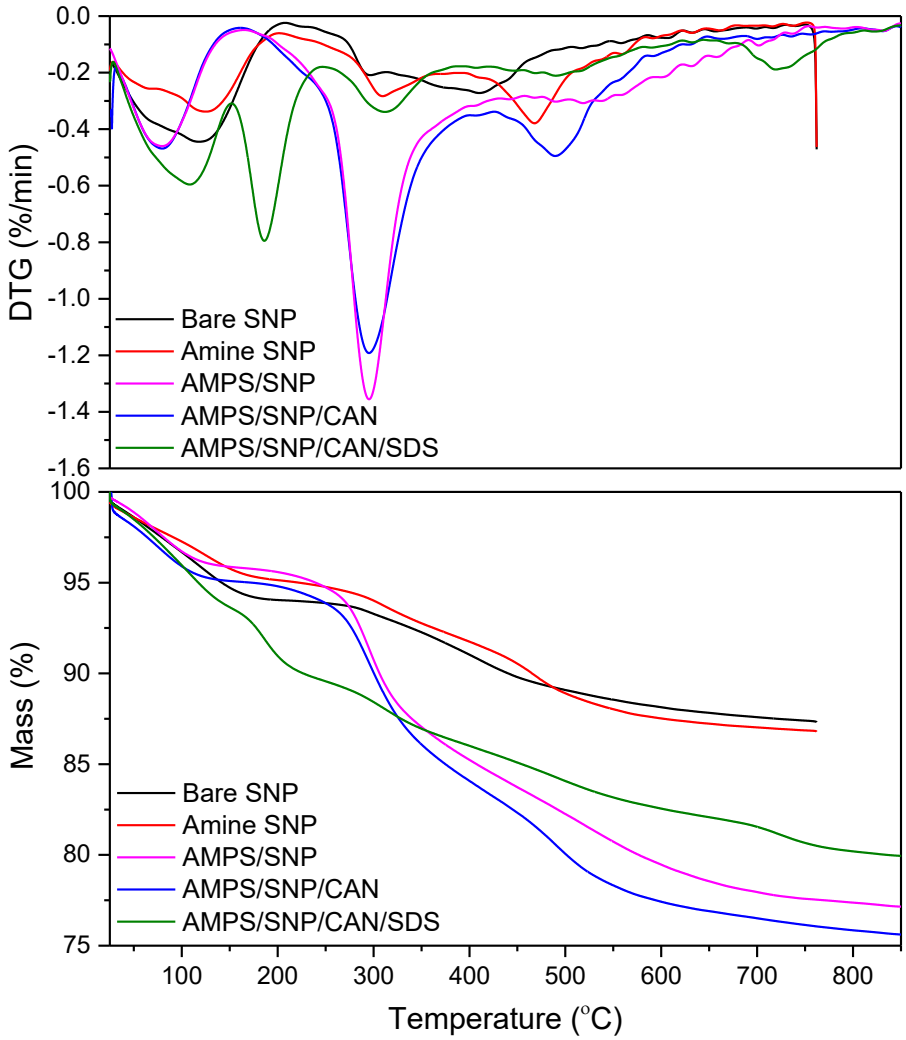


Figure 80 – TGA and DTG profiles for AMPS graft polymerizations compared to bare and amine silica nanoparticles (ASNP).

7.3.4 TEM

Samples were studied under TEM to examine the formation of polymer growth on the surface of silica nanoparticles. Figure 81 (a) and (b) show the formation of PAMPS polymeric masses surrounding silica nanoparticles. This reaffirms that the introduction of CAN is necessary to initiate the polymerization on the surface of the nanoparticles. TEM for silica nanoparticles with AMPS, without CAN, revealed a general dispersion of nanoparticles with no significant masses or change in formation to be detected.

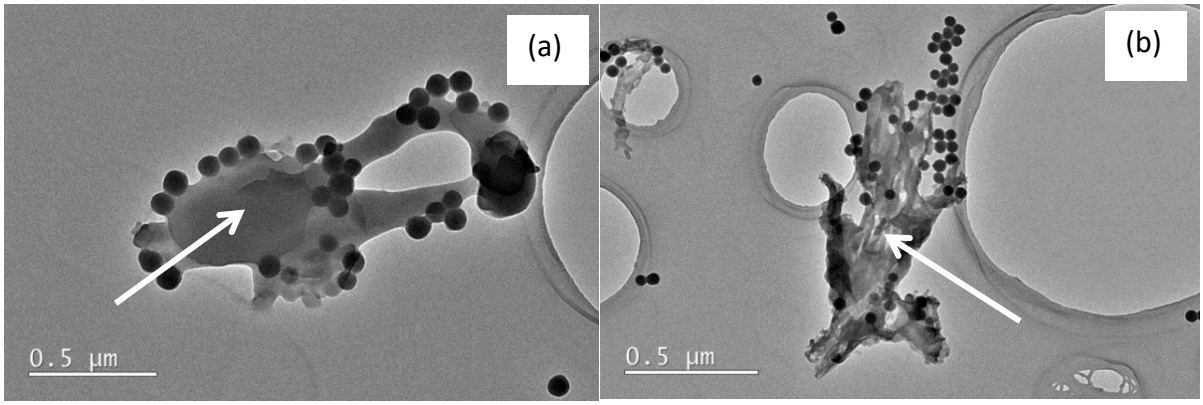


Figure 81 – TEM images of an AMPS/ amine silica nanoparticles (ASNP)/CAN sample, showing polymeric mass surrounding ASNPs, highlighted with white arrows.

Samples with AAm were also examined, revealing similar polymeric masses as Figure 81 (a) and (b), and no evidence of any significant polymeric growth in samples with AAm and silica nanoparticles alone. An interesting finding was observed for samples with AAm/SNP/CAN/SDS, Figure 82 (a) and (b). Spherical structures initially thought to be silica nanoparticles were seen, but due to their structure and larger sizes were subject to closer examination. Upon magnification, it was revealed that organized one-directional porous nanoparticles had been synthesised in the sample. These nanoparticles are assumed to be made of silica and have been synthesised serendipitously. Their presence was reconfirmed by resynthesizing the same sample and examining it under TEM. The presence of SDS within the sample likely contributed to the synthesis of the organised porous structure. SDS was used as a stabilizer in this system[198], although SDS also possesses the ability to act as a surfactant for mesoporous silica nanoparticle synthesis[200].

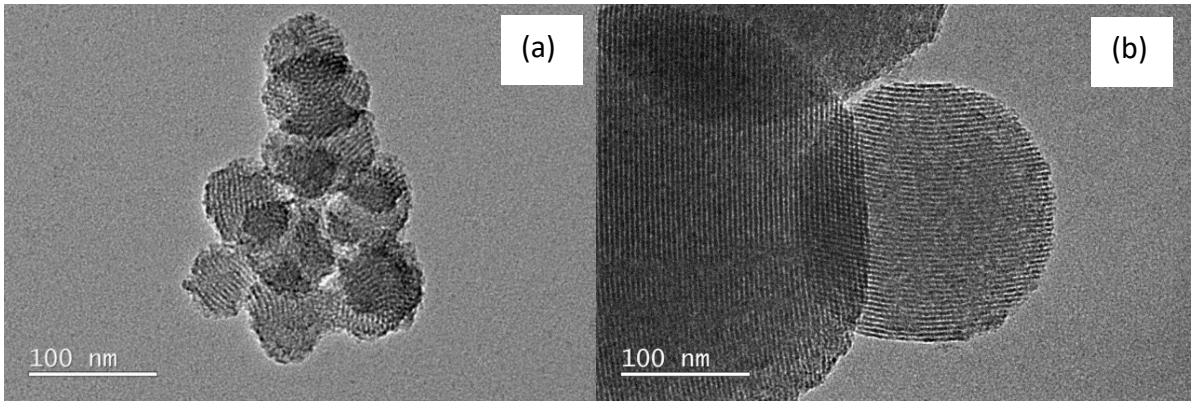


Figure 82 – TEM images of an AAm/ amine silica nanoparticles (ASNP)/CAN/SDS sample.

7.3.5 Polymer conversion

PAMPS and PAAm conversion profiles were explored under argon and GOx systems using ^{1}H NMR based on trioxane peaks at 0 h and 24 h samples. A control sample was run using the monomers with CAN to understand how effective the polymerization was without the presence of SNP, or SDS. Figure 83 compares the conversion percentage of AAm and AMPS, respectively, with both argon and GOx degassing.

Figure 83 shows that all results proved GOx had higher conversion percentage compared to argon degassing. This reflects the findings in Chapter 6 that showed GOx stops oxygen inhibition of free radicals reacting with the monomers in solution. An interesting finding was AAm/SNP with argon only had 1 % conversion, whereas with GOx an increase to 58 % conversion was witnessed. A possible explanation for this is that H_2O_2, a by-product of GOx/G, plays a part in initiating the polymerization. This can occur during the formation of and its subsequent degradation back to water where peroxy radicals may form, potentially initiating the polymerization. This was also evident for AMPS/SNP in Figure 83. Monomers were reacted with CAN alone; resulting in 85 % with argon and 94 % with GOx, for AAm, suggesting CAN is effective creating PAAm. The results for AMPS/CAN were less notable, with only 57 % with argon and 66 % with GOx. Conversion percentage decreased with the addition of SNP to the system, but reached 98 % and 100 % with the use of SDS for AAm and AMPS, respectively.

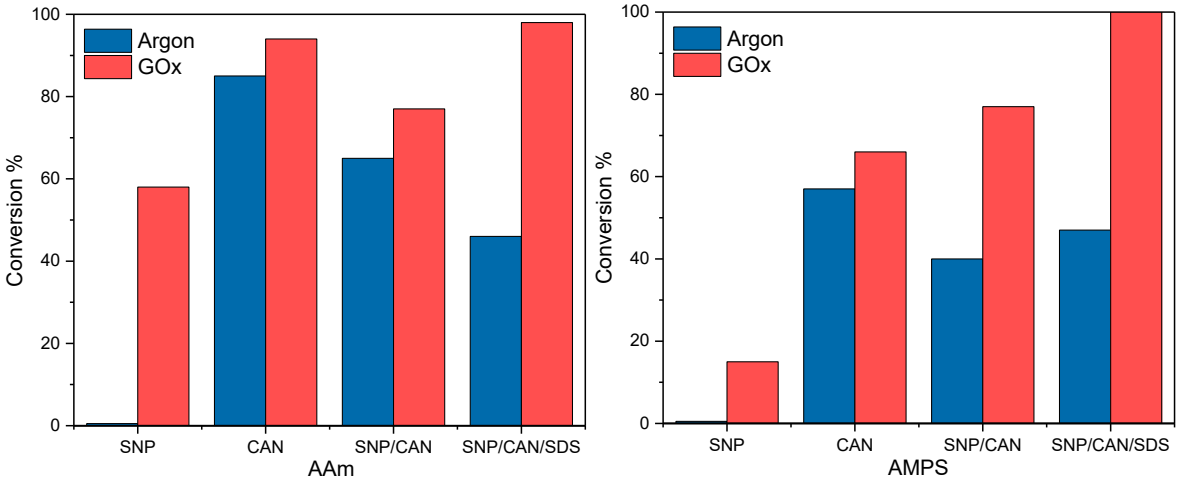


Figure 83 – Conversion profile of AAm (left) and AMPS (right) with argon and GOx.

7.3.6 Hydrogels

DNHGs were successfully synthesised in a two-step sequential thermal graft polymerization. PAMPS were grafted on the surface of ASNPs with CAN as an initiator, in the presence of GOx, to form the first network hydrogel. Upon gelation, the first network hydrogel was swollen in a monomer solution of AAm and ASNPs with CAN as the initiator, in the presence of GOx, and reacted to form a double network at 40 °C. Samples were then swollen in water at room temperature until a mass plateau was achieved, and subsequently subjected to compression studies.

Residual monomer and ASNPs were found during synthesis, specifically during swelling of the second network (AAm) in the PAMPS/ANC gel. This suggests that the hydrogels synthesised may differ in properties according to how much monomer and ASNPs were lost during synthesis. Ultimately, this was expected to impact swelling ability of the ASNP gels, as well as their mechanical properties.

7.3.7 Swelling studies

ASNP hydrogels were swollen in deionised water from a dried state until a plateau in water content was reached. Figure 84 shows the swelling profile over time for the ASNP gels. The ASNP gels exhibited fast water up take of approximately 19 % at 1 h, followed by a more gradual and controlled trend to reach an average of 63.44 ± 1.76 % at 240 h. The final swelling value was 274 ± 9.21 %. The swelling profile of ASNP gels was lower in comparison to Chapter 6 Section 6.4.1 which saw water content ≥ 65 %, and chapter 5 ≥ 1160 %. This is largely due to the presence of ASNPs in both polymer networks. The presence of ASNPs reduces the free space for water uptake due to tighter cross linking by not allowing the DNHG to expand as freely. Also, ASNPs in both networks take up more space in the material as opposed to having one network cross linked via nanoparticles. Ultimately, this resulted in a slower and more controlled swelling profile containing less water. These water content values are considered in the lower range of the water content found in native articular cartilage (70 %).

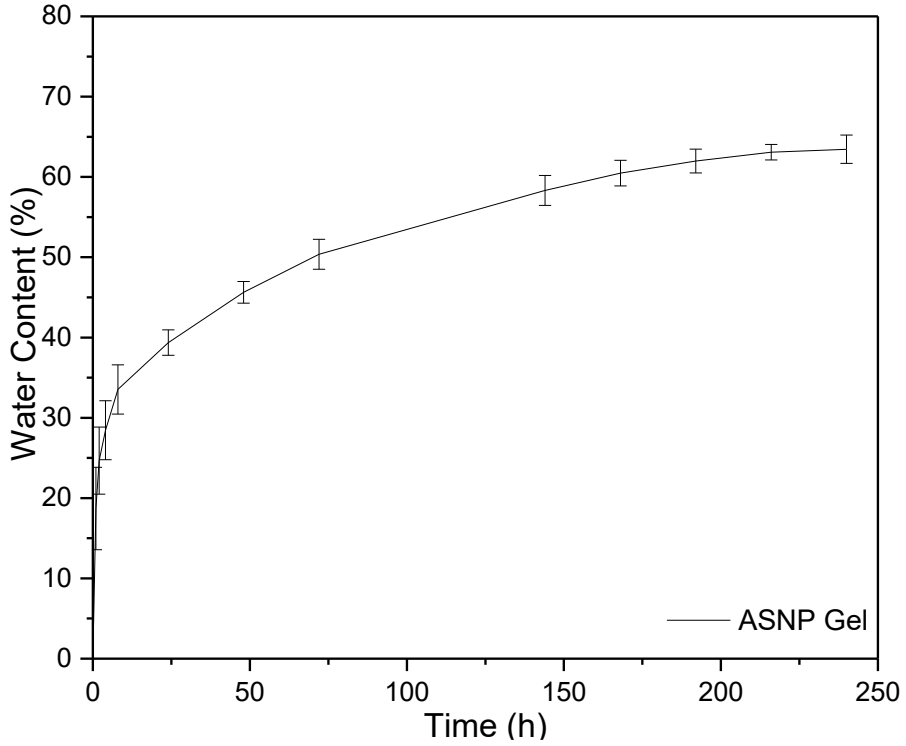


Figure 84 - Swelling profile for the amine silica nanoparticle (ASNP) hydrogel with PAMPS and PAAm polymer grafts.

Table 33 - Swelling and water content for the amine silica nanoparticle (ASNP) hydrogel with PAMPS and PAAm polymer grafts.

	ASNP Gel
Water Content (%)	63.44 % ± 1.76
Swelling (%)	274 % ± 9.31

7.3.8 Mechanical testing

ASNP gels were tested under compression after swelling. Due to the difficulty in achieving homogenous distribution of ASNPs in both networks during synthesis, samples were expected to have a range of mechanical properties. Results from the swelling studies also suggested mechanical properties may vary as water uptake exhibited a high standard deviation.



Figure 85 - Images of a double network amine silica nanoparticles (ASNP) hydrogel with PAMPS and PAAm polymer grafts under compression at different strains.

Figure 86 shows the compression curves for ASNP gels, and Table 34 provides a summary of the results. An average compressive stress of 13.9 ± 5.5 MPa with fracture strain of 69.6 ± 6.4 % was achieved for ASNP gels, greater than the DNHGs synthesised in the previous chapters. The values for these hydrogels are comparable to the compressive strength of articular cartilage, with values ranging between 5 MPa and 20 MPa. The variation exhibited in the properties of the ASNP gels, however, are due to inherent difficulty in the synthesis route. As discussed earlier, AAm monomers and ASNPs are not fully swollen within the first network. The residual AAm monomers and ASNPs therefore dictate the difference in properties seen in the swelling studies and compressive strength. Nonetheless, the improved compressive strength relative to the previous chapters was attributed to the covalently bonded polymer grafts on the surface of the ASNPs. This was in contrast to the method of cross linking loose polymers with ASNPs. The ASNP gels sustained strains up to 75 %, likely due to the internal structure of material. The polymers on the surface of the ASNPs are likely to interact and cross link with neighbouring polymer-ASNP structures, leading to an increase in resistance to stress. This will increase the compressive strength and allow the material to resist larger strains, as witnessed in the strain values in Table 34. Ultimately, graft polymerization proved to produce better properties for DNHGs, although synthesis optimization is required to create homogenous hydrogels with consistent results. The deviations in compressive strength suggest that this type of hydrogel is highly tailorable, depending on the concentration and efficiency of integrating the two polymer-ASNP grafted networks.

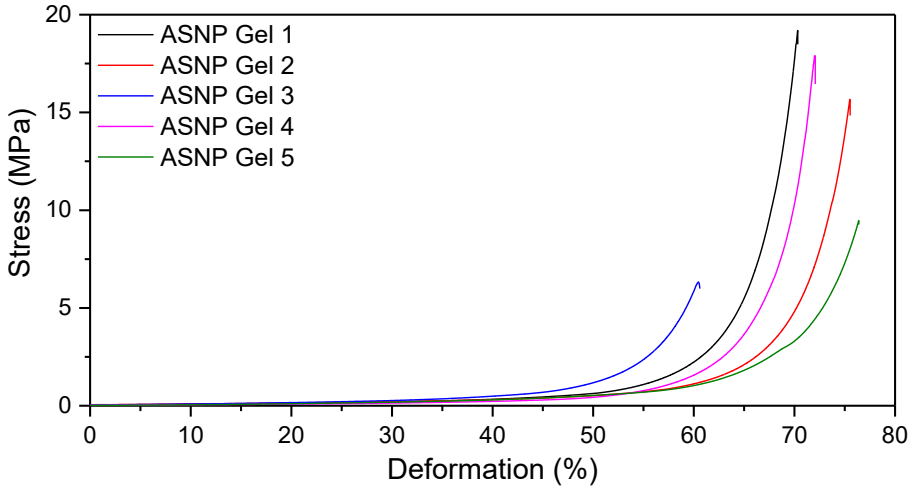


Figure 86 - Compression curves for the amine silica nanoparticle (ASNP) hydrogel with PAMPS and PAAm polymer grafts.

Table 34 - Fracture stress and strain for amine silica nanoparticle (ASNP) gels with PAMPS and PAAm polymer grafts.

	ASNP Gel
Fracture Compressive Stress (MPa)	13.9 ± 5.5
Fracture Strain (%)	69.6 ± 6.4

7.4 Conclusion

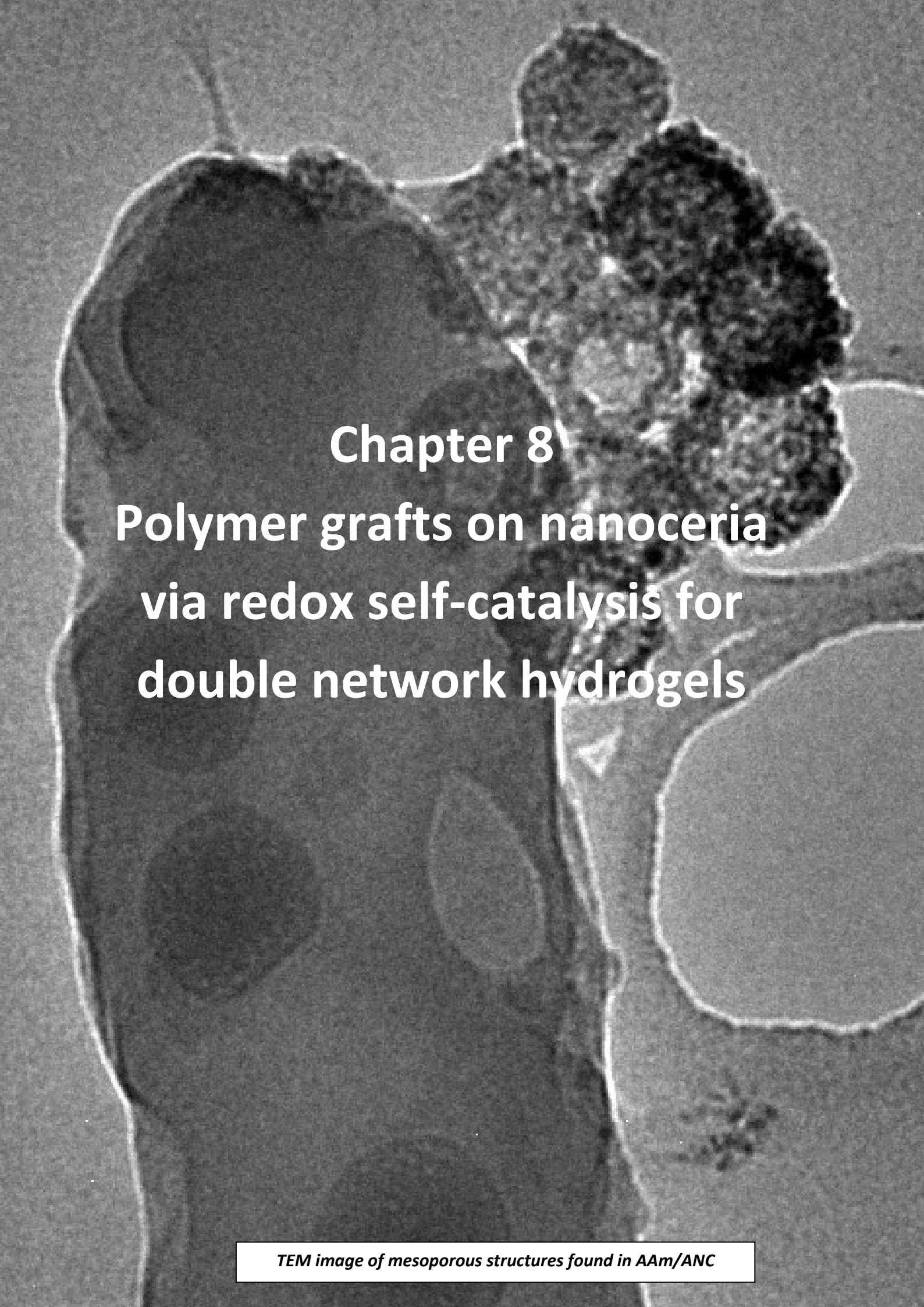
This chapter explored the ability to graft PAMPS and PAAm on the surface of amine functionalized SNPs as a form of novel network for a DNHG system. A comparison between argon degassing and GOx on grafted polymers and polymer conversion revealed that GOx produced more favourable results. The largest grafts, revealed from TGA, were found with the use of CAN alone, whereas conversion was highest when a combination of CAN/SDS was used. The formation of the DNHG revealed swelling and water content were reduced in comparison the DNHGs from Chapter 5 and Chapter 6 due to more covalently linked and tightly cross linked networks. Compressive strength of 13.1 ± 6.4 MPa was achieved, also higher than previously synthesised DNHGs in this

research. Synthesis route optimization is required to increase material property consistency. Ultimately, a novel synthesis of a PAMPS/PAAm DNHG was achieved by grafting both networks on ASNPs, providing more depth and opportunity for tailorability.

Next chapter

The success of CAN as a redox initiator for the system developed in this chapter can be explored further by replacing silica nanoparticles with nanoceria nanoparticles. The by-product of GOx/G is H_2O_2 and benefited the reaction by re-oxidising the cerium based initiator, CAN, allowing it to become more effective. Nanoceria nanoparticles have the ability of changing states back and forth from Ce^{4+} to $Ce^{3+;}$ hence they have the ability to act as redox initiators. This would be considered a self-catalysis polymerization where an initiator would not be required, hence removing the need for CAN. The next chapter explores the synthesis of amine functionalised nanoceria and its use as a self-catalysis tool for graft polymerization of AAm and AMPS, and the potential for forming a double network hydrogel through this route. The potential impact of GOx and its by-product will also be examined in the next chapter by exploring improved conversion rates.

Chapter 8
Polymer grafts on nanoceria via redox self-catalysis for double network hydrogels



TEM image of mesoporous structures found in AAm/ANC

8 Polymer grafts on nanoceria via redox self-catalysis, for double network hydrogels

8.1 Introduction

The previous chapters have explored the use of silica based nanoparticles for the creation of nanocomposite double network hydrogels. Progress was achieved in the biomaterials with the introduction of GOx as a degassing agent that enhanced the reaction kinetics by eliminating oxygen. GOx also increased polymer conversion percentage for with lowered concentrations of photoinitiator. Ultimately, the use of silica nanoparticles as cross linkers was then changed to become the basis for polymer grafting. Improved polymer grafting on the surface of nanoparticles was achieved through the combination of GOx and CAN, due to the re-oxidization capability of H_2O_2, a GOx by-product. This then lead to the idea of replacing silica nanoparticles with nanoceria nanoparticles as the basis for polymer grafting.

Therefore, this chapter will explore the use of nanoceria nanoparticles as the base for polymer grafting. An objective of this chapter is to explore whether it is possible to use the naturally changing states of nanoceria to initiate graft polymerizations on the surface.

8.2 Methods and materials

8.2.1 Materials

Acrylamide (AAm; ≥ 99 %) and 2-acrylamido-2-methyl-1-propanesulfonic acid (AMPS; 99 %); N, N'-methylenebisacrylamide (BIS; 99 %); photoinitiator 2-hydroxy-4'-(2-hydroxyethoxy)-2-methylpropiophenone (synonym Irgacure 2959; 98 %), 1, 3, 5 –trioxane (≥ 99 %); (3-aminopropyl) triethoxysilane (APTES; ≥ 98 %), deuterium oxide (D_2O; 99.9 atom % D),

cerium(IV) ammonium nitrate (CAN; ≥ 99.99 % trace metals basis), cerium (III) nitrate hexahydrate ($Ce(NO_3)_3 \bullet 6H_2O$ ≥ 99.99 % trace metals basis), sodium dodecyl sulfate (SDS; ≥ 98.5 %), ammonium hydroxide (NH_4OH; 28-30 % NH_3 basis) 2-propanol (≥ 99.5 %), hydrochloric acid (HCl; 1 M) and urea were purchased from Sigma-Aldrich (UK). No additional processing and/or purifications were performed. D-glucose (G) and glucose oxidase (GOx; from aspergillus niger as a lyophilized powder) were purchased from Sigma-Aldrich (UK) and stored in phosphate buffer saline (PBS) aliquots at -20 °C when received.

8.2.2 Method

8.2.2.1 Amine nanoceria synthesis[161]

2 g of urea and 7 g of $Ce(NO_3)_3 \bullet 6H_2O$ were dissolved in two separate beakers with 20 ml of 2-propanol. 0.5 ml HCl was added to each beaker while stirring until both solutions were fully dissolved. Urea was then added drop wise into the $Ce(NO_3)_3$ solution whilst stirring. 14 ml of aqueous NH_4OH was then added and a precipitate was formed and allowed to stir for 3 minutes until it was homogenously mixed. The solution was exposed to 600 W microwaves, 4 times for 10 seconds each, or until a crackling sound was heard. 14 ml deionised H_2O was added to stop the reaction once the solution was removed from the microwave. The solution was then washed and centrifuged using the Eppendorf 5430 with water 3 times at 7,830 rpm, and kept as a stock suspension in water with a concentration of 1.7 g CeO_2/ 50 ml deionised water.

Nanoceria was functionalized by sonicating 340 mg of CeO_2 in 150 ml EtOH until fully dispersed, then while under stirring 9 ml of APTES was added. The solution was left to stir at room temperature for 24 hours, and finally washed/ centrifuged with EtOH 3 times at 7,830 rpm. The final product was dried at 60 °C to obtain a powder of amine functionalised CeO_2 (ANC). This process is represented in a schematic drawing in Figure 87.

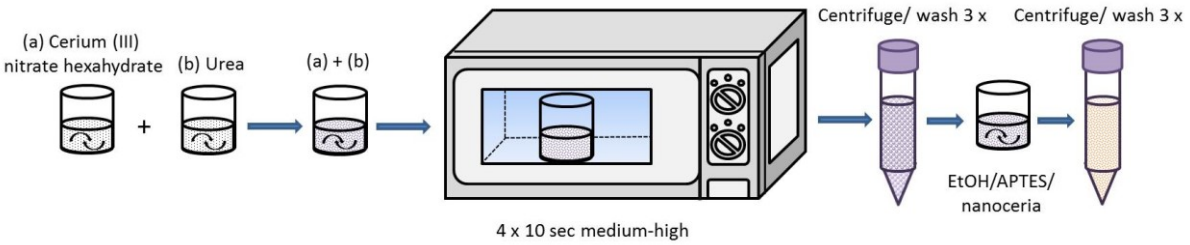


Figure 87 – Schematic representation showing the synthesis and functionalization of nanoceria with APTES.

8.2.2.2 Polymer grafts on nanoceria

150 mg of ANC was dispersed in 5 ml of deionised H_2O and sonicated until fully dispersed. 5 mg of trioxane and 4.5 g of AMPS were dissolved in 35 ml deionised in a round bottom flask, with a final concentration of 0.24 M AMPS. The dissolved ANC was added to the AMPS monomer solution and mixed for 5 minutes. A 20 µl sample was taken and topped up with 500 ml of D_2O, for ^1H NMR analysis of the 0 h reference. The solution was degassed for 20 minutes in a hot bath set at 40 °C and left to stir for 24 hours. A 24 h sample was taken for ^1H NMR analysis of the final polymer conversion. The final solution was wash/ centrifuged, using the Eppendorf 5430, 3 times with water at 7,830 rpm and dried at 60 °C.

The process was repeated a second time with CAN 0.7 g being added to the monomer solution, and a third time with CAN 0.7 g with 1.5 g SDS being added to the monomer solution.

The same process was repeated for AAm.

8.2.2.3 Polymer grafts in the presence of GOx

5 mg of trioxane and 4.5 g AMPS were dissolved in deionized H_2O and titrated to 5.4 pH using NaOH (0.25 M). The monomer solution was topped up to 35 ml with deionized

H_2O with a final concentration of 0.24 M AMPS. 150 mg ANC was dispersed in 5 ml H_2O and sonicated for an hour then added to the monomer solution. The pH is expected to increase to 8 – 9 once the ANC is added; therefore HCl (1 M) was used to bring down the pH to 5.4. GOx/G was added at a final concentration of 200 nM to the monomer/ ANC solution. The solution was transferred to a round bottom flask and the process continued as described above. Repeats were also done to include CAN, and CAN/SDS. This was then repeated with 2 x, 3 x and 4 x the concentration of ANC.

The entire process was repeated, without titration, for AAm. The pH was checked once the ANC was added and if needed, brought down to 5.4 pH using HCl before adding GOx/G. This is represented below in Figure 88.

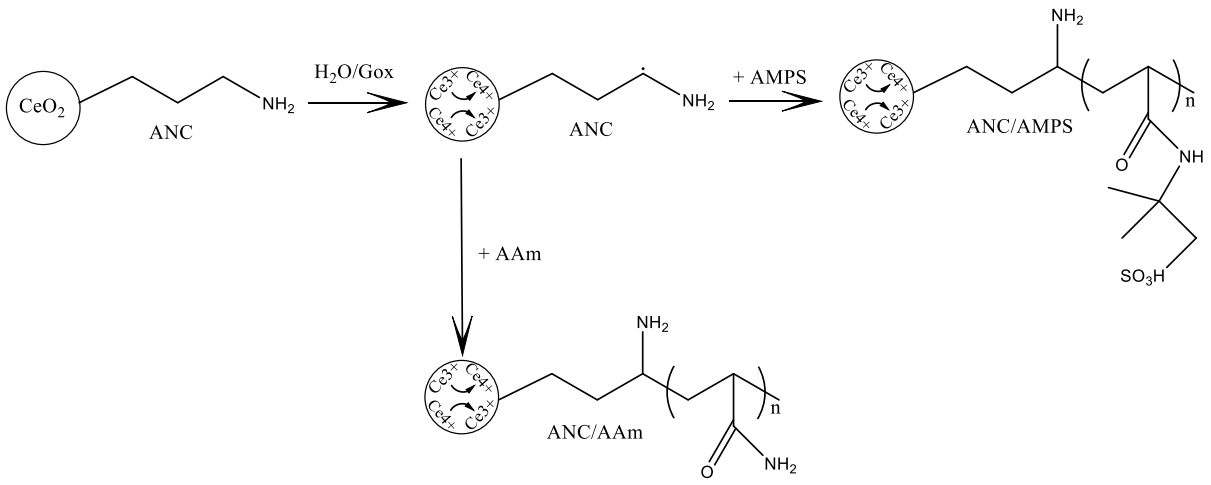


Figure 88 – Schematic showing the self-catalysis of polymer grafts on the surface of amine functionalized nanoceria.

8.2.2.4 Hydrogel synthesis

The first network was formed by dispersing 300 mg of ANC in 5 ml H_2O and sonicating the mixture until it was fully dispersed. 4.5 g AMPS was titrated to 5.4 pH using NaOH (0.25 M), to a final concentration of 0.24 M AMPS. ANC was then added to the AMPS

monomer solution and the pH corrected to 5.4, if required. GOx/G was added to the monomer/ANC solution and mixed for 5 minutes. The solution was then put into aliquots of 2 ml in polystyrene moulds and placed in a sonication bath set to 40 °C to ensure homogenous ANC distribution. Once the solutions in the moulds have gelled, the moulds were placed in an oven at 40 °C for 24 h, and then for 6 h at 60 °C to denature GOx and dry the first network.

The hydrogels were removed from the moulds and soaked in a monomer solution of 2.54 M AAm with containing 150 mg ANC, 0.1 wt % BIS and GOx/G. Once the hydrogels were swollen, they were placed in moulds and put into a 40 °C oven to form the second network. The final hydrogels were then dried at 60 °C and, at their dry state, placed in water to swell for a week. This process is highlighted in Figure 89.

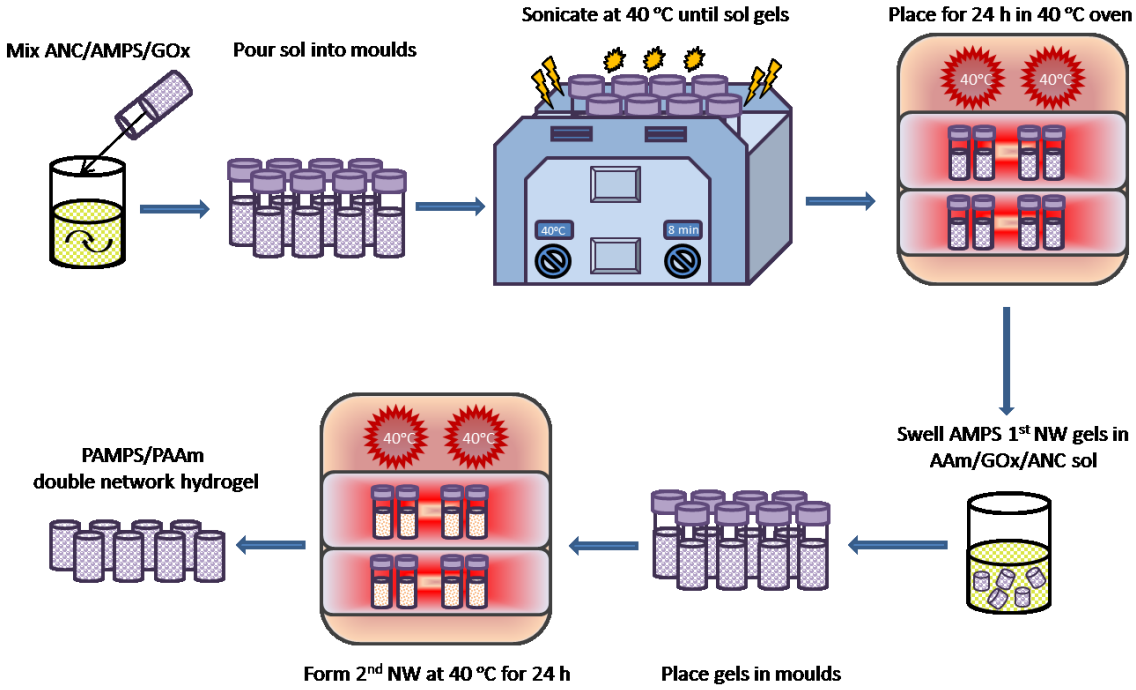


Figure 89 – Schematic showing the synthesis route of nanoceria based double network hydrogels in the presence of GOx.

8.3 Results and discussion

8.3.1 Nanoceria synthesis

Nanoceria was successfully synthesized and functionalized by APTES. DLS results showed bare nanoceria sizes at 70 nm (0.26 PDI). These relatively large sizes are mainly due to aggregation of nanoceria nanoparticles in the solution. Post functionalization size analysis by DLS showed a reduction in size to 14 nm (0.23 PDI). The reduction in size reflects the improved monodispersity of the nanoceria in solution due to its modified surface with amine groups from APTES. The overall size of individual nanoceria nanoparticles did not change pre and post functionalization. The zeta potential for bare nanoceria was + 48 mV and amine nanoceria had a reduced surface charge of + 30 mV. Figure 90 (a) and (b) show bare nanoceria under TEM, while Figure 90 (c) and (d) show amine nanoceria. TEM images revealed more disperse structures for the functionalized nanoparticles compared to non-functionalized nanoparticles.

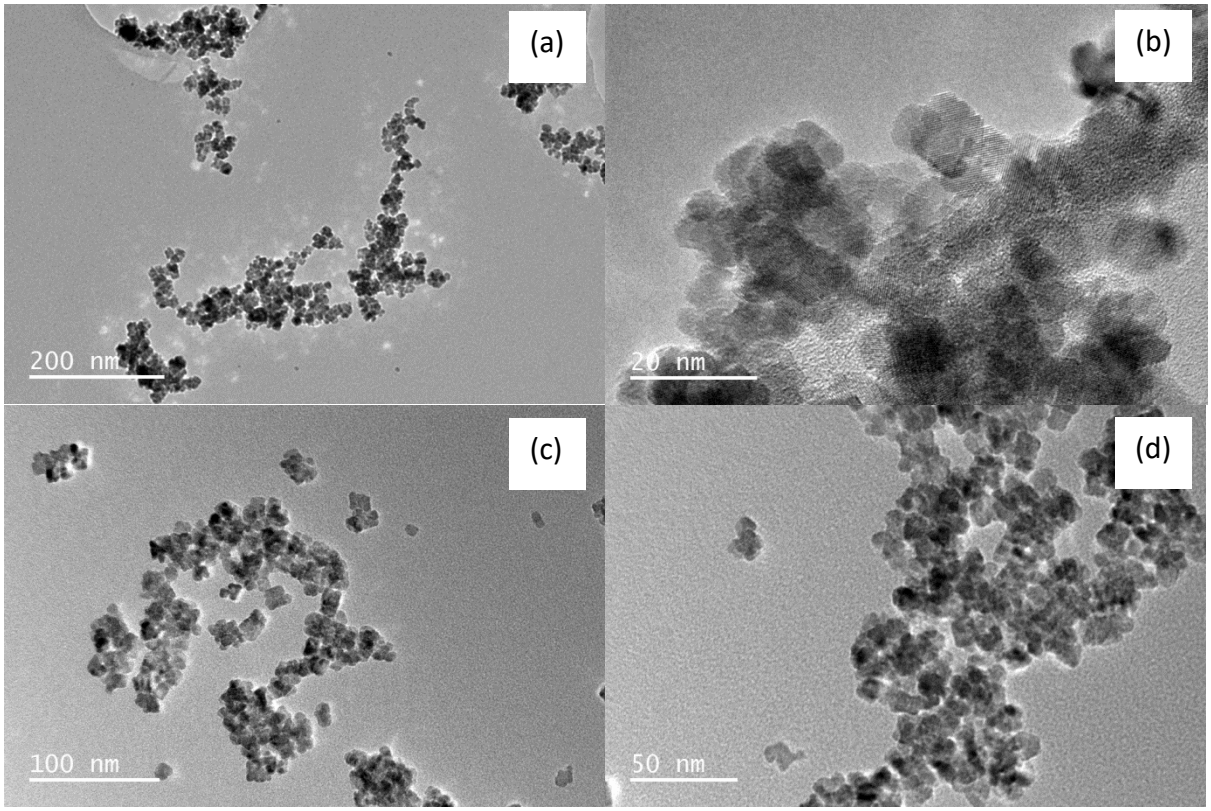


Figure 90 – TEM images of (a – b) bare nanoceria, (c –d) amine functionalized nanoceria.

FTIR was used to confirm surface modification with APTES, Figure 91. Bands associated with Si-O-Si at 1160 cm^{-1}, NH bending at 1156 cm^{-1}, NH stretching 3324 cm^{-1}, CH_2 stretching 1450 cm^{-1} all indicate successful surface modification of the nanoceria by APTES[201]. Bands at 550 cm^{-1} represent Ce-O stretching from CeO_2[202].

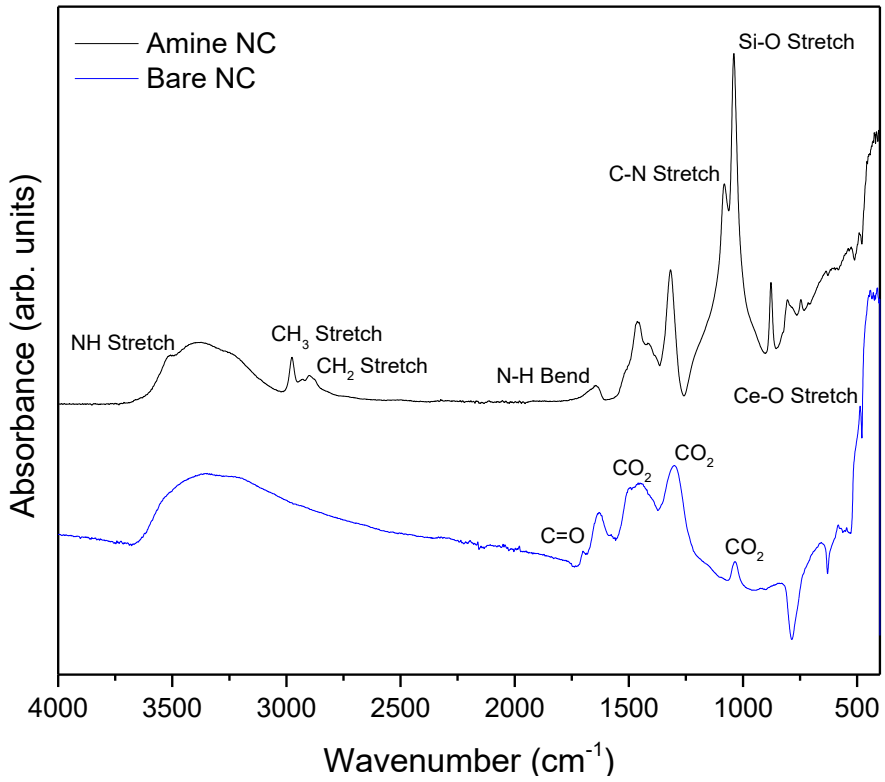


Figure 91 – FTIR spectra of bare (NC) and amine nanoceria (ANC).

8.3.2 Polymer grafts

Amine nanoceria (ANC) were used as the first building block for grafting PAMPS and PAAm to examine the possibility of synthesising polymeric networks from the surface of nanostructures. Monomers were polymerized *in-situ* with ANC, with the addition of CAN, and CAN and SDS, under inert argon atmospheres, as described in the methods section.

8.3.3 UV-Vis

UV-Vis analysis was conducted on all samples to examine the success of polymer grafts on the surface of ANC. Figure 92 shows the changes in cerium ion states within the bare

and functionalized nanoceria. Ce^{4+} is found at wavelength 200 nm, whereas Ce^{3+} is found at 300 nm. Bare ANC have a higher concentration of Ce^{4+} on the surface, and a lower concentration of Ce^{3+}. Once functionalized with amine groups, the distribution oxidation states reverse and Ce^{3+} increases in concentration on the surface.

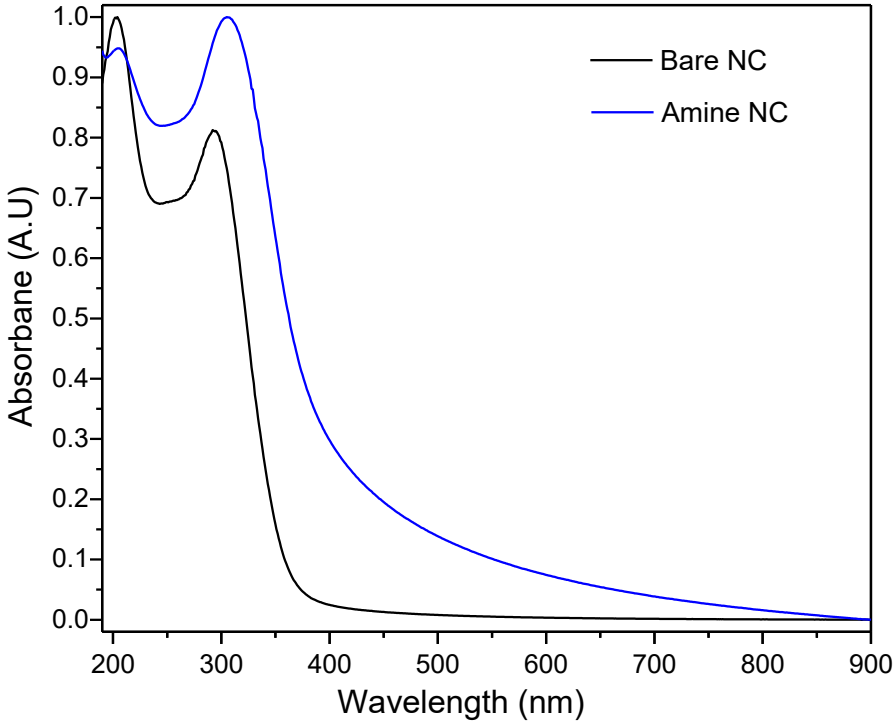


Figure 92 – UV-Vis spectra of bare (NC) and amine nanoceria (ANC).

All the reactions involving AAm and ANC produce grafts on the surface of the amine functionalized ANC, as seen in Figure 93. A disappearance in Ce^{4+} and a reduction in Ce^{3+} for all reactions with AAm provide evidence that grafts were present on the surface. SDS was not completely removed from the sample despite several washes, with a peak present between 220 nm – 260 nm. AAm/ANC and AAm/ANC/CAN presented the least amount of Ce^{3+} remaining on the surface therefore indicate high polymer graft coverage.

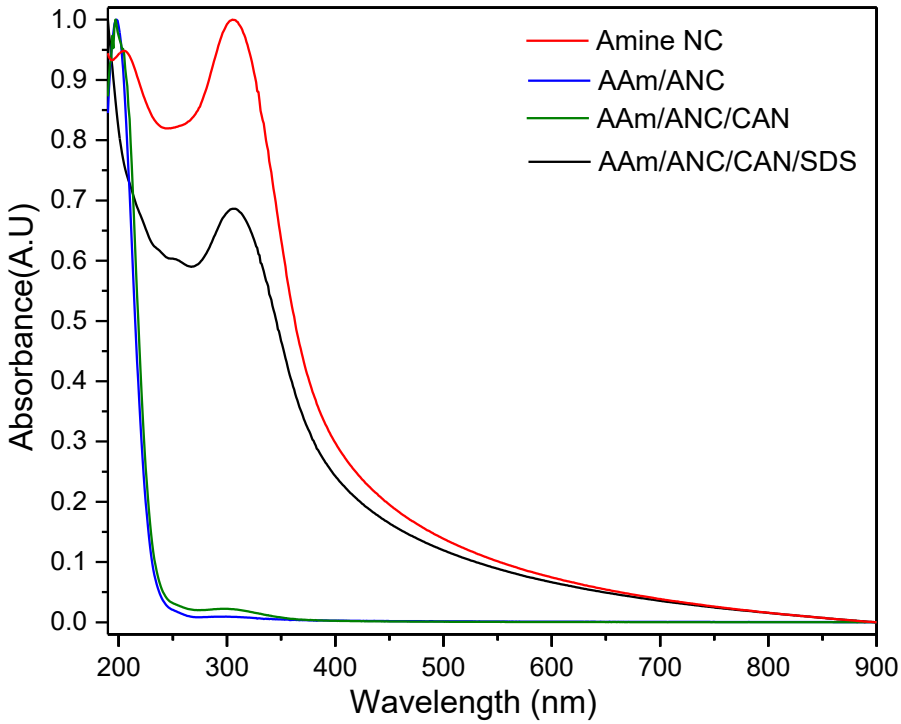


Figure 93 – UV-Vis of AAm reactions with amine nanoceria (ANC), ANC/CAN and ANC/CAN/SDS compared to ANC.

UV-Vis for AMPS reveals successful graft polymerizations occurred on the surface of the ANC, as seen in Figure 94. Similarly to AAm, a disappearance in Ce^{4+} and reductions in Ce^{3+} reveal grafts were indeed on the surface of the ANC. AMPS/ANC and AMPS/ANC/CAN had the clearest polymer peaks at 200 nm with the biggest reductions in Ce^{3+} indicating they had the best graft polymerization.

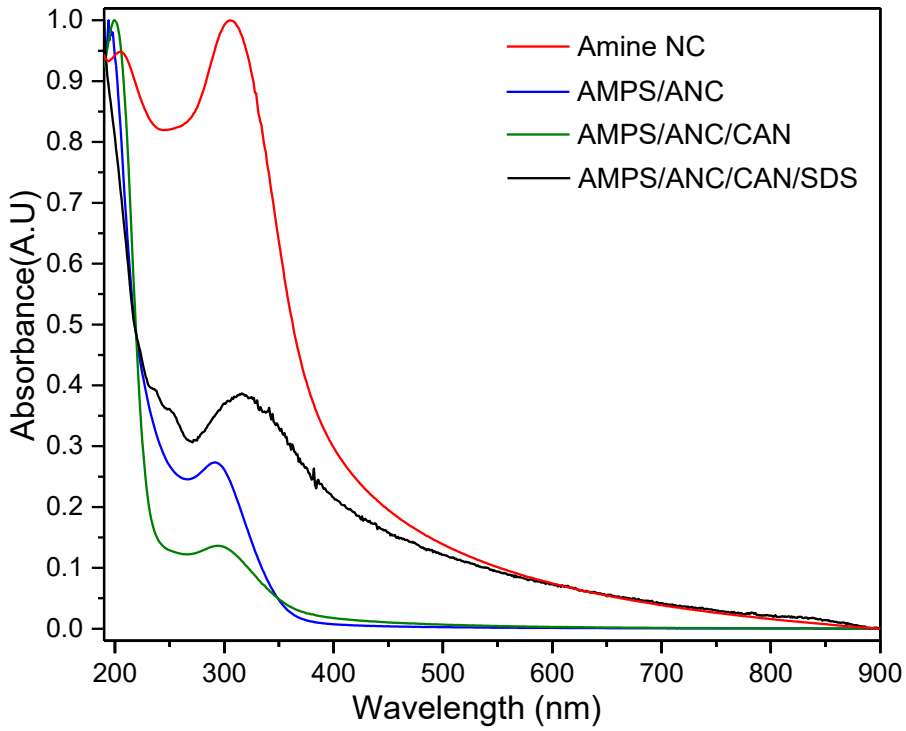


Figure 94 – UV-Vis of AMPS reactions with amine nanoceria (ANC), ANC/CAN and ANC/CAN/SDS compared to ANC.

8.3.4 FTIR

Samples were ground to a fine powder and dried at 60 °C before FTIR analysis. Figure 95 shows the results for AAm in combination with ANC/CAN/SDS compared to PAAm and ANC. Table 35 gives a summary of the bands found in AAm grafted polymers on the surface of ANC. All samples including AAm and ANC showed polymer growth, suggesting ANC on its own was able to result in polymer growth. AAm/ANC gelled during experimentation and therefore the FTIR reading does not reflect the bands intensities relative to the other samples. Gelling of the sample is a strong indicator that cross linking within the polymer grafted nanoceria had occurred. The disappearance of bands at 952 cm^{-1} in all samples, representing Ce-O-Si bonds from APTES on the surface of ANC, indicates thick polymer layers covering the surface have formed. All spectrums that represent grafted polymers exhibit bands at 1652 cm^{-1} and 1620 cm^{-1}, reflecting the presence of amide bonds from PAAm. Residual SDS was found in

AAm/ANC/CAN/SDS in bands between 2850 cm^{-1} – 2956 cm^{-1}, despite several wash/ centrifuge cycles[199]. From the FTIR spectra provided, it can be assumed, based on band intensity and similarity to PAAm, that AAm/ANC/CAN was the most successful at grafting polymers on the surface of ANC.

Table 35 - Summary of FTIR bands for AAm grafted polymers on the surface of amine nanoceria (ANC) [71, 161, 192, 203].

	Bond	Type	Wavenumber (cm^{-1})
A	C-H	Stretching	2956 2918 2850
B	CH_2 CH_3	Stretching	2966 2932
C	C=O	Stretching, coupled with N-H bending	1652-1659
D	N-H	Primary amine	1620
E	C-N	Stretching primary amide	1420
F	CO_2		1319
F	N-H	Bending	1238
G	Ce-O-Si	Stretching	952
H	C-H	Out-of-plane rocking	942
I	Ce-O	Stretching	550

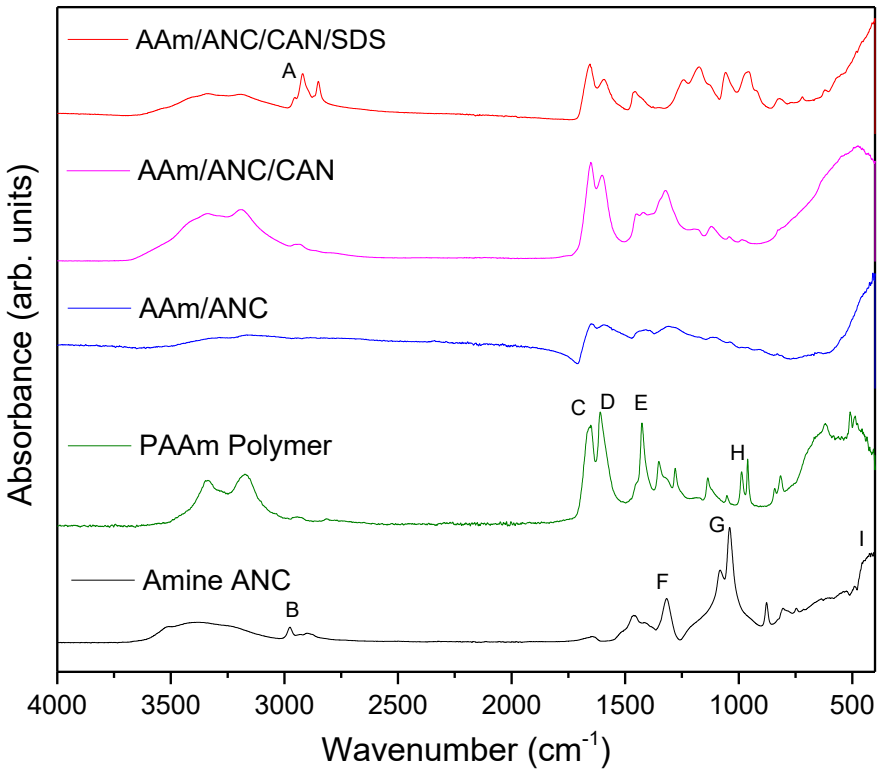


Figure 95 – FTIR spectra of AAm reactions with amine nanoceria (ANC), ANC/CAN and ANC/CAN/SDS compared to ANC and PAMPS.

Figure 96 shows the results for AMPS in combination with ANC, CAN and SDS, compared to amine ANC and PAMPS. Table 36 provides a summary of the bands present in AMPS grafted polymers on the surface of ANC. Polymer bands were present for all samples with AMPS/ANC, for sulfonic acid groups at 1040 cm^{-1}, reflecting the PAMPS spectra. This suggests a large amount of polymer was grafted on the surface of ANC. Therefore, it was proved that ANC has the ability to initiate and propagate polymer grafts without the need of a chemical initiator. Similar bands with reduced intensity were seen for AMPS/ANC/CAN, suggesting lower graft amounts. Residual SDS was detected in AMPS/ANC/CAN/SDS, between 2950 cm^{-1} – 2956 cm^{-1} samples and lower polymer bands were exhibited[199]. Ultimately, all three combinations result in polymer grafts, reconfirmed from UV-Vis data.

Table 36 - Summary of FTIR bands for AMPS grafted polymers on the surface of amine nanoceria (ANC) [80, 161, 192, 203].

	Bond	Type	Wavenumber (cm^{-1})
A	C-H	Stretching	2956 2918 2850
B	CH_2 CH_3	Stretching	2966 2932
C	C=O	Stretching, coupled with N-H bending	1652-1659
D	N-H	Primary amine	1620
E	CO_2		1319
F	N-H	Bending	1238
G	Ce-O-Si	Stretching	952
H	R–S(=O)–R'		1040
I	Ce-O	Stretching	550

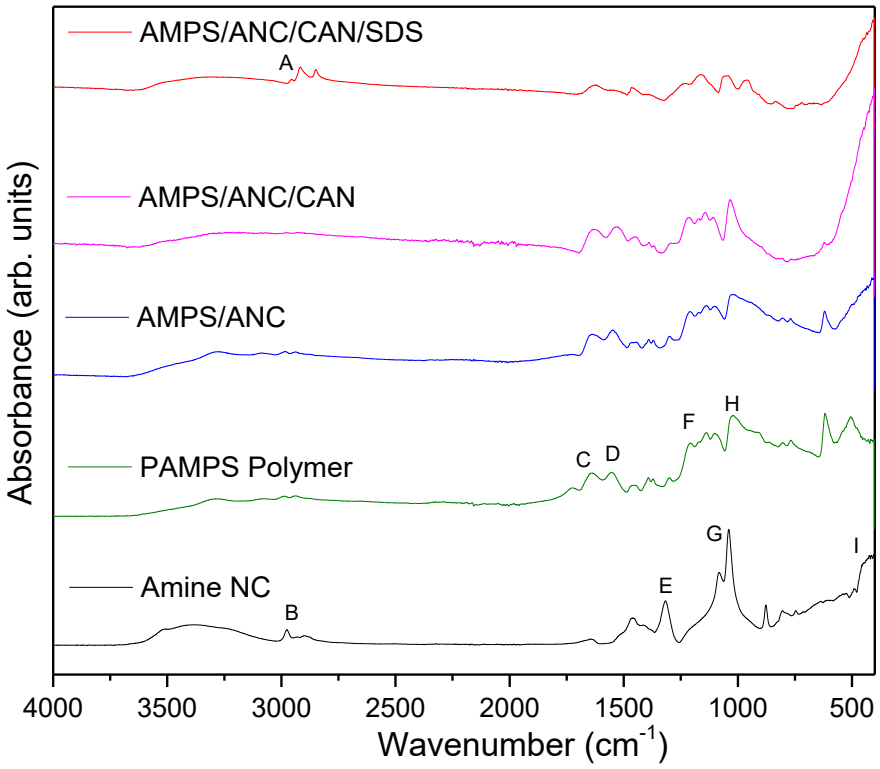


Figure 96 – FTIR spectra of AMPS reactions with amine nanoceria (ANC), ANC/CAN and ANC/CAN/SDS compared to ANC and PAMPS.

8.3.5 TGA

TGA was conducted on AMPS and AAm samples that were reacted with ANC, ANC/CAN and ANC/CAN/SDS to examine the mass of polymer grafted on nanoceria.

The highest mass loss was exhibited by AAm/ANC/CAN showing 96 % mass loss, Figure 97, which reflects the strong bands seen in FTIR for the same sample. For the sample containing SDS, a mass loss of 75 % was exhibited suggesting SDS may inhibit graft polymerization on the surface of the ANC as the sample with AAm/ANC/CAN had a higher mass loss. AAm/ANC samples had the lowest mass loss at 21 %, suggesting grafting was not very efficient without the use of an initiator and stabilizer.

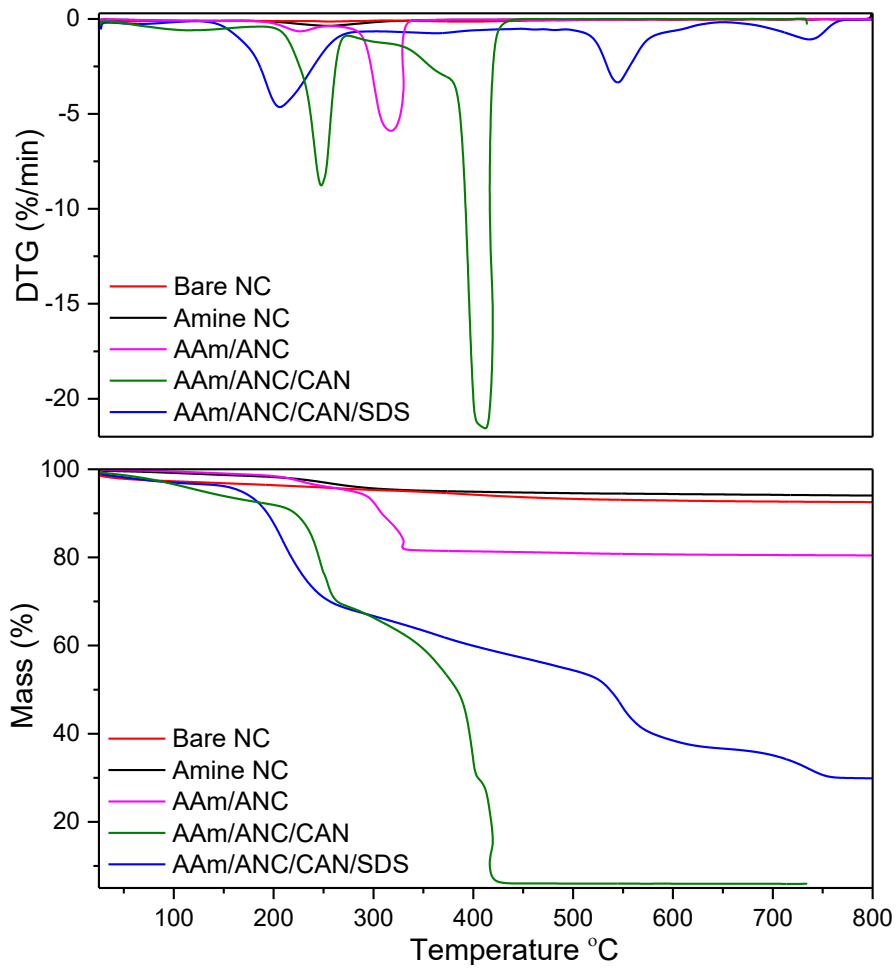


Figure 97 – TGA and DTG profile of AAm with amine nanoceria (ANC), ANC/CAN and ANC/CAN/SDS compared to bare and amine ANC.

Contrary to AAm/ANC, AMPS/ANC had the biggest mass loss, with 58 % mass loss, Figure 98. This result matches the FTIR spectra that suggested AMPS/ANC had the highest amount of polymer grafts on the surface of the ANC. Further contrary to AAm samples, AMPS samples containing CAN and CAN/SDS both had approximately 17 % mass loss. This suggests the graft polymerization was more effective with ANC alone.

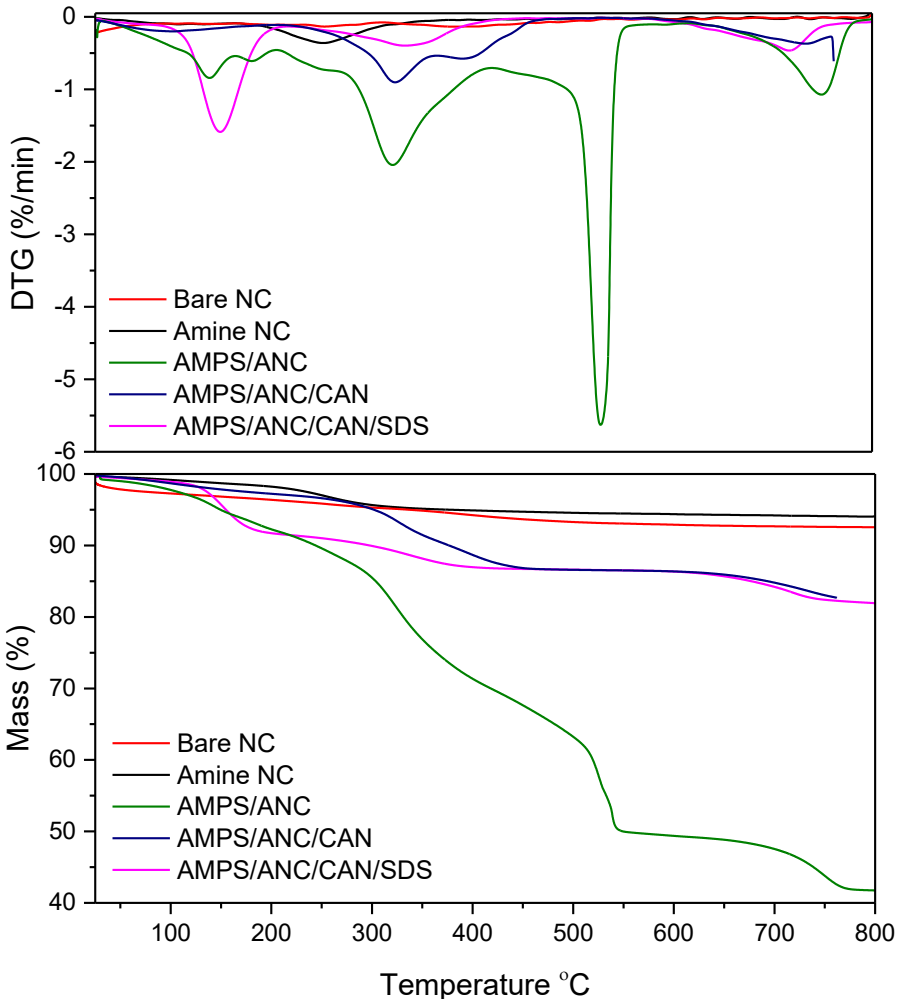


Figure 98 – TGA and DTG profile of AMPS with amine nanoceria (ANC), ANC/CAN and ANC/CAN/SDS compared to bare and amine ANC.

8.3.6 TEM

Samples were examined using TEM imaging to understand the physical formation of polymer grafts on the surface of ANC. An interesting observation was that polymer reactions with ANC formed new nanoparticles. In section 7.3.4, TEM images revealed that the presence of SDS created mesoporous silica nanoparticles. In contrast, the TEM images displayed in Figure 99 (a – d) show new nanoparticle formation that occurred in the presence of only ANC with either AMPS or AAm.

The combination of ANC and PAMPS formed nanoparticles with nanoporous structures, Figure 99 (c). The new nanoparticle structures suggest they are of low density due to their translucence. Nanoceria can be seen around the samples in contrast. Nanoceria tend to be around 10 – 20 nm, whereas the new nanoparticles have a diameter between 200 – 250 nm.

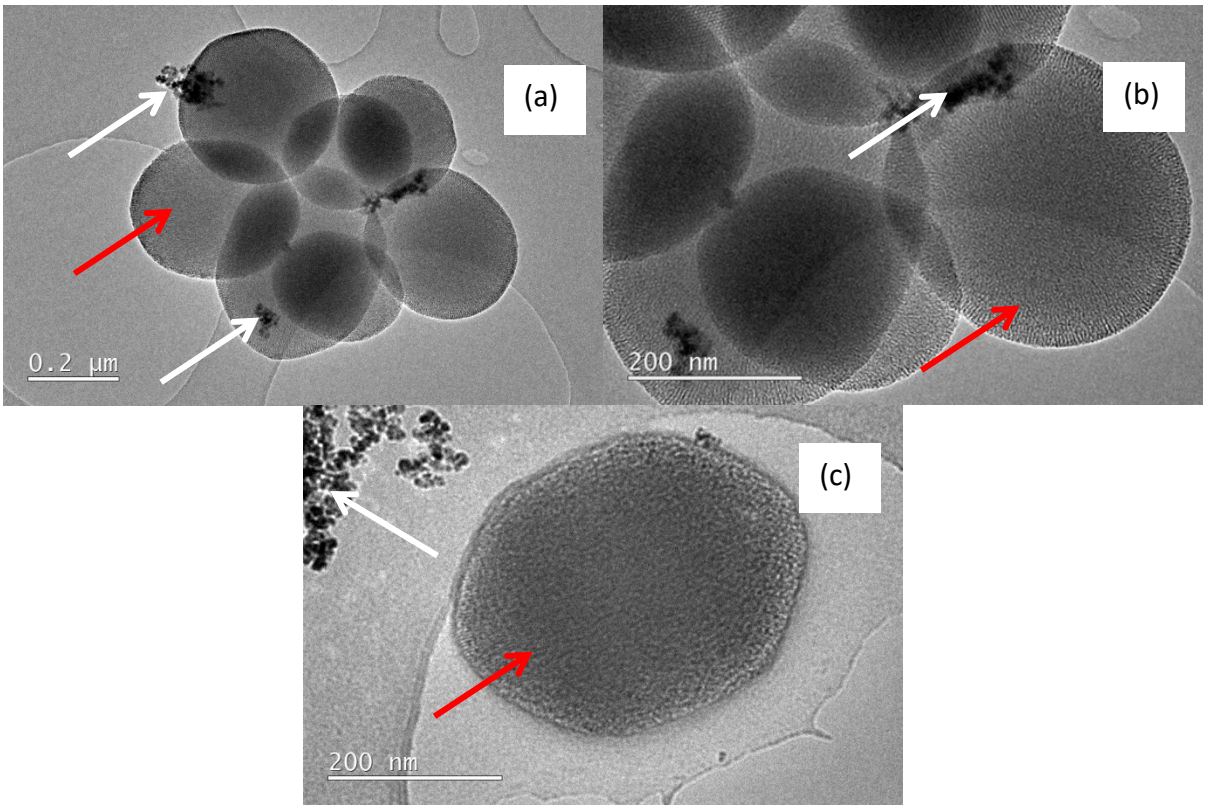


Figure 99 – TEM images of an AMPS/ANC sample at different magnifications showing ANC (white arrows) and newly formed porous AMPS based particles (red arrows).

PAAm, however, formed new nanoparticles that seem denser, with ANC around their circumference, Figure 100 (a – d). The majority of nanoparticles in this sample exhibited a circumference surrounded by ANC, implying that this could either be due to the electrochemical gradient on the surface of ANC and the new nanoparticles, causing them to attach in such a manner, or the way in which the new nanoparticles were formed. The new nanoparticles formed are between 50 – 80 nm in size.

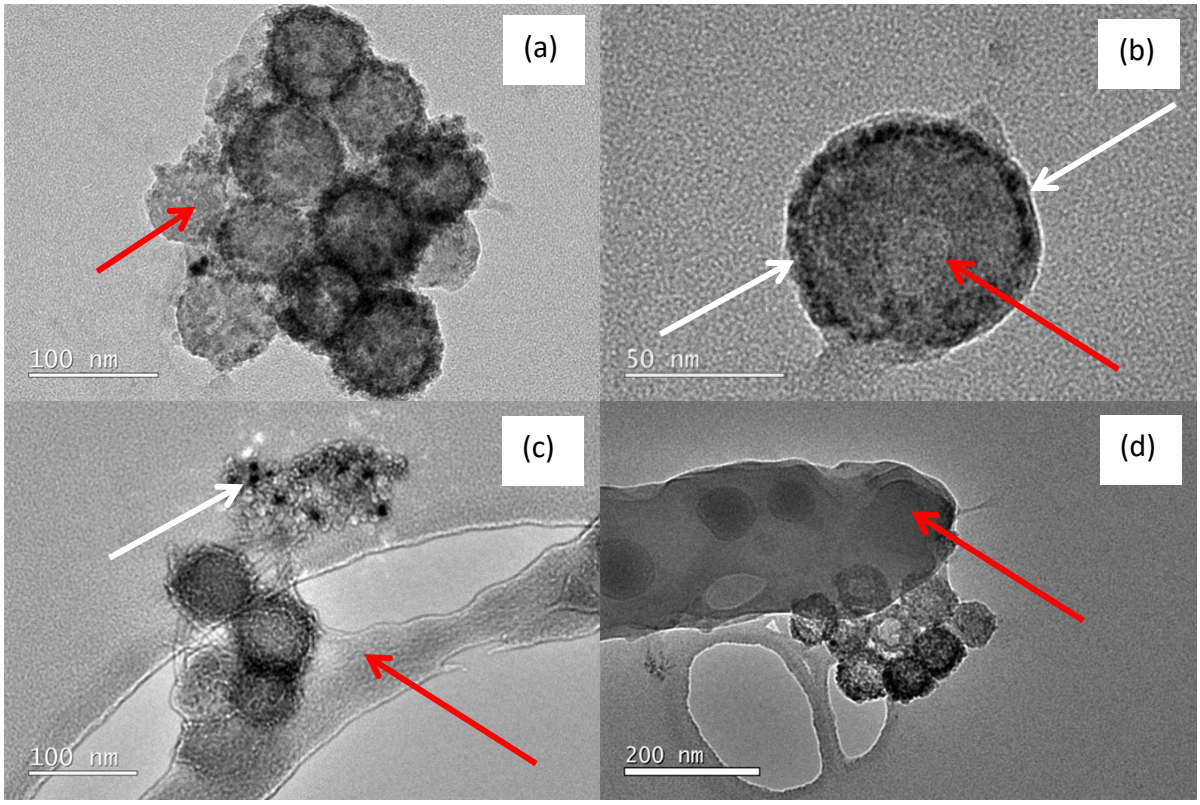


Figure 100 – TEM images of an AAm/ANC sample at different magnifications showing ANC (white arrows) and newly formed AAm based particles (red arrows) and AAm polymeric masses. ANC were found to attach around the circumference of the newly formed AAm particles.

8.3.7 Polymer conversion

Polymer conversion was measured using ^{1}H NMR based on trioxane peaks in 0 h and 24 h samples. The ability for nanoceria to initiate the self-catalysis redox initiated polymerization of both PAMPS and PAAm was noted by polymer conversion in AAm/ANC and AMPS/ANC systems.

Figure 101 shows AAm/ANC with argon resulted in lower conversions under all cases when compared to GOx. This suggests that GOx is more efficient at degassing the monomer solution, removing more oxygen species than through simple argon purging. Under argon gas, AMPS samples resulted in very similar conversion of around 50 % for

all cases. This suggests that either all systems were equally effective, or the presence or degassing with argon was insufficient and resulted in a rate limiting step. Samples for AAm reflected the results found in TGA; the combination of AAm/ANC/CAN resulted in the highest conversion, followed by samples containing SDS. These two samples witnessed 100 % conversion once GOx was added. Both AAm and AMPS exhibited an increase of approximately 30 % when GOx was added to the samples only containing ANC. This was likely due to a combination of two factors, first, the efficiency at which GOx degasses oxygen, creating a better kinetic profile for both polymers. Secondly, the ability of GOx to deplete oxygen further benefited the redox reaction from nanoceria by having an impact on the Ce^{3+}/ Ce^{4+} valence states. The by-product H_2O_2 re-oxidises Ce^{3+} to Ce^{4+} allowing the reaction to become faster and more efficient, Equation 8.1, explaining why conversion increases in the presence of GOx[164].

$$2Ce^{3+} + H_2O_2 \rightarrow 2Ce^{4+} + 2OH^- \qquad \text{Equation 8.1}$$

The reaction in Equation 8.1 releases protons and O_2 that is then reused by GOx to reproduce H_2O_2 once again. This cyclic process leads to the enhanced conversion profiles exhibited in Figure 101 by AMPS and AAm when comparing argon and GOx based reactions. Ultimately, GOx can be considered a degassing agent and a process facilitator.

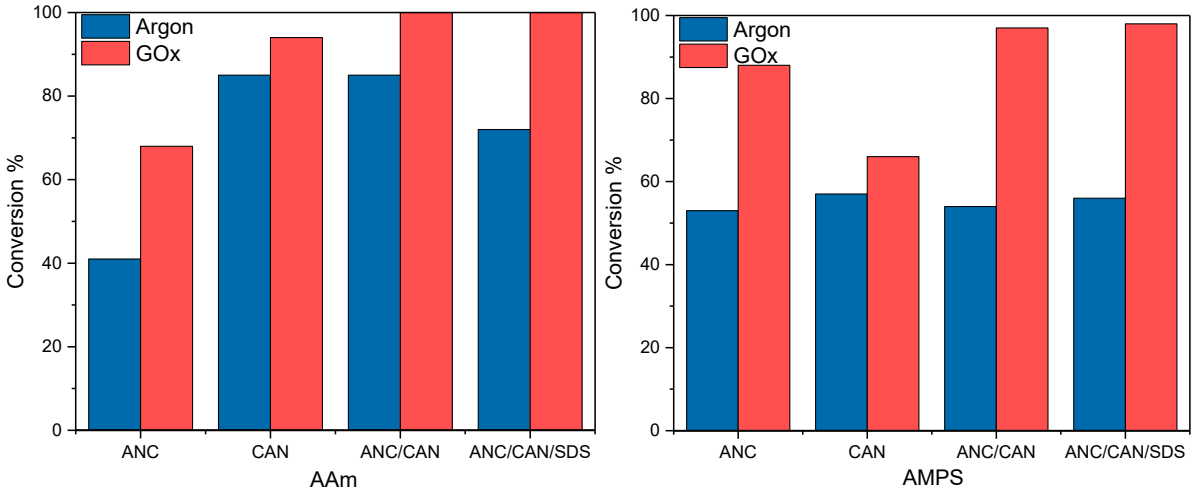


Figure 101 – Conversion profiles of reactions for AAm (left) and AMPS (right) with amine nanoceria (ANC), under argon and GOx.

Tests were conducted to find the highest polymer conversion as a result of only using ANC. This was achieved by increasing the ANC concentration up to x 2, x 3 and x 4. The results are displayed in Figure 102. The best concentration for both AMPS and AAm to achieve their highest conversion without the addition of CAN and SDS was found to be at two times that of the original concentration of ANC. At ANC x 3 the conversion for both begins to decrease, and at x 4 the conversion dropped significantly. At increased concentrations of ANC x 2 it can be expected that more monomers come into contact with nanoceria therefore the polymerization becomes more efficient with GOx. GOx enhances the reaction by eliminating oxygen species, and by releasing H_2O_2 that replenishes the Ce^{4+} ions in nanoceria. Oversaturation of the system begins at ANC x 3 where the conversion begins to decrease, making it more difficult for monomers to come in contact with active surfaces of nanoceria. The solution became notably more dense likely making diffusion of more difficult. ANC x 4 had a similar effect of oversaturation with a denser solution, although it was also suspected that GOx could have also become denatured due to high nanoceria concentrations.

Ultimately, ANC x 2 provided AMPS/ANC with a conversion of 91 % and AAm/ANC with a conversion of 84 %. This was considered a significant finding as it meant CAN and SDS would not be required for hydrogel synthesis, reducing the requirement for purification steps to remove those chemicals. This was also significant due to the success of the

combination of GOx working in unison with nanoceria to allow a self-catalysed system to form a polymeric nanocomposite network.

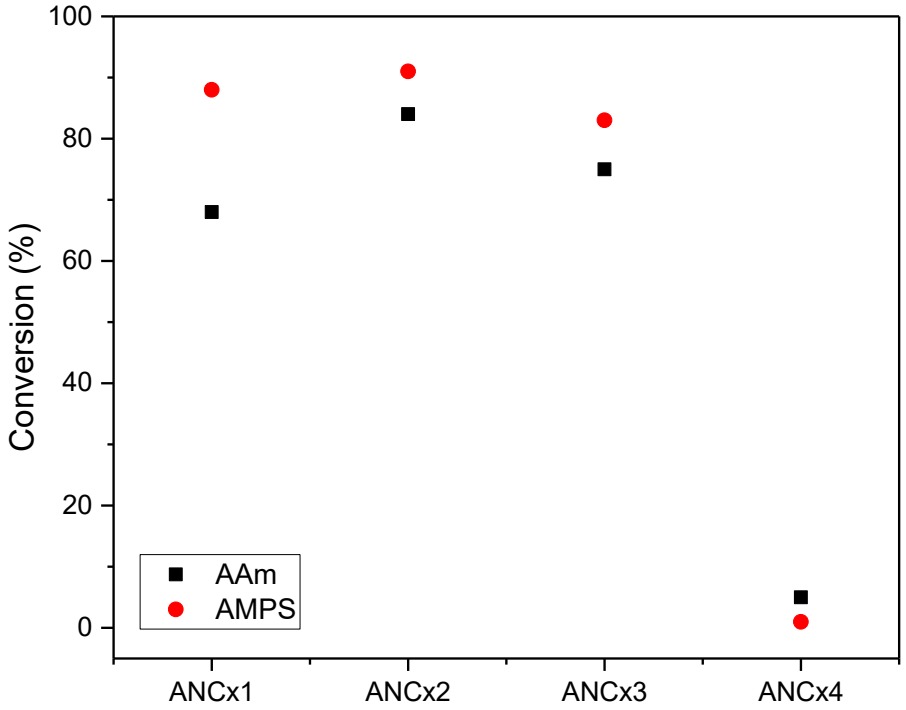


Figure 102 – Conversion profiles for AAm and AMPS and with varying amine nanoceria (ANC) concentrations, in the presence of GOx.

TGA analysis was conducted on samples with increased ANC concentrations in the presence of GOx to examine the effect of increased polymer conversion on graft mass on nanoceria. Figure 104 shows AAm with ANC x4 had the lowest mass loss indicating the lowest graft mass on nanoceria, whereas AAm with ANC x2 had the highest mass loss. These results match the conversion profile discussed earlier. This indicates that ANC x2 is the best concentration for PAAm to achieve a combination of grafting mass on the surface of ANC whilst maintaining high conversion.

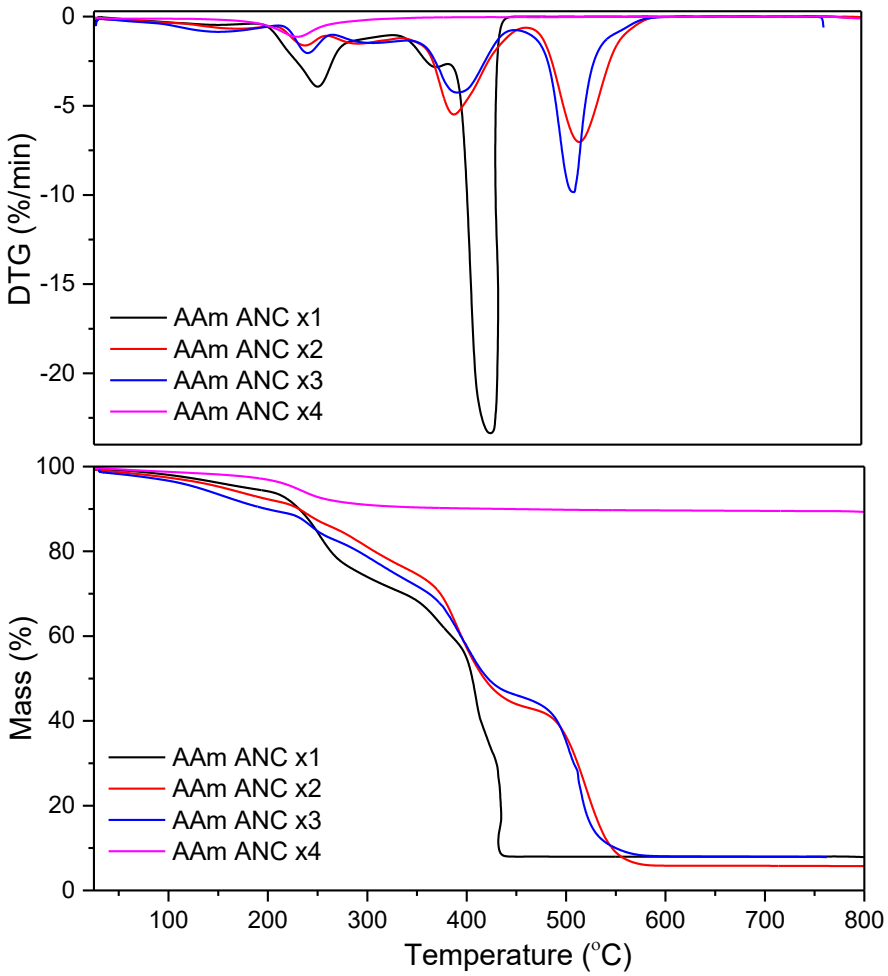


Figure 103 – TGA and DTG profiles for AAm in the presence of GOx at varying amine nanoceria (ANC) concentrations.

Similarly, TGA results for AMPS, Figure 104, with varying ANC concentrations reflect the conversion profile with ANC x2 and ANC x4 exhibiting the highest and lowest mass loss, respectively. An interesting observation for PAMPS was a clear mass loss peak at 650 °C that is more intense under GOx degassing compared to argon-degassed samples discussed previously. This is likely to due to a more homogenous graft polymerization as a consequence of improved kinetics and a more controlled system caused by the introduction of GOx. The largest mass loss exhibited by PAMPs grafted polymers on ANC was with concentration ANC x2, similarly to PAAm grafted polymers. This coincides with the concentration that achieved the highest conversion for both polymers. ANC x4 achieved the lowest mass graft, as seen in Figure 104, due to the low conversion.

Therefore, ANC x2 achieved the best combination of grafting mass and conversion for PAMPS.

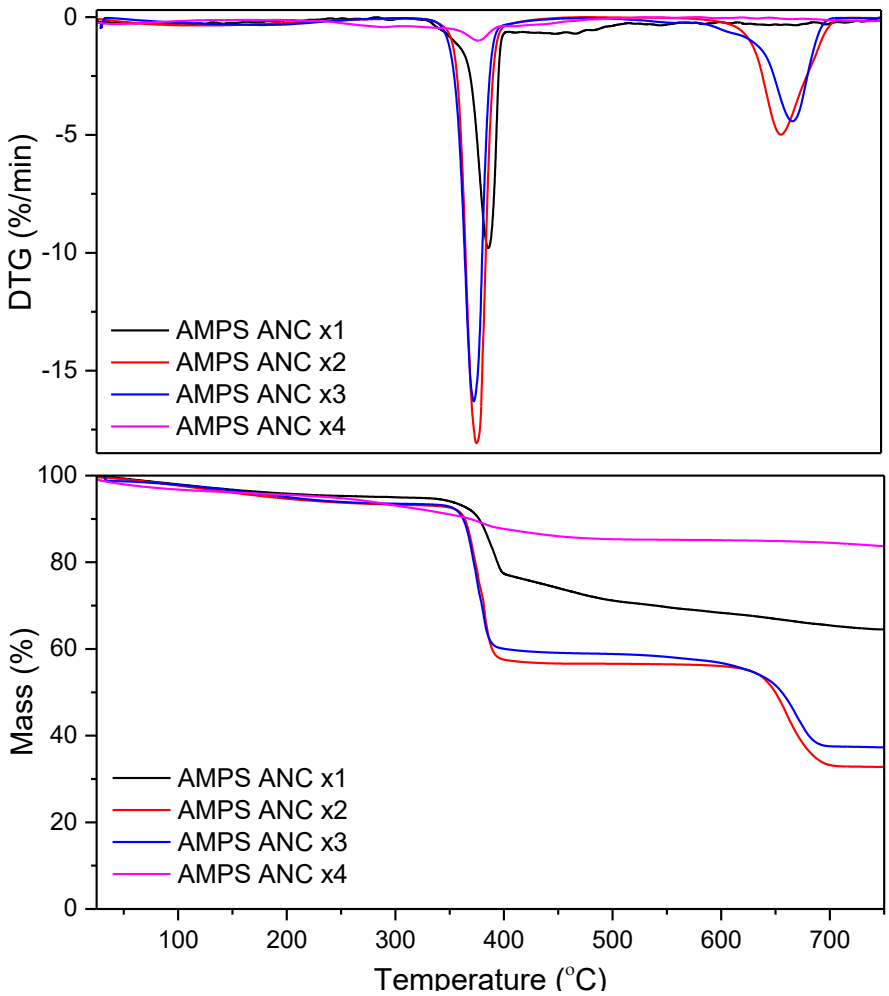


Figure 104 – TGA and DTG profiles for AMPS in the presence of GOx at varying amine nanoceria (ANC) concentrations.

8.3.8 Hydrogels

Double network hydrogels were successfully synthesized with ANC/PAMPS in the first network and ANC/PAAm in the second network. The final products are referred to as ANC gels, and were synthesized based on one concentration with triplicate repeats.

Figure 105 (a) shows ANC/PAMPS after synthesis and Figure 105 (b) shows the double network ANC gel after sequential addition of PAAm, in its hydrated state. It is worth mentioning that residual amounts of ANC and monomer were left over after swelling the first network in a solution of ANC/AAm. This is mainly due to the saturation of the first network. This residual later was extracted before placing the sample at 40 °C for the polymerization of the second network.

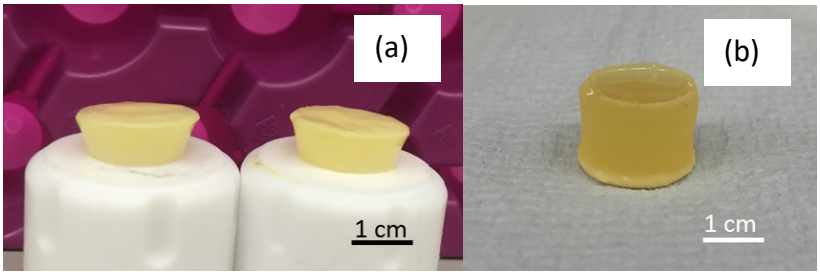


Figure 105 – images of (a) AMPS/ANC first network hydrogel after synthesis, (b) double network hydrogel after sequential synthesis containing PAMPS and PAAm.

8.3.9 Swelling studies

ANC gels were swollen from a dry state until a plateau in water uptake was reached, as seen in Figure 106. Although the samples were heavily cross linked, they were still able to uptake 87.38 ± 2.35 % water. A plateau was reached at 72 h with small incremental changes at 168 hr. The majority of the water uptake occurs within the first 8 hr, similarly to results in the previous chapters. ANC gels exhibited swelling of 811 ± 151 %. Swelling was considered relatively low in comparison with the water uptake, confirming the tightly cross linked nature of the material.

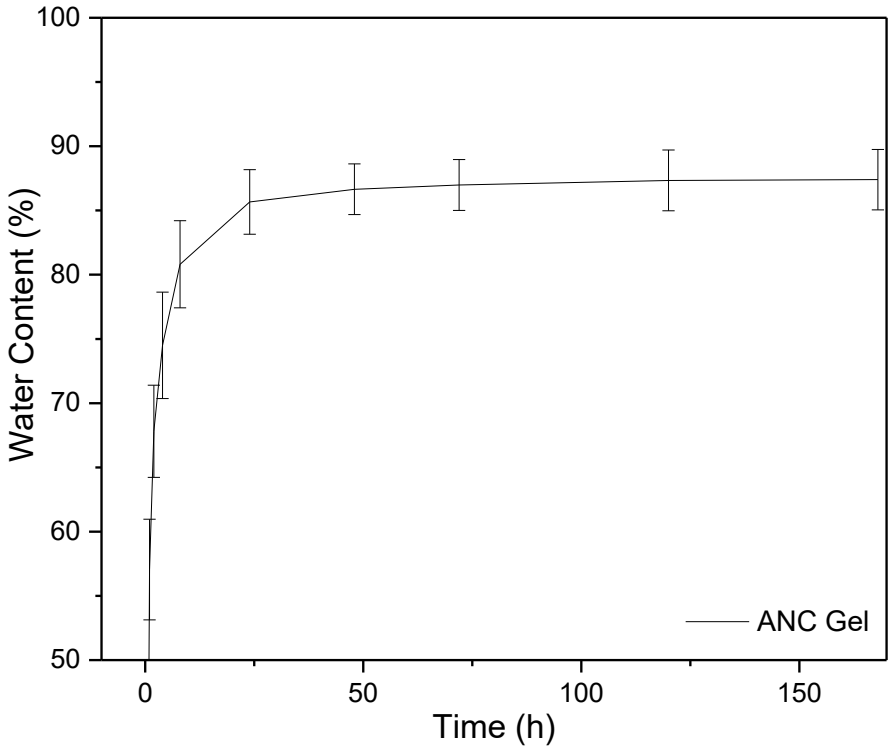


Figure 106 – Swelling profile for a double network amine nanoceria (ANC) hydrogel with PAMPS and PAAm polymer grafts.

Table 37 - Swelling and water content for the double network amine nanoceria (ANC) hydrogel with PAMPS and PAAm polymer grafts.

	ANC Gel
Water Content (%)	87.38 % ± 2.35
Swelling (%)	811 % ± 151

8.3.10 Mechanical testing

ANC gels were tested under mechanical compression under failure. All samples were swollen in water until a plateau prior to testing. Figure 107 shows an example of a sample compressed up to 50 % between two compression plates.

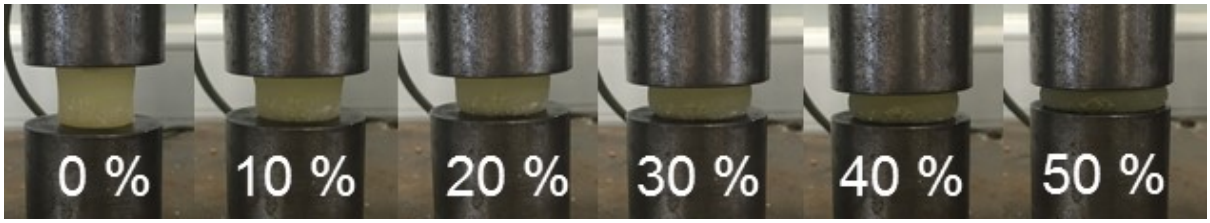


Figure 107 – Images of a double network amine nanoceria (ANC) hydrogel with PAMPS and PAAm polymer grafts under compression at different strains.

Samples with perfectly flat surfaces were difficult to synthesize due to the swelling nature of the material, instead, concave surfaces were formed as seen in Figure 105 (b). The tightly cross linked ANC gels exhibited an improved compressive strength relative to previous materials. A fracture compressive stress of 1.76 ± 0.10 MPa was recorded with strain of 60.94 ± 1.59 %, Figure 108. This increase in mechanical integrity can be attributed to the formation of a more integrated nanoparticle-polymer matrix, in both networks. The complex structure allows the material to withstand increased stress without breaking up to 60 % strain. It is also more likely that the polymers are better integrated into the nanoceria due to the surface polymer graft polymerization, as opposed to the previous method of polymer chains cross linked by nanoparticles. This provides stronger reinforcement in the material against compressive stresses. A higher density of nanoparticles will also be in contact with the polymers due to the reduced size of the nanoparticles, resulting in increased surface area for polymer grafting. Physical entanglements or bridge cross linking within ANC/PAMPS and ANC/PAAm is also possible. These combinations would all have benefited the ANC gels resulting in the improved mechanical strength, and provide insight into the potential tailorability of the material.

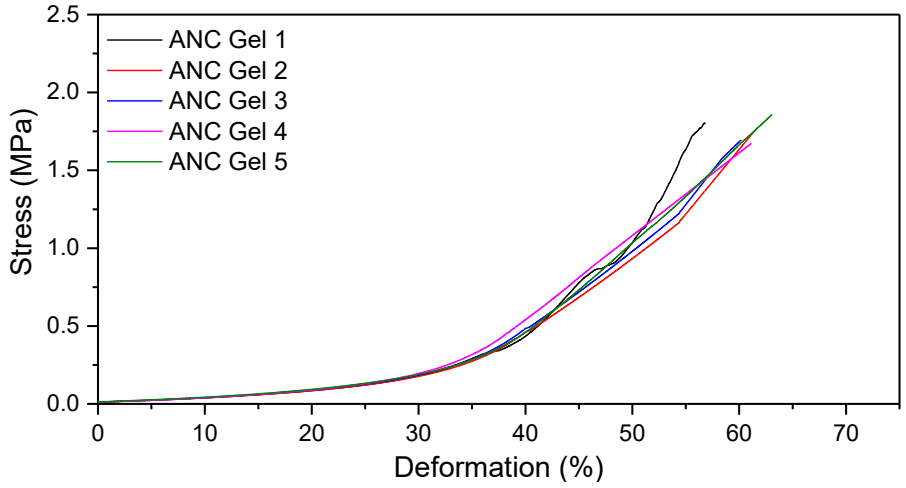


Figure 108 – Compression curves for the double network amine nanoceria (ANC) hydrogel with PAMPS and PAAm polymer grafts.

Table 38 - Compression and strain values for the double network amine nanoceria (ANC) hydrogel with PAMPS and PAAm polymer grafts.

	ANC Gel
Fracture Compressive Stress (MPa)	1.76 ± 0.10
Fracture Strain %	60.94 ± 1.59

8.3.11 SEM

ANC gels were freeze dried for 48 hours and imaged using back scattered SEM, (Figure 109). SEM imaging revealed thick struts within the material that made up pore like structures (Figure 109 a). Further examination of the struts and inner walls of the material clearly showed that ANC was present (Figure 109 a and b). ANC were predominantly found within exposed structures rather on the surface of the material. This suggests that ANC were covered with polymers due to the graft polymerization during synthesis. The materials ability to withstand ≤ 60 % strain is likely due to the dense polymeric networks sharing the load due to their covalent links with ANC. SEM also revealed that ANC gels were not as porous as materials synthesised in previous

chapters. This is likely due to the nanocomposite structure of the material where both networks are composed of ANC/polymer networks, as opposed to only the first network containing nanoparticles in Chapter 4 – 6.

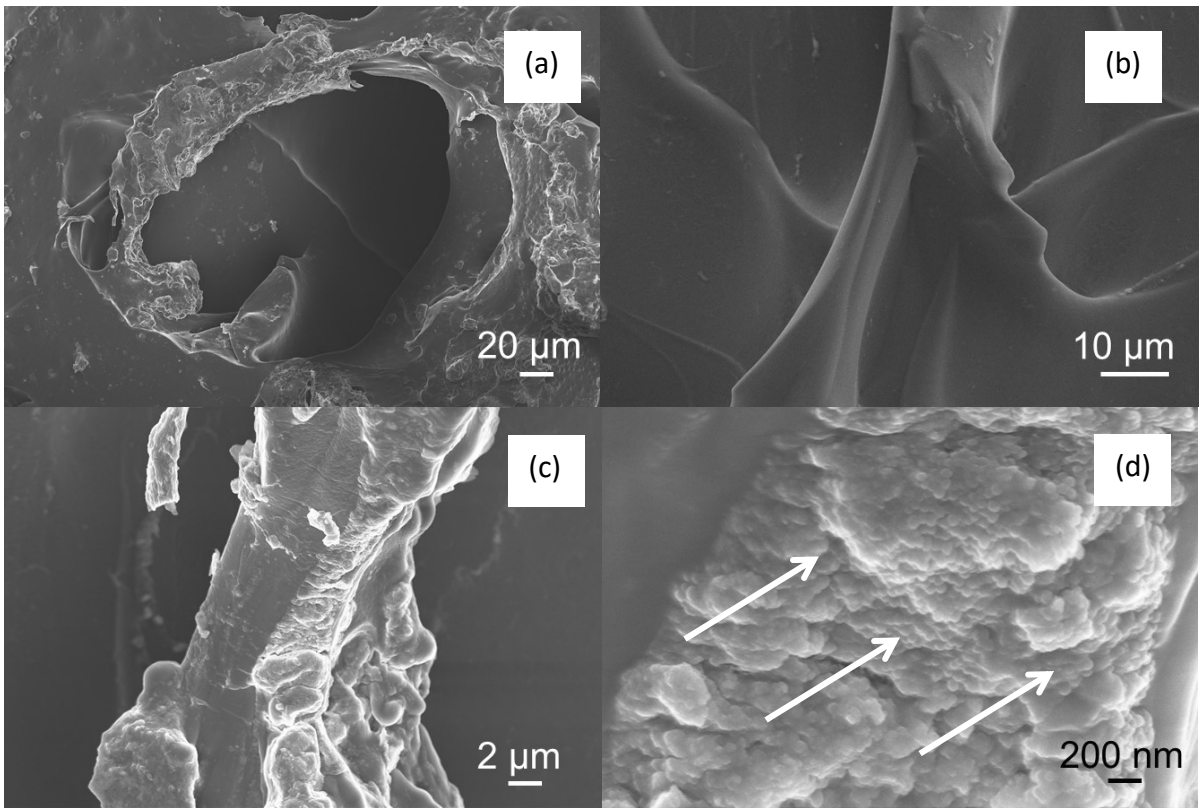


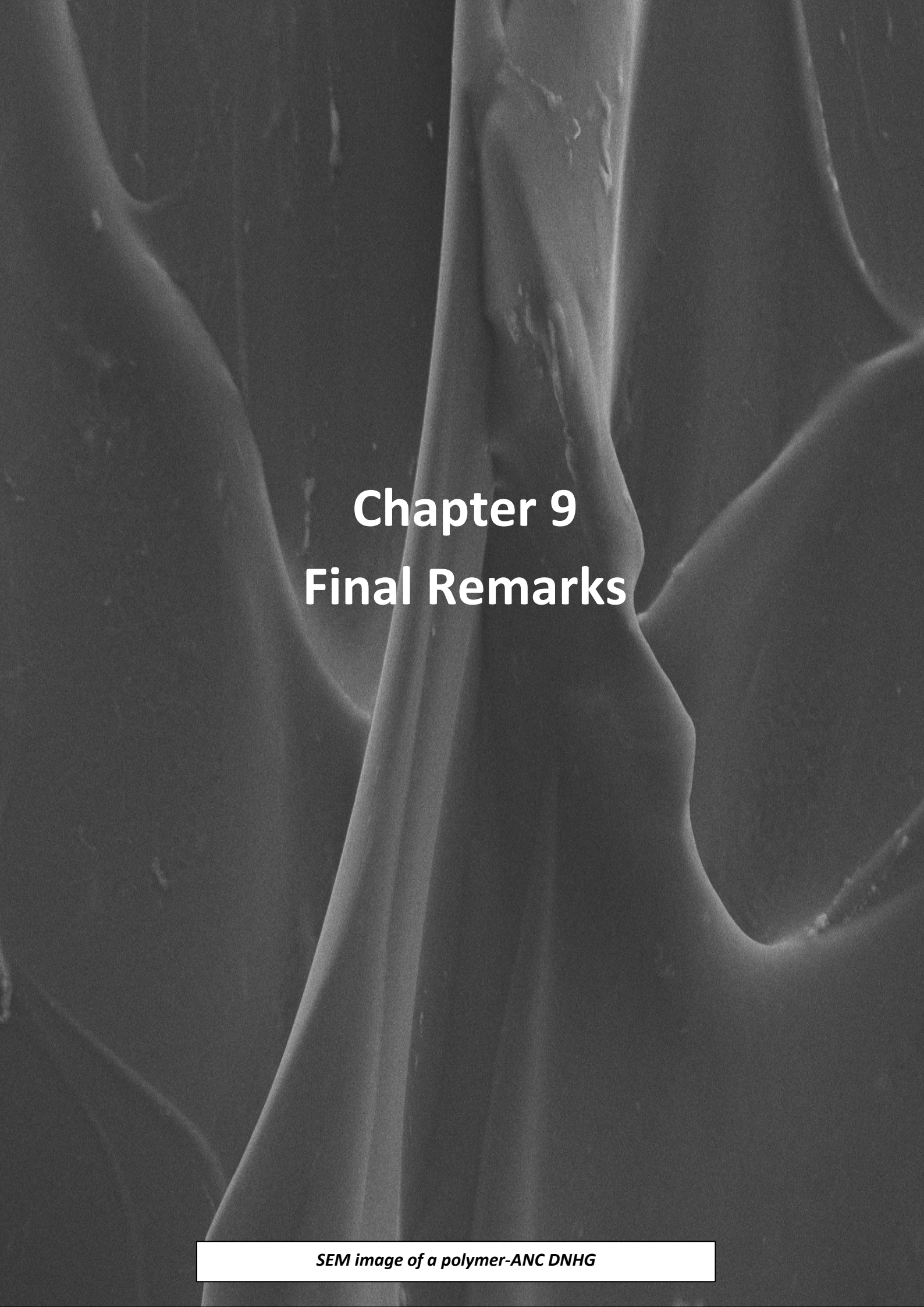
Figure 109 - SEM images of amine nanoceria (ANC) hydrogels with PAMPS and PAAm polymer grafts at varying magnifications. ANC are highlighted with white arrows.

8.4 Conclusion

This chapter explored the use of nanoceria as a starting point for a self-catalysis system, with GOx as a polymerization mediator and enhancer, as well as an oxygen degassing agent. PAMPS and PAAm were both successfully grafted on the surface of ANC with significantly improved conversion profiles with the addition of GOx. Both polymers were investigated in detail to find the best combination for the synthesis of a novel double network hydrogel. Ultimately, CAN and SDS were made redundant in the

synthesis route due to the combined efficacy of ANC and GOx at promoting graft polymerization. A strong double network hydrogel was synthesised based on the best concentration of ANC for both polymers in combination with GOx. It was revealed that the material could hold close to 90 % water content while benefiting from both networks containing nanocomposite structures.

Chapter 9
Final Remarks



SEM image of a polymer-ANC DNHG

9 Final remarks

9.1 Conclusions

This thesis investigated the synthesis of a series of double network hydrogels (DNHGs) with nano particles as macro cross linkers in the first network. The aim for these materials was for cartilage tissue repair and replacement. An aim of this research was to explore the effect on mechanical properties by varying the size and loading density of silica nanoparticles (SNPs) in the first network of DNHGs. This would allow for tailorability of the material.

In this work, two DNHGs were investigated to provide a comprehensive understanding of size and loading density. Firstly, carbodiimide chemistry was successfully used to cross link PAAc using ANSPS in the first network of a PAAc/PAAm DNHG. This was novel method of cross linking the first network of a DNHG had not been attempted prior to this research. No additional cross linking reagents were used, to ensure that gelation was purely based on the carbodiimide reaction. The results show that varying the size of ASNPs and loading concentration impacts the particle retention, mechanical properties and swelling ability of the hydrogels. It was found that overloading the DNHGs with ASNPs had occurred at 20 wt % and higher, where mechanical properties declined. This was attributed to a few factors, namely; agglomeration of ASNPs due to insufficient sonication during synthesis of the first network, inhomogeneous distribution of ASNPs due to a settling effect where ASNPs sink to the bottom during synthesis and particle losses due to leaking or percolation which create structural voids. Ultimately, an increase in compressive strength of 1,280 % was achieved with 50 nm ASNPs at 10 wt % loading, relative to the control. This DNHG provides insight into the potential use of carbodiimide chemistry in forming cross links with nanoparticles in hydrogels. This opens the door for further investigation with other polymers as well as other types of nanoparticles.

Next, PAMPS/PAAm DNHGs were formed with VSNPs in the first network. To understand the depth and effect of macro cross linking via nanoparticles, PAMPS was

photopolymerized in-situ with VSNPs. No additional cross linking agents were used, therefore once gelation occurred it was assumed that cross linking in the first network was successful. Sequentially, the second network was formed by photopolymerization of PAAm. In comparison to PAAc/PAAm hydrogels, PAMPS/PAAm hydrogels experienced overall larger particle losses when investigated by TGA. This was accounted for by the static nature of the photopolymerization allowing for VSNPs to settle at the bottom, causing inhomogeneous distribution before gelation occurs. Nonetheless, an increase in compressive strength of 900 % was achieved with 150 nm VSNPs at 20 wt % loading. FTIR data revealed that unreacted monomers remained present post-synthesis of the DNHG; hence an investigation into the kinetics and polymer conversion was carried out.

It was revealed that oxygen inhibition caused a lag in the commencement of the photopolymerization by impacting reaction kinetics, as well as a reduced polymer conversion. The introduction of GOx as a degassing agent allowed for minimal and non-cytotoxic photoinitiator concentrations to be used whilst achieving 100 % polymer conversion. This optimized the synthesis route by utilising less energy, lower concentration of photoinitiators, and shorter reaction times. The DNHGs benefited from increased polymer entanglement due to an increased polymer amount in the material as opposed to loose monomers. Both first and second networks were investigated for cytotoxic effects. It was found that GOx must be denatured at 60 °C post photopolymerization to ensure cell survival.

Subsequently, a novel pair of DNHGs was synthesised by grafting PAMPS and PAAm on the surface of nanoparticles. The first DNHG consisted of ASNPs with polymer grafts in both networks, and the second DNHG consisted of polymer grafts on amine nanoceria (ANC) in both networks. Cerium was used as the reaction initiator for SNP based grafting, whereas it was also a catalyst for ANC based grafts. Ultimately, ANC did not require an additional form of cerium catalyst (ammonium cerium nitrate) as it provided the self-catalytic properties itself. ASNP based hydrogels were successfully formed using thermal graft polymerization in the presence of GOx as a degassing agent and had improved mechanical properties compared to the in-situ photopolymerization counterparts in the previous chapter. Grafting the polymers on ASNPs drastically increased the mechanical properties of PAMPS/PAAm DNGHs, resulting in compressive

strengths up to 20 MPa, comparable to native articular cartilage. ANC based hydrogels benefited from a cyclic reaction between GOx by-products (H_2O_2) and the Ce^{3+}/ Ce^{4+} valence states of ANC. Polymer grafted on ANC in the presence of GOx experienced enhanced polymer conversion and kinetics due to the combination of oxygen removal and constant revival of ANC as a catalyst. The final ANC gels resulted in strong mechanical properties with compressive strengths up to 1.9 MPa. The pair of hydrogels synthesised by graft polymerization show promise potential tailorability based on nanoparticle size, loading density and polymer concentration.

Table 39 - A summary of the properties of articular cartilage and the properties of the double network hydrogels developed in this thesis

		Compressive Strengths (MPa)	Compressive Strain (%)	Water Content (%)
	Articular cartilage	~ 22 - 37	~ 30 - 80	~ 70
w/o Gox	DNHG containing SNP	0.8 ± 0.8	75.0 ± 6.0	88.2 ± 0.3
w/ GOx	DNHG containing SNP	3.6 ± 0.4	55.4 ± 4.1	68.3 ± 0.7
w/ GOx	DNHG grafted with SNP	13.9 ± 5.5	69.6 ± 6.4	63.4 ± 1.8
w/ GOx	DNHG grafted with NC	1.8 ± 0.1	60.9 ± 1.6	87.4 ± 2.4

The results from this thesis provide insight into the importance, and benefits, of oxygen inhibition. It also highlights the ability to control cross links in the first network of DNHGs using nanoparticles of varying size and concentration. Table 39 shows that DNHGs increase in compressive strength when GOx is present when compared to a DNHG without GOx, increasing from 0.8 MPa to 3.6 MPa, respectively. DNHG with grafted SNPs achieved an average of 14 MPa, within the higher range of DNHG properties achieved in current literature[63]. The presence of GOx also results in water content closer to that of native articular cartilage. In current literature, DNHGs are either synthesised in open vessels, or purged with nitrogen in an attempt to create an oxygen free atmosphere. The potential to use this effective degassing method to improve on DNHGs from literature could lead to advances in mechanical properties closer to native cartilage. In Chapter 6, the kinetics and conversion profiles of PAMPS and PAAm provided evidence into the need for an oxygen free atmosphere. The full

conversion of monomers during polymerisation produces a non-toxic material, removing the need for post synthesis steps such as purification and filtration. Under an oxygen rich atmosphere, or a nitrogen purged system, it was shown that it was not possible to reach 100 % conversion, despite high photoinitiator concentrations (2 wt %; commonly, 1 wt % is used for polymerisations). Under the presence of GOx it was shown that the reaction rate was faster, with conversion reaching 100 % with 0.05 wt % photoinitiator. These results indicate that current research in biomaterials requires more control over oxygen rich systems to be able to utilise the full potential of their material properties. In fact, GOx is a natural enzyme that can lead to more cost effective synthesis routes with faster kinetics that are easily scalable to larger operations. The progress in modern day material synthesis requires optimised synthesis routes, including the physical synthesis platform. In this case, closed vessel systems can become part of the past and open vessel synthesis a part of the future. The use of GOx has the potential to be incorporated into vast hydrogel synthesis systems, as well as other polymer based biomaterials, including 3D printed scaffolds.

Table 39 also provides a comparison between DNHGs that are synthesised by cross linking via SNPs, and DNHGs that are synthesised by grafting polymers onto the surface of SNPs. Current literature focuses on a general method of creating DNHGs with a nanocomposite structure where polymerisation occurs in an independent solution to the nanoparticles. Chapter 7 introduced a novel form of DNHG synthesis where the polymerisation is initiated *in-situ* from the surface of functionalised SNPs, to subsequently form the hydrogel networks. This method was introduced to increase the polymer-nanoparticle interactions, to give rise to enhanced mechanical properties. In combination with GOx, these DNHGs exhibited increased compressive strength close to that of native articular cartilage. The resulting hydrogels were more resistant to stress due to the stronger polymer-nanoparticle interactions between the hydrogel networks. This exciting material opens the door for optimisation and further research into hydrogels with tailorable properties based on their nanocomposite structures. The potential for graft polymerisation to be used in hydrogel synthesis can give rise to other novel materials with a wide range of properties depending on the type of polymer, and type and size of nanoparticles used. The use for such materials is not limited to

cartilage engineering applications, but can be used for both soft and hard tissue. The results from Chapter 7 and Chapter 8 can be the first step to a new form of hybrid nanocomposite hydrogel system that will enable highly tailorable properties based on the intricate nanostructure of the material.

An important result from Chapter 8 was the cyclic reaction between the valence states of nanoceria and GOx. A cyclical reaction occurred when the initiating system of nanoceria was reset due to the by-products of GOx, and vice-versa, resulting in an auto-catalytic system. This exciting result benefits from GOx as an oxygen quencher and as part of the reaction mechanism for the graft polymerisation. To date, there has been no literature between nanoceria and GOx in polymerisation techniques and biomaterial synthesis. This new graft polymerisation can have an impact on the development of new biomaterials, as well as enhancing previous ones. The techniques for degassing and polymerisation used in this thesis are not limited to hydrogel synthesis and can be applied to other 3D scaffold designs for a variety of tissue engineering applications. In conclusion, an optimized route was created for the synthesis of tailorable DNHGs with nanocomposite structures. Nanoparticle size and loading density, as well as polymer concentration and polymerization route were varied to understand the effect on mechanical properties. GOx achieved enhanced kinetics and improvements to the materials, opening the door for further investigation and incorporation into reaction mechanisms. The initial cytotoxicity studies revealed promising results for the single network polymers in the presence of GOx, leading the way to further *in-vitro*, and possibly *in-vivo*, studies for the future scope of this thesis. Finally, the combination of nanoparticles with GOx provided insight into a novel self-catalytic system, under controlled thermal conditions, for the synthesis of nanoceria-polymer based hydrogel with promising results.

9.2 Future work

The conclusions of this research reflected upon the different synthesis routes available to develop a strong and suitable DNHG for cartilage tissue engineering applications. The success of using ANC as a base for graft polymerization in the presence of GOx opens the door for further investigation. Varying the size of ANC prior to the graft polymerization should be studied to examine the impact on mechanical strength and conversion profiles due to the varying abundance of Ce^{4+}/ Ce^{3+} valence states. A detailed kinetics study that examines O_2, H_2O_2 and the changing valence states in nanoceria as well as polymer conversion is vital in understanding the mechanism of this self-catalysis system. These findings can be translated onto other polymers suitable for use in DNHG systems and other biomaterial applications. Further, natural cartilage is subject to daily cyclic compressions from routine activities; hence, the immediate future work should focus on dynamic mechanical analysis of the hydrogels. This is to understand the materials sustainability under cyclic loading. The materials synthesised in this thesis are considered non-biodegradable, therefore, a medium to long term study in a simulated body fluid must be considered to examine the potential degradation or stability of the material in the body. The solution this test is carried out within would be used for GPC analysis and ^{1}H NMR as well as inductively coupled plasma (ICP) analysis to examine polymer sizes that are released, content released and ions released, respectively. SEM has been used in this research to examine possible pore sizes of the hydrogels, a more accurate measurement can be achieved through mercury porosimetry. These measurements can reveal possible mesh size between pores as well as any impacts higher cross linking densities may have on pore size and interconnect diameters. To develop the materials in this research further, long term cytotoxicity studies and cell attachment profiles are required. Although the single networks showed positive results, it is important to determine whether the final material meets the criteria of cell proliferation and survival. Lastly, following the results and conclusions of mentioned future work, *in vivo* studies can be carried out in small mammal specimens such as rabbits, to understand how these materials would react in the body and to reveal further work that is required to enhance the material.

References

1. *13th Annual Report National Joint Registry for England, Wales, Northern Ireland and the Isle of Man*, 2016.
2. V. C. Mow, A. Ratcliffe and A. Robin Poole, *Biomaterials*, 1992, **13**, 67-97.
3. N. Kitamura, T. Kurokawa, T. Fukui, J. P. Gong and K. Yasuda, *BMC Musculoskeletal Disorders*, 2014, **15**, 222-222.
4. H. J. Kong, C. J. Kim, N. Huebsch, D. Weitz and D. J. Mooney, *Journal of the American Chemical Society*, 2007, **129**, 4518-4519.
5. G. A. Ateshian, *Nature materials*, 2007, **6**, 89-90.
6. N. Han, J. K. Johnson, P. A. Bradley, K. S. Parikh, J. J. Lannutti and J. O. Winter, *Journal of Functional Biomaterials*, 2012, **3**.
7. Q. Wang, R. Hou, Y. Cheng and J. Fu, *Soft Matter*, 2012, **8**, 6048-6056.
8. R. A. A. Muzzarelli, F. Greco, A. Busilacchi, V. Sollazzo and A. Gigante, *Carbohydrate Polymers*, 2012, **89**, 723-739.
9. E. B. Hunziker, T. M. Quinn and H. J. Häuselmann, *Osteoarthritis and Cartilage*, 2002, **10**, 564-572.
10. S. Akizuki, V. C. Mow, F. Müller, J. C. Pita, D. S. Howell and D. H. Manicourt, *Journal of Orthopaedic Research*, 1986, **4**, 379-392.
11. S. Wakitani, T. Goto, S. J. Pineda, R. G. Young, J. M. Mansour, A. I. Caplan and V. M. Goldberg, *JBJS*, 1994, **76**, 579-592.
12. N. J. Castro, S. A. Hacking and L. G. Zhang, *Annals of Biomedical Engineering*, 2012, **40**, 1628-1640.
13. T. Hardingham, S. Tew and A. Murdoch, *Arthritis Research & Therapy*, 2002, **4**, S63.
14. J. S. Temenoff and A. G. Mikos, *Biomaterials*, 2000, **21**, 431-440.
15. C. Chung and J. A. Burdick, *Advanced drug delivery reviews*, 2008, **60**, 243-262.
16. H. Madry, L. Gao, H. Eichler, P. Orth and M. Cucchiarini, *Stem Cells International*, 2017, **2017**, 1609685.
17. L. L. Johnson, *Arthroscopy : the journal of arthroscopic & related surgery : official publication of the Arthroscopy Association of North America and the International Arthroscopy Association*, 1986, **2**, 54-69.
18. J. A. Buckwalter, *The Journal of orthopaedic and sports physical therapy*, 1998, **28**, 192-202.
19. D. G. Stokes, G. Liu, I. B. Coimbra, S. Piera-Velazquez, R. M. Crowl and S. A. Jimenez, *Arthritis and rheumatism*, 2002, **46**, 404-419.
20. E. A. Makris, A. H. Gomoll, K. N. Malizos, J. C. Hu and K. A. Athanasiou, *Nature reviews. Rheumatology*, 2015, **11**, 21-34.
21. M. El-Deen, M. Garcia-Finana and Z. M. Jin, *Proceedings of the Institution of Mechanical Engineers. Part H, Journal of engineering in medicine*, 2006, **220**, 733-742.
22. R. Gandhi, H. Smith, K. A. Lefaivre, J. R. Davey and N. N. Mahomed, *The Journal of arthroplasty*, 2011, **26**, 29-35.
23. J. R. Steadman, W. G. Rodkey, S. B. Singleton and K. K. Briggs, *Operative Techniques in Orthopaedics*, 1997, **7**, 300-304.
24. D. D. Frisbie, J. T. Oxford, L. Southwood, G. W. Trotter, W. G. Rodkey, J. R. Steadman, J. L. Goodnight and C. W. McIlwraith, *Clinical orthopaedics and related research*, 2003, 215-227.

25. K. Mithoefer, R. J. Williams, 3rd, R. F. Warren, T. L. Wickiewicz and R. G. Marx, *The American journal of sports medicine*, 2006, **34**, 1413-1418.
26. K. Mithoefer, T. McAdams, R. J. Williams, P. C. Kreuz and B. R. Mandelbaum, *The American journal of sports medicine*, 2009, **37**, 2053-2063.
27. K. Mithoefer, T. J. Gill, B. J. Cole, R. J. Williams and B. R. Mandelbaum, *Cartilage*, 2010, **1**, 113-120.
28. G. Kish, L. Modis and L. Hangody, *Clinics in sports medicine*, 1999, **18**, 45-66, vi.
29. R. Gudas, R. J. Kalesinskas, V. Kimtys, E. Stankevicius, V. Toliusis, G. Bernotavicius and A. Smailys, *Arthroscopy : the journal of arthroscopic & related surgery : official publication of the Arthroscopy Association of North America and the International Arthroscopy Association*, 2005, **21**, 1066-1075.
30. M. Marcacci, E. Kon, M. Delcogliano, G. Filardo, M. Busacca and S. Zaffagnini, *The American journal of sports medicine*, 2007, **35**, 2014-2021.
31. M. Brittberg, A. Lindahl, A. Nilsson, C. Ohlsson, O. Isaksson and L. Peterson, *The New England journal of medicine*, 1994, **331**, 889-895.
32. L. Peterson, H. S. Vasiliadis, M. Brittberg and A. Lindahl, *The American journal of sports medicine*, 2010, **38**, 1117-1124.
33. G. Bentley, L. C. Biant, R. W. Carrington, M. Akmal, A. Goldberg, A. M. Williams, J. A. Skinner and J. Pringle, *The Journal of bone and joint surgery. British volume*, 2003, **85**, 223-230.
34. K. Mithoefer, *Sports medicine and arthroscopy review*, 2013, **21**, 31-37.
35. G. Filardo, E. Kon, A. Di Martino, F. Iacono and M. Marcacci, *The American journal of sports medicine*, 2011, **39**, 2153-2160.
36. W. Bartlett, J. A. Skinner, C. R. Gooding, R. W. Carrington, A. M. Flanagan, T. W. Briggs and G. Bentley, *The Journal of bone and joint surgery. British volume*, 2005, **87**, 640-645.
37. P. Vavken and D. Samartzis, *Osteoarthritis and Cartilage*, 2010, **18**, 857-863.
38. M. L. Oyen, *International Materials Reviews*, 2014, **59**, 44-59.
39. J. L. Drury and D. J. Mooney, *Biomaterials*, 2003, **24**, 4337-4351.
40. H. Tan, C. R. Chu, K. A. Payne and K. G. Marra, *Biomaterials*, 2009, **30**, 2499-2506.
41. H. Tan, C. M. Ramirez, N. Miljkovic, H. Li, J. P. Rubin and K. G. Marra, *Biomaterials*, 2009, **30**, 6844-6853.
42. P. Gupta, K. Vermani and S. Garg, *Drug Discovery Today*, 2002, **7**, 569-579.
43. J. Coburn, M. Gibson, P. A. Bandalini, C. Laird, H.-Q. Mao, L. Moroni, D. Seliktar and J. Elisseeff, *Smart structures and systems*, 2011, **7**, 213-222.
44. J. P. Gong, Y. Katsuyama, T. Kurokawa and Y. Osada, *Advanced Materials*, 2003, **15**, 1155-1158.
45. A. Agrawal, N. Rahbar and P. D. Calvert, *Acta biomaterialia*, 2013, **9**, 5313-5318.
46. K. S. Anseth, C. N. Bowman and L. Brannon-Peppas, *Biomaterials*, 1996, **17**, 1647-1657.
47. C. Chung, M. Beecham, R. L. Mauck and J. A. Burdick, *Biomaterials*, 2009, **30**, 4287-4296.
48. S. J. Bryant and K. S. Anseth, *Journal of biomedical materials research*, 2002, **59**, 63-72.
49. K. T. Nguyen and J. L. West, *Biomaterials*, 2002, **23**, 4307-4314.
50. R. El-Ayoubi, C. DeGrandpré, R. DiRaddo, A.-M. Yousefi and P. Lavigne, *Journal of Biomaterials Applications*, 2009, **25**, 429-444.

51. M. R. Safran, H. Kim and S. Zaffagnini, *The Journal of the American Academy of Orthopaedic Surgeons*, 2008, **16**, 306-311.
52. C. J. Little, N. K. Bawolin and X. Chen, *Tissue engineering. Part B, Reviews*, 2011, **17**, 213-227.
53. F. T. Moutos, L. E. Freed and F. Guilak, *Nature materials*, 2007, **6**, 162-167.
54. R. U. Repo and J. B. Finlay, *The Journal of bone and joint surgery. American volume*, 1977, **59**, 1068-1076.
55. J. S. Jurvelin, M. D. Buschmann and E. B. Hunziker, *Journal of biomechanics*, 1997, **30**, 235-241.
56. L. S. Teixeira, J. Feijen, C. A. van Blitterswijk, P. J. Dijkstra and M. Karperien, *Biomaterials*, 2012, **33**, 1281-1290.
57. S. J. Buwalda, K. W. Boere, P. J. Dijkstra, J. Feijen, T. Vermonden and W. E. Hennink, *Journal of controlled release : official journal of the Controlled Release Society*, 2014, **190**, 254-273.
58. M. Malkoch, R. Vestberg, N. Gupta, L. Mespouille, P. Dubois, A. F. Mason, J. L. Hedrick, Q. Liao, C. W. Frank, K. Kingsbury and C. J. Hawker, *Chemical Communications*, 2006, DOI: 10.1039/B603438A, 2774-2776.
59. B. Baroli, *Journal of Chemical Technology & Biotechnology*, 2006, **81**, 491-499.
60. A. S. Sawhney, C. P. Pathak and J. A. Hubbell, *Macromolecules*, 1993, **26**, 581-587.
61. P. A. Levett, F. P. Melchels, K. Schrobback, D. W. Hutmacher, J. Malda and T. J. Klein, *Acta biomaterialia*, 2014, **10**, 214-223.
62. A. K. Ekenseair, K. W. M. Boere, S. N. Tzouanas, T. N. Vo, F. K. Kasper and A. G. Mikos, *Biomacromolecules*, 2012, **13**, 2821-2830.
63. M. A. Haque, T. Kurokawa and J. P. Gong, *Polymer*, 2012, **53**, 1805-1822.
64. N. K. Simha, C. S. Carlson and J. L. Lewis, *Journal of materials science. Materials in medicine*, 2004, **15**, 631-639.
65. A. Nakayama, A. Kakugo, J. P. Gong, Y. Osada, M. Takai, T. Erata and S. Kawano, *Advanced Functional Materials*, 2004, **14**, 1124-1128.
66. Z. L. Wu, T. Kurokawa and J. P. Gong, *Bulletin of the Chemical Society of Japan*, 2011, **84**, 1295-1311.
67. D. Myung, W. Koh, A. Bakri, F. Zhang, A. Marshall, J. Ko, J. Noolandi, M. Carrasco, J. R. Cochran, C. W. Frank and C. N. Ta, *Biomedical microdevices*, 2007, **9**, 911-922.
68. S. S. Jang, W. A. Goddard and M. Y. S. Kalani, *The Journal of Physical Chemistry B*, 2007, **111**, 1729-1737.
69. L. Weng, A. Gouldstone, Y. Wu and W. Chen, *Biomaterials*, 2008, **29**, 2153-2163.
70. G. A. Abraham, A. A. de Queiroz and J. S. Roman, *Biomaterials*, 2001, **22**, 1971-1985.
71. J.-Y. Sun, X. Zhao, W. R. K. Illeperuma, O. Chaudhuri, K. H. Oh, D. J. Mooney, J. J. Vlassak and Z. Suo, *Nature*, 2012, **489**, 133-136.
72. C.-J. Wu, A. K. Gaharwar, P. J. Schexnailder and G. Schmidt, *Materials*, 2010, **3**.
73. M. Shen, L. Li, Y. Sun, J. Xu, X. Guo and R. K. Prud'homme, *Langmuir*, 2014, **30**, 1636-1642.
74. A. K. Gaharwar, P. J. Schexnailder, B. P. Kline and G. Schmidt, *Acta biomaterialia*, 2011, **7**, 568-577.
75. J. Yang and J. Zhao, *Materials Letters*, 2014, **120**, 36-38.
76. S. M. Lim, S. H. Oh, H. H. Lee, S. H. Yuk, G. I. Im and J. H. Lee, *Journal of Materials Science: Materials in Medicine*, 2010, **21**, 2593-2600.

77. C. Azuma, K. Yasuda, Y. Tanabe, H. Taniguro, F. Kanaya, A. Nakayama, Y. M. Chen, J. P. Gong and Y. Osada, *Journal of Biomedical Materials Research Part A*, 2007, **81A**, 373-380.
78. K. Yasuda, J. Ping Gong, Y. Katsuyama, A. Nakayama, Y. Tanabe, E. Kondo, M. Ueno and Y. Osada, *Biomaterials*, 2005, **26**, 4468-4475.
79. K. A. Athanasiou, M. P. Rosenwasser, J. A. Buckwalter, T. I. Malinin and V. C. Mow, *Journal of orthopaedic research : official publication of the Orthopaedic Research Society*, 1991, **9**, 330-340.
80. N. Kitamura, K. Yasuda, M. Ogawa, K. Arakaki, S. Kai, S. Onodera, T. Kurokawa and J. P. Gong, *The American journal of sports medicine*, 2011, **39**, 1160-1169.
81. Q. M. Yu, Y. Tanaka, H. Furukawa, T. Kurokawa and J. P. Gong, *Macromolecules*, 2009, **42**, 3852-3855.
82. H. R. Brown, *Macromolecules*, 2007, **40**, 3815-3818.
83. W. Stöber, A. Fink and E. Bohn, *Journal of Colloid and Interface Science*, 1968, **26**, 62-69.
84. S. K. Park, K. D. Kim and H. T. Kim, *Colloids and Surfaces A: Physicochemical and Engineering Aspects*, 2002, **197**, 7-17.
85. L. M. Rossi, L. Shi, F. H. Quina and Z. Rosenzweig, *Langmuir*, 2005, **21**, 4277-4280.
86. Slowing, II, J. L. Vivero-Escoto, C. W. Wu and V. S. Lin, *Adv Drug Deliv Rev*, 2008, **60**, 1278-1288.
87. H. Gao, W. Shi and L. B. Freund, *Proceedings of the National Academy of Sciences of the United States of America*, 2005, **102**, 9469-9474.
88. S. S. Davis, *Trends in biotechnology*, 1997, **15**, 217-224.
89. J. P. Gong, *Soft Matter*, 2010, **6**, 2583-2590.
90. K. Haraguchi and H.-J. Li, *Macromolecules*, 2006, **39**, 1898-1905.
91. G. Gao, G. Du, Y. Cheng and J. Fu, *Journal of Materials Chemistry B*, 2014, **2**, 1539-1548.
92. Y. An, M. Chen, Q. Xue and W. Liu, *Journal of Colloid and Interface Science*, 2007, **311**, 507-513.
93. M. Marini, B. Pourabbas, F. Pilati and P. Fabbri, *Colloids and Surfaces A: Physicochemical and Engineering Aspects*, 2008, **317**, 473-481.
94. R. Dong, S. Krishnan, B. A. Baird, M. Lindau and C. K. Ober, *Biomacromolecules*, 2007, **8**, 3082-3092.
95. A. Williams and I. T. Ibrahim, *Chemical Reviews*, 1981, **81**, 589-636.
96. M. Rafat, F. Li, P. Fagerholm, N. S. Lagali, M. A. Watsky, R. Munger, T. Matsuura and M. Griffith, *Biomaterials*, 2008, **29**, 3960-3972.
97. K. H. Bouhadir, D. S. Hausman and D. J. Mooney, *Polymer*, 1999, **40**, 3575-3584.
98. W. E. Hennink and C. F. van Nostrum, *Advanced Drug Delivery Reviews*, 2012, **64**, 223-236.
99. H. Brondsted, C. Andersen and L. Hovgaard, *Journal of controlled release : official journal of the Controlled Release Society*, 1998, **53**, 7-13.
100. P. Gacesa, *Carbohydrate Polymers*, 1988, **8**, 161-182.
101. F. Yokoyama, I. Masada, K. Shimamura, T. Ikawa and K. Monobe, *Colloid and Polymer Science*, 1986, **264**, 595-601.
102. B. D. Fairbanks, M. P. Schwartz, C. N. Bowman and K. S. Anseth, *Biomaterials*, 2009, **30**, 6702-6707.
103. O. W. Webster, *Science*, 1991, **251**, 887.

104. M. D. Goodner and C. N. Bowman, in *Solvent-Free Polymerizations and Processes*, American Chemical Society, 1999, vol. 713, ch. 14, pp. 220-231.
105. T. E. Long and M. O. Hunt, *Solvent-Free Polymerizations and Processes*, American Chemical Society, 1999.
106. D. Dendukuri, P. Panda, R. Haghgooie, J. M. Kim, T. A. Hatton and P. S. Doyle, *Macromolecules*, 2008, **41**, 8547-8556.
107. S. J. Bryant, C. R. Nuttelman and K. S. Anseth, *Journal of biomaterials science. Polymer edition*, 2000, **11**, 439-457.
108. C. G. Williams, A. N. Malik, T. K. Kim, P. N. Manson and J. H. Elisseeff, *Biomaterials*, 2005, **26**, 1211-1218.
109. A. Sabnis, M. Rahimi, C. Chapman and K. T. Nguyen, *Journal of Biomedical Materials Research Part A*, 2009, **91A**, 52-59.
110. A. K. Gaharwar, C. Rivera, C.-J. Wu, B. K. Chan and G. Schmidt, *Materials Science and Engineering: C*, 2013, **33**, 1800-1807.
111. I. Mironi-Harpaz, D. Y. Wang, S. Venkatraman and D. Seliktar, *Acta biomaterialia*, 2012, **8**, 1838-1848.
112. W. Xiao, J. He, J. W. Nichol, L. Wang, C. B. Hutson, B. Wang, Y. Du, H. Fan and A. Khademhosseini, *Acta biomaterialia*, 2011, **7**, 2384-2393.
113. C. Zhong, J. Wu, C. A. Reinhart-King and C. C. Chu, *Acta biomaterialia*, 2010, **6**, 3908-3918.
114. G. C. Ingavle, S. H. Gehrke and M. S. Detamore, *Biomaterials*, 2014, **35**, 3558-3570.
115. S. J. Bryant, C. R. Nuttelman and K. S. Anseth, *Journal of Biomaterials Science, Polymer Edition*, 2000, **11**, 439-457.
116. I. Mironi-Harpaz, D. Y. Wang, S. Venkatraman and D. Seliktar, *Acta biomaterialia*, 2012, **8**, 1838-1848.
117. C. Decker and A. D. Jenkins, *Macromolecules*, 1985, **18**, 1241-1244.
118. F. Oytun, M. U. Kahveci and Y. Yagci, *Journal of Polymer Science Part A: Polymer Chemistry*, 2013, **51**, 1685-1689.
119. J.-P. Fouassier, Munich; New York; Cincinnati.
120. S. C. Ligon, B. Husár, H. Wutzel, R. Holman and R. Liska, *Chemical Reviews*, 2014, **114**, 557-589.
121. E. Andrzejewska, *Progress in Polymer Science*, 2001, **26**, 605-665.
122. S. Inbar, H. Linschitz and S. G. Cohen, *Journal of the American Chemical Society*, 1982, **104**, 1679-1682.
123. C. E. Hoyle and C. N. Bowman, *Angewandte Chemie International Edition*, 2010, **49**, 1540-1573.
124. W.-Y. Chiang and W.-J. Shu, *Die Angewandte Makromolekulare Chemie*, 1988, **160**, 41-66.
125. R. Shenoy and C. N. Bowman, *Macromolecules*, 2010, **43**, 7964-7970.
126. L. Cokbaglan, N. Arsu, Y. Yagci, S. Jockusch and N. J. Turro, *Macromolecules*, 2003, **36**, 2649-2653.
127. J. Lalevée, M.-A. Tehfe, D. Gigmes and J. P. Fouassier, *Macromolecules*, 2010, **43**, 6608-6615.
128. R. K. Sharma and J. L. Fry, *The Journal of Organic Chemistry*, 1983, **48**, 2112-2114.
129. C. Walling and M. J. Gibian, *Journal of the American Chemical Society*, 1965, **87**, 3413-3417.

130. P. Barto, in *Stereolithography*, ed. P. J. Bártolo, Springer US, 2011, vol. 1, ch. 7, pp. 169-170.
131. K. Studer, C. Decker, E. Beck and R. Schwalm, *Progress in Organic Coatings*, 2003, **48**, 92-100.
132. Y. Yagci, S. Jockusch and N. J. Turro, *Macromolecules*, 2010, **43**, 6245-6260.
133. J.-P. Fouassier, in *Photoinitiation, Photopolymerization, and Photocuring: Fundamentals and Applications*, ed. J.-P. Fouassier, Hanser Gardner Publications, 1995-01, vol. 1, ch. 5, p. 199.
134. F. R. Wight, *Journal of Polymer Science: Polymer Letters Edition*, 1978, **16**, 121-127.
135. A. K. O'Brien and C. N. Bowman, *Macromolecules*, 2006, **39**, 2501-2506.
136. R. Chapman, A. J. Gormley, K.-L. Herpoldt and M. M. Stevens, *Macromolecules*, 2014, **47**, 8541-8547.
137. Z. Tao, R. A. Raffel, A. K. Souid and J. Goodisman, *Biophysical journal*, 2009, **96**, 2977-2988.
138. A. J. Gormley, R. Chapman and M. M. Stevens, *Nano Letters*, 2014, **14**, 6368-6373.
139. L. Xu, N. Sheybani, W. A. Yeudall and H. Yang, *Biomaterials science*, 2015, **3**, 250-255.
140. D. R. Albrecht, V. L. Tsang, R. L. Sah and S. N. Bhatia, *Lab on a Chip*, 2005, **5**, 111-118.
141. J. Baier Leach, K. A. Bivens, C. W. Patrick Jr and C. E. Schmidt, *Biotechnology and Bioengineering*, 2003, **82**, 578-589.
142. C. G. Williams, A. N. Malik, T. K. Kim, P. N. Manson and J. H. Elisseeff, *Biomaterials*, 2005, **26**, 1211-1218.
143. R. Shenoy and C. N. Bowman, *Biomaterials*, 2012, **33**, 6909-6914.
144. B. J. Berron, L. M. Johnson, X. Ba, J. D. McCall, N. J. Alvey, K. S. Anseth and C. N. Bowman, *Biotechnology and Bioengineering*, 2011, **108**, 1521-1528.
145. T. von Werne and T. E. Patten, *Journal of the American Chemical Society*, 1999, **121**, 7409-7410.
146. A. El Harrak, G. Carrot, J. Oberdisse, J. Jestin and F. Boué, *Polymer*, 2005, **46**, 1095-1104.
147. T. Wu, Y. Zhang, X. Wang and S. Liu, *Chemistry of Materials*, 2008, **20**, 101-109.
148. S. Kim, E. Kim, S. Kim and W. Kim, *Journal of Colloid and Interface Science*, 2005, **292**, 93-98.
149. P. Salarizadeh, M. Abdollahi and M. Javanbakht, *Iranian Polymer Journal*, 2012, **21**, 661-668.
150. T. Sahu, S. Singh Bisht, K. Ranjan Das and S. Kerkar, *Current Nanoscience*, 2013, **9**, 588-593.
151. U. Taylor, D. Tiedemann, C. Rehbock, W. A. Kues, S. Barcikowski and D. Rath, *Beilstein journal of nanotechnology*, 2015, **6**, 651-664.
152. E. Moretti, G. Terzuoli, T. Renieri, F. Iacoponi, C. Castellini, C. Giordano and G. Collodel, *Andrologia*, 2013, **45**, 392-396.
153. S. Horikoshi and N. Serpone, in *Microwaves in Nanoparticle Synthesis*, Wiley-VCH Verlag GmbH & Co. KGaA, 2013, DOI: 10.1002/9783527648122.ch5, pp. 75-105.
154. K. Reed, A. Cormack, A. Kulkarni, M. Mayton, D. Sayle, F. Klaessig and B. Stadler, *Environmental Science: Nano*, 2014, **1**, 390-405.
155. K. Matsui, T. Kyotani and A. Tomita, *Advanced Materials*, 2002, **14**, 1216-1219.
156. J. M. Dowding, S. Das, A. Kumar, T. Dosani, R. McCormack, A. Gupta, T. X. T. Sayle, D. C. Sayle, L. von Kalm, S. Seal and W. T. Self, *ACS Nano*, 2013, **7**, 4855-4868.
157. M. Niederberger, *Accounts of Chemical Research*, 2007, **40**, 793-800.

158. S. Abanades, A. Legal, A. Cordier, G. Peraudeau, G. Flamant and A. Julbe, *Journal of Materials Science*, 2010, **45**, 4163-4173.
159. S. Deshpande, S. Patil, S. V. N. T. Kuchibhatla and S. Seal, *Applied Physics Letters*, 2005, **87**, 133113.
160. S. Soren, M. Bessoi and P. Parhi, *A rapid microwave initiated polyol synthesis of cerium oxide nanoparticle using different cerium precursors*, 2015.
161. A. Pinna, L. Malfatti, G. Galleri, R. Manetti, S. Cossu, G. Rocchitta, R. Migheli, P. A. Serra and P. Innocenzi, *RSC Advances*, 2015, **5**, 20432-20439.
162. I. Celardo, J. Z. Pedersen, E. Traversa and L. Ghibelli, *Nanoscale*, 2011, **3**, 1411-1420.
163. E. G. Heckert, A. S. Karakoti, S. Seal and W. T. Self, *Biomaterials*, 2008, **29**, 2705-2709.
164. C. Lv, W. Di, Z. Liu, K. Zheng and W. Qin, *Analyst*, 2014, **139**, 4547-4555.
165. R. Guo, Y. Wang, S. Yu, W. Zhu, F. Zheng, W. Liu, D. Zhang and J. Wang, *RSC Advances*, 2016, **6**, 59939-59945.
166. T. J. Sworski, H. A. Mahlman and R. W. Matthews, *The Journal of Physical Chemistry*, 1971, **75**, 250-255.
167. B. Sitharaman, *Nanobiomaterials handbook*, CRC Press, 2016.
168. H. Chen, F. Yang, R. Hu, M. Zhang, B. Ren, X. Gong, J. Ma, B. Jiang, Q. Chen and J. Zheng, *Journal of Materials Chemistry B*, 2016, **4**, 5814-5824.
169. M. Jerabek, Z. Major and R. W. Lang, *Polymer Testing*, 2010, **29**, 302-309.
170. E. S. Gil and S. M. Hudson, *Progress in Polymer Science*, 2004, **29**, 1173-1222.
171. A. K. Bajpai, S. K. Shukla, S. Bhanu and S. Kankane, *Progress in Polymer Science*, 2008, **33**, 1088-1118.
172. E. Ruel-Gariépy and J.-C. Leroux, *European Journal of Pharmaceutics and Biopharmaceutics*, 2004, **58**, 409-426.
173. D. Sehgal and I. K. Vijay, *Analytical Biochemistry*, 1994, **218**, 87-91.
174. S. Sam, L. Touahir, J. Salvador Andresa, P. Allongue, J. N. Chazalviel, A. C. Gouget-Laemmel, C. Henry de Villeneuve, A. Moraillon, F. Ozanam, N. Gabouze and S. Djebbar, *Langmuir*, 2010, **26**, 809-814.
175. J. V. Staros, R. W. Wright and D. M. Swingle, *Analytical Biochemistry*, 1986, **156**, 220-222.
176. A. Hatch, G. Hansmann and S. K. Murthy, *Langmuir*, 2011, **27**, 4257-4264.
177. S. Van Vlierberghe, P. Dubruel and E. Schacht, *Biomacromolecules*, 2011, **12**, 1387-1408.
178. J. Zaragoza, N. Babhadiashar, V. O'Brien, A. Chang, M. Blanco, A. Zabalegui, H. Lee and P. Asuri, *PLOS ONE*, 2015, **10**, e0136293.
179. A. S. Hoffman, *Advanced Drug Delivery Reviews*, 2012, **64**, 18-23.
180. A. Li, A. Wang and J. Chen, *Journal of Applied Polymer Science*, 2004, **92**, 1596-1603.
181. B. Smitha, S. Sridhar and A. A. Khan, *Macromolecules*, 2004, **37**, 2233-2239.
182. C. Peniche, W. Argüelles-Monal, N. Davidenko, R. Sastre, A. Gallardo and J. San Román, *Biomaterials*, 1999, **20**, 1869-1878.
183. X. H. Wang, D. P. Li, W. J. Wang, Q. L. Feng, F. Z. Cui, Y. X. Xu, X. H. Song and M. van der Werf, *Biomaterials*, 2003, **24**, 3213-3220.
184. D. H.-K. Ma, J.-Y. Lai, H.-Y. Cheng, C.-C. Tsai and L.-K. Yeh, *Biomaterials*, 2010, **31**, 6647-6658.
185. T. Iwasita and E. Pastor, *Electrochim Acta*, 1994, **39**, 531-537.
186. Y. Maeda, T. Higuchi and I. Ikeda, *Langmuir*, 2000, **16**, 7503-7509.

187. J. I. Ngadaonye, M. O. Cloonan, L. M. Geever and C. L. Higginbotham, *Journal of Polymer Research*, 2011, **18**, 2307-2324.
188. P. Ferreira, J. F. J. Coelho and M. H. Gil, *International Journal of Pharmaceutics*, 2008, **352**, 172-181.
189. A. Beganskienė, V. Sirutkaitis, M. Kurtinaitienė, R. Juškėnas and A. Kareiva, *Mater Sci (Medžiagotyra)*, 2004, **10**, 287-290.
190. A. Lankoff, M. Arabski, A. Wegierek-Ciuk, M. Kruszewski, H. Lisowska, A. Banasik-Nowak, K. Rozga-Wijas, M. Wojewodzka and S. Slomkowski, *Nanotoxicology*, 2012, **7**, 235-250.
191. M. Ashraful Alam, M. Takafuji and H. Ihara, *Journal of Colloid and Interface Science*, 2013, **405**, 109-117.
192. O. Stoilova, N. Koseva, N. Manolova and I. Rashkov, *Polymer Bulletin*, 1999, **43**, 67-73.
193. Y. A. Aggour, *Acta Polymerica*, 1993, **44**, 97-99.
194. S. Çavuş, *Journal of Polymer Science Part B: Polymer Physics*, 2010, **48**, 2497-2508.
195. H. Zhu and X. Yao, *Journal of Macromolecular Science, Part A*, 2013, **50**, 175-184.
196. J. V. C. K. D. G. Bradley, *Photoinitiators for free radical cationic & anionic photopolymerisation*, J. Wiley in association with SITA Technology, 2 edn., 1998.
197. C. G. Armstrong and V. C. Mow, *JBJS*, 1982, **64**.
198. M. Abdollahi, M. Rouhani, M. Hemmati and P. Salarizadeh, *Polymer International*, 2013, **62**, 713-720.
199. J. Zhang, X. Xie, C. Li, H. Wang and L. Wang, *RSC Advances*, 2015, **5**, 29757-29765.
200. F. Gai, T. Zhou, G. Chu, Y. Li, Y. Liu, Q. Huo and F. Akhtar, *Dalton Transactions*, 2016, **45**, 508-514.
201. F. Caputo, M. Mameli, A. Sienkiewicz, S. Licoccia, F. Stellacci, L. Ghibelli and E. Traversa, *Scientific Reports*, 2017, **7**, 4636.
202. A. A. Ansari, P. R. Solanki and B. D. Malhotra, *Journal of Biotechnology*, 2009, **142**, 179-184.
203. S. R. S. Ting, J. M. Whitelock, R. Tomic, C. Gunawan, W. Y. Teoh, R. Amal and M. S. Lord, *Biomaterials*, 2013, **34**, 4377-4386.